

*ÉCOLE DOCTORALE de Physique et Chimie-Physique*  
Institut de Physique et Chimie des matériaux de Strasbourg

**THÈSE** présentée par :

**Guillaume CHAUMY**

soutenue le : 11 décembre 2019

pour obtenir le grade de : **Docteur de l'université de Strasbourg**

Discipline/ Spécialité : Physique de la matière condensée

**Tunable metal-organic interfaces for  
spin electronics**

**THÈSE dirigée par :**

**M. Bernard DOUDIN**  
**M. Paolo SAMORÌ**

Professeur, Université de Strasbourg  
Professeur, Université de Strasbourg

**RAPPORTEURS :**

**Mme. Laetitia BERNARD**

**M. Peter DOWBEN**

Chargée de recherche, Swiss Federal Laboratories for  
Materials Science and Technology  
Professeur, University of Nebraska-Lincoln

---

**AUTRES MEMBRES DU JURY :**

**M. Michel CALAME**  
**M. Stéphane MÉRY**

Professeur, University of Basel  
Chargé de recherche, CNRS (IPCMS)



## Table of Contents

List of abbreviations .....	IV
Remerciements (acknowledgments in French) .....	VII
Résumé de thèse (summary in French) .....	IX
Introduction .....	1
<b>Part 1 FUNDAMENTALS AND BACKGROUNDS</b> .....	<b>7</b>
I. Organic semiconductors .....	9
I.1. Conjugated polymers .....	9
I.1.1. Conjugated polymer thin films.....	11
I.1.2. Charge carriers .....	13
I.1.3. Disorder.....	15
I.2. Charge transport .....	15
I.2.1. Miller-Abrahams' hopping rate.....	16
I.2.2. Marcus hopping rate .....	16
I.2.3. Gaussian disorder model .....	17
I.2.4. Variable range hopping .....	20
I.2.5. The metal-insulator transition and the mobility edge .....	22
I.3. Charge injection .....	25
I.3.1. Energy levels at interface .....	25
I.3.2. Schottky effect and barrier height .....	27
I.3.3. Injection limited current .....	30
I.3.4. Tuning charge injection.....	32
I.4. Doping .....	33
I.4.1. Chemical doping.....	34
I.4.2. Electrochemical doping.....	35
I.5. Devices .....	36
I.5.1. Organic field-effect transistors .....	37
I.5.2. Electrolyte-gated organic field-effect transistors .....	41
I.5.3. Geometry-dependent properties.....	43
I.5.4. Contact resistance.....	44
I.5.5. Mobility extraction.....	47
I.5.6. Downscaling of (EG)OFETs .....	48

II. Organic spintronics.....	61
II.1. Spintronic concepts.....	61
II.1.1. Magnetic materials.....	62
II.1.2. Magnetoresistances.....	64
II.1.3. Spin injection.....	70
II.1.4. Spin detection.....	74
II.2 Organic materials for spin electronics.....	76
II.2.1. Relevance of organic materials and their drawbacks.....	76
II.2.2. Organic spin-valves.....	78
II.2.3. Spinterfaces.....	82
II.2.4. Fringe-field issues in organic spintronics.....	84
<b>Part 2 NUMERICAL COMPUTATION AND EXPERIMENTAL WORK.....</b>	<b>93</b>
III. Current crowding effect.....	95
III.1. Extended injection/detection interfaces.....	95
III.2. Outcomes for organic electronics and spintronics.....	98
III.2.1. Tuning of the channel length.....	99
III.2.2. How current crowding impacts the MR of spin-valves.....	100
IV. Interface resistance of EGOFETs.....	107
IV.1. PBTTT thin film.....	107
IV.2. The low contact resistance of EGOFETs.....	110
IV.2.1. Contact resistance extrapolation.....	110
IV.2.2. Gate-dependent contact resistance.....	114
IV.2.3. Temperature-dependent contact resistance.....	116
IV.2.4. Scaling of the contact resistance.....	117
IV.3. Magnetic electrodes for spin injection.....	121
IV.4. Limiting the transfer length influence.....	124
V. EGOFETs in a magnetic field.....	131
V.1. Magnetotransport.....	131
V.2. Interface versus bulk magnetoresistance.....	135
Conclusion and perspectives.....	145
A. Device fabrication.....	151
A.1. Electrodes patterning.....	151
A.2. PBTTT deposition.....	154

A.3. Electrolyte gel .....	155
B. PBTTT-based EGOFETs .....	159
B.1. Room temperature electrical characterization.....	159
B.2. Low temperature electrical characterization .....	165
C. Design issues for planar devices involving high-conductivity organics.....	173
C.1. Point effect.....	173
C.2. Channel broadening.....	174
D. Hall measurements on EGOFETs .....	177

## List of abbreviations

1DT	1-decanethiol
6T	Sexithiophene
AMR	Anisotropic magnetoresistance
DOS	Density of state
DP	D'yakonov-Perel
EDL	Electric double layer
EGOFET	Electrolyte-gated field-effect transistor
EY	Elliot-Yafet
FET	Field-effect transistor
FM	Ferromagnetic
FN	Fowler-Nordheim
FOTS	Tridecafluorooctyltrichlorosilan
gFP	Gated 4-probe
GMR	Giant magnetoresistance
HFI	Hyperfine interaction
HMDS	Hexamethyldisilazane
HOMO	Highest occupied molecular level
IETS	Inelastic electron tunnelling spectroscopy
IL	Injection limited
ISHE	Inverse spin-Hall effect
KPM	Kelvin probe microscopy
LED	Light emitting diode
LSMO	$\text{La}_{1-x}\text{Sr}_x\text{MnO}_3$
LUMO	Lowest occupied molecular level
MR	Magnetoresistance
MRAM	Magnetoresistive random-access memory
MTJ	Magnetic tunnel junction
NM	Non-magnetic
ODOS	Occupied density of state
OFET	Organic field-effect transistor
OLED	Organic light emitting diode
OMAR	Organic magnetoresistance

OSC	Organic semiconductor
OSV	Organic spin-valve
OTS	Octadecyltrichlorosilane
P3HT	Poly(3-hexylthiophène)
PBTTT	poly(2,5-bis(3-tetradecylthiophen-2-yl)thieno[3,2-b]thiophene)
PFDT	1H, 1H, 2H, 2H-perfluorodecanethiol
RS	Richardson-Schottky
SAM	Self-assembled monolayer
SC	Semiconductor
SHIPS	Spin-hybridization-induced polarized state
SOC	Spin-orbit coupling
SSD	Solid-state drives
STT	Spin torque transfer
SV	Spin-valve
TC/BC	Top contact/bottom contact
TG/BG	Top gate/bottom gate
TLM	Transmission line method
TMR	Tunnel magnetoresistance
UHV	Ultra high vacuum



## Remerciements

Je souhaite tout d'abord remercier les membres de mon jury Laetitia Bernard, Peter Dowben, Michel Calame et Stéphane Méry qui ont accepté d'évaluer mon travail de thèse. J'en suis d'autant plus reconnaissant qu'ils m'ont ménagé lors de la séance de questions, qui, bien que courte, fut instructive.

Un énorme merci, bien évidemment, à mes deux directeurs de thèse Bernard Doudin et Paolo Samorì, sans qui rien n'aurait été possible. Les nombreux conseils et discussions m'ont guidé à travers le monde de l'électronique organique, et la collaboration IPCMS-ISIS fut très enrichissante.

Je dois également beaucoup à Tindara Verduci et Silvia Zanettini, précédentes doctorantes du groupe, qui m'ont permis de me lancer dans les meilleures conditions dans cette thèse en me transmettant leur expérience avec patience et pédagogie.

La bonne humeur et la bonne ambiance du bureau 1053 ont été importantes durant ces trois ans, où nous avons plutôt bien jonglé entre discussions pas toujours sérieuses, et travail appliqué. J'adresse donc un grand merci à Donald Mouafo, Ulrich Noumbe, Peter Dunne, Léo Colombier, Loïc Moczko et Xin Zhang. Cette convivialité s'étend à l'ensemble du laboratoire grâce aux initiatives de l'ADDEPT et ses irréductibles membres, François Roulland en tête, rendant la vie à l'IPCMS plus facile. Je n'oublie pas non plus les coéquipiers (et adversaires) rugbymen et footballeurs dont la liste est bien trop longue pour être écrite ici.

La fabrication d'échantillons m'a demandé de passé beaucoup de temps en salle blanche où l'aide de Romain Bernard, Sabine Siegwald et Hicham Majjad a été plus que précieuse, et avec qui j'ai parlé de choses diverses et variées au-delà du cadre professionnel. La coupe du tournoi de pétanque trônant dans le bureau de Romain atteste de notre bonne entente. En tout cas, un grand merci à vous également.

Le cryostat nous a fait passer de mauvaises nuits (en tout cas à moi !) mais j'ai toujours pu compter sur la « team cryostat » composée principalement de Jean-François Dayen et Fabien Chevrier pour gérer la situation au mieux. J'ai appris énormément à leurs côtés.

Un peu esseulé à l'IPCMS sur mon sujet de thèse, j'ai pu compter sur Marc-Antoine Stoeckel, à l'ISIS, pour m'éclairer dans les moments de doute, ainsi que Marco Carroli et Agostino Galanti. Merci également à Éloïse Devaux pour sa disponibilité pour les découpes FIB.

Merci à coach Etienne Lorchat, François Fernique, Arthur Baumann et Kévin Lévêque-Simon que j'ai connus à la fac et finalement suivis en thèse avec un peu de retard. Enfin, merci à toutes les personnes que j'ai rencontré ces trois dernières années, que ce soit pour un coup de main ou une simple pause café, parfois à rallonge.

Pour finir, merci à ma famille pour leur présence à ma soutenance et tout au long de ma (longue) scolarité et bien sûr un immense merci à Laurine pour tout ce que tu m'apportes au quotidien.



# Résumé de thèse

## Introduction

L'objectif de cette thèse est de réaliser des dispositifs hybrides organique-inorganiques ayant une résistance d'interface appropriée pour l'électronique de spin, en vue de la fabrication de vannes de spin organiques. Les matériaux organiques ont attiré l'attention de la communauté scientifique en raison de leurs propriétés uniques telles que leur facilité et faible coût de fabrication, leur modularité chimique, leur flexibilité mécanique et leur utilisation en solution à basse température ( $< 180$  °C) sur de grandes surfaces. De plus, certains semi-conducteurs organiques sont biocompatibles pour des applications en médecine. Dans l'optique du transport de spin, leur avantage est qu'ils gardent l'information de spin beaucoup plus longtemps que les matériaux inorganiques, grâce à leur structure chimique essentiellement constituée de carbone et d'hydrogène.

Le potentiel de l'électronique organique est conséquent, notamment par la diversité de méthode de dépôt comme l'impression ou la pulvérisation en aérosol et la réalisation d'électronique flexible. Des dispositifs organiques ont émergé ces dernières années comme les transistors à effet de champ organiques (OFETs), les diodes électroluminescentes organiques (OLEDs) et les cellules photovoltaïques organiques (OPVs). La technologie OLED est d'ores et déjà commercialisée par LG pour ses écrans à contraste dit infini, et des panneaux solaires organiques enroulables sont également en vente par différentes entreprises.

L'essor des matériaux organiques est récent car leur mobilité électronique a été pendant longtemps trop faibles pour des applications industrielles, notamment à cause de leurs désordres moléculaires et du transport par saut. Cependant, les efforts de la communauté scientifique ont abouti à la synthèse de nouveaux matériaux dont les performances électriques sont adaptées à la fabrication de dispositifs électroniques<sup>1</sup>. Le problème majeur qui reste néanmoins à surmonter est la résistance d'interface entre les électrodes métalliques et les matériaux organiques, généralement trop élevée pour une électronique organique efficiente. Une piste suivie dans cette thèse pour réduire la résistance de contact est l'utilisation de la structure de transistor à effet de champ organique à grilles électrolytiques (EGOFET, figure A). Les EGOFETs

présentent en effet une faible résistance d'interface<sup>2</sup>, en plus de permettre un dopage très efficace du canal organique<sup>3</sup>.

La spintronique vise à utiliser le spin des électrons comme information, en plus ou à la place de leurs charges. Ce domaine ouvre la porte à de nouveaux dispositifs qui pourrait s'affranchir de l'effet Joule et avoir de meilleures performances et une plus faible consommation électrique que la technologie actuelle. La spintronique a fait ses débuts en 1988 avec la découverte de la magnétorésistance géante<sup>4,5</sup> (GMR) qui s'est traduite par le développement des disques durs, révolutionnant le stockage d'information.

Le choix de matériaux organiques pour des applications en électronique de spin est motivé par la capacité des matériaux carbonés à conserver l'information de spin pendant une « longue » période, de l'ordre de la microseconde, environ trois ordres de grandeur plus longue que les matériaux inorganiques<sup>6,7</sup>. Cette échelle de temps est suffisamment grande pour permettre la manipulation des spins dans les dispositifs. Toutefois, comme les matériaux organiques sont de moins bons conducteurs que leurs homologues inorganiques, la distance que peut parcourir un porteur de spin avant de perdre l'information est seulement légèrement supérieure dans les matériaux organiques. La structure EGOFET est donc d'autant plus importante puisqu'elle permet d'atteindre des conductivités électriques particulièrement élevées.

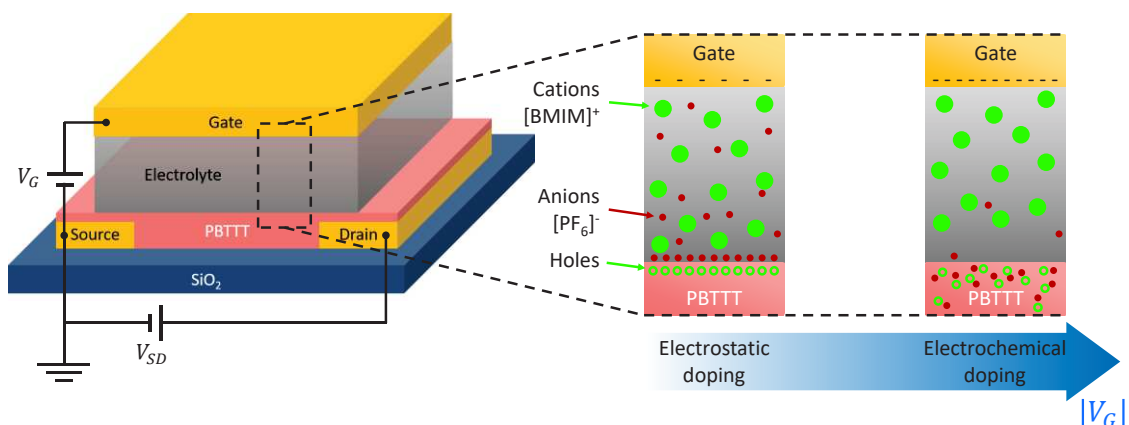


**Figure A** Schéma de principe d'un transistor à effet de champ organique à grille électrolytique. Sous l'effet du potentiel de grille, les ions mobiles de l'électrolyte (les anions dans notre cas) migrant vers l'interface entre l'électrolyte et le canal organique. En réponse au champ électrique créé par ces charges, les porteurs de charge du canal s'accumulent à la jonction des deux matériaux ce qui forme un canal conducteur et augmente la conductivité du polymère (dopage électrostatique). Pour des tensions de grille plus élevée, les anions peuvent pénétrer dans le canal pour entrer dans le régime de dopage électrochimique ce qui augmente fortement la densité de porteurs dans tout le volume du canal. Cette dernière propriété est exclusive aux transistors organiques.

La géométrie typique en spintronique est la vanne de spin. Il s'agit de deux électrodes ferromagnétiques de champs coercitifs différents, séparées par un canal non-magnétique généralement semi-conducteur, organique ou inorganique. En appliquant un champ magnétique, l'aimantation relative des deux électrodes peut être basculée de parallèle à anti-parallèle. Il en résulte une variation significative de la résistance de l'échantillon selon sa configuration,

ce qui correspond à la GMR. Cependant, pour obtenir un signal important, deux conditions doivent être remplies :

1. La longueur de diffusion de spin ( $l_{sf}$ ), c'est-à-dire la distance que peut parcourir un porteur avant de perdre l'information de spin, doit être plus longue que le canal ( $L$ ).
2. La résistance d'interface spécifique ( $r_b^*$ ) doit être dépendante du spin et comprise dans une fenêtre définie par les conditions de Fert & Jaffrès<sup>8</sup> centrée autour de  $r_N = \rho l_{sf}$ , où  $\rho$  est la résistivité du canal.

La longueur de diffusion de spin atteint possiblement 200 nm dans le cas du poly[2,5-bis(3-tetradecylthiophen-2-yl)thieno[3,2-b]thiophene] (PBTBT), polymère principale de cette étude<sup>9,10</sup>. Pour satisfaire la première condition, il est donc nécessaire de réaliser des EGOFETs sub-micrométriques.

La seconde condition concernant la résistance d'interface spécifique, c'est-à-dire la résistance de contact normalisée par la surface d'injection/détection, repose sur l'inadéquation des conductivités de l'électrode métallique et du semi-conducteur organique. Si  $r_b^*$  est trop faible, les porteurs de spin seront préférentiellement refoulés à l'interface ferromagnétique/organique car la conductivité du polymère est au moins cent fois plus faible. Au contraire, si  $r_b^*$  est trop grand, des porteurs pourront traverser la première interface, mais ne pourront pas s'échapper du canal semi-conducteur pour être détectés car ils vont rencontrer une énorme résistance de contact à l'interface organique/ferromagnétique. Quand ils finiront par franchir l'interface, ils auront perdu l'information de spin car ils auront passé trop de temps dans le canal. La fenêtre de résistance spécifique de contact s'écrit :

$$\frac{L}{l_{sf}} < \frac{r_b^*}{r_N} < \frac{l_{sf}}{L}$$

Cette inégalité montre bien l'importance de la balance entre la longueur du canal et la longueur de diffusion de spin qui est déterminante pour obtenir un signal de spin significatif.

Cette thèse a pour but de moduler la résistance d'interface par la température, le dopage, l'application d'un champ magnétique, le choix des matériaux et la géométrie de l'échantillon pour obéir aux conditions de Fert & Jaffrès, et ainsi fabriquer une vanne de spin organique fonctionnelle. La structure EGOFETs permettant le dopage électrochimique du PBTBT pour atteindre un transport quasi-métallique et une résistance d'interface très faible est un élément clé de ce travail. C'est d'autant plus vrai que cette structure est adaptée à l'échelle millimétrique, autant que nanométrique, pour satisfaire la première condition citée plus haut, mais aussi parce que la résistance de contact semble diminuer en réduisant la longueur des EGOFETs. Poussé par les résultats obtenus avec les électrodes en or, le cobalt a été utilisé pour réaliser des pistes métalliques magnétiques nécessaires pour l'étude de phénomène dépendant en spin.

Basé sur les précédents résultats du groupe, nous sommes effectivement parvenus à fabriquer des EGOFETs nanométriques ( $L \sim 80$  nm) ayant de remarquables propriétés de transistors et de faibles résistances de contact. Nous avons particulièrement pointé du doigt l'effet de *crowding* qui augmente l'aire d'injection et de détection effective de ce type d'échantillon<sup>11,12</sup>. Cette élongation réduit la résistance d'interface mais est problématique dans l'optique d'application en spintronique car la distance parcourue par les porteurs est augmentée, et peut facilement

dépasser la longueur de diffusion de spin. Le signal de magnétorésistance, qui diminue exponentiellement avec la longueur du canal, est donc fortement impacté. Pour estimer l'influence du *crowding*, nous avons développé une simulation numérique qui tient compte de la longueur du canal effectif en partant des équations de magnétorésistance de Valet-Fert<sup>13</sup>. L'effet de *crowding* induit également des relations inhabituelles entre les résistances du canal effectif, la résistance d'interface effective et la résistance totale de l'échantillon qui ont des conséquences importantes pour la magnétoresistance des EGOFETs.

Dans ce résumé en français, nous nous limiterons à donner un bref aperçu des résultats expérimentaux correspondants aux chapitres trois à cinq du cœur du manuscrit.

### L'effet de *crowding*

Dans un échantillon planaire, l'effet de *crowding* d'une structure superposée implique l'injection (et la détection) des charges depuis la surface supérieure des électrodes, en plus de leur surface latérale. Le courant circulant dans le canal devient alors non-uniforme, allongeant le trajet des porteurs de charge (et de spin) dans le polymère.

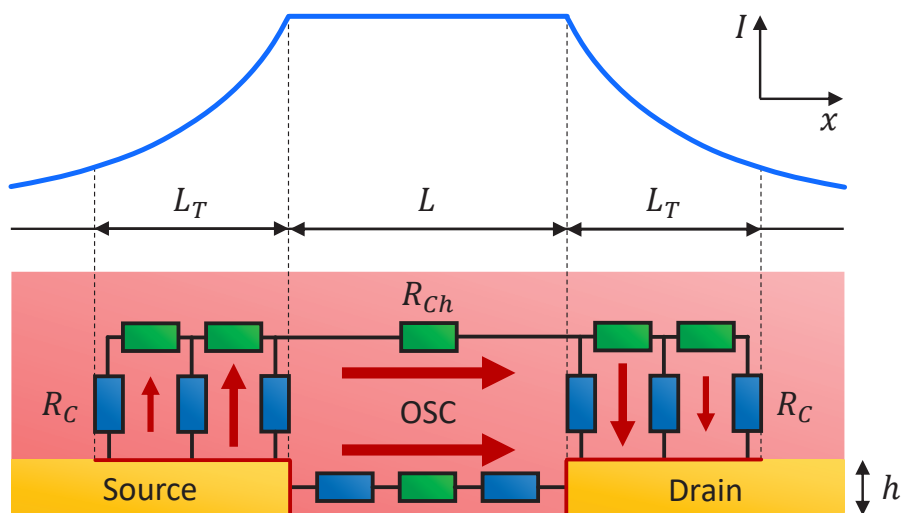


**Figure B** Représentation de l'effet de *crowding*. La surface supérieure des électrodes est impliquée dans l'injection de courant, ce qui allonge la longueur effective du canal de deux fois la longueur de transfert. La véritable aire d'injection est mise en avant par la ligne rouge. La grille n'est pas dessinée pour simplifier le schéma.

La figure B représente le circuit équivalent d'un échantillon en modélisant l'effet de *crowding* par un réseau de résistances en parallèle au-dessus des électrodes. L'analyse d'un tel circuit révèle une (dé)croissance exponentielle du courant au-dessus de la source (du drain) sur une longueur caractéristique appelée longueur de transfert ( $L_T$ ).  $L_T$  reflète l'équilibre entre la résistance de contact spécifique ( $r_b$ ) et la résistivité du canal ( $\rho$ ), et s'écrit<sup>14</sup> :

$$L_T = \sqrt{\frac{r_b}{\rho} h_{canal}}$$

où  $h_{canal}$  est l'épaisseur du canal.  $r_b$  est la normalisation de la résistance de contact ( $R_C$ ) par l'aire d'injection/détection ( $A$ ) :  $r_b = R_C A$  ; c'est donc une propriété intrinsèque du système, au même titre que la résistivité. On notera que l'équation précédente est auto-cohérente étant donné que l'aire  $A$  dépend elle-même de la longueur de transfert. De manière générale, on peut écrire :

$$r_b = R_C^{L_T} W (h + L_T)$$

où  $W$  est la largeur du canal et  $h$  la hauteur des électrodes. L'indice  $L_T$  à la résistance de contact indique qu'il faut utiliser la résistance de contact qui prend en compte l'effet de crowding. Le calcul de  $R_C$  en négligeant la longueur de transfert tient en fait compte de la résistance du canal au-dessus des électrodes, et donc  $R_C^{L_T} < R_C$ . On a cependant bien  $r_b$  et non  $r_b^{L_T}$  car c'est une propriété intrinsèque, l'aire d'injection pour la normalisation a simplement été mieux définie.

Expérimentalement, les longueurs de transfert publiées dans la littérature suivent  $4L_T = L$  à l'échelle micrométrique, et ne passent pas sous les 600 nm à l'échelle nanométrique<sup>15-17</sup>. La longueur de transfert est donc le plus souvent (beaucoup) plus longue que la distance entre les électrodes. La longueur effective des échantillons ( $L_{eff} = L + 2L_T$ ) est donc possiblement très différente de la longueur initiale souhaitée. Il faut donc être prudent lors de l'analyse de dispositifs dans une structure superposée.

Dans le cas où  $L_T \gg L, h$ , c'est-à-dire que le courant passe essentiellement par le dessus des électrodes, l'effet de *crowding* induit une équivalence telle que :

$$2R_C^{L_T} = R_{Ch}^{L_T} = \frac{1}{2} R_{Totale}$$

où  $R_{Ch}^{L_T}$  est la résistance du canal en tenant compte de l'allongement dû à la longueur de transfert et  $R_{Totale} = R_{Ch}^{L_T} + 2R_C^{L_T}$ .  $L_T$  s'adapte pour que les résistances du canal et de l'interface s'équilibrent et contribuent autant l'une que l'autre à la résistance de l'échantillon.

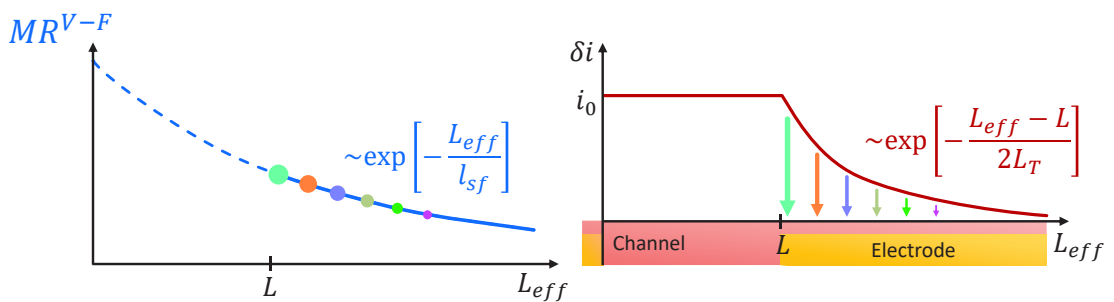


**Figure C** À gauche : décroissance de la magnétorésistance avec la longueur du canal d'après les équation de Valet & Fert. À droite : distribution du courant en présence de *crowding*. L'amplitude locale du courant ( $\delta i$ ) pondère la magnétorésistance de la figure de gauche, comme montré par le code couleur.

Il est donc possible de moduler la longueur de l'échantillon en jouant sur la résistivité du canal ou la résistance d'interface du système puisque la longueur de transfert sera modifiée. Par exemple, le choix d'un niveau de dopage plus faible augmenterait la résistivité du canal ce qui

raccourcirait  $L_T$  et donc  $L_{eff}$ . Cette variation de longueur mène à une nouvelle relation entre la résistance totale, la résistance d'interface spécifique et la résistivité :

$$R_{Totale} = \frac{4}{W} \sqrt{\frac{r_b \rho}{h}}$$

fondamentalement différente de l'habituelle somme linéaire d'un terme d'interface et d'un terme lié au canal. Dans l'idée de détecter un signal de magnétorésistance, on remarque que la variation de  $r_b$  ou  $\rho$  peut reproduire le signal attendu sans avoir d'injection ou de transport de spin.

L'effet de *crowding* impact également l'amplitude de la magnétorésistance. Comme énoncé dans l'introduction, la longueur du canal doit être plus courte que la longueur de diffusion de spin  $l_{sf}$ , estimée à 200 nm pour le PBTTT. Or la longueur de transfert atteint facilement le micromètre, ce qui implique une longueur effective nettement plus longue que  $l_{sf}$ . Pour quantifier les conséquences de l'effet de *crowding* sur la magnétorésistance, nous avons effectué une simulation basée sur les équations de Valet-Fert en incluant la non-uniformité du courant due au *crowding*.

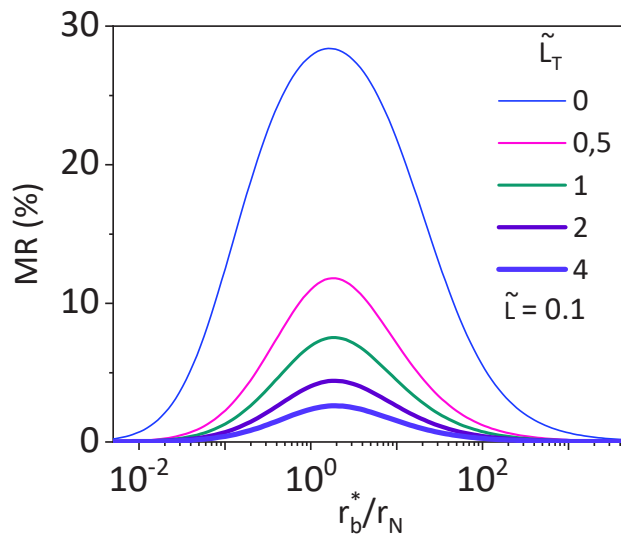


**Figure D** Magnétorésistance tenant compte de l'effet de *crowding*, pour différentes longueurs de transfert, en fonction de la résistance spécifique (de spin) de l'interface normalisée par la résistivité de spin du canal. L'unité de longueur est  $l_{sf} = 200$  nm.

La magnétorésistance tenant compte de la longueur de transfert ( $MR^{LT}$ ) est considérée comme la moyenne pondérée des magnétorésistances des courants locaux  $\delta i$  qui construisent le courant total  $i_0$  (figure C) :

$$MR^{LT}(L) = \frac{\int_L^\infty MR^{V-F}(L_{eff}) \delta i(L_{eff}) dL_{eff}}{\int_L^\infty \delta i(L_{eff}) dL_{eff}}$$

Les valeurs de  $L_T$  ont été choisies entre zéro (référence) et quatre fois la longueur de diffusion de spin. Les distances accentuées d'un tilde sont exprimées en unité de  $l_{sf}$ , considérée de 200 nm telle que la longueur du canal considérée est  $\tilde{L} = 0,1 \Leftrightarrow L = 20$  nm.

La conséquence principale de l'effet de *crowding* est une diminution drastique du signal attendu même pour la plus faible longueur de transfert (figure D). L'amplitude de magnétorésistance perd dès lors un ordre de grandeur pour  $L_T = 800$  nm ( $\tilde{L}_T = 4$ ), longueur souvent atteinte dans la littérature. De manière générale, nous n'attendons pas de signal supérieur à quelques pourcents dans les structures superposées, d'autant plus que des valeurs optimales des propriétés magnétiques des électrodes ont été choisies pour le calcul, difficilement réalisable expérimentalement.

En conclusion, l'effet de *crowding* est un outil utile pour diminuer la résistance de contact d'un dispositif en agrandissant la surface impliquée dans l'injection et la détection du courant. Cependant, l'allongement de la longueur effective du système implique une forte diminution du signal de spin qu'on peut espérer dans une telle géométrie.

### La résistance d'interface des EGOFETs

La réduction des dimensions caractéristiques des transistors est nécessaire pour améliorer les performances des dispositifs électroniques tels que les processeurs. Ce faisant, la résistance du canal diminue de manière linéaire avec la longueur. Cependant, la résistance d'interface ne change pas, et cette dernière peut surpasser la résistance du canal actif à partir d'une certaine longueur critique. Continuer de rétrécir le transistor au-delà de cette valeur critique est inutile puisque c'est finalement l'interface qui domine les propriétés de l'échantillon. Dans le cas des transistors organiques, cette distance est typiquement de plusieurs micromètres à cause de la résistance de contact nettement plus élevée comparée aux systèmes à base de silicium. La réalisation de transistors nanométriques nécessite donc un travail de fond pour réduire la résistance de contact.

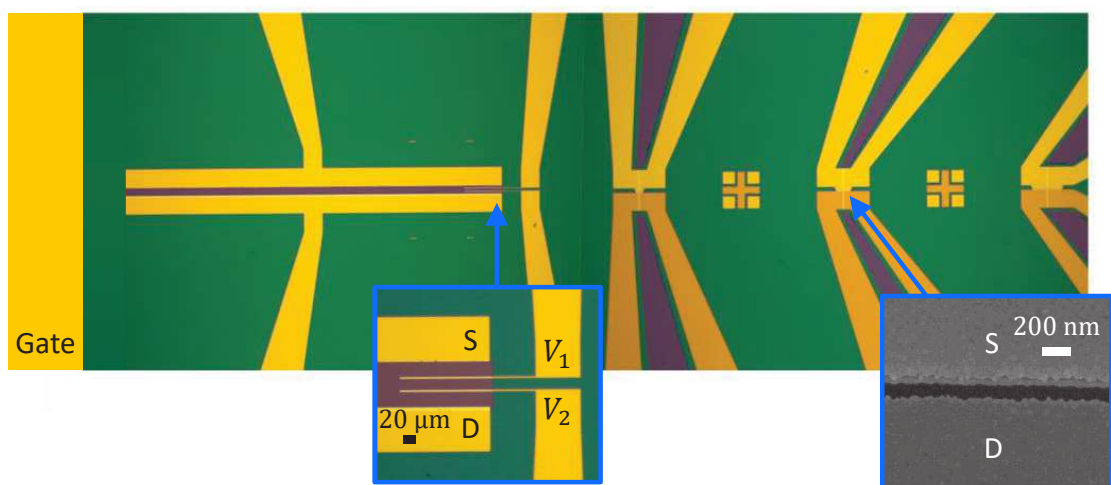


**Figure E** Image optique d'un échantillon typique de ce travail avec un transistor millimétrique (à gauche) et trois nanométriques (à droite). Les deux images encadrées montrent plus en détail les électrodes 4-points (à gauche) et le canal nanométrique (à droite, microscopie électronique).

L'échantillon typique de cette thèse est présenté sur la figure E. Chaque échantillon possède un transistor millimétrique doté de deux électrodes 4-points au sein du canal organique, et trois transistors nanométriques dont les électrodes sont en contact avec deux pistes métalliques pour effectuer une mesure pseudo-4-points. La méthode 4-points est nécessaire pour déterminer précisément la conductivité du polymère, et permettre de calculer séparément les résistances source et drain en assumant une chute de potentiel linéaire dans le canal. Idéalement, la mesure 4-points devrait être appliquée à l'échelle nanométrique, mais la longueur du canal de quelques dizaines de nanomètre rend extrêmement difficile l'ajout des deux électrodes supplémentaires entre la source et le drain. La mesure pseudo-4-points élimine au moins la résistance des pistes métalliques en déterminant le potentiel au plus proche du canal. Ensuite, la résistance du canal est soustraite de la résistance totale en partant de l'hypothèse que la conductivité du transistor millimétrique est valable à l'échelle nanométrique. C'est pourquoi il est impératif d'avoir les deux échelles sur le même échantillon, cela assure une meilleure reproductibilité des propriétés électriques entre les deux différentes échelles. On notera que la mesure pseudo-4-points ne permet pas de distinguer la résistance de la source de celle du drain.

Un aperçu des résistances spécifiques de contact de nombreux EGOFETs est donné sur la figure F, où le cadran de gauche montre les résultats à l'échelle millimétrique tandis que le cadran de droite expose ceux à l'échelle nanométrique. Étant donné que l'objectif final est l'injection et la détection de spin, nous avons fabriqué des dispositifs avec des électrodes en cobalt (symboles bleus), l'or étant utilisé majoritairement pour une étude préliminaire et des points de référence (symboles noirs). La résistance spécifique de contact a été calculée en tenant compte de l'effet de *crowding*, elle s'écrit alors :

$$r_b = \left( \frac{R_C W}{2} \right)^2 \sigma h$$

en négligeant la hauteur de l'électrode ( $h$ ) par rapport à  $L_T$ . On notera que c'est bien  $R_C$  et non  $R_C^{LT}$  qui intervient dans cette équation. Pour les échantillons millimétriques, les résistances spécifiques d'interface source et drain ont été moyennées pour la comparaison avec l'échelle nanométrique.

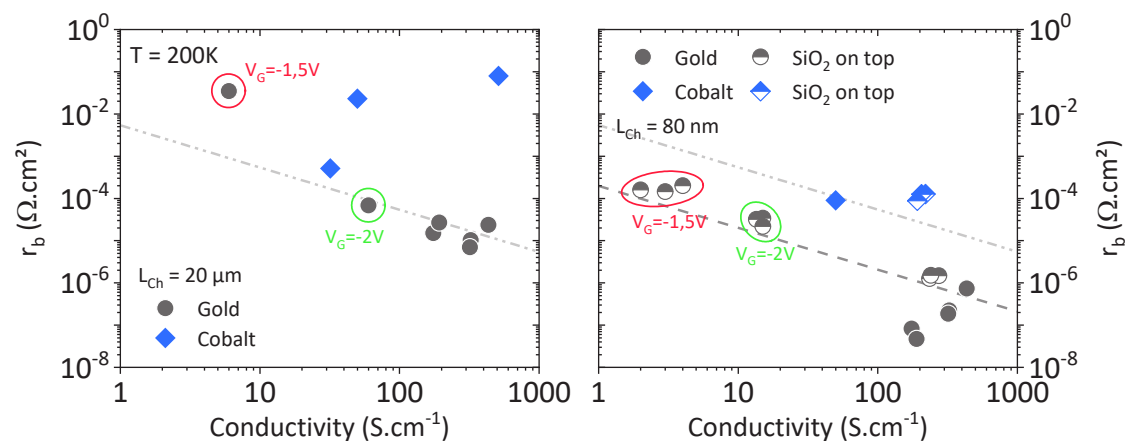


**Figure F** Résistance spécifique d'interface en fonction de la conductivité pour des EGOFETs millimétriques (à gauche) et nanométriques (à droite), avec des électrodes en or (ronds noirs) et en cobalt (losanges bleus). Sauf indication contraire, la tension de grille est le maximum supporté par l'échantillon (en général autour de  $-3,1$  V).

La première chose importante qu'on vérifie sur la figure F est que  $r_b$  est deux à trois ordres de grandeur plus faible que celle des transistors organiques à effet de champ (sans grille électrolytique) reportée dans la littérature avec des électrodes en or. De plus, en réduisant l'échelle des EGOFETs,  $r_b$  diminue encore d'un facteur 10 voir 100, devenant les plus faibles valeurs observées à notre connaissance.

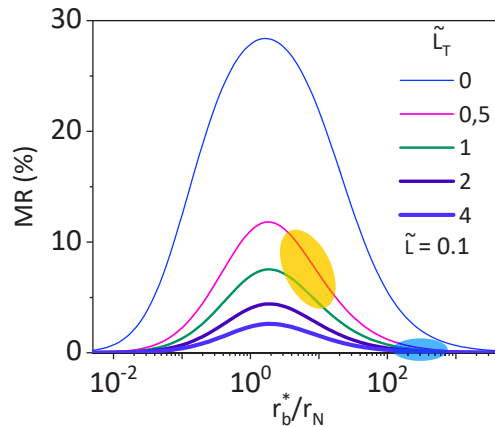


**Figure G** Magnétorésistance espérée d'après les valeurs de résistance spécifiques d'interface mesurées, en tenant compte de l'effet de *crowding*. La zone jaune identifie les valeurs avec l'or, et la zone bleue avec les électrodes en cobalt.

Pour valider notre définition de  $r_b$ , nous avons également fabriqué des échantillons dont le dessus des électrodes est recouvert d'oxyde de silicium pour que le courant ne passe que par le côté des électrodes (symbole à moitié plein). Dans ce cas,  $r_b = R_c Wh$  et on voit que les valeurs sont similaires aux premiers échantillons présentant l'effet de *crowding*, comme attendu d'une propriété intrinsèque.

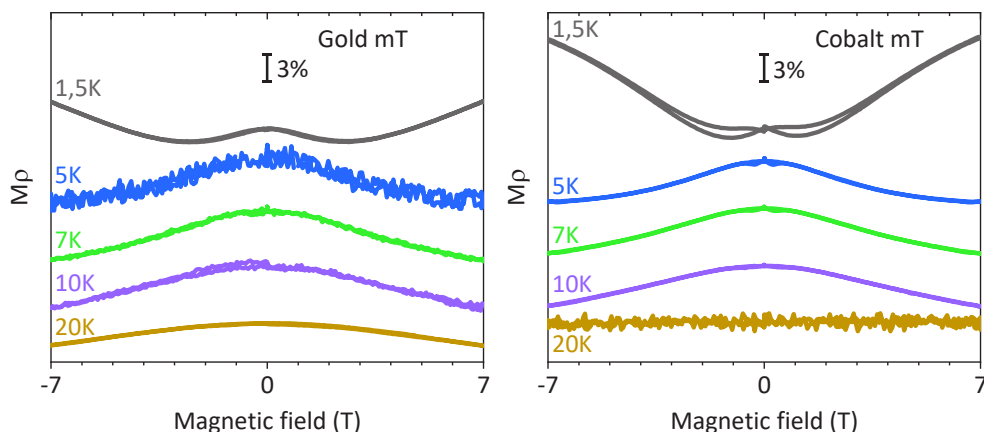


**Figure H** Magnétorésistivité des EGOFETs millimétriques à base d'or (à gauche) et de cobalt (à droite) pour différentes températures. Le champ magnétique est perpendiculaire aux canaux.

Concernant le cobalt, les valeurs de  $r_b$  sont plus dispersées, mais restent dans l'ensemble plutôt faibles, en particulier à l'échelle nanométrique. Cependant, en reportant ces mesures sur

le graphique de magnétorésistance incluant l'effet de *crowding* (figure G), on voit que l'amplitude du signal attendu dans une vanne de spin organique, dans la géométrie présentée ici avec des électrodes de cobalt, devrait être très faible et probablement difficilement mesurable. Les valeurs de  $r_b$  trop élevées du cobalt sont en partie dues à la longueur de transfert, particulièrement longue ( $> 1 \mu\text{m}$ ) comparée à celle de l'interface avec l'or ( $L_T \sim 200 \text{ nm}$ ).

### Les EGOFETs dans un champ magnétique

Les parties précédentes se sont montrées assez pessimistes quant à la possibilité d'injecter et surtout de détecter des spins dans les dispositifs organiques superposés. Nous n'avons d'ailleurs pas observé de signal de spin dans nos structures. Cependant, l'application d'un champ magnétique externe reste intéressante pour la compréhension du transport électronique. De plus, de par le design de nos échantillons, nous avons l'opportunité d'étudier la résistance d'interface en fonction du champ magnétique, qui n'a pas encore été reportée dans la littérature.

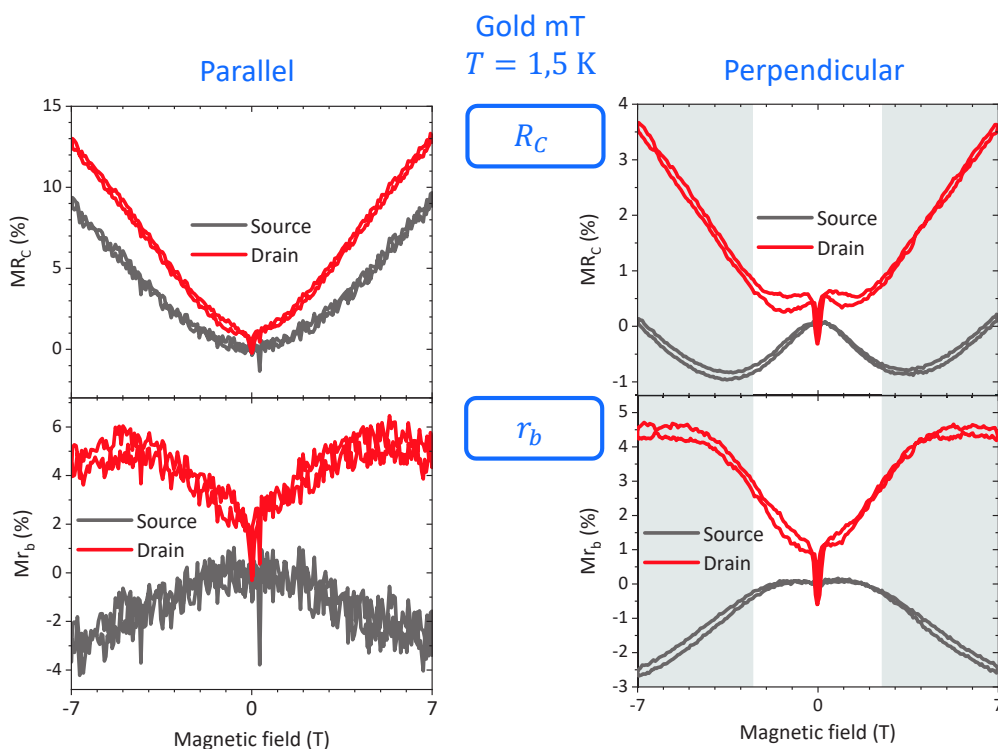


**Figure I** Magnétorésistances d'interface (en haut) et magnétorésistances spécifiques d'interface (en bas) en configuration parallèle (à gauche) et perpendiculaire (à droite) d'un EGOFET millimétrique en or.

En premier lieu, nous avons analysé la variation de résistivité du polymère dans un champ magnétique perpendiculaire et parallèle au courant. Si la configuration parallèle a montré une magnétorésistivité positive parabolique typique des matériaux organiques, la configuration perpendiculaire ne suit pas le comportement standard (figure H). En effet, aux champs les plus faibles ( $< 2 \text{ T}$ ), la magnétorésistivité est négative, c'est-à-dire que le polymère conduit mieux le courant sous l'effet du champ. Aux champs les plus forts, la composante parabolique s'impose

et on retrouve une magnétorésistivité positive qui tient son origine dans les interactions électron-électron, ce qui explique que son amplitude augmente en refroidissant l'échantillon.

La magnétorésistivité négative provient de la localisation faible, connue de la physique des semi-conducteurs inorganiques<sup>18,19</sup>. Quand un porteur de charge rencontre un centre de diffusion, il change de direction de manière aléatoire. Il est donc possible, après de multiples diffusions, que ce porteur parcourt une boucle fermée en repassant par un centre de diffusion déjà visité. Ces boucles peuvent être traversées dans le sens horaire ou anti-horaire ce qui crée une interférence constructive des fonctions d'onde de ces deux directions, augmentant la probabilité du porteur de passer par ces chemins fermés (localisation) plutôt que de continuer son trajet. Le champ magnétique perpendiculaire aux boucles, équivalent à notre configuration perpendiculaire car le canal est quasiment bidimensionnel, brise la cohérence des deux fonctions d'onde qui n'interfèrent donc plus, et la résistivité diminue. L'observation de localisation faible est importante car elle est le signe d'un transport diffusif comme dans les métaux, ce qui est possiblement bénéfique pour le transport de spin.

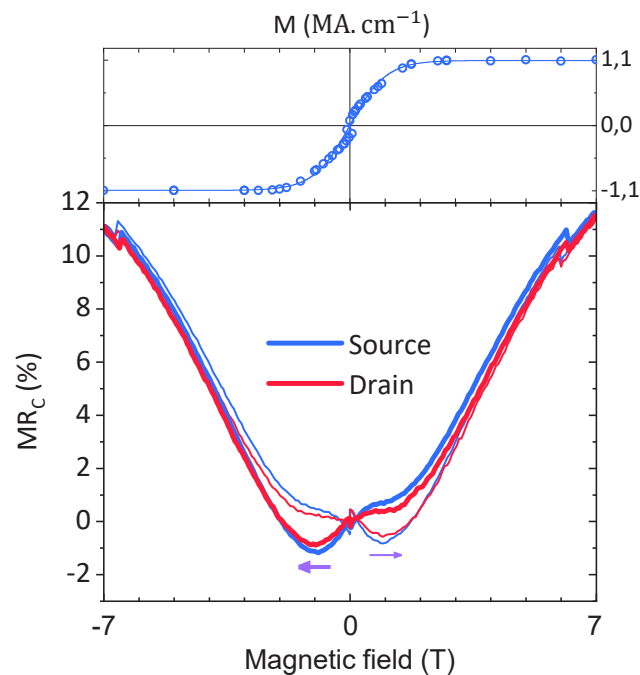


**Figure J** Magnétorésistances d'interface d'un EGOFET à base de cobalt. L'aimantation en fonction du champ magnétique d'une couche de cobalt similaire aux électrodes est également montré au-dessus.

Pour finir, nous avons extrait la résistance de contact des EGOFETs soumis au champ magnétique. La figure I présente les courbes de résistances de contact et de résistances spécifiques de contact qui correspondent à l'échelle millimétrique, à 1,5 K, dans les orientations parallèle et perpendiculaire. Les résistances source et drain ont été distinguées. La première observation est la différence importante entre  $R_C$  et  $r_b$ . Tandis qu'en parallèle  $MR_C$  est positive et parabolique pour les deux interfaces,  $Mr_b$  se comporte à l'opposé pour la source et est également très différent pour le drain. Dans le cas perpendiculaire,  $R_C$  et  $r_b$  semblent également antagonistes. Il

paraît donc en effet important de considérer  $r_b$  plutôt que  $R_C$  comme nous le proposons dans cette thèse.

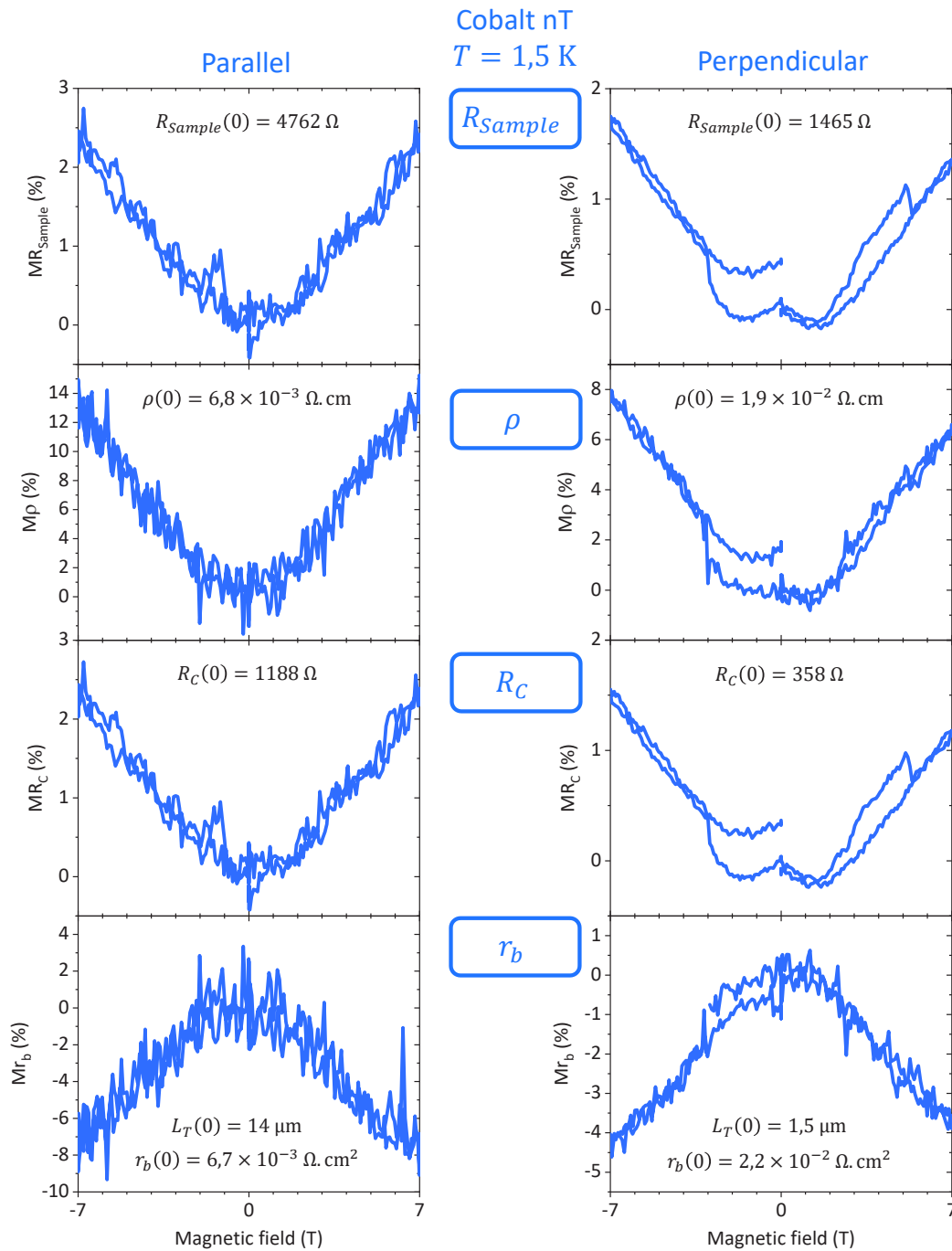


**Figure K** De haut en bas : magnétorésistances totale, magnétorésistivités, magnétorésistances d'interface et magnétorésistances spécifiques d'interface d'un EGOFET à base de cobalt. L'orientation parallèle est à gauche et la perpendiculaire à droite.

On note aussi que la résistance spécifique d'interface est très similaire, en forme et amplitude, dans les deux orientations, suggérant une indépendance à l'angle d'application du champ, contrairement à ce qu'on peut voir pour  $R_C$ .

Le mécanisme sous-jacent à la variation de résistance (spécifique) d'interface n'est pas encore identifié, mais au vu des magnétorésistances présentées ici, il est important d'étudier de plus près l'effet du champ magnétique sur les interfaces.

La même procédure a été appliquée aux échantillons ayant des électrodes de cobalt. Dans le cas parallèle, toutes les courbes sont paraboliques et les magnétorésistances source et drain se superposent. Cependant, quand le champ est perpendiculaire à l'échantillon, on observe une hystérèse asymétrique jusqu'à  $\pm 2$  T (figure J) pour les résistances d'interface mais aussi pour la résistivité. Étant donné que les électrodes sont magnétiques, nous avons soupçonné la contribution de l'hystérèse des électrodes de cobalt. Nous avons donc mesuré l'aimantation d'un film de cobalt de même épaisseur, pour obtenir la courbe en haut de la figure J, qui ne montre aucune hystérèse, ou tout du moins un champ coercitif très proche de 0 T. Nous ne sommes pour l'instant pas capable de fournir une explication satisfaisante à cette hystérèse asymétrique, pour laquelle des recherches plus approfondies sont nécessaires.

Enfin, nous avons étudié l'impact du champ magnétique sur les EGOFETs à base de cobalt à l'échelle nanométrique qui sont indispensables pour la réalisation de vanne de spin. On remarque tout de suite sur la figure K, l'inversion de  $Mr_b$  comparé aux autres courbes. Ceci est dû à la longueur de transfert qui domine complètement la valeur de  $r_b$  et qui tend à se raccourcir quand la résistivité augmente. Ces résultats réunissent les conditions idéales pour vérifier la validité des équations précédentes, à savoir  $R_{Totale} \propto \sqrt{r_b \rho}$  et  $2R_C^{LT} = R_{Ch}^{LT}$ , car  $L_T \gg L, h$ . La figure L confirme ces relations, ce qui prouve encore une fois l'importance de bien définir  $r_b$ .

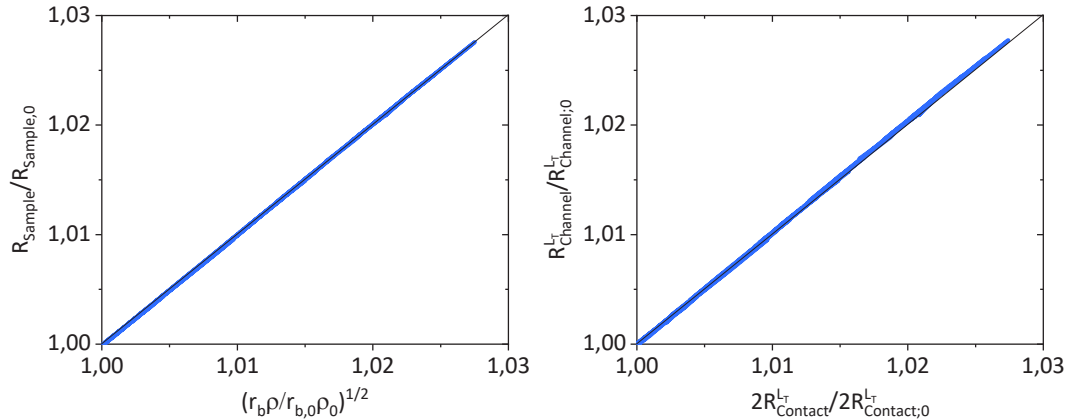


**Figure L** Vérification de la proportionnalité  $R_{Totale} \propto \sqrt{r_b \rho}$  (à gauche) et de la relation  $2R_C^{LT} = R_{Ch}^{LT}$  (à droite).

## Conclusion

L'objectif final de cette thèse était la réalisation d'une vanne de spin organique. Les conditions à remplir sont principalement une longueur de diffusion de spin supérieure à la longueur du canal, et une résistance de contact qui suit les recommandations de Fert & Jaffrès.

Pour satisfaire le premier prérequis, nous avons fabriqué des transistors organiques à effet de champ à grille électrolytique à l'échelle nanométrique. Le choix du polymère est également

important puisqu'une mobilité électronique élevée implique une plus grande longueur de diffusion de spin. Le niveau de dopage atteignable grâce à l'électrolyte permet aussi d'obtenir un canal organique particulièrement conducteur, se rapprochant des métaux, allongeant encore la distance sur laquelle l'information de spin peut être maintenue.

La seconde condition requiert essentiellement une réduction drastique de la résistance spécifique d'interface, la plupart du temps bien trop grande pour une injection/détection de spin optimale. Là encore, la structure EGOFET se montre particulièrement efficace, en réduisant significativement la résistance d'interface métal/polymère.

Un point clé de ce travail a été de bien définir l'aire d'injection/détection via la prise en compte de l'effet de *crowding* pour déterminer le plus rigoureusement possible la résistance spécifique d'interface  $r_b$ . Nous sommes convaincus que cette propriété devrait être la grandeur standard pour la comparaison de résistance d'interface dans la littérature.

De même, la longueur de transfert doit être considérée dans le domaine de la spintronique, afin d'avoir une meilleure appréciation de  $r_b$ , mais également pour estimer la longueur de canal effectif parcourue par les porteurs de spin. D'après la simulation présentée dans cette thèse, l'effet de *crowding* est extrêmement préjudiciable à l'obtention d'un signal de spin à cause de l'allongement du trajet entre l'injection et la détection. Une solution pourrait être de limiter la longueur de transfert en ajoutant une couche isolante au-dessus des électrodes.

Enfin l'application d'un champ magnétique externe a mis en évidence un transport quasi-métallique par l'observation de localisation faible. De plus, nous avons mesuré la magnéto-résistance spécifique d'interface des transistors et montré une éventuelle indépendance à l'angle entre le champ et le canal. L'étude sous champ d'un échantillon dont la longueur de transfert est particulièrement longue a permis de vérifier la validité des deux relations atypiques  $R_{Totale} \propto \sqrt{r_b \rho}$  et  $2R_C^{LT} = R_{Ch}^{LT}$ , provenant directement de l'effet de *crowding*. Ces équations posent la question de l'origine des signaux des vannes de spin. En effet, une variation de la résistance d'interface pourrait en principe reproduire un signal de spin en changeant la résistance totale du système sous l'application d'un champ. Il est donc primordial de s'interroger sur le rôle des interfaces lors de mesures magnétiques.

## Bibliographie

- (1) Paterson, A. F.; Singh, S.; Fallon, K. J.; Hodsden, T.; Han, Y.; Schroeder, B. C.; Bronstein, H.; Heeney, M.; McCulloch, I.; Anthopoulos, T. D. Recent Progress in High-Mobility Organic Transistors: A Reality Check. *Adv. Mater.* **2018**, *1801079*, 1–33.
- (2) Braga, D.; Ha, M.; Xie, W.; Frisbie, C. D. Ultralow Contact Resistance in Electrolyte-Gated Organic Thin Film Transistors. *Appl. Phys. Lett.* **2010**, *97* (19).
- (3) Panzer, M. J.; Frisbie, C. D. High Carrier Density and Metallic Conductivity in Poly(3-Hexylthiophene) Achieved by Electrostatic Charge Injection. *Adv. Funct. Mater.* **2006**, *16* (8), 1051–1056.
- (4) Baibich, M. N.; Broto, J. M.; Fert, A.; Van Dau, F. N.; Petroff, F.; Eitenne, P.; Creuzet, G.; Friederich, A.; Chazelas, J. Giant Magnetoresistance of (001)Fe/(001)Cr Magnetic Superlattices. *Phys. Rev. Lett.* **1988**, *61* (21), 2472–2475.
- (5) Grünberg, P.; Schreiber, R.; Pang, Y.; Brodsky, M.; Sowers, H. Layered Magnetic Structures: Evidence for Antiferromagnetic Coupling. *Phys. Rev. Lett.* **1986**, *57* (19), 2442–2445.
- (6) Dediu, V. A.; Hueso, L. E.; Bergenti, I.; Taliani, C. Spin Routes in Organic Semiconductors. *Nat. Mater.* **2009**, *8* (9), 707–716.
- (7) Szulczewski, G.; Sanvito, S.; Coey, M. A Spin of Their Own. *Nat. Mater.* **2009**, *8* (9), 693–695.
- (8) Fert, A.; Jaffrès, H. Conditions for Efficient Spin Injection from a Ferromagnetic Metal into a Semiconductor. *Phys. Rev. B* **2001**, *64* (18), 184420.
- (9) McCulloch, I.; Heeney, M.; Bailey, C.; Genevicius, K.; MacDonald, I.; Shkunov, M.; Sparrowe, D.; Tierney, S.; Wagner, R.; Zhang, W.; et al. Liquid-Crystalline Semiconducting Polymers with High Charge-Carrier Mobility. *Nat. Mater.* **2006**, *5* (4), 328–333.
- (10) Watanabe, S.; Ando, K.; Kang, K.; Mooser, S.; Vaynzof, Y.; Kurebayashi, H.; Saitoh, E.; Sringhaus, H. Polaron Spin Current Transport in Organic Semiconductors. *Nat. Phys.* **2014**, *10* (4), 308–313.
- (11) Kennedy, D. P.; Murley, P. C. A Two-Dimensional Mathematical Analysis of the Diffused Semiconductor Resistor. *IBM J. Res. Dev.* **1968**, *12* (3), 242–250.
- (12) Murrmann, H.; Widmann, D. Current Crowding on Metal Contacts to Planar Devices. *IEEE Trans. Electron Devices* **1969**, *16* (12), 1022–1024.
- (13) Valet, T.; Fert, A. Theory of the Perpendicular Magnetoresistance in Magnetic Multilayers. *Phys. Rev. B* **1993**, *48* (10), 7099–7113.
- (14) Chiang, C. S.; Martin, S.; Kanicki, J.; Ugai, Y.; Yukawa, T.; Takeuchi, S. Top-Gate Staggered Amorphous Silicon Thin-Film Transistors: Series Resistance and Nitride Thickness Effects. *Japanese J. Appl. Physics, Part 1 Regul. Pap. Short Notes Rev. Pap.* **1998**, *37* (11), 5914–5920.
- (15) Wang, S. D.; Yan, Y.; Tsukagoshi, K. Understanding Contact Behavior in Organic Thin Film Transistors. *Appl. Phys. Lett.* **2010**, *97* (6), 63305–63308.
- (16) Natali, D.; Chen, J.; Maddalena, F.; García Ferré, F.; Di Fonzo, F.; Caironi, M. Injection Length in Staggered Organic Thin Film Transistors: Assessment and Implications for Device Downscaling. *Adv. Electron. Mater.* **2016**, *2* (8), 1600097.

## Bibliographie

---

- (17) Xu, Y.; Liu, C.; Scheideler, W.; Darmawan, P.; Li, S.; Balestra, F.; Ghibaudo, G.; Tsukagoshi, K. How Small the Contacts Could Be Optimal for Nanoscale Organic Transistors? *Org. Electron. physics, Mater. Appl.* **2013**, *14* (7), 1797–1804.
- (18) Lee, P. A.; Ramakrishnan, T. V. Disordered Electronic Systems. *Rev. Mod. Phys.* **1985**, *57* (2), 287–337.
- (19) Aleshin, A. N. Charge Carrier Transport in Conducting Polymers on the Metal Side of the Metal-Insulator Transition: A Review. *Phys. Solid State* **2010**, *52* (11), 2307–2332.

# Introduction

The story of organic electronics began in 1977 when Alan Heeger, Alan MacDiarmid and Hideki Shirakawa discovered an increase of electrical conductivity of seven orders of magnitude of trans-polyacetylene through chemical doping<sup>1</sup>. The interest carried on this new kind of material relied on the low-cost fabrication, lightweight, chemical engineering and possible biocompatibility. Moreover, the mechanical flexibility of organic materials allows new type of devices, and the processability from solution makes easier large-scale production. Even if xerography takes early advantages of these materials<sup>2</sup> it is only 15 to 25 years after their work that organic electronics really developed, particularly after mastering the construction of basic electronics devices (diodes, transistors) using organic semiconductors<sup>3,4</sup>.

Nowadays, organic electronics is widely investigated and some devices emerge as organic field-effect transistors (OFETs), organic light emitting diodes (OLEDs) and organic photovoltaic cells (OPVs). OLEDs screen become key market players for televisions or smartphones thanks to the higher contrast, deeper black and lower energetic consumption. Organic photovoltaic cells reach recently an efficiency higher than 10%<sup>5,6</sup> and raise slowly to industrial scale with for example rolled-up solar panels easy to transport. Bioelectronics based on organic materials is also an active research field, aiming for instance to biocompatible sensors<sup>7</sup>.

Organic materials were first difficult to integrate in electronic devices because of their poor carriers mobility. Nevertheless, years passing, their transport efficiency improves and is nowadays suitable for applications. The main issue that remains to overcome is the large contact resistance of organic-inorganic junctions. Because of the fundamental difference structure of polymers compared to metals, performances of hybrid devices are limited by their difficulty to inject charge carriers. Electrolyte-gated organic field-effect transistors (EGOFETs) however, presents very interesting low contact resistances as reported by Braga and co-workers<sup>8</sup>. EGOFET structure will be the typical sample analysis in this thesis to gain better insight in their interface properties. Moreover, EGOFETs exhibited very high conductivity<sup>9</sup>, making them excellent candidates for the aim of this thesis that is the realization of organic spin-valve (OSV).

Indeed, another important aspect of organic electronics is the weak spin-orbit coupling and hyperfine interaction of materials, giving hope to exploit the spin degree of freedom of electrons. Such properties lead to long spin diffusion time needed to detect spin signal in spin-valve (SV) geometry. Spin-based electronics, or spintronics, is one solution to overcome the limit of current silicon-based devices whose downscaling become more and more difficult. The famous Moore's law, *i.e.* the doubling of the number of processors per chip every two years, is now abandoned mainly because of the heat produced in electric circuits when more and more silicon devices are jammed into the same small area. Using the spin information could alleviate this issue.

The principle of SV is the resistance modulation through an external magnetic field. It is made of 2 ferromagnetic (FM) electrodes spaced by a semiconductor. In this project we are interested in the realization of OSVs where the spacer will be an organic semiconductor (OSC). Two main properties must be fulfilled for efficient spin injection-detection:

1. The spin diffusion length ( $l_{sf}$ ) in the OSC must be larger than the channel length ( $L$ ) between injector and detector:  $l_{sf} \gg L$ .
2. The specific spin contact resistivity between FM electrodes and OSC ( $r_b^*$ ) should obey to Fert & Jaffrès' conditions<sup>10</sup>, meaning be spin-dependent and close to OSC spin impedance ( $r_N$ ):  $r_b^* \approx r_N = \rho_N l_{sf}$ .

The spin diffusion time is expected large in OSCs, but it unfortunately doesn't imply a long spin diffusion length since it depends on the conductivity of the material. OSCs are known as "bad" semiconductors, and their reported  $l_{sf}$  remains small, in the tens of nanometer range<sup>11</sup>, possibly reaching 200 nm<sup>12</sup>. Nevertheless, spin-dependent properties were exhibited by Dediu *et al.*<sup>13</sup> and Xiong *et al.*<sup>14</sup> in lateral and vertical geometry respectively. Magnetoresistances in organic spintronic devices were also reported in several articles<sup>15-18</sup>, with indications of spin-dependent injection. The fabrication of channel shorter than  $l_{sf}$  being not a technological limit, nano-scale EGOFETs were investigated in this project for suitable  $l_{sf}$  versus  $L$  architectures.

The second condition relies on the resistance mismatch between the FM/OSC interface resistance and the OSC channel resistance. A spin-dependent contact resistance is mandatory to filter spins depending on their orientation compared to the magnetic field, but its amplitude is limited to a certain range. If  $r_b^*$  is too large compared to  $r_N$ , spin carriers cannot escape the OSC, and if  $r_b^*$  is too low, spins backflow in the injecting electrode. This condition is a major issue in the organic spintronics field, as the interface resistance in organic devices is much larger than in inorganic systems and dominates the total resistance. The EGOFET geometry possibly overcomes this issue as it will be shown in this manuscript.

This thesis focuses on the interface between organic materials and metals. The aim is to tune the contact resistance by temperature, doping, external magnetic field and geometric modulation to eventually match with the Fert and Jaffrès' conditions to go one step further to the realization of OSVs. The EGOFETs investigated allow high conductivity in organic materials through electrochemical doping<sup>19</sup> with expectations to reach a metallic-like behaviour, assumed to be favourable for spin transport. Such devices were fabricated at the millimeter-scale as well

as the 100 nm-scale for conductivity extraction and channel lengths suitable for spintronic applications respectively. Encouraged by our results using gold electrodes, we extend these to ferromagnetic (cobalt) electrodes, required for spin-dependent studies.

Following previous results from our group, we achieved successful downscaling of EGOFETs with remarkable transistor properties and small interface resistance values<sup>20</sup>. We also realized a key issue in our planar device geometry, where injection/detection interface areas need to take into account the so-called current crowding. Indeed, in planar (staggered) lateral geometries, electric current flows also from the top surface of electrodes, in addition to their edges. It leads to an elongated effective channel length compared to the distance patterned between electrodes and a non-uniformity of the current. The current crowding effect is a tool to reduce the interface resistance by the extension of the active injection area. However, as carriers have to cross a longer distance before their detection, it impacts the spin transfer as the spin information must be kept over longer distance, which should be critically compared to  $l_{sf}$ . This issue was investigated by a numerical simulation, in order to estimate how much the magnetoresistance is affected by the crowding effect. Furthermore, in the simplest approximation, crowding makes the active channel and the interface resistance contribute equally to the total sample resistance value. This has important consequences for the magnetoresistance signal of a transistor device, as will be discussed in this work. One should note that this issue was completely overlooked in the literature.

The manuscript is divided in an introductory part giving the background concepts of organic electronics and spintronics, followed by a discussion of the crowding effect and how it can impact the contact resistance and the magnetoresistance in an organic spin-valve. Experiments will then mainly focus on studies of EGOFETs and the measurement of the contact resistance and its behaviour under magnetic field.

Chapter I reviews the organic electronics from the molecular structure to the electric properties of organic thin films. We focus here on the concepts needed for the thesis, making a drastic choice in topics and details in the explanations. Usual models used in the literature to describe electronic transport are introduced as well as the charge injection process. Finally, properties of organic transistor devices are discussed, giving insight into electrochemical doping of transistor devices (EGOFETs).

Chapter II is devoted to spintronics. First, basic concepts of inorganic spintronics are summarized and the diffusive model for spin valves in trilayers, the so-called model of Valet-Fert, is introduced. The spin injection is an important part of this chapter as it relies on the interface resistance. The literature on organic spintronics is discussed with a summary of the main findings of the field. We emphasize the key issues that remain to be clarified for spin-dependent organic devices, as well as possible artefacts when interpreting organic spin valve results are reviewed.

Chapter III introduces the concept of current crowding. The principle of the crowding is explained and its outcome for interface resistances and spintronics is investigated. The unusual variation of the total resistance versus the interface resistance and the resistivity of the channel is more thoroughly developed and the expected magnetoresistance signal decrease due to crowding is quantified through numerical simulation. We also develop a simple equation set that can allow us to estimate how a device total resistance can vary under external stimuli. We are

here mainly interested on using a magnetic field as external excitation (for spintronics applications), but the discussion can be applied to other external parameters. This chapter allows us to pinpoint the targeted values for the interface resistance (or more specifically its resistance per unit area) and defines the roadmap of the experiments performed during the thesis.

Chapter IV present our experiments on EGOFETs, identified as best-suited devices for minimizing the contact resistance, and best-suited for high conductivity organic channels through high doping level. We then explore the contact resistance of EGOFETs by taking into account the current crowding effect. It is mandatory to investigate devices at multiple length scales. At the (sub)millimeter length scale, insight into source and drain resistances, as well as the materials' conductivity can be gained experimentally. This is then used on nanometer-scale devices, where only the sum of the two contributions can be measured. We also investigate other types of devices, making possible the comparison of the properties with or without crowding. These studies allow us to get a better coherent picture of our results on the interface resistance with gold and cobalt electrodes, investigated from room temperature to 1,5 K. We point out the importance of the consideration of the current crowding for accurate determination of the interface resistance per unit area and discuss how it compares to the requirements found for inorganic materials in spintronics studies.

Chapter V present how the transistor devices from Chapter IV behave under magnetic field. As the total resistance is an entanglement of channel and interface resistance, we take advantage of our large-scale devices to get insight into the separate magnetoresistance of channel and interface, not previously reported in the literature. We also examine how the interpretation of the results change when taking crowding effects into account.

The conclusions of this work are presented in the last chapter, with emphasis on the perspectives of using crowding in lateral structures at our advantage for creating multi-stimuli devices.

A large part of the experimental effort of this thesis was dedicated to mastering the fabrication of metal interconnect, as well as establishing a reproducible protocol for building the devices. These rather technical issues are detailed in the appendix, in order to avoid distracting the reader by technicalities in the main part of the manuscript.

**Bibliography**

- (1) Chiang, C. K.; Fincher, C. R.; Park, Y. W.; Heeger, A. J.; Shirakawa, H.; Louis, E. J.; Gau, S. C.; MacDiarmid, A. G. Electrical Conductivity in Doped Polyacetylene. *Phys. Rev. Lett.* **1977**, *39* (17), 1098–1101.
- (2) Borsenberger, P. M.; Weiss, D. S. *Organic Photoreceptors for Xerography*; Press, C., Ed.; 1998.
- (3) Kudo, K.; Yamashina, M.; Moriizumi, T. Field Effect Measurement of Organic Dye Films. *Jpn. J. Appl. Phys.* **1984**, *23* (1), 130.
- (4) Burroughes, J. H.; Bradley, D. D. C.; Brown, A. R.; Marks, R. N.; Mackay, K.; Friend, R. H.; Burns, P. L.; Holmes, A. B. Light-Emitting Diodes Based on Conjugated Polymers. *Nature* **1990**, *347* (6293), 539–541.
- (5) Baran, D.; Ashraf, R. S.; Hanifi, D. A.; Abdelsamie, M.; Gasparini, N.; Röhr, J. A.; Holliday, S.; Wadsworth, A.; Lockett, S.; Neophytou, M.; et al. Reducing the Efficiency-Stability-Cost Gap of Organic Photovoltaics with Highly Efficient and Stable Small Molecule Acceptor Ternary Solar Cells. *Nat. Mater.* **2017**, *16* (3), 363–369.
- (6) Huang, W.; Cheng, P.; Yang, Y.; Cheng, H.-W.; Meng, L.; Qin, M.; Zhu, C.; Chang, S.-Y.; Zhan, X.; Zhu, J.; et al. Ternary System with Controlled Structure: A New Strategy toward Efficient Organic Photovoltaics. *Adv. Mater.* **2018**, *30* (8), 1705243.
- (7) Inal, S.; Rivnay, J.; Suiu, A. O.; Malliaras, G. G.; McCulloch, I. Conjugated Polymers in Bioelectronics. *Acc. Chem. Res.* **2018**, *51* (6), 1368–1376.
- (8) Braga, D.; Ha, M.; Xie, W.; Frisbie, C. D. Ultralow Contact Resistance in Electrolyte-Gated Organic Thin Film Transistors. *Appl. Phys. Lett.* **2010**, *97* (19).
- (9) Zanettini, S.; Dayen, J. F.; Etrillard, C.; Leclerc, N.; Kamalakar, M. V.; Doudin, B. Magnetoconductance Anisotropy of a Polymer Thin Film at the Onset of Metallicity. *Appl. Phys. Lett.* **2015**, *106* (6), 2–6.
- (10) Fert, A.; Jaffrès, H. Conditions for Efficient Spin Injection from a Ferromagnetic Metal into a Semiconductor. *Phys. Rev. B* **2001**, *64* (18), 184420.
- (11) Szulczewski, G.; Sanvito, S.; Coey, M. A Spin of Their Own. *Nat. Mater.* **2009**, *8* (9), 693–695.
- (12) Watanabe, S.; Ando, K.; Kang, K.; Mooser, S.; Vaynzof, Y.; Kurebayashi, H.; Saitoh, E.; Sirringhaus, H. Polaron Spin Current Transport in Organic Semiconductors. *Nat. Phys.* **2014**, *10* (4), 308–313.
- (13) Dediu, V.; Murgia, M.; Maticcotta, F. C.; Taliani, C.; Barbanera, S. Room Temperature Spin Polarized Injection in Organic Semiconductor. *Solid State Commun.* **2002**, *122* (3–4), 181–184.
- (14) Xiong, Z. H.; Wu, D.; Vardeny, Z. V.; Shi, J. Giant Magnetoresistance in Organic Spin-Valves. *Nature* **2004**, *427* (6977), 821–824.
- (15) Pramanik, S.; Stefanita, C. G.; Patibandla, S.; Bandyopadhyay, S.; Garre, K.; Harth, N.; Cahay, M. Observation of Extremely Long Spin Relaxation Times in an Organic Nanowire Spin Valve. *Nat. Nanotechnol.* **2007**, *2* (4), 216–219.
- (16) Santos, T. S.; Lee, J. S.; Migdal, P.; Lekshmi, I. C.; Satpati, B.; Moodera, J. S. Room-Temperature Tunnel Magnetoresistance and Spin-Polarized Tunneling through an

- Organic Semiconductor Barrier. *Phys. Rev. Lett.* **2007**, *98* (1), 3–6.
- (17) Wang, F. J.; Yang, C. G.; Vardeny, Z. V.; Li, X. G. Spin Response in Organic Spin Valves Based on La<sub>2</sub>Sr<sub>13</sub>MnO<sub>3</sub> Electrodes. *Phys. Rev. B - Condens. Matter Mater. Phys.* **2007**, *75* (24), 1–7.
- (18) Morley, N. A.; Rao, A.; Dhandapani, D.; Gibbs, M. R. J.; Grell, M.; Richardson, T. Room Temperature Organic Spintronics. *J. Appl. Phys.* **2008**, *103* (7), 5–8.
- (19) Laiho, A.; Herlogsson, L.; Forchheimer, R.; Crispin, X.; Berggren, M. Controlling the Dimensionality of Charge Transport in Organic Thin-Film Transistors. **2011**, *108* (37).
- (20) Verduci, T.; Chaumy, G.; Dayen, J. F.; Leclerc, N.; Devaux, E.; Stoeckel, M. A.; Orgiu, E.; Samori, P.; Doudin, B. Current Crowding Issues on Nanoscale Planar Organic Transistors for Spintronic Applications. *Nanotechnology* **2018**, *29* (36).

# **PART 1**

## **FUNDAMENTALS AND BACKGROUNDS: ORGANIC ELECTRONICS AND SPINTRONICS**



# Chapter I

## Organic semiconductors

Organic electronics offer the possibility of large area, low-cost production (drop casting, spin-coating, printing...), low temperature processability ( $< 200\text{ }^{\circ}\text{C}$ ), mechanical flexibility and chemical tunability, making them relevant for industrial purposes. In recent years, the production of novel and better-controlled organic materials lead to improvement in numerous physico-chemical properties which lead to major step forward in the device performances, such as the carriers' mobility increasing from  $10^{-3}\text{ cm}^2.\text{V}^{-1}.\text{s}^{-1}$  30 years ago to  $1 - 40\text{ cm}^2.\text{V}^{-1}.\text{s}^{-1}$  more recently.

This first chapter aims to introduce electronic transport in organic materials, limiting our discussion to polymer-type of materials, and emphasizing the key concepts and types of devices that relate to the experimental presented in the second part of the manuscript. The charge transport processes, as well as the charge injection at the metal-organic interface are the core of the discussion, and their relationships with the polymer chemical structure is overviewed.

### I.1. Conjugated polymers

Polymers are polydisperse molecules composed of periodically repeated subunits (monomers). The so-called conjugated polymers are polymers alternating simple and multiple C – C bonds along the backbone. The electronic structure of carbon ( $[\text{C}] = 1s^2 2s^2 2p^2$ ) is of key relevance for the electronic transport. To achieve a more stable form, the  $2s$ ,  $2p_x$  and  $2p_y$  orbitals hybridize in an in-plane  $sp^2$ -orbital. The remaining  $2p_z$ -orbital points out perpendicular to the molecular plane (**Figure I.1**). When two carbon atoms bound together, they form a strong  $\sigma$ -bond through  $sp^2$ -orbital wavefunctions overlapping. The two remaining  $p_z$ -orbitals, however, interact more weakly and lead to  $\pi$ -bond on each side of the chain plane. The delocalization of  $\pi$ -electrons allows charge carriers to travel along the polymer, eventually giving a conductive or semiconductive character to these materials.

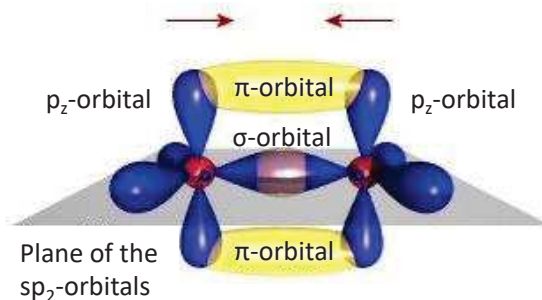


**Figure I.1** Representation of  $\sigma$ - and  $\pi$ -orbitals between  $sp^2$ -hybridized atoms. The  $\sigma$ -orbital corresponds to a higher overlap, thus to a stronger interaction than the  $\pi$  one. The  $sp^2$ -hybridization leads to a plane of  $\sigma$ -bonds with out of plane  $\pi$ -orbitals.

In the case of polymers, with tens or thousands of carbon atoms, hybridization can involve a large number of atoms. First, assuming that all carbon atoms are equidistant, interaction between two neighbouring atoms gives rise to  $sp^2$ -hybridization with each carbon contributing to one  $p_z$ -electron to the  $\pi$ -band, forming a “highway” for charge carriers along the backbone through  $\pi$ - $\pi$  overlapping. In this case, polymers can possibly exhibit metallicity as carrier could freely move along the chain<sup>1</sup>.

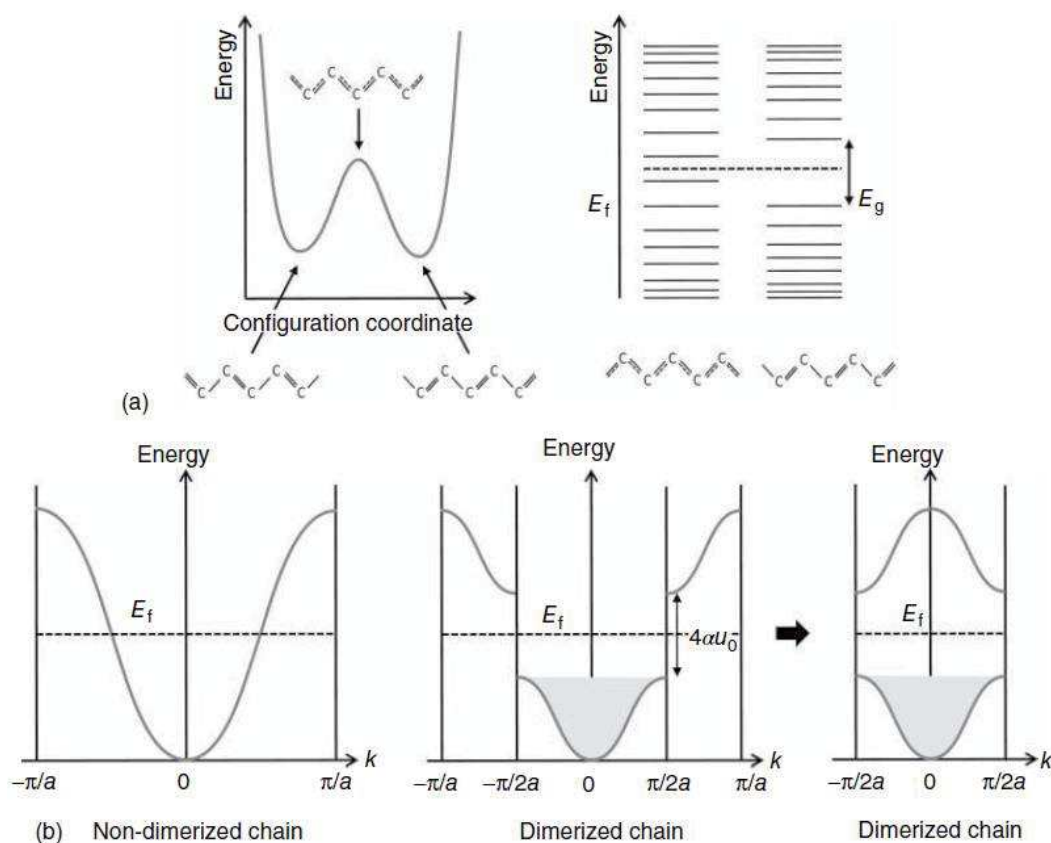


**Figure I.2** a) Potential energy of a polymer chain versus the configuration coordinate showing the spacing between carbon atoms. The peak in energy corresponds to the non-dimerized chain where all carbon atoms are equally spaced, whereas the two wells are the energy of both equivalent dimerized chains. The energy landscape is depicted on the right. b) The dispersion relation for non-dimerized and dimerized chain. A gap appears when carbon atoms pair. Reprinted from Köhler and Bäessler<sup>2</sup>.

However, Rudolf Peierls showed that 1D metals are unstable with respect to distortion<sup>3</sup>. Carbons atoms are no more equidistant but the alternation of single and double bonds (conjugation) changes their spacing, with carbon atoms involved in double bonds being closer to each other than those part of single bonds (**Figure I.2a**). The Peierls distortion double the unit cell (**Figure I.2b**), constituted then of 2 carbon atoms, opening a gap in the electronic structure by splitting the  $\pi$ -band into a fully occupied  $\pi$ -band (bonding orbital) and an empty  $\pi^*$ -band (anti-bonding orbital). Peierls distortion is the origin of the semiconducting properties of polymers. The  $\pi$ -band is the highest occupied molecular orbital (HOMO) while the  $\pi^*$ -band is the lowest unoccupied molecular orbital (LUMO). These levels are often assigned to the highest level of valence band and lowest level of conduction band in an analogy with classical band transport.

Before getting into more details into charge transport, a key feature of polymers is their multi-scale ordering structure, which drives the understanding of charge transport in ensemble of molecules.

### I.1.1. Conjugated polymer thin films

An interesting feature of conjugated polymer is their solution processability. Different techniques like spin-coating, drop casting or even printing are viable methods to process these materials. Thanks to weak Van der Waals interactions between chains, they dissolve, *i.e.* separate, in solution and assemble again when deposit on a substrate. The weakness of Van der Waals interactions let the dissociation in solution occur at relatively low temperature (< 200 °C) which is hundreds of degrees lower than what is needed for inorganic materials currently used for electronics, interesting for industrial production.

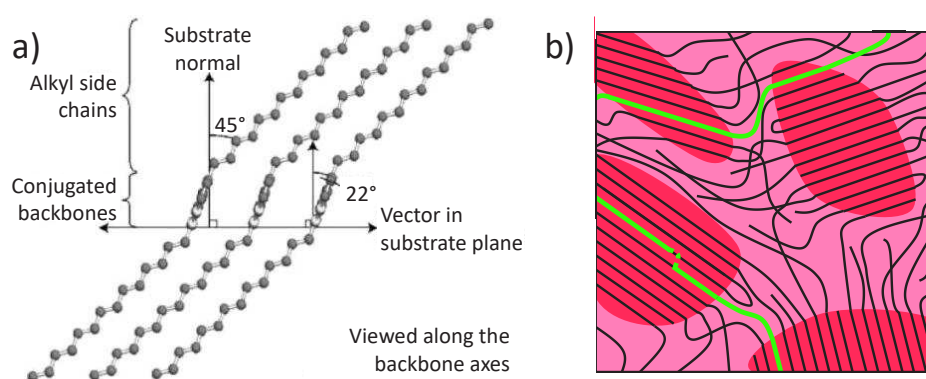


**Figure I.3** a) Structure of a crystalline region of a conjugated polymer - poly(2,5-bis(3-tetradecylthiophen-2-yl)thieno[3,2-b]thiophene) (pBTTT) - on a substrate in edge-on orientation. Reprinted from DeLonchamp *et al.*<sup>4</sup> b) Schematic drawing of the thin film morphology of a semi-crystalline polymer. Black lines are the backbone of different polymer chains, parallel in the crystalline regions (more pronounced pink areas) and disordered in amorphous region (lighter pink area). The green lines are hypothetical paths for carriers.

Once deposited on a substrate (silicon oxide, quartz, flexible plastics ...) the morphology of the film strongly influence the electrical performances. Typically, to reduce the surface tension, the backbone of carbon chains doesn't lie on dielectric substrates. Instead, "rings" are almost

perpendicular ( $68^\circ$ ) to the sample plane and the backbone is parallel to it (**Figure I.3a**). Again, conjugated polymers benefit from the out-of-plane  $p_z$ -orbitals that tend chains to form  $\pi$ - $\pi$  stacking, possibly leading to well-ordered crystalline regions (**Figure I.3b**), whose properties are close to metal. Well-ordered areas extend only on the micrometer scale, hence organic semiconductors (OSCs) are known as semi-crystalline, meaning that crystalline regions are separate by amorphous domains. Usually, alkyl side-chains, which are tethered to the conjugated polymers in order to confer them a good solubility in organic solvents, separate the backbones from the substrate (edge-on orientation), but the face-on orientation, rings directly in contact with a dielectric substrate, in high temperature rubbing during the thin film deposition can also occur<sup>5</sup>. The electrical performance is strongly reduced by disordered domains because the polymer suffers of torsion and bending suppressing orbitals overlapping. The effect of disorder, inescapable in organic electronics, will be discussed all along this chapter.

The morphology of polymers is tunable even after deposition. Thermal annealing is the common way to tailor the crystallinity. The annealing temperature allows for example to reach either terrace (around  $180^\circ\text{C}$ )<sup>6</sup> or ribbon phase ( $> 240^\circ\text{C}$ )<sup>7</sup> for poly[2,5-bis(3-tetradecylthiophen-2-yl)thieno[3,2-b]thiophene] (pBTTT, **Figure I.4**). Mobility, which quantifies the ease of charge motion under applied electric field (see details in the next section), up to  $2\text{ cm}^2\cdot\text{V}^{-1}\cdot\text{s}^{-1}$  is reported in the terrace phase<sup>6</sup> characterized by ordered areas in random direction. In ribbon phase, polymer chains are much longer and form “stripes”. Surprisingly, mobilities are 1 to 2 orders of magnitude lower in the ribbon phase<sup>8,9</sup> although it is the most ordered phase. The origin of the poor mobility in the latter phase may be a higher sensitivity to defects at the interface. In all phases, the remaining limiting factor is the grain boundaries formed by polymer chains huddled up on themselves and acting as strong charge traps. It is worth noting finally that the highest mobility is along the backbone and not in the  $\pi$ - $\pi$  stacking direction<sup>5</sup>.

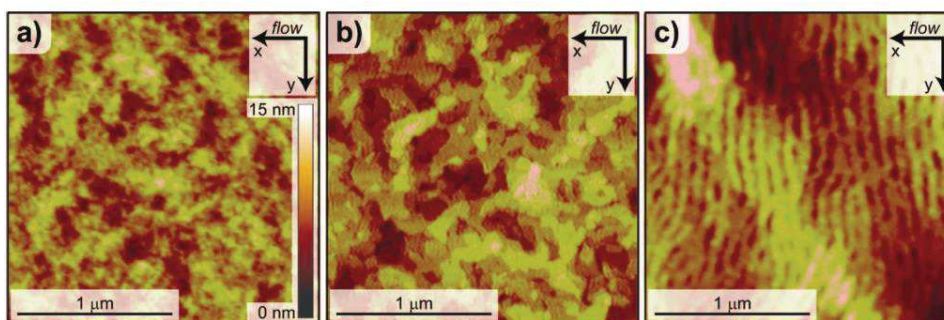


**Figure I.4** Different phase of pBTTT: a) as-cast; b) terrace phase and c) ribbon phase. Reprinted from Delongchamp *et al.*<sup>7</sup>.

The chemical tuning can be used to tailor the thin film morphology. For example, Poly(3-hexylthiophène) (P3HT) exists in different geometry, depending on the relative orientation of side carbon chains. The regioregularity, *i.e.* the side chains pointing all in the same direction, improves drastically the electrical performances. If alkyl chains organized randomly along the chain, regiorandom P3HT, it limits the stacking of the polymer and hamper the formation of large ordered regions<sup>10</sup>.

### I.1.2. Charge carriers

The mobility ( $\mu$ ) is the key quantitative indicator of intrinsic electrical properties of semiconducting materials. It quantifies how fast charge carriers can move when an electric field  $E$  is applied:

$$v_d = \mu E \quad (1.1)$$

where  $v_d$  is the drift velocity. Low mobility values is a key major issue to overcome for organic thin films, with values as low as a  $10^{-6} - 10^{-3} \text{ cm}^2 \cdot \text{V}^{-1} \cdot \text{s}^{-1}$  for amorphous and undoped organic films, many orders of magnitude lower than their inorganic counterparts. For comparison, amorphous silicon presents a mobility around  $1 \text{ cm}^2 \cdot \text{V}^{-1} \cdot \text{s}^{-1}$  while it increases to  $10^3 \text{ cm}^2 \cdot \text{V}^{-1} \cdot \text{s}^{-1}$  for highly ordered silicon crystals. Nowadays, mobilities of organic materials reported in literature equal or even overpass (mostly small molecules) amorphous silicon in organic field effect transistor (OFET) geometry, what is well resumed and carefully analysed in the paper of Paterson *et al.*<sup>11</sup>. Achieving such high values of mobility measures the high degree of potential of organic electronics for applications.

In the experimental part, the quantity mostly used to characterize the quality of polymer thin films is the conductivity ( $\sigma$ ), that depends on the mobility but also on the carrier density ( $n$ ):

$$\sigma = en\mu \quad (1.2)$$

where  $e$  is the elementary charge.

In contrast to inorganic ordered materials, charge carriers are not simple electrons or holes in conjugated polymers. The nature of polymers adds degrees of freedom through distortion and conformation. Two main kinds of carriers can be involved in electric transport depending of the backbone of macromolecules: solitons and polarons.

If the ground state of the polymer is degenerate, solitons carry the current. Solitons behave as solitary wave propagating without deformation and dissipation. Speaking simply, solitons can move along the backbone balancing between two potential wells corresponding to the two degenerate levels, meaning without energy changes (**Figure I.2a**). Solitons form usually in chain containing an odd number of carbons since an unpaired electron remains. The presence of a soliton leads to the appearance of a localized electronic level at mid-gap, which is half-occupied in the case of a neutral soliton and empty (doubly occupied) in the case of a positively (negatively) charged soliton (**Figure I.5**). Charged soliton formation is possible because of the degeneracy: there is no extra distortion energy to pay to separate charges as the geometric structure as well as the energy landscape is the same in both direction, then charges just go apart from each other through Coulomb repulsion.

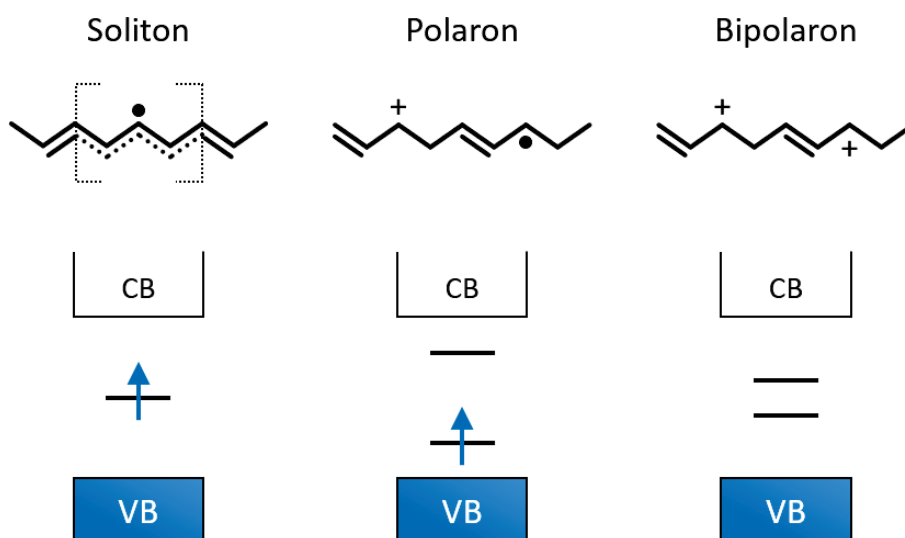


**Figure I.5** Schematics of soliton, polaron and bipolaron on a conjugated polymer with their respective energy levels.

On the other hand, if the ground state is non-degenerate, polaron transport takes place. Removing (adding) an electron of a neutral molecule leads to a charged excited state. Then a distortion occurs, not only of the newly charge molecule but also of the surrounding “crystal lattice” that localizes the charge and changes the mean distance between neighbouring molecules<sup>12,13</sup>. The charge moving, it carries the distortion with it, the combination of the two being the so-called polaron. However, the oxidation process lowers the ionization energy by  $\Delta\varepsilon$ , then the formation of polaron, needing an energy  $E_{dis}$  to distort the chain, competes with  $\Delta\varepsilon$ . If  $\Delta\varepsilon$  is larger than  $E_{dis}$ , polaron can form with a binding energy defines as  $E_p = \Delta\varepsilon - E_{dis}$ .  $E_p$  is also known as “geometric reorganization energy”, remembering that chains must reshape. Then, when the carrier is moving from one molecule to another, the initial chain will go back to its former structure, while the final polymer has to adapt. Austin and Mott demonstrated that the minimum activation energy to jump from one molecule to its neighbour is half of the polaron energy  $E_p$ <sup>14</sup>. Due to the non-degenerate ground state, polaron formation induces two localized mid-gap levels (**Figure I.5**). Therefore, polarons can be positively or negatively charged (not neutral) and carry a one-half spin.

Going further, if a second reduction occurs, either a second polaron is created elsewhere on the chain or the electron is taken from the former polaron, leading to a so-called bipolaron (**Figure I.5**). A bipolaron is a pair of like charges maintain together through the lattice distortion they create themselves. To get a bipolaron, the energy gain by the interaction with the lattice has to overcome the Coulomb repulsion between the quasiparticles. In order to determine if it is more favourable to form one bipolaron or two polarons, Brédas and Street calculated their corresponding distortion energy  $E_{dis}$ . They demonstrated that  $E_{dis}$  is nearly the same for one bipolaron or two polarons<sup>12</sup>. What will tip the balance in favour of one or the other is the decrease in ionization energy. In the case of bipolaron, the ionization energy is strongly reduced compared to the two polarons situation. Therefore, bipolarons are thermodynamically more favourable despite the Coulomb repulsion.

The question of whether carriers are polarons or bipolarons is of key relevance for spintronic applications. Indeed, bipolarons are spinless quasiparticles since the bipolaron levels are empty or fully occupied for  $p$ -type (holes) or  $n$ -type (electrons) semiconductor respectively. Bipolaron transport regime is thus expected to be useless for spin transport.

### I.1.3. Disorder

The morphology of the polymer strongly affects the carrier transport through the channel, as mentioned in section I.1.1. Disorder induces a lowering of the  $\pi$ -orbitals overlapping, altering the  $\pi$ -conjugation. Therefore, the coherence length of charge carriers is strongly dependent on the degree of disorder of the channel. Disorder has different origins divided in two categories, the static being distinguished from dynamic disorder<sup>15</sup>.

Static disorder, or structural or diagonal disorder, refers to variation of intermolecular distances and orientations of backbones of neighbour chains. The origin of this kind of disorder is the twisting of molecules, chemical impurities and inhomogeneous electrostatic bath due to a random orientation of polar groups of the OSC. It competes with Van der Waals interactions that favour a specific orientation of the polymer chains with respect to each other. Static disorder leads to time-independent spatial variations of the energy and hopping distances from site to site.

Dynamic disorder is related to thermal fluctuations of chains. The electron-phonon interactions lead to time-dependent fluctuation of electronic coupling between molecules, which directly translates in variation of site energies, the energy of a carrier in a particular position that depends on its surrounding, and transfer integrals, that quantify the hopping probability from one orbital to its neighbour, *i.e.* the site-to-site tunnelling.

These disorders relate to a heterogeneous landscape of energy levels and orbitals overlapping in polymer thin films. Therefore, charge carriers are not fully free since the neighbour sites need to match in energy and spatial gap.

Finally, to further complicate the system, the structure (electronic and geometric) of chains changes with the material on which it lays, at least for the first layers. For example, the morphology of the thin film on metallic electrodes can differ from the one on the dielectric substrate because of interface property variations between materials.

## I.2. Charge transport

Understanding the transport phenomenon is fundamental before thinking about designing organic-based devices. If analogies between organic and inorganic semiconductors are useful, the charge transport is radically different. In OSCs case, carriers hop from one site to the next one, explaining partially why their mobility is limited compare to their counterpart. Since hopping transport is a thermally assisted tunnelling transport, charges experience a dwell time on each site before reaching the next molecule.

### I.2.1. Miller-Abrahams' hopping rate

Miller-Abrahams' hopping rate, developed in 1960, was the initial model used for OSC charge transport study<sup>16</sup>. It relies on an asymmetric jump rate depending if the final state is higher or lower in energy than the initial one. While a downhill jump is easy through energy dissipation, an activation energy is needed for uphill transfer. The Miller-Abrahams' hopping rate  $\nu_{ij}$  between two sites,  $i$  (initial) and  $j$  (final), separated by a distance  $r_{ij}$ , expresses as:

$$\nu_{ij} = \nu_0 \exp[-2\gamma r_{ij}] \begin{cases} \exp\left[-\frac{\varepsilon_j - \varepsilon_i}{k_B T}\right], & \varepsilon_j > \varepsilon_i \\ 1, & \varepsilon_j \leq \varepsilon_i \end{cases}, \quad (1.3)$$

where  $\nu_0$  is the attempt-to-hop frequency,  $\gamma$  is the inverse of the localization radius of the electron wavefunction and  $\varepsilon_i$  and  $\varepsilon_j$  are energies of site  $i$  and  $j$ , respectively. The attempt frequency factor  $\nu_0$  is usually around  $10^{13} \text{ s}^{-1}$ , close to the phonon frequency as hopping transport is phonon-assisted<sup>17</sup>. Indeed, each carrier hops involved at least one phonon, either emitted if  $\varepsilon_j \leq \varepsilon_i$  or absorbed if  $\varepsilon_j > \varepsilon_i$ . The first exponential term is the exchange coupling, it is the tunnelling rate between two sites of equal energy but spatially distant.  $\gamma^{-1}$  is of the order of  $1 - 10 \text{ nm}$ <sup>17,18</sup> and depends on the electronic coupling between sites. The last term is the Boltzmann factor, normalized to 1 when the final site is lower in energy, and exhibits a thermal activation probability for upward jumps. An important assumption takes place here: the probability to find a carrier or an empty site at a given energy does not depend on the energy gap between the site and the Fermi energy  $\varepsilon_F$ . Indeed, if  $\varepsilon_i$  and  $\varepsilon_j$  are both high energy levels above  $\varepsilon_F$ , sites are mostly unoccupied and the probability to have a charge carrier on this pair of sites is low. On the contrary if both energies are below  $\varepsilon_F$ , most sites are occupied and only a small number of empty sites are available<sup>19</sup>.

The temperature dependence implies a semiconductor character since the higher the temperature, the higher the number of phonons, thus the higher the probability for the carrier to absorb a phonon with the appropriate energy. When the temperature goes down and tends to 0, hopping can only take place downward, since thermal-activated processes reach negligible probability values, to end up with the lowest energy state where no carrier has a surrounding more favourable site. Therefore, the conductivity vanishes at low temperature.

In the presence of an electric field  $\vec{E}$ , the additional term  $-e\vec{E} \cdot \vec{r}_{ij}$  is added to the Boltzmann factor to favour hopping in the direction of the field. On the contrary, there is no fostering of downhill jumps, assumed to always occur whatever the energy difference.

However, Miller-Abrahams' model doesn't involve the geometric reorganization energy of charged molecules. This polaronic effect requires another model: the Marcus hopping rate.

### I.2.2. Marcus hopping rate

Rudolph Marcus received the Nobel Prize in Chemistry in 1992 for his work on electron transfer in chemical systems<sup>20</sup>. If its model applies to different phenomenon from photosynthesis to

corrosion, it is also useful to describe carriers hop between molecules in semiconducting organic thin films.

Marcus' model from 1956 derives from the Fermi's golden rule in a semiclassical approach where occupation probability follows the Boltzmann factor. In this framework, and assuming no entropy changes, the activation energy writes

$$E_a = \frac{(\lambda + \Delta E)^2}{4\lambda}, \quad (1.4)$$

where  $\Delta E = \varepsilon_j - \varepsilon_i$ , and  $\lambda$  is the reorganization energy. Fermi's golden rule leads then to the Marcus hopping rate

$$v_{ij} = \frac{J_{ij}^2}{\hbar} \sqrt{\frac{\pi}{\lambda k_B T}} \exp\left[-\frac{(\lambda + \Delta E)^2}{4\lambda k_B T}\right], \quad (1.5)$$

where  $J_{ij}$  is the electronic coupling between sites decaying exponentially with the distance ( $J_{ij} = J_0 \exp[-2\gamma r_{ij}]$ ) and included the collision frequency and the transmission coefficient<sup>2</sup>. Here also, the effect of electric field can be added, in the same way than previously done for Miller-Abrahams model.

Marcus theory is more complete and closer to experimental measures than Miller-Abrahams one, but it is also more difficult to apply since it added an additional parameter ( $\lambda$ ). For this reason, the first theory is more often used. More sophisticated models such as Marcus-Levich-Jortner<sup>21,22</sup> or Lanzani<sup>23</sup> theories also exist, that take place when the semi-classical point of view collapses.

### 1.2.3. Gaussian disorder model

To describe charge transport, knowing the hopping rate is not enough. The jump probability has to combine with the energy landscape of the material. In 1993, Heinz Bässler proposed that carriers hop through randomly distributed sites with a Gaussian energy spectrum<sup>24</sup>. The motivation was first to explain electronic transport in photoconductors used for electrophotolithography, but Bässler's model, so-called Gaussian disorder model (GDM), applies for any disordered material showing incoherent hopping transport and is widely used in the organic electronic community. Bässler's work is based on Monte Carlo simulations and neglects polaronic effect. Therefore, the Miller-Abrahams hopping rate was preferred.

For the Monte Carlo simulation, Bässler considers a cubic lattice of  $N$  sites separate by the conjugation length of polymers, *i.e.* the length of uninterrupted  $\pi$ -bonds. Each site is a localized electronic state with a Gaussian energy distribution

$$g(\varepsilon) = \frac{N}{\sigma\sqrt{2\pi}} \exp\left[-\frac{\varepsilon^2}{2\sigma^2}\right], \quad (1.6)$$

where  $\sigma$  is the standard deviation of the density of state (DOS) usually chosen around 0,1 eV that expresses the randomness of the intermolecular interactions<sup>24,25</sup>, particularly important for conjugated polymer due to the variation of conjugation length and thus of energies. The energy  $\varepsilon$  is relative to the middle of the DOS, *i.e.* the Gaussian is centred at 0. The choice of Gaussian shape was motivated by the absorption spectra of disordered organic materials and from the central limit theorem that would lead to a Gaussian envelope from the large amount of random interactions. There was first no deeper physical or chemical reason. However, since the Gaussian had to compete with a simplest exponential DOS, new arguments favoured the Gaussian shape, particularly for low carrier concentration<sup>19</sup>. Experimentally, Hulea and co-workers managed to prove a Gaussian distribution at least at the middle of the DOS<sup>26</sup>.

Consider charge carriers generated at arbitrary sites following the Gaussian distribution. They will first hop to lower energy sites and relax to the tail of the DOS performing a random walk. However, at finite temperature, a quasi-equilibrium take place between the downhill jumps and the thermal activated uphill jumps. Indeed, the number of nearby states lower in energy decreases strongly with the relaxation of the system, that makes an uphill jump eventually easier. The mean energy of carriers  $\varepsilon_\infty$  is then given by the long-time limit of the statistically weighted average

$$\varepsilon_\infty = \lim_{t \rightarrow \infty} \varepsilon(t) = \frac{\int_{-\infty}^{+\infty} \varepsilon g(\varepsilon) \exp\left[-\frac{\varepsilon}{k_B T}\right]}{\int_{-\infty}^{+\infty} g(\varepsilon) \exp\left[-\frac{\varepsilon}{k_B T}\right]} = -\frac{\sigma^2}{k_B T} \quad (1.7)$$

where  $g(\varepsilon)$  is the Gaussian distribution from equation I.6. The occupied DOS (ODOS) will take place in the tail of the gaussian DOS (**Figure I.6**). It is worth noting that the weight used for the average is the Boltzmann factor, assuming that the carrier density is low enough to neglect carrier-carrier interactions which would involve the Fermi-Dirac statistics.

$\varepsilon_\infty$  is highly dependent on the temperature, the lower the thermal agitation, the lower the mean carrier energy. However, for temperature below a critical value,  $\varepsilon_\infty$  tends to curve upwards. Indeed, for low enough temperature, the probability of thermal agitation is so small that carriers are stuck once they reach a sufficiently low state, and they cannot overcome a little energy barrier to fall in a deeper energy well<sup>27-29</sup> (**Figure I.7**).

In analogy with the mobility edge in amorphous inorganic materials which is the highest localized level, the so-called effective transport energy  $\varepsilon_t$  is defined, that assigns states responsible for electronic transport. After relaxation, all states are localized and carriers reside in the tail of the DOS. If thermal agitation promotes a carrier to a nearby site, but no more favourable states are available from this new state, it will come back to its initial site. However, if the new state energy is close enough to the centre of the DOS, the probability to continue its pathway through series of jumps becomes higher. The energy at which subsequent jumps are achievable is the effective transport energy  $\varepsilon_t$  laying in between the mean energy  $\varepsilon_\infty$  and the center of the DOS (**Figure I.7**).

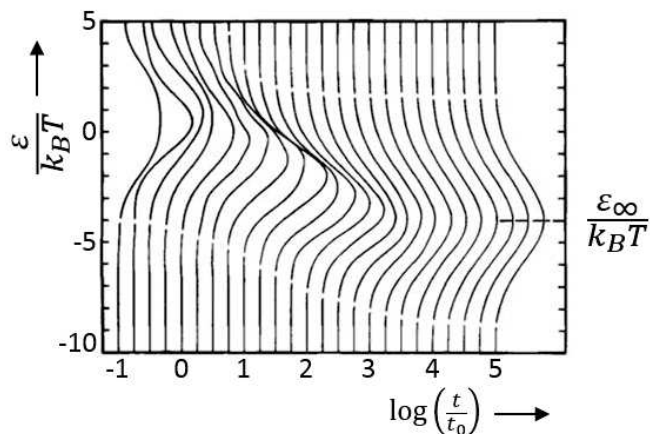


**Figure I.6** Temporal evolution of non-interacting carriers. The distribution tends to a Gaussian DOS centred at  $\varepsilon_\infty$ . Reprinted from Köhler and Bässler<sup>2</sup>.

The discussion above is valid as long as the dopant concentration is low enough to neglect carrier-carrier interactions. However, high doping level is reachable in organic materials through different techniques and in particular for the experiments described in the following chapters. As these interactions become important the key difference will be the used statistics that will change to Fermi-Dirac distribution.

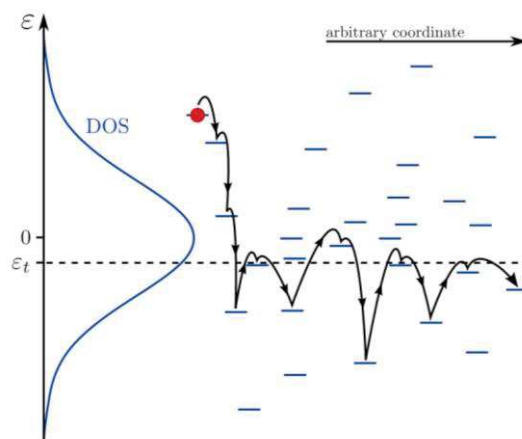


**Figure I.7** Diagram of the energetic path of a charge carrier. Once at low energy, it cannot continue to decrease and oscillates around the transport energy. Reprinted from Baranovskii *et al.*<sup>19</sup>.

With a higher carrier density, the ODOS may be filled until a Fermi level above  $\varepsilon_\infty$ . Then the thermal activation is easier and charge transport is weakly temperature dependent since jumps occur no more from a localized state within the ODOS to the transport energy but from the Fermi level. As the average energy difference between initial states and the transport level decreases, the mobility increases. However, the additional charges broaden the DOS that partially counterbalance the increase of Fermi level, limiting the reduction of activation energy (**Figure I.8**).

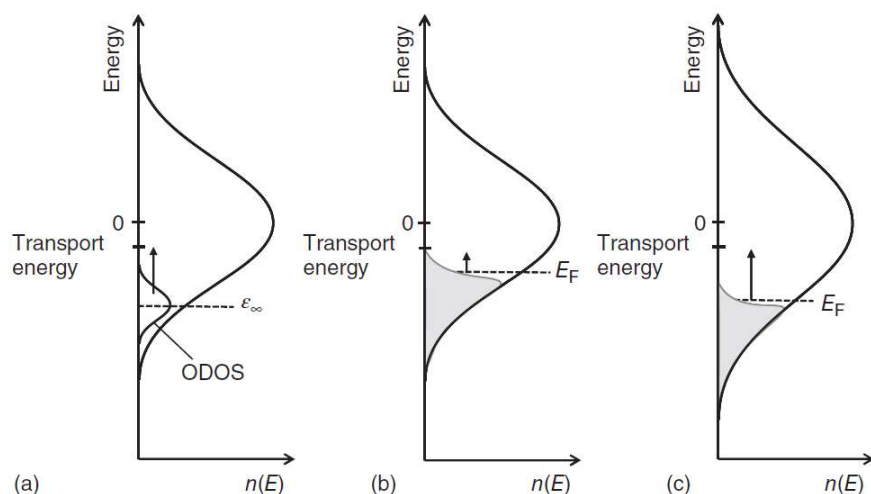


**Figure I.8** Density of states with its occupied area for: a) low carrier concentration; b) higher carrier concentration; and c) higher carrier concentration including the broadening due to the counter-charges. Reprinted from Köhler and Bässler<sup>2</sup>.

Indeed, the role of dopants doesn't limit to an increase of the number of carriers. The presence of counter-charges broadens and shapes the DOS. Arkhipov and his co-workers showed that, among the increase of dopant concentration, the tail of the DOS broadens creating additional deep traps<sup>30</sup> (**Figure I.9**). This effect appears already for a dopant concentration of  $10^{17} \text{ cm}^{-3}$  that is well below what is achievable in electrochemically doped devices (up to  $10^{22} \text{ cm}^{-3}$  reported<sup>31</sup>). The maximum of the stretched exponential DOS is also shifted to higher values. Therefore, adding dopants may lead to weird situation where the conductivity increases with the dopant concentration while the mobility decreases<sup>32</sup>.

One has to emphasize also that the Gaussian disorder model doesn't account for correlation between sites. However, considering a random distribution of dipole moments, the long-range dipole electrostatic potential indeed leads to coupling between neighbour sites. These interactions are included in the correlated disordered model (CDM) and is particularly important for molecules with high dipolar moments or low field measurements to match well with experimental data<sup>33,34</sup>.

### 1.2.4. Variable range hopping

Focusing again on the Miller-Abrahams hopping rate, there is mainly two parameters that compete for a carrier to choose its next site: the distance and the energy of the final state. Therefore, the path of a charge is not simply along the closest (in energy or in distance) unoccupied site. If a charge is surrounded by much higher energy site, it could be more interesting to tunnel further away to a lower energy state.

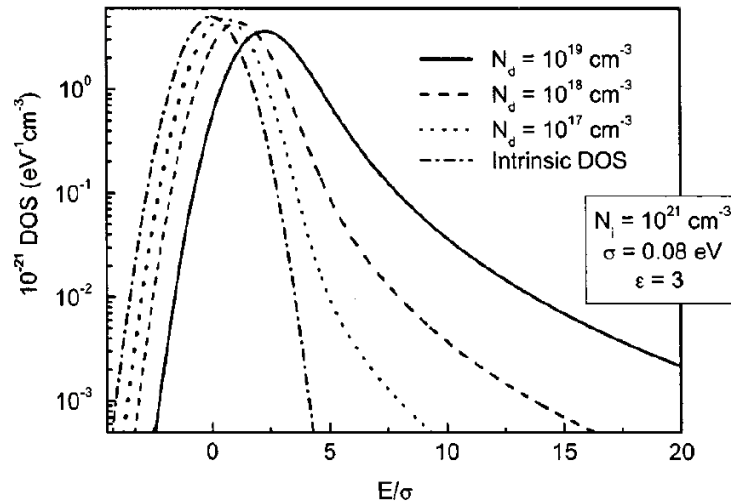


**Figure I.9** Density of states for different doping levels. Reprinted from Arkhipov *et al.*<sup>30</sup>.

As stated in equation I.3, the ability of carriers to overcome an energy difference depends on the temperature. Indeed, for high enough temperature charges may prefer closer site higher in energy than more distant site lower in energy. It leads to a temperature dependent hopping length, which give its name Variable range hopping (VRH). This model was introduced by Mott in 1968<sup>35</sup> and remains nowadays the most used low temperature transport mechanism in localized systems. The spatial distance a carrier is able to cross is governed only by the localization radius ( $\gamma^{-1}$ ).

VRH translates in a variation of conductivity with temperature following<sup>36</sup>:

$$\sigma(T) = \sigma_0 \exp \left[ - \left( \frac{T_0}{T} \right)^{\frac{1}{d+1}} \right] \quad (1.8)$$

where  $\sigma_0$  is the conductivity limit for an infinite temperature and  $d$  is the dimension of the considered system.  $T_0$  is the limiting temperature where model of thermally activated transport doesn't apply anymore and also helps to quantify the disorder.

If  $k_B T$  is much larger than the energy scale of the density of states, the hopping transport becomes energy independent and merges into nearest neighbour hopping (NNH) discussed by Miller and Abrahams<sup>16</sup>. In this case, the thermally activated transport shows a conductivity going like:

$$\sigma(T) = \sigma_0 \exp \left[ - \frac{E_a}{k_B T} \right] \quad (1.9)$$

where  $E_a$  is an activation energy.

### I.2.5. The metal-insulator transition and the mobility edge

A first classification between metals and non-metals was given by Wilson in 1931<sup>37,38</sup>. His argument was based on the work of Sommerfeld and Bloch dealing with the early quantum mechanics: energies of electrons are located in bands; if bands are full or empty, it is a non-metal, if one or more bands are partly full, it is a metal. The resistivity of metals tends towards zero at absolute zero while it tends towards infinity for non-metals. However, Wilson's model failed to explain the insulating behaviour of some materials such as nickel oxide. Indeed, this model was based on a one-electron placed in a perfectly ordered lattice picture, neglecting the interaction between electrons and impurities. Therefore, new models came out particularly after the works of Philip Anderson and Neville Mott that own them the Nobel Prize in 1977.

#### Mott transition

The metal to insulator transition insight results from considering a periodic lattice of same depth, but including electron-electron interactions<sup>39</sup>. The system is described as a regular sublattice of impurities with a periodicity  $b_0$  much larger than the host lattice one. Then one assumes that the characteristic size  $a_j$  of the  $j$ -site wave function is small compare to  $b_0$ . In other words, the wave function overlap between impurities is negligible, and the main contribution to the energy comes from the closest neighbours only.

Performing the calculation, Mott showed a band of allowed energies, instead of individual energy levels, with an energy width  $V_b \propto I \propto \exp(-b_0/a)$ . Due to the exponential decay of the overlap integral ( $I$ ), the band narrows with the distance between impurities (**Figure I.10**). However, as long as a single-electron point of view is kept, the conductivity of impurity electrons would remain of metallic nature, whatever the impurity concentration is.

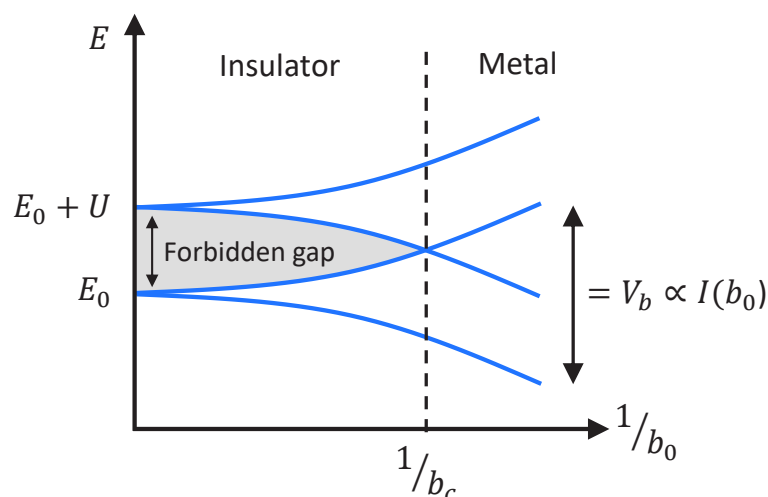


**Figure I.10** Variation of electron bands versus the sublattice period. Increasing  $b_0$  narrows the bands and creates a forbidden gap, changing the material from metallic to insulating. Adapted from Shklovskii & Efros<sup>40</sup>.

Considering now that two electrons of opposite spin locate on the same site. The Coulomb repulsion ( $U$ ) leads to a difference in energy between sites depending if there is ( $E_0 + U$ ) or not

( $E_0$ ) another electron. For large value of  $b_0$ , the overlap integral is small compare to the interaction energy  $U$ , therefore a forbidden gap exists, and the material is an insulator. In other words, there is a huge energy barrier for electrons to cohabit on the same site, because  $U \gg V_b$ . While  $b_0$  decreases, it reaches a critical value  $b_c$  where the two-level bands intersect and the gap vanishes. From this point, the material behaves as a metal. This kind of transition is referred as Mott metal-to-insulator transition.

### Anderson transition

Philip Anderson explained in his paper from 1958 that disorder alone leads to localization of carrier<sup>41</sup>. He developed a model where electrons meet a periodic lattice of potential wells having various depths. The fluctuation of the potential from well to well is random but limited in a window of  $\pm 1/2 V_0$  around the mean value  $V_0$  (**Figure I.11**). The randomness of these pits account for disorder. Then the localization question arises: what is the criterion for a carrier to be localized or delocalized?

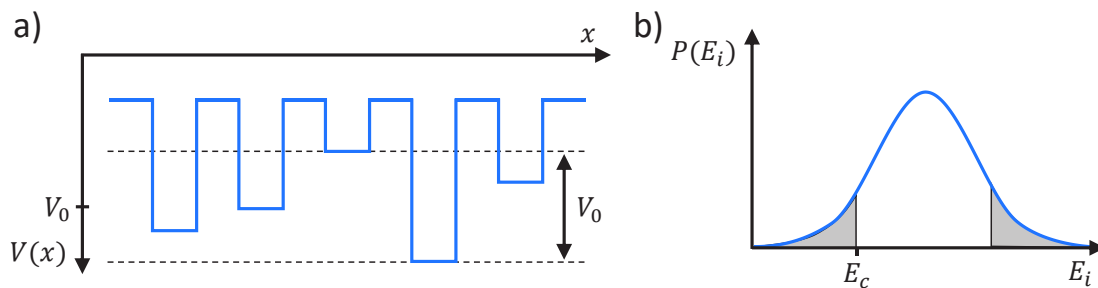


**Figure I.11** a) Representation of the random distribution of potential wells in the Anderson model. b) Energy distribution of carrier showing the critical energy  $E_C$  that delineates localized states (grey area) from delocalized ones. Adapted from Mott and Devis<sup>39</sup>.

For an electron to be delocalized, the wave function of sites must overlap over a macroscopic distance, creating an extended coherent state. Therefore, for an infinite system, one writes  $\lim_{t \rightarrow \infty} |\psi_i(t)|^2 = 0$  where  $\psi_i(t)$  is the wave function on site  $i$ . On the other hand, if the carrier is localized, neighbouring sites feel only the tail of the wave function dropping exponentially and the probability in the long time limit  $\lim_{t \rightarrow \infty} |\psi_i(t)|^2$  remains finite. The latter case is the so-called Fermi glass.

Anderson defines a parameter  $V_0/I$ , where  $I$  is the overlap integral between two sites, to predict the behaviour of charges: if  $V_0/I$  is too large all states are localized. A critical value  $(V_0/I)_c$  separates the localized from delocalized regime. When the ratio becomes smaller than  $(V_0/I)_c$ , delocalized states appear, and for values well below the critical one, main part of the band states is delocalized. Anderson originally obtains  $(V_0/I)_c \sim 10z$ , where  $z$  is the coordinate number<sup>42</sup>, and was then reduced to  $3 - 4z$  by other authors<sup>43,44</sup>.

The changeover being continuous, both types of sites coexist in a range of  $V_0/I$  around  $(V_0/I)_c$ . In this case, there exists a critical energy called mobility edge ( $E_C$ ) separating localized states from delocalized ones. The simplest definition of  $E_C$  is:

$$\begin{cases} \sigma(E) = 0, & E < E_C \\ \sigma(E) > 0, & E > E_C \end{cases} \quad (I.10)$$

Then if the Fermi energy  $E_F$  of a material can be tune such as it crosses  $E_C$ , a transition from metallic, where  $\sigma(E_F)$  is finite, to non-metallic, where  $\sigma(E_F)$  vanishes at zero temperature, occurs. This kind of transition is known as Anderson transition. The relative position of  $E_F$  and  $E_C$  can be changed in several ways such as: changing the composition, the number of electrons in the conduction band or the degree of disorder, applying uniaxial strain or changing the magnetic field in magnetic semiconductors.

Mott and Anderson transitions show both localization of charge carrier but their origin is fundamentally different: for Mott transition it comes from electron-electron interactions and for Anderson transition it results from disorder.

Summarizing the behaviour of a Fermi glass versus temperature, for several Fermi energy, would lead to the curves in **Figure I.12**. At high temperature, the energy of some carriers take place above the mobility edge and the material is metallic. When the Fermi energy is lowered, the metallic state remains until the conductivity reaches the so-called minimum metallic conductivity ( $\sigma_{min}$ ) that depends strongly on the distance between atoms in the lattice ( $a$ ). For example, with  $a \sim 3 \text{ \AA}$ , Mott extracted a  $\sigma_{min}$  ranging from 250 to 1000  $\text{S} \cdot \text{cm}^{-1}$ . If the Fermi energy is further decreased, Anderson localization sets in. This critical value for the conductivity will occur during our experiments.

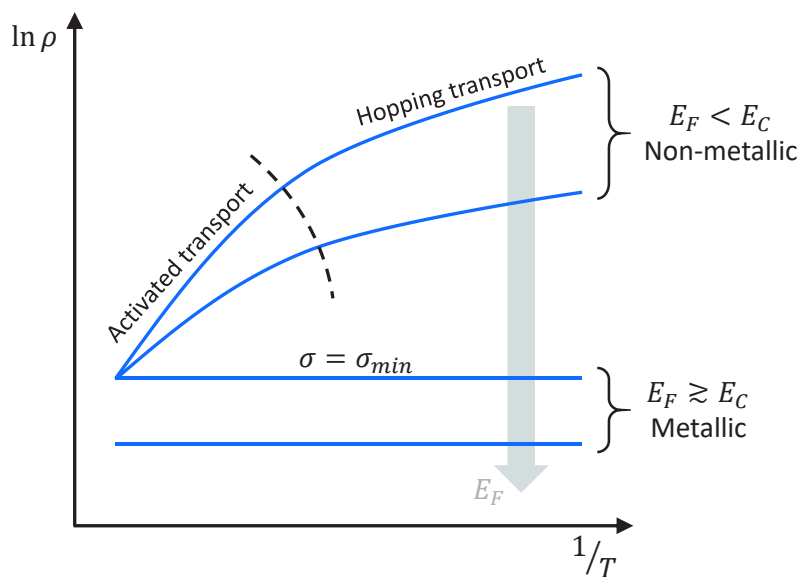


**Figure I.12** Resistivity of a material versus  $T^{-1}$  for different Fermi levels from lower to higher than  $E_C$ . Adapted from Mott *et al.*<sup>45</sup>.

When  $E_F < E_C$ , there are two mechanisms of conduction:

1. At higher temperatures, charge carriers are excited to the mobility edge and the conductivity follows

$$\sigma = \sigma_{min} \exp \left[ -\frac{E_C - E_F}{k_B T} \right] \quad (1.11)$$

2. At lower temperatures, charge carriers hop from site to site and nearest neighbour (NNH) and variable range (VRH) processes dominate.

### I.3. Charge injection

The successful discovery of high mobility organic materials ( $\mu > 1 \text{ cm}^2 \cdot \text{V}^{-1} \cdot \text{s}^{-1}$ ) initiated the development of new organic devices such as large area and/or low-cost flexible displays<sup>46,47</sup> or sensors<sup>48,49</sup>. However, downscaling organic electronic circuits in order to increase the working frequency reveals another issue to overcome: the poor charge injection from metallic electrodes to organic semiconductors. Indeed, the channel being smaller and smaller, contacts at the organic-inorganic interfaces might dominate the resistance of the device, limiting the supply (removal) of charges to (from) the active channel. This becomes particularly critical for the lateral configuration geometries of devices we investigate in this thesis. The contact performance limitation in hybrid devices is a main issue to solve for industrialization of organic-based applications and explains in particular why the miniaturization of ensembles of hybrid devices is still very far from the one reached in standard inorganic architectures.

#### I.3.1. Energy levels at interface

When two materials are brought into contact, they establish a common Fermi level  $E_F$  by exchanging carriers and reach thermal equilibrium. The material with the highest  $E_F$  (the metal for example) provides electrons to the second material (the semiconductor) that leads to a contact potential across the interface equal to the difference of  $E_F$  of both materials: the diffusion of carriers gives rise to a space charge region in the semiconductor and an electrical field takes place that tends to drive them back to the metal. Moreover, electrons leaving the metal left behind a lack of charge causing a positively charge metallic surface. It refers as an image charge that screens the electric field.

A major difference occurs if one look at metal/metal interface or metal/semiconductor interface. Contrary to metals, semiconductors have a gap in the DOS, defined by the HOMO (maximum of the valence band) and LUMO (the minimum of the conduction band) in the case of organic (inorganic) materials. The aim is then, in an organic device, to choose (or tune) the metal  $E_F$  to optimize the charge injection. If one wants to inject electrons, the Fermi energy of the metal must be at least close to, or better higher than the LUMO level (**Figure I.13a**). If it is holes that need to be injected,  $E_F$  needs to be lower than the HOMO. This is not to take too literally since thermal agitation and the gaussian distribution of HOMO and LUMO level give some freedom to these conditions. Furthermore, the gap of semiconductors reduces at the interface with a metal due to the screening of image charge potential as shown by Knupfer and Paasch<sup>50</sup> (**Figure I.13b**).

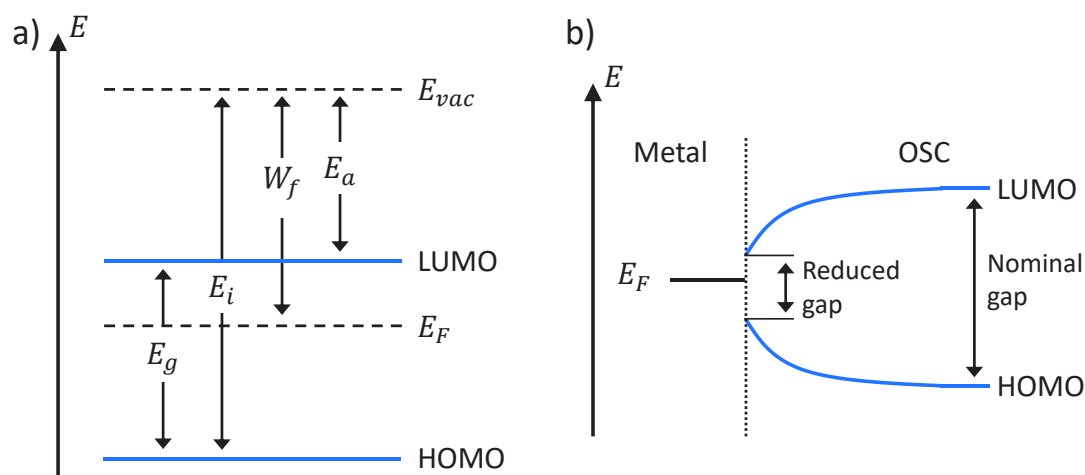


**Figure I.13** a) Energy diagram of an organic semiconductor. Energy gap  $E_g$ , ionization energy  $E_i$  (energy required to extract an electron from the HOMO), work function  $W_f$ , electron affinity  $E_a$  (energy required to add an electron to the LUMO) and vacuum energy  $E_{vac}$  are represented. b) Local distortion of HOMO and LUMO levels of OSC due to image charge screening. The bending occurs over few nanometres.

Another important energy of the metal to deal with is the working function ( $W_f$ ). It is defined as the energy needed to extract one electron from the Fermi level to the vacuum level ( $E_{vac}$ ), *i.e.* in free space, at rest, just outside the surface.  $W_f = E_{vac} - E_F$  is the energy barrier that prevents electrons at  $E_F$  to escape the material. It is a meaningful value only at the surface of a solid. Furthermore, the density of charges is redistributed at the surface compare to the bulk. It means that the surface component of  $W_f$  changes if the solid is in vacuum or in contact with another material. Indeed, at interfaces the charge redistribution leads to surface dipole from spill-out of electrons (**Figure I.14a**). However, when molecules are placed close to the surface, the Coulomb repulsion of their own electrons limit the spill-out effect, and  $W_f$  is affected (**Figure I.14b**). In the case of organic materials, it is important to think about it as they have a huge  $\pi$ -electron cloud out of the plane of the backbone pushing back the metal electrons at an organic-inorganic interface. Hwang *et al.*<sup>51</sup> for example, observed a shift of the work function as high as 1 eV for gold (widely used in this thesis), which is clearly non-negligible. It is important to remind also that the Fermi level of the metal is altered too as there is diffusion of charge at the interface.

With the phenomena described in this section, it is easy to understand the difficulty to define interfaces, as the main part of parameters we know from a material in vacuum are not relevant, and even worse they change for every material combination. Adding that the determination of these values needs often specific instruments like ultraviolet or X-ray photoelectron spectroscopy (UPS/XPS), the knowledge of real energies at contacts is not obvious.

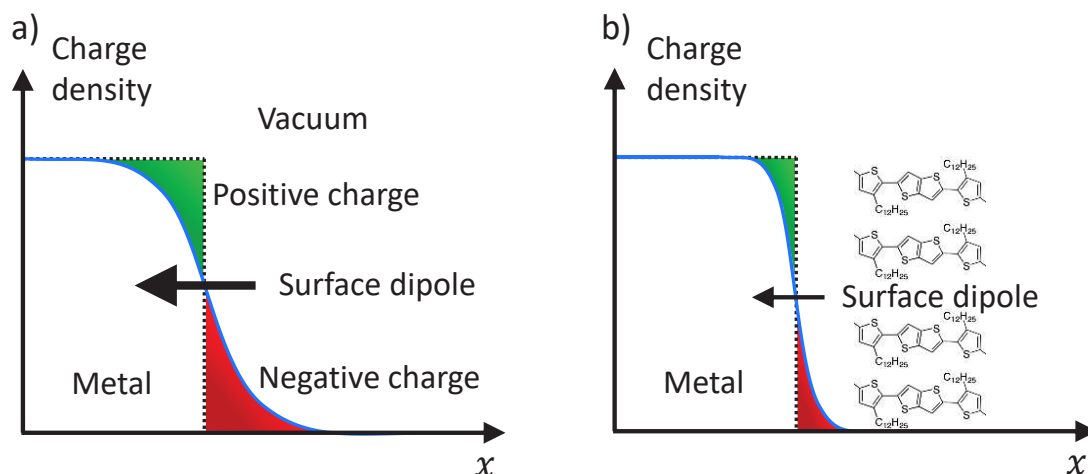


**Figure I.14** Charge density at the edge of a metal on the interface with vacuum (a) and physisorbed molecules - conjugated polymer for illustration (b). A negative charge density takes place due to the redistribution of charges at the interface, letting a positive charge density in the metal that forms a surface dipole. The dipole is weaker when molecules are present because their electron clouds repels charges from the metal.

### I.3.2. Schottky effect and barrier height

Well known from inorganic semiconductor-based devices, the Schottky effect applies also to metal-OSC junctions. As previously mentioned, a charge diffusion takes place between materials having different Fermi levels. In the case of metal/semiconductor (SC) contacts, the diffusion of electrons occurs from metal to SC if it is a *p*-type SC, and in the opposite direction if the SC is *n*-type (**Figure I.15**). It leads to a depletion (accumulation) region what bends up (down) energy levels in the *n*-type (*p*-type) SC. We emphasize that in the case of organic materials, there is no band bending as they generally don't show band transport. Instead, there is more likely energy levels shifting close to the interface. The Schottky barrier height is defined as  $\phi_B = W_f - E_a$  (for *n*-type) or  $\phi_B = E_g - (W_f - E_a)$  (for *p*-type), and quantifies the energy to overcome for an electron (hole) to be injected in the semiconductor. It is worth noting that Schottky effect is often discussed in *p-n* junctions where there is accumulation on one side and depletion on the other. However, in our devices, the OSC is in contact with a metal, much more conductive. Then, all charges involved are located at the metal interface whereas they spread over several nanometres inside the OSC. Therefore, the space charge region occurs mainly in the OSC part of the interface and is negligible in the metal.

While the diffusion of electrons occurs, an electric field takes place because of the image charges discussed earlier, leading to thermal equilibrium. The resulting electrostatic potential  $V$ , relatively to  $E_F$ , of a charge carrier at distance  $x$  from the interface in an external field  $\vec{E}_{ext}(V_{SD})$  (in the  $-x$  direction) and with an energy site  $E$ , is given by<sup>52</sup>:

$$V(x, E) = \phi_B - \frac{e^2}{16\pi\epsilon x} - e|\vec{E}_{ext}|x + E \quad (1.12)$$

$\phi_B$  is the barrier height without image charge and external field (*i.e.* the difference between work functions of both materials),  $e$  is the elementary charge and  $\varepsilon = \varepsilon_0 \varepsilon_r$  the permittivity of the OSC with  $\varepsilon_0$  the vacuum permittivity and  $\varepsilon_r$  its dielectric constant.

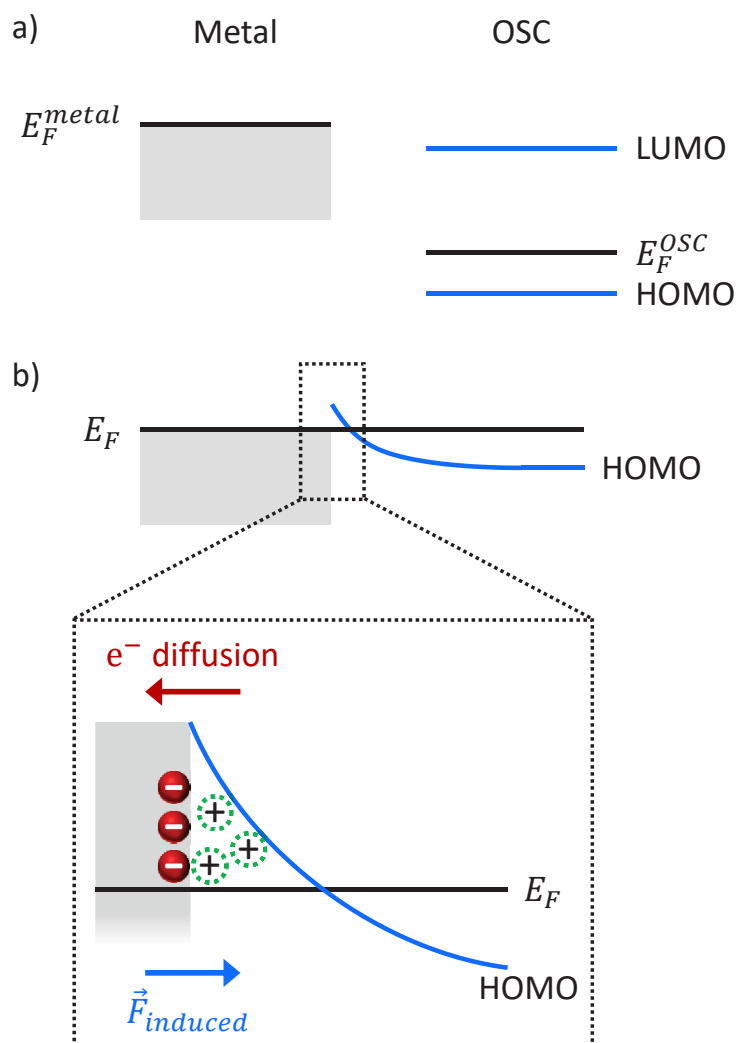


**Figure I.15** a) Isolated metal and OSC energy levels. b) Energy levels when the metal and the OSC are putted into contact. First, electron diffusion occurs and is then counterbalanced by the electric field created by the lack of charges in the metal, the so-called image charges. It results a related electric force on electrons ( $\vec{F}_{induced}$ ) that tends to drive them back in the metal. Equilibrium between diffusion and Coulomb attraction takes place.

The competition between the image charge screening ( $\propto x^{-1}$ ) and the applied voltage ( $\propto x$ ) leads to a local maximum value of the potential<sup>53</sup> given by solving  $dV(x, E)/dx|_{x=x_{max}} = 0$  (**Figure I.16**):

$$x_{max} = \sqrt{\frac{e}{16\pi\varepsilon|\vec{E}_{ext}|}} \rightarrow V_{max} = \phi_B - \Delta\phi = \phi_B - e\sqrt{\frac{e|\vec{E}_{ext}|}{4\pi\varepsilon}} \quad (I.13)$$

The barrier height is thus reduced by  $\Delta\phi$  when the image charge is considered. The higher the external field, the closer is the maximum of the barrier from the interface. It is worth noting that the potential lowering from image charges is larger for organic materials since their dielectric constant is lower than inorganic materials one.

Applying a forward voltage (negative voltage on  $n$ -type semiconductor) also shifts up the Fermi level of the semiconductor and favour electron injection. Arkhipov *et al.*<sup>52</sup> showed that to have a relevant Schottky effect, *i.e.* a significant barrier lowering, the electric field need to be at least  $10^5 \text{ V} \cdot \text{cm}^{-1}$  (Figure I.17).

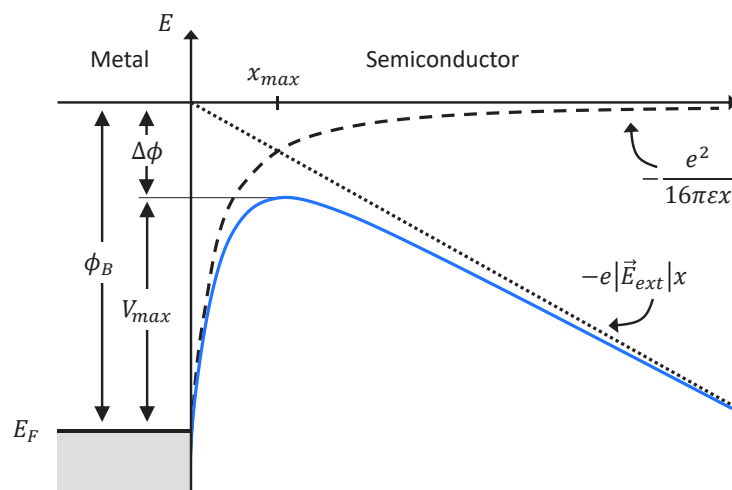


**Figure I.16** Potential energy profile due to the lowering from the image charge and the applied external field at the metal-semiconductor interface. Adapted from Sze and Ng<sup>53</sup>.

Many intertwined phenomena happen at interfaces as suggested in the few last paragraphs. If the Schottky effect helps, injection remains one of the main limitations for hybrid organic-inorganic devices as the current of the overall system may strongly depend on the carrier injection capability of interfaces.

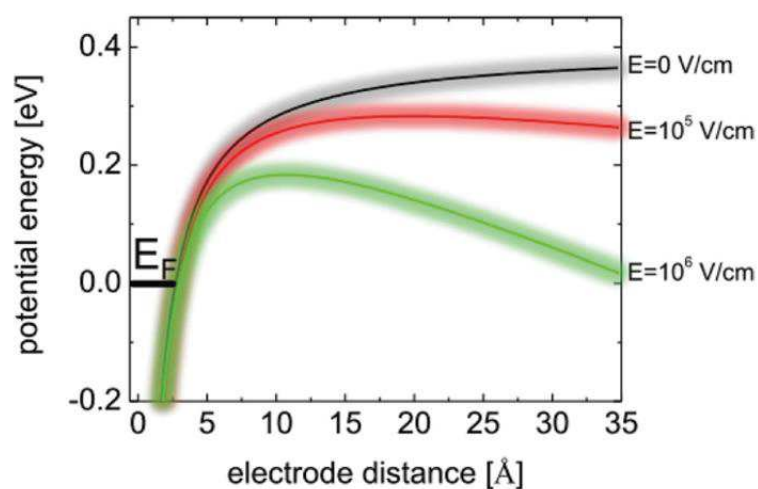


**Figure I.17** Potential energy distribution at the metal-semiconductor interface for three values of the applied external electric field (nominal barrier  $\phi_B = 0,4 \text{ eV}$ ).

Solid lines show the average electrostatic LUMO energy due to the superposition of the image charge field and the external electric field. The larger the external electric field, the lower the maximum of the potential energy becomes (Schottky effect). The glow around solid lines qualitatively reminds that states are statistically distributed due to energetic disorder. Reprinted from Natali & Caironi<sup>54</sup>, based on Arkhipov *et al.*<sup>52</sup> calculation.

### 1.3.3. Injection limited current

Once the carrier overpasses the potential barrier, it can either continue its path or be caught back by the electrode due to the image-charge attraction. For clarity we limit the following to the injection of an electron from the metal into the semiconductor.

Arriving in the semiconductor, with its much lower mobility compared to the metal (as it is the case for OSCs), the carriers experience a big cloud of charges because the diffusion into the bulk, away from the interface, is difficult. Thus, the backflow is in average more favourable and the injection is said to be space charge limited (SCL). It means that the poor mobility of OSC doesn't affect only the charge transport but also the injection. SCL conduction is exhibited through linear current-voltage characteristic curves in log-log scale at low bias and quadratic at high bias. The assumption behind the SCL is that the contact is able to provide as much carrier as needed, what it then an ohmic contact. However, ohmic contacts are challenging to do in organic electronics because of the considerably higher bandgap of OSCs compare to inorganic SCs. Therefore organic devices are usually injection limited (IL).

IL conduction is known from inorganic devices and two main descriptions exist: tunnelling injection (Fowler-Nordheim model) and thermionic emission (Richardson-Schottky model). The former was introduced in 1928<sup>55</sup> to describe the electron emission from a metal into vacuum in the scope of scanning transmission microscopy. It is the standard idea of tunnelling, where the carrier has a finite probability to cross the barrier even if its energy is lower. However, they add the effect of a (strong) external field ( $-e|\vec{E}_{ext}|x$ ) that modifies a rectangular tunnel barrier (from metal-vacuum interface, whatever the thickness) into a triangular one (**Figure I.18a**). They predicted a current density following:

$$j^{FN}(|\vec{E}_{ext}|) \propto |\vec{E}_{ext}|^2 \exp \left[ -\frac{4}{3} \frac{\sqrt{2m_{eff}} \phi_B^3}{\hbar e |\vec{E}_{ext}|} \right] \quad (I.14)$$

where  $\hbar$  is the reduced Planck constant and  $m_{eff}$  the effective mass of carriers. However, Fowler-Nordheim tunnelling doesn't consider the image charge potential. Even more crucial, the distance the carrier must travel in order to cross the barrier by tunnelling is side-lined but seems to be very long. Indeed, the barrier length is often several times longer than the intermolecular distance even for low injection barrier. Thus, the probability to reach the organic material without experiencing inelastic scattering is very low.

The second model is the Richardson-Schottky thermionic emission<sup>56</sup>. The potential considered in this model is the one discussed within the Schottky effect section, it means that the

image charge is present (**Figure I.18b**). The concept here is to deal with an electron that is first thermally activated above the energy barrier and then injected over the lowered barrier ( $\phi_B - \Delta\phi$ ). The current is then:

$$j^{RS}(|\vec{E}_{ext}|) = A^*T^2 \exp\left[-\frac{\phi_B - \Delta\phi}{k_B T}\right] = A^*T^2 \exp\left[-\frac{\phi_B - \alpha\sqrt{|\vec{E}_{ext}|}}{k_B T}\right] \quad (1.15)$$

where  $\alpha = \sqrt{e^3/4\pi\epsilon}$  and  $A^*$  is the Richardson constant. There are two important differences with the previous Fowler-Nordheim model: the temperature and the field dependence. The current here follows an Arrhenius-type variation ( $\ln j^{RS} \propto T$ ) that describes the decrease of electron energies while lowering the temperature in the metal. Indeed, at lower temperature, the amount of charge having an energy equal or higher than the barrier reduces exponentially. Secondly, the field dependence is of Poole-Frenkel-type ( $\ln j^{RS} \propto \sqrt{F}$ )<sup>57</sup>.  $A^*$  depends on the material but contains also a corrective factor that takes into account the backflow of electrons at the interface. In the case of low-mobility OSCs, the high carrier density near the junction hampers the majority of carrier to cross the barrier in this model.

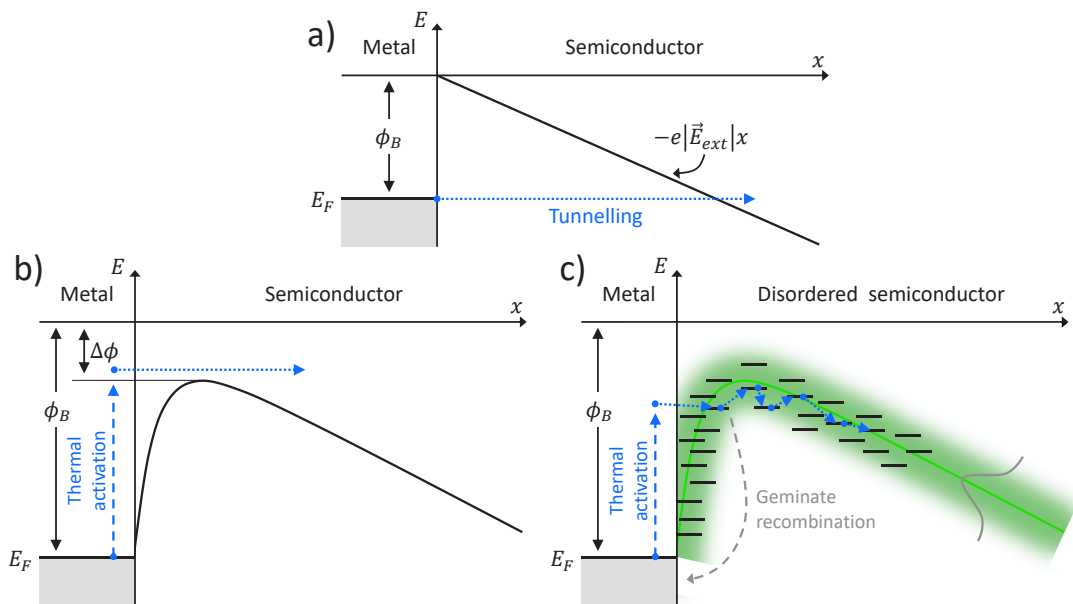


**Figure I.18** Electron injection from metal to semiconductor through a) Fowler-Nordheim tunnelling, b) Richardson-Schottky thermionic emission and c) hopping in a disordered organic material. The thermal activation in c) is lower than in b) because the charge energy can be lower than the barrier for injection to occur.

Both models described above were developed for inorganic crystalline material, but they hardly match OSCs. Indeed, a hidden assumption of these theory is the long scattering length of electrons in the semiconductor intrinsic to their band transport. However, short mean-free path ( $\sim 1$  nm) are expected in organic materials because of the weak Van der Waals interaction between molecules and their hopping transport mechanism. It is then very unlikely that an electron would manage to overcome an energy barrier several nanometre away (at least 0,8 nm for a

field of  $10^6 \text{ V. cm}^{-1}$ , see **Figure I.17**) knowing that a typical jump distance in OSCs is 0,6 nm. It means that charge injection into OSCs should be a multiple step process.

Bässler and co-workers developed a new theory based on a two-step process in a 3-papers work<sup>52,58,59</sup> where they investigated such an interface through Monte Carlo simulation followed by analytical calculation. First, the charge carrier is thermally activated as in the thermionic emission model, but the energy require is lower because it doesn't have to overpass the maximum of the potential barrier (**Figure I.18c**). Indeed, the carrier needs only enough energy to reach the (localized) tail states of the Gaussian DOS of the disordered material. Then two possibilities arise: recombination with the image charge or jump deeper in the bulk. The latter is the second step needed for the charge injection. Once in the tail state of the DOS, the carrier performs a random walk within the energetically and spatially disordered hopping sites, seen as a continuous diffusive motion in an Onsager-like process<sup>60,61</sup>.

### I.3.4. Tuning charge injection

In order to enhance the performances of organic devices, it is necessary to think about interfaces because they are often the limiting factor. Moreover, with the high mobility race of these last years, the bulk conductivity becomes more and more competitive with inorganic ones but doesn't solve the problem of high contact resistance, which becomes the main bottleneck.

The first and maybe easiest way to tune the charge injection is to select the good combination of metal and organic materials. As the barrier height  $\phi_B$  depends on the metal work function, choosing a material that matches well with the level of the organic semiconductor (HOMO or LUMO depending if it is a *p*- or *n*-type OSC) is the first step to reduce the contact resistance. However, as already mentioned, the work function is dependent of the surrounding material, hence the choice is not straightforward.

Another way to handle efficient charge injection is the surface treatment of electrodes with self-assembled monolayers (SAMs). Immersion in solution of 1H, 1H, 2H, 2H-perfluorodecanethiol (PFDT) or 1-decanethiol (1DT) for example leads to a shift of work function (upward or downward) because of the monolayer formation of these molecules at the surface of electrodes<sup>62,63</sup>. If main works have been performed on gold electrodes, there is also some promising achievement on ferromagnetic electrodes, where SAMs were also claimed to be useful as passivation layer<sup>64</sup>. Graphene growth on nickel was also performed and showed interesting results<sup>65</sup>.

The temperature is also a way to control the barrier. As previously seen, the disordered-induced Gaussian ODOS centre lies  $-\sigma^2/k_B T$  below the one of the DOS. Then the lowest the temperature, the farther is the ODOS from the original LUMO, favouring electron injection (**Figure I.19**). Of course, lowering the temperature also implies the reduction of the number of high energy electrons and possibly counterbalances the injection enhancement. These two competitive phenomenon can be modelled by a temperature-dependent barrier reduction such as  $\Delta\phi_B = -\sigma^2/2k_B T$  as long as the temperature is high enough to hold the Maxwell-Boltzmann distribution valid<sup>66</sup>. From the Monte Carlo simulation of Arkhipov *et al.*<sup>58</sup>, the two competitive

effects seem to cancel out each other for moderate barriers ( $\phi_B \leq 0.4$  eV) and improve injection for higher barriers. Hitherto, the disorder was only a limiting factor for device performances, but here we show that it can sometimes be useful. One interesting outcome is that lowering the temperature is expected to decrease the mobility of OSCs, but can potentially improve the charge injection, making therefore temperature a useful tool to tune the two contributions to the total resistance of a device.

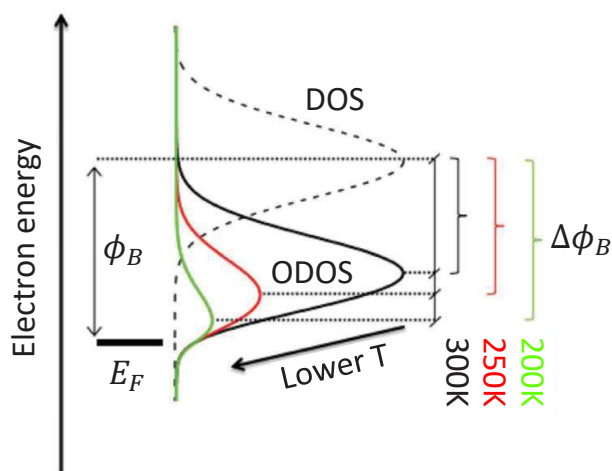


**Figure I.19** Effect of the temperature on the ODOS centre level, and corresponding barrier reduction  $\Delta\phi_B$ . The nominal barrier  $\phi_B$  is set to 400 meV. At 300 K the barrier lowering, *i.e.* the centre of the ODOS compare to the centre of the DOS, is already around 120 meV. Reprinted from Natali & Caironi<sup>54</sup>.

In the end, anticipating the spintronic part of the manuscript, interfaces are of paramount importance for spin injection and detection. Hybrid metal/organic systems are especially sensitive due to the different nature of the transport in the two types of materials.

One parameter that was not yet discussed but is of key relevance is the doping effect on charge injection. Upon doping, the energy level alignment, the morphology, the mobility and the disorder change, sometimes strongly, because of the high doping values achievable in organic materials. If the contact resistance tends to decrease while the dopant concentration increases, the ratio between contact resistance and bulk resistance is not always constant and one may turn from a bulk limited injection to a contact limited one through high doping level of the bulk<sup>67,68</sup>. A short introduction to doping OSCs is given next.

## I.4. Doping

Doping a material consists of intentionally introducing impurities into a semiconductor to modulate its properties. In most of the cases, the aim is to turn from an intrinsic poorly conductive semiconductor to an extrinsic highly conductive semiconductor by increasing the charge carrier concentration. However, optical and structural properties are also altered by adding dopants in the material. It is a well know process widely used nowadays and is the basic step of the fabrication of transistors whether there are inorganic or organic.

Actually, the interest on organic material for electronics comes from the successful doping of polyacetylene with iodine dopant by Chiang *et al.* in 1977<sup>69</sup>. They manage to increase its conductivity from  $10^{-5}$  S. cm<sup>-1</sup> to more than  $10^2$  S. cm<sup>-1</sup> demonstrating the first organic material with tunable resistivity and a metal-insulator transition.

Different doping methods exist: chemical<sup>70,71</sup> and electrochemical<sup>26,71</sup> doping, interfacial doping (charge injection from electrodes), photoexcitation/charge dissociation and acid or base treatment<sup>72,73</sup>. Only the two formers will be discussed here.

### I.4.1. Chemical doping

The chemical doping is the one used by Chiang and colleagues: oxidation (*p*-doping) or reduction (*n*-doping) mechanism occurs by charge transfer between the host polymer and the dopants (**Figure I.20**). The dopants can be introduced by direct mixing in the polymer solution or evaporation on the organic thin film. Chemical doping is an efficient and easy method, but the doping level is not easily controlled, and it is usually irreversible. Therefore, there is no off-state (low-conductivity state) and the choice of the dopant is not straightforward in the case of organic semiconductor. Indeed, the HOMO of OSCs is about 5 – 6 eV under the vacuum level, then a *p*-type dopant must be a quite good electron acceptor. For *n*-type dopant it is even worse: as the gap is large, the HOMO of the dopant must be very high to overpass the LUMO of the OSC.

Chemical doping is expected to increase the disorder in the organic channel as it adds “impurities”. However, Kang *et al.*<sup>6</sup> showed an enhancement of the crystallinity of the organic channel upon doping, with an interchain spacing slightly increased. They used 2,3,5,6-tetrafluoro-7,7,8,8-tetracyanoquinodimethane (F4-TCNQ) as dopant for pBTTT. They reported that F4-TCNQ intercalates in the alkyl side-chain regions without disturbing the  $\pi$ - $\pi$  interaction between polymer chains while improving the interdigitation of alkyl functions. This is in contradiction with a previous work from Cochran *et al.*<sup>74</sup> with the same materials but a different doping method. Both are chemical doping, but the former is an evaporation of F4-TCNQ on top of the thin film, which then diffuse within the channel whereas the latter is a co-deposition of the polymer and the dopant.

Another drawback of chemical doping is the limited stability. The electrical properties change with time because dopants diffuse within the polymer, leading to a heterogeneous film (especially true for low and intermediate doping levels). The irreversibility in the chemical processes can also result in irreversible degradation of performance with time, making the chemical doping unlikely for applications.

Chemically doped polymers are often used in a field-effect transistor (FET) geometry, where the conductivity of the channel is modulated through electrostatic doping. Even if the number of carriers is constant in a given sample using this doping method, the pinning of the effective channel via a gate electrode remains possible.

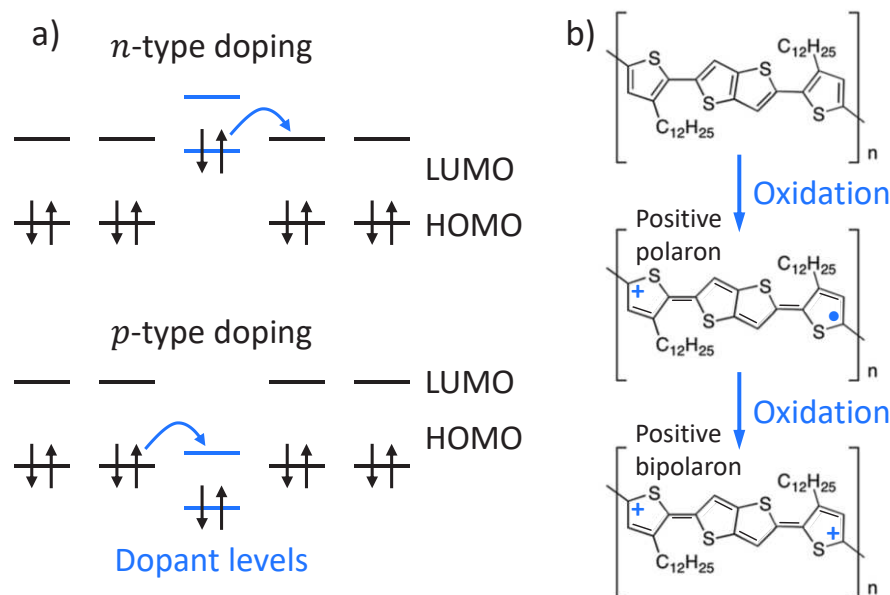


**Figure 1.20** a) Energetic landscape of a doped OSC. For *n*-type doping, the donor dopant gives electron to the host OSC. For *p*-type doping, the acceptor dopant pull electrons away from the OSC, leading to an increase of hole density. b) Changing of the pBTTT structure upon oxidation, *i.e.* *p*-doping. On the top, the undoped polymer gets oxidized to form a positive polaron through a lack of charge and an unpaired electron. Note the new bond alternation pattern on the chain. If a second electron removing occurs near the first one, a bipolaron may form.

### 1.4.2. Electrochemical doping

Electrochemical doping requires a conducting electrolyte connected to the OSC. Electrolytes contain mobile ions, therefore applying a voltage difference between the organic channel and another electrode connected only to the electrolyte causes an accumulation of charges on both sides of the OSC/electrolyte interface (**Figure 1.21a**). It forms an electric double layer ions/carriers across the interface that increases the conduction of the OSC. The capacitance (per unit area) is here much larger than the one obtained through a dielectric of finite thickness, used in the standard electrostatic gating method, making electrochemical gating of interest for imposing very large electric field to the OSC thin film under moderate gate voltage values.

Furthermore, polymers are possibly permeable to ions. Then, when the oxidation (reduction) of the OSC by extraction (injection) of charges by the metallic electrode occurs, ions from the electrolyte penetrate into the polymer to counterbalance the lack (excess) of charges (**Figure 1.21b**). The density of charge can be strongly increased at the expense of disorder. Indeed, the morphology of the thin film will be affected by these foreign molecules, as it is the case for chemical doping. It is important to remark also that the energy levels of the dopants are not as vital in the case of electrochemical doping as in the chemical one. The carriers stay on the polymer and are not jumping to the dopants. The carrier density increases because the organic chains become and remain charged, due to the electron extraction or injection from the metallic electrode and the addition of ions.

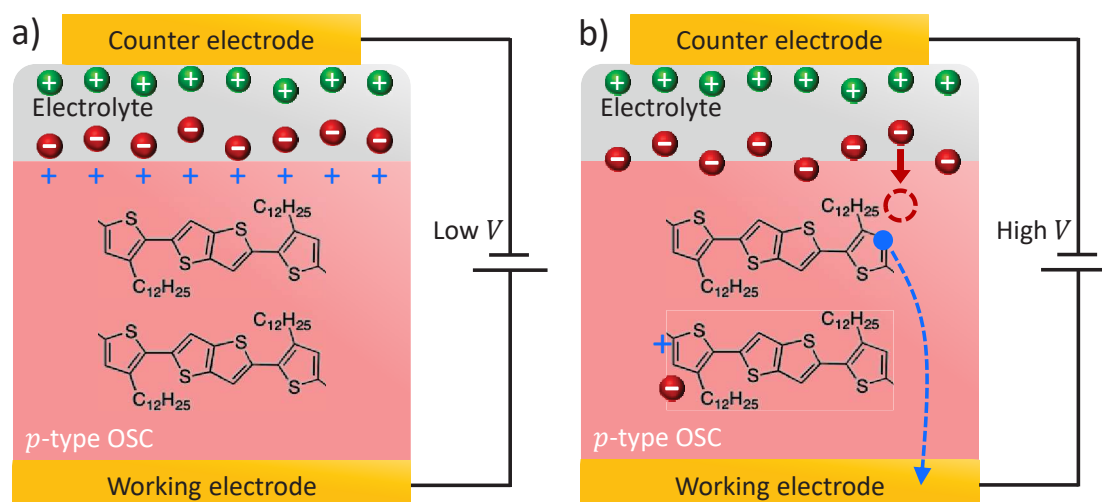


**Figure I.21** a) For low potential, ions migrate on interfaces according to their charge. It forms the well-known electric double layer. b) If the polymer is permeable, ions can penetrate into the polymer for high enough applied potential. Dopants (anions here) ensure the electric neutrality while extraction of electrons (small blue dot) of the polymer upon applied voltage. The structural rearrangement of the polymer is not shown here.

One of the main advantages of electrochemical doping is the reversibility of the process: as there is no disruption of the  $\sigma$ -bonds of the chain, the channel can be dedoped by suppressing the applied voltage. The undoped polymer is recovered, however with possibly some structural memory of the doping. Controlling the doping level is also much easier, as the amplitude of the voltage relates directly the doping. It is worth noting that the penetration of ions is within the entire volume of the thin film, and not limiting to a 2D channel near the interface as it is the case for traditional field-effect transistors (FETs). This makes the sample more sensitive to “bulk” disorder but relatively independent of the “interface” disorder of the first layer(s) of the polymer film that is generally worse in bottom-gate geometry due to the interface with the dielectric substrate.

The control of the carrier density with a simple voltage adjustment is a reliable way to study conduction mechanism over a wide range of carrier concentration, several orders of magnitude higher than conventional FET devices. The typical geometry for electrochemical doping of OSCs is the electrolyte-gated organic field-effect transistors (EGOFETs). It will be the standard system of this thesis. Exciting results are already published where organic materials are on the onset of metallicity<sup>31,75,76</sup>, show band-like transport<sup>77</sup> or even behave fully as a metal<sup>78</sup>. In the following we detail how these doping concepts are used in transistor devices construction and operation.

## I.5. Devices

Among the manifold organic devices, we focused on EGOFETs for the understanding of electronic transport in the bulk of OSCs but also at interfaces. More classical organic field-effect

transistors (OFETs) with bottom gating are also discussed because of the better comparison with the literature.

The transistor effect in bulk materials was pointed out for the first time in 1947 by John Bardeen, William Shockley and Walter Brattain. The concept is to improve the electric conduction of a channel by applying a perpendicular electric field. Nowadays, transistors are the building block of electronics and computing, and there are present into the millions in all daily devices. At such a scale, one can easily understand the interest in organic materials for their ease processability and low-cost potentials.

### I.5.1. Organic field-effect transistors

The first demonstration of a working organic transistor stem from the research of White *et al.* published in 1984<sup>79</sup>. They were able to measure a change of one order of magnitude of the conduction of polypyrrole while applying a gate voltage through an electrolyte solution. It was not a field-effect transistor but a “chemiresistor” because it was based on the solid-state oxidation and reduction of the organic channel by the electrolyte. Two years later, Tsumura *et al.*<sup>80</sup> showed the first OFET using poly(thiophene) bottom-gated by a standard Si/SiO<sub>2</sub> substrate.

Field-effect transistors are three-terminal devices: source, drain and gate (**Figure I.22a**). The active channel, organic for OFETs, is in contact with the source, that provides charges, and the drain, that extracts charges. The gate electrode is separated from the three latter components by an insulating layer referred as gate dielectric. The stacking of the gate electrode, the dielectric and the channel can be pictured as a parallel-plate capacitor with the capacity per unit area:

$$C_i = \frac{\varepsilon}{d} \quad (1.16)$$

where  $d$  is the thickness of the dielectric layer of permittivity  $\varepsilon$ . As any capacitor, applying a potential difference between the two sides ( $V_G$ ) leads to charge accumulation on each plate at the interface with the dielectric. When the potential on the gate electrode is negative (positive), it forms a thin 2D layer of high density holes (electrons) in the  $p$ -type ( $n$ -type) semiconductor. The amplitude of  $V_G$  must overpass the threshold voltage ( $V_T$ ) to affect the channel conduction.  $V_T$  relate to an activation potential needed to overcome electrostatics resulting from impurities such as the eventual additional charge from the doping of the semiconductor. These extra charges are neutralized before the gate voltage begin to act on the channel. Therefore, the effective applied gate voltage is  $V_G - V_T$  and the free charges per unit area ( $Q$ ) is given by:

$$Q = C_i(V_G - V_T) \quad (1.17)$$

when there is no source-drain voltage. This simple equation shows the importance of the dielectric. Its aim is to accumulate as much free charges as possible, making the permittivity of the chosen material a key intrinsic property. The dielectric thickness can also be changed but one has to ensure its insulator behaviour to avoid leakage current ( $I_{SG}$ ). The common dielectric widely used is silicon oxide because it is cheap and well documented from a process point of

view, but it is far to be the best choice: the maximum induced carrier density is  $< 10^3 \text{ cm}^{-2}$  due to its low capacitance, and a leaking current occurs below a thickness of 100 nm. However, other materials with higher dielectric constant are available: high-k insulators<sup>81-84</sup>, ultra-thin cross-linked polymers<sup>85-89</sup> and self-assembled monolayers<sup>90-93</sup> for example.

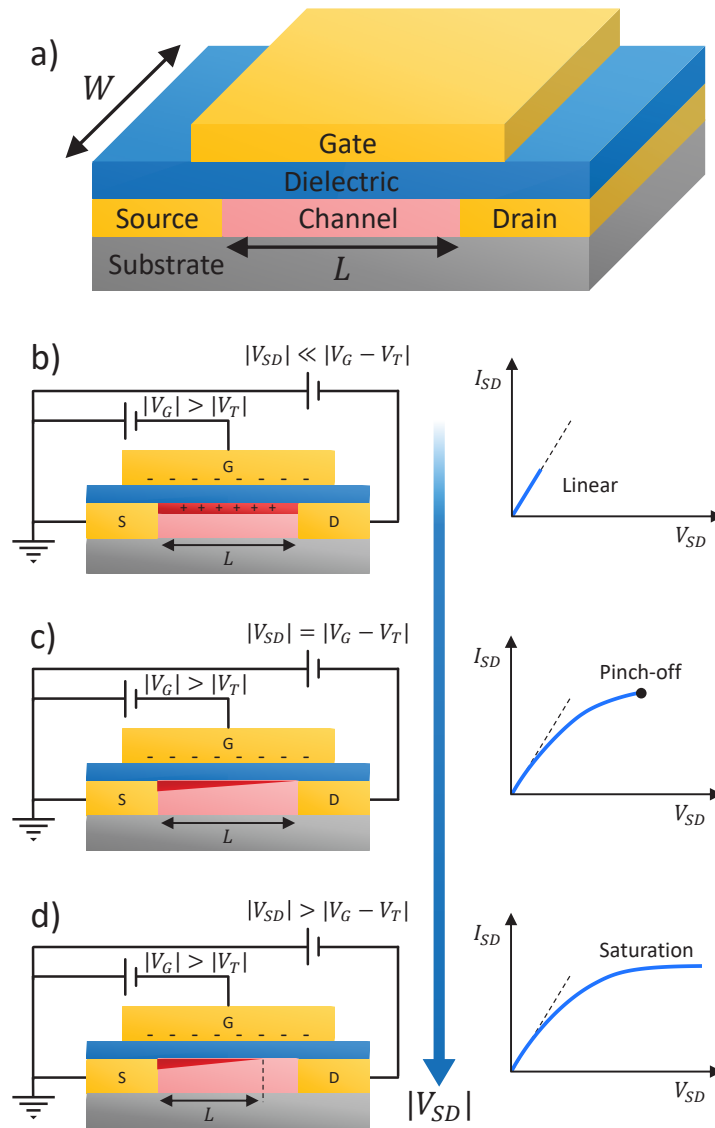


**Figure I.22** a) Schematic of top-gated (O)FETs. b), c) and d) Represent the charge distribution (red) in the active channel for different operating regime: linear (b), pinch-off (c) and saturated (d). The gate voltage involves a charge accumulation that creates a high carrier density channel at the interface with the dielectric (in red). The output curve is also shown for each regime.

Coming back to OFETs,  $V_G$  has to compare to the source-drain potential ( $V_{SD}$ ). As long as  $V_{SD}$  is small enough, more precisely as long as the perpendicular electric field is (much) larger than the longitudinal one, the source-drain current ( $I_{SD}$ ) increases linearly with  $V_{SD}$  and the thin conducting channel is almost homogenous along the interface (**Figure I.22b**). This condition makes the gradual channel approximation valid and the current in the linear regime writes:

$$I_{SD}^{lin.} = \frac{W}{L} \mu_{lin.} C_i (V_G - V_T) V_{SD} \quad (1.18)$$

with the density of carrier as

$$Q(x) = C_i (V_G - V_T - V(x)) \quad (1.19)$$

which, in this case, is only slightly different from the former density as  $V(x)$ , coming from the potential drop between the source and the drain, *i.e.*  $V_{SD}$ , is small compared to  $V_G$ . The mobility in the linear regime is

$$\mu_{lin.} = \frac{L}{WC_i V_{SD}} \frac{\partial I_{SD}^{lin.}}{\partial V_G} \quad (1.20)$$

When  $V_{SD} = V_G - V_T$ , the channel becomes pinched-off: the density of accumulated carriers is zero at the interface between the channel and the drain electrode (**Figure I.22c**). A depletion region forms near to the drain electrode that turns the device into the space-charge limited regime. The size of the depletion area increases while  $V_{SD}$  increases and it supersedes the highly conductive channel. Therefore, the effective channel length is reduced compared to  $L$  and the system is in the saturation regime (**Figure I.22d**). The current is then

$$I_{SD}^{sat.} = \frac{W}{2L} \mu_{sat.} C_i (V_G - V_T)^2 \quad (1.21)$$

and from the derivative with respect to  $V_G$

$$\mu_{sat.} = \frac{2L}{WC_i} \left( \frac{\partial \sqrt{I_{SD}^{sat.}}}{\partial V_G} \right)^2 \quad (1.22)$$

The typical measurements performed on FETs is the variation of  $I_{SD}$  with  $V_{SD}$  and  $V_G$ , the former is the so-called output curve (**Figure I.23a**) and the second the transfer curve (**Figure I.23b-c**).

Several key device parameters are extracted from these curves: the working regime, the mobility, the threshold voltage, the subthreshold behaviour and the  $I_{On}/I_{Off}$  ratio. Before calculating any parameter of the FET, one must know the regime in which the measurements are performed. Indeed, the set of equations to use require the knowledge of the linear or the saturation regime of the device operation. Therefore, output curve is often the first measurement. Then, the mobility is deduced from equations **I.20** or **I.22** applied to transfer curves data. This is a key property, characteristic of the quality of the channel, particularly in the OFET case where disorder leads to reproducibility issues.

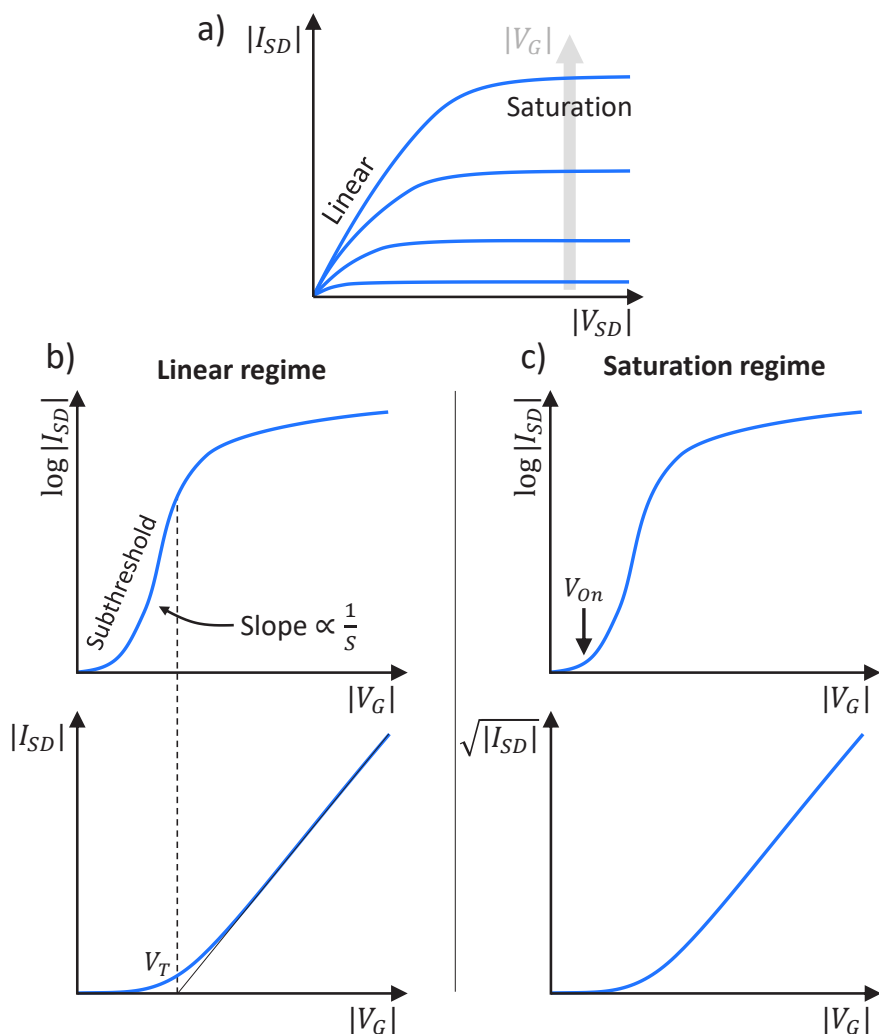


**Figure I.23** a) Typical output curves ( $I_{SD}$  vs.  $V_{SD}$ ) of (O)FETs. At small source-drain voltage, the current increases linearly and saturated for high  $V_{SD}$ . The linear response spreads over a biggest range of  $V_{SD}$  while the gate potential is increased. b) Linear regime transfer curves in semi-log plot (top) and linear plot (bottom). c) Saturation regime transfer curves in semi-log plot (top) and the square root of  $I_{SD}$  versus  $V_G$ . The semi-log plots give information about the “On” potential and the subthreshold behaviour. The two bottom plots allow the determination of the threshold voltage and the mobility of the channel.

The threshold voltage ( $V_T$ ) should be small, ideally zero, to have a low-voltage operating FET translating into low consumption devices. In order to calculate it, the linear behaviour of  $I_{SD}$  (in the linear case) or  $\sqrt{I_{SD}}$  (in the saturation case) versus  $V_G$  at high gate voltage is extrapolated until it crosses the  $x$ -axis, giving  $V_T$ . It is strongly dependent on the semiconductor and the dielectric of the device: built-in dipoles, impurities, interface state and charge traps all possibly contribute to the threshold voltage. It tends to increase over time in OFET and is partially responsible for hysteresis in output curves.

The  $I_{On}/I_{Off}$  ratio is usually required to exceed  $10^6$  to well discriminate the two states. The off-state is the source-drain current for  $V_G < V_{On}$ , where  $V_{On}$  is the onset voltage, *i.e.* the gate voltage at which the current increases abruptly. The off-state current is strongly related to the

leakage current (the current between the source and the gate electrode) and is thus highly dependent on the dielectric and the geometry of the FET.

Finally, the subthreshold swing ( $S$ ) refers to the inverse of the slope of the transfer curve for  $V_G < V_T$ . It basically gives the susceptibility of the source-drain current to the gate voltage. Its unit is  $\text{mV} \cdot \text{dec}^{-1}$  and let know how much the gate voltage must be increased to multiplied  $I_{SD}$  by 10. The lower is  $S$ , the faster is the switching from off- to on-state.

In the FET geometry, there is no huge functioning difference between organic and inorganic channels. Indeed, even if the carrier type is different (positive/negative polarons versus holes/electrons), the gate voltage creates channel made of a thin sheet highly conductive compare to the bulk. The performances and the stability in time are however quite different with mobilities/conductivities of inorganic materials being several orders of magnitude higher than their organic counterpart and having a longer lifetime. To improve the organic devices properties, alternative geometries have been proposed. One of them is the electrolyte-gated organic field-effect transistor (EGOFET) that was already known from inorganic semiconductor physics but is even more relevant for organic purposes.

## 1.5.2. Electrolyte-gated organic field-effect transistors

Electrolytes are compounds with mobile ions: cations (positive ions), anions (negative ions) or both. They can be liquid or solid such as polymer electrolytes<sup>94</sup>, ionic liquids/gels<sup>95,96</sup> or blended mesoporous materials<sup>97</sup>. The principle of EGOFETs is to replace the dielectric by an electrolyte (**Figure I.24a**). The advantage is basically to diminish the thickness of the insulator layer reducing to a distance around 1 nm. The capacitance can then exceed  $10 \mu\text{F} \cdot \text{cm}^{-2}$  which is roughly 3 orders of magnitude higher than what one would expect in classical FETs with  $\text{SiO}_2$ <sup>98</sup>. As discussed in last section, the higher the capacitance the higher the carrier density, thus charge concentrations that reaches  $10^{15} \text{cm}^{-2}$  at low gate voltage<sup>99</sup> (usually not exceeding 3 V) become routinely possible for EGOFETs.

As ions are mobile in the electrolyte, they migrate upon applying the gate voltage. When  $V_G$  becomes high enough, they form a charged layer at the interface with the OSC and the situation is quite similar to the FETs case – the formation of electrical double layer (EDL) – but with a dielectric thickness that is the spacing between the semiconductor and the electrolytes molecules. Therefore, with only few volts the electric field can easily reach  $10^9 \text{V} \cdot \text{cm}^{-1}$  whereas 200 V would be necessary to create such high field in FETs with 200 nm thick  $\text{SiO}_2$  that would probably damage the sample. Of course, the same accumulation occurs on the gate electrode with an opposite charge, and the electrolyte remains neutral in between. Therefore, the capacitance is given by the equivalent circuit of two capacitances in series:

$$C_{\text{electrolyte}} = \frac{C_{EDL_1} C_{EDL_2}}{C_{EDL_1} + C_{EDL_2}} \quad (1.23)$$

which reduces to  $1/2 C_{EDL}$  assuming  $C_{EDL_1} \approx C_{EDL_2}$  and is independent of the thickness of the dielectric because the neutrality in the middle of the electrolyte provides no voltage drop in this region. The mobility of EGOFETs' carrier is often better than in a FET geometry thanks to the

higher charge concentration formed at the electrolyte/OSC interface. Indeed, if more charges are available, more localized tail states are filled and easier it is to reach the delocalized states above the mobility edge.

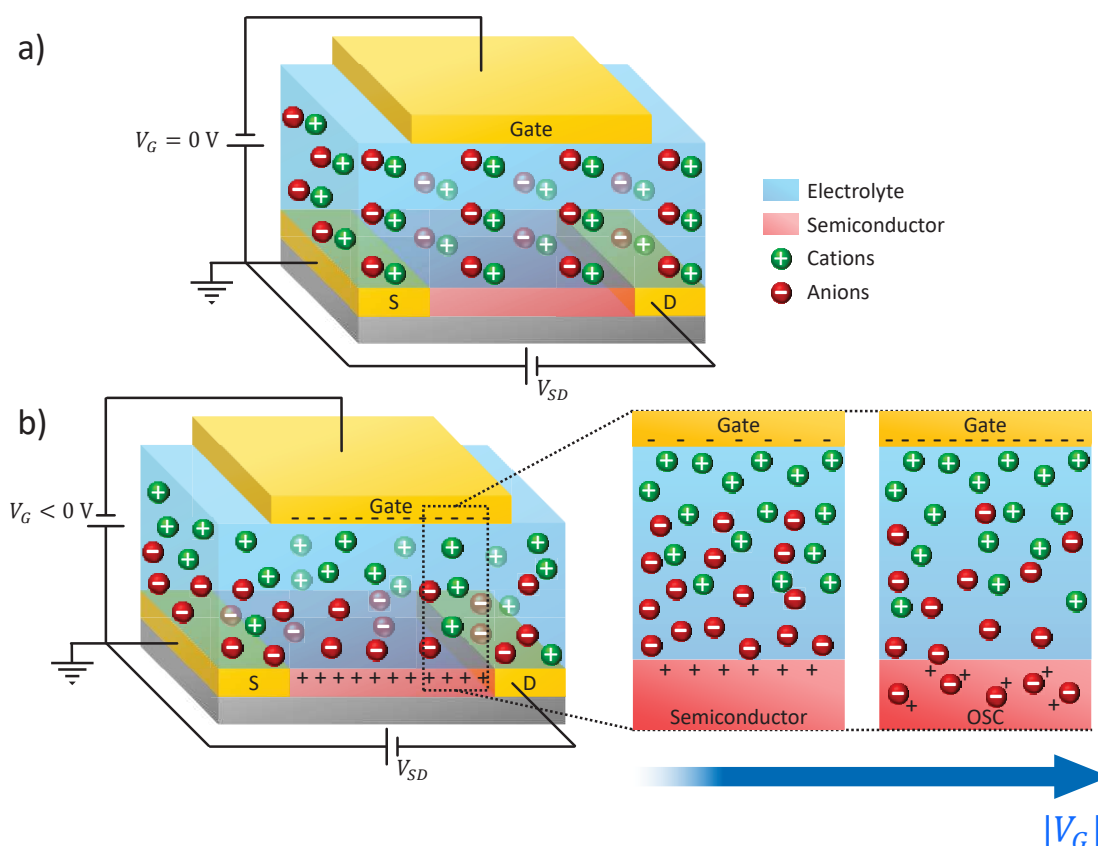


**Figure I.24** Schematic of an EGOFET for  $V_G = 0$  V (a) and  $V_G < 0$  V (b) for a *p*-type OSC. The negative gate voltage creates an accumulation of electrons on the gate electrode that pushes anions from electrolyte onto the interface with the OSC. In order to counterbalance these charges a conductive 2D channel forms in the OSC. Because of its permeability, anions can penetrate the organic channel for strong enough gate voltage.

The previous description holds as long as the EDLs are well defined. However, OSCs are often permeable to ions used in the electrolyte. The ions accumulate at the interface with the semi-conducting channel are able to penetrate into the OSC and it turns the device from electrostatic doping to bulk electrochemical doping. The dopants concentration can be as high than  $10^{22} \text{ cm}^{-3}$ , *i.e.* several orders of magnitude larger<sup>31</sup> than what is usually done for inorganic semiconductors. Furthermore, the doping level is tunable with the gate voltage<sup>100</sup> and is reversible by returning to  $V_G = 0$  V. Therefore, EGOFETs are particularly relevant for carrier transport and metal-insulator transition studies.

One way to probe the operating regime of the transistor (electrostatic or electrochemical) is to look at the transfer curve. Due to the slow motion of dopant ions, a significant hysteresis is usually observed for the highest doping, whereas none (or a small one) is present for lower gate voltage. A shoulder is also visible in transfer curves, that refers usually to the transition between electrostatic and electrochemical doping.

An important limitation of the doping capability of electrolytes is the clustering of ions. Anions or cations may aggregate and form local ordered structure. Therefore, they are not participating to the doping process. Tokuda and co-workers demonstrated that only 30 – 50 % of ions in ionic liquid contribute to ion conduction<sup>101,102</sup>. Nketia-Yawson and colleagues found a way out by adding high- $k$  materials into ion gel solution<sup>103</sup>. They ended up with solid-state electrolyte having high doping efficiency thanks to the high- $k$  compound that limit the cluster formation. The other non-negligible advantage of this new kind of electrolyte is the possibility to evaporate metal on top of it, that is not possible with usual soft ion gels or ionic liquids.

Nowadays, EGFETs are widely study for bioelectronics applications<sup>104,105</sup>, often as bio-compatible sensors<sup>106</sup> up to single-molecule detection<sup>107</sup>. Electrolyte gating was also used to induce superconductivity in low-dimensional channel<sup>108</sup>, tunable thermoelectric effect<sup>109</sup> and metal-insulator transition<sup>78</sup>. The latter motivated us to study EGFETs in which high conductivities are reported<sup>75</sup>.

### I.5.3. Geometry-dependent properties

The OFET shown in **Figure I.24** is only one of the possible geometries, in this case bottom contact (BC) – it is not visible for simplicity but the OSC should also be on the top of electrodes – and top-gate (TG). However, top contact (TC) is also doable by metal deposition on top of the OSC, and bottom-gate (BG) is in fact the most common gating geometry with Si/SiO<sub>2</sub> substrate. Their four combinations were investigated and some differences in OFET performances were demonstrated.

Usually the coplanar geometry, *i.e.* the source and drain electrodes are in the same plane than the active channel, is distinguished from the staggered geometry where the channel and electrodes are not in the same plane (**Figure I.25**). A major difference is the path carriers must follow in order to reach the drain. In the coplanar case (TGTC and BGBC), the injection (detection) occurs directly from the contacts (accumulated channel) to the accumulated channel (contacts). On the contrary, for staggered devices (TGBC and BGTC), charges have first to travel through the poorly conductive bulk OSC to arrive in the active channel. In a first approximation, one could expect then a lower interface resistance  $R_C$  in the coplanar devices, however it is the opposite because of the spreading of the gate effect further away (screened by the electrodes in the coplanar geometry)<sup>110</sup>.

The injection area is also very different because there is an overlap of the gate electrode over source and drain contacts, then carriers are more likely injected from the top (TGBC) or bottom (BGTC) of source and drain, making the channel length hard to define (see chapter III). For coplanar devices, the channel is well defined in the case of BGBC, the current is injected and detected from the edge of contacts and the conducting channel is typically a few nanometers thick, whereas TGTC OFETs are more complicated.

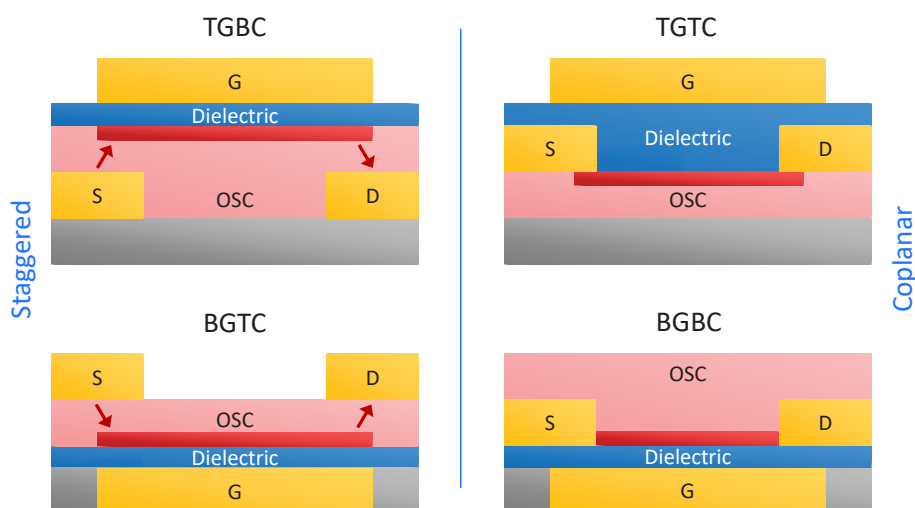


**Figure 1.25** The four different OFET geometries. Staggered ones are on the left and coplanar on the right. The deep red area is the accumulation channel.

The measured mobility is also dependent on the chosen geometry. In staggered devices, as the carrier must pass through the bulk of the active channel, a space charge area may form easier than in the coplanar geometry. Moreover, in the case of BG, the conduction occurs mainly in the first layers of the organic channel, which are much sensitive to the dielectric surface, while top-gated OFETs rely on the top of the OSC which may have a relatively different transport capability.

In the case of EGOFETs, the electrolyte is usually side-gated due to the difficulty for evaporating top contacts over a soft thick electrolyte. There is no change compared to the top-gating configurations, expect a possible slow gating process due to the limited ions mobility in the electrolyte and distant gate electrode.

### 1.5.4. Contact resistance

Beyond the high mobility search for optimizing the performance of organic semiconductors, which results into high conductivity organic channels, there is another big issue to overcome: the contact resistance. By measuring the total resistance ( $R_{Tot}$ ) of FETs, one measures not only the channel resistance ( $R_{Ch}$ ) but also the source ( $R_S$ ) and drain ( $R_D$ ) interface resistances and even the pads resistance ( $R_{Pads}$ ) involving the metallic interconnects on the chip:

$$R_{Tot} = R_{Ch} + R_S + R_D + R_{Pads} \quad (1.24)$$

$R_S$  and  $R_D$  will often be identical in the following and refer simply as contact resistance ( $R_C$ ) defined here as their average, *i.e.*  $2R_C = R_S + R_D$ . The pads resistance is generally neglected, but we will see later that this assumption have to be carefully analysed in the case of high conductivity organic channel where  $R_{Ch}$  may be smaller than  $R_{Pads}$ .

The main problem in the case of OFETs is the mismatch between  $R_C$  and  $R_{Ch}$ . Indeed, several studies show a contact resistance much higher than the channel resistance<sup>111–113</sup>. It is all the

more worrying that the downscaling of OFETs will likely decrease  $R_{Ch}$  (for a given width of the channel, and its decreasing length) but not  $R_C$  and favour a contact limited transport for small scale OFETs. This issue is less problematic in the case of inorganic FETs as direct tunnelling generally occurs and different optimization processes (not suitable for OFETs) exist, making  $R_C$  much smaller than in OFETs.

Usually the parameter relevant to discuss the contact resistance in different geometry is the specific contact resistance  $R_C W$  ( $R_C$  multiplied by the width of the channel). Indeed, as the accumulation occurs over few nanometres only in bottom-gated FETs, independently of the length of the channel, the only geometrical parameter that scales  $R_C$  is the width. Therefore,  $R_C W$  is introduced to normalize the contact resistance among various geometries.

An important question arises from the latter paragraph: what about EGOFETs? As mentioned in the last section, the doping is 3D when an electrolyte is used with a permeable OSC. Then the approximation of an almost 1D injection area is no more valid and the whole section of the electrode is involved. Therefore,  $R_C A$  [ $\Omega \cdot \text{m}^2$ ] with  $A$  the 2D injection area may be more appropriate than  $R_C W$  [ $\Omega \cdot \text{m}$ ]. A deeper discussion will be proposed later in this manuscript, but  $R_C W$  will still be used for comparison with the literature.

### Contact resistance measurements

Measurement of contact resistances is documented in the literature using: transmission line method (TLM), gated four-probe technique (gFP) and Kelvin probe microscopy (KPM).

TLM consists of measuring  $R_{Tot}$  for various length and fixed width<sup>114–117</sup> (**Figure I.26a**). As we expect that only  $R_{Ch}$  is proportional to the channel length, the crossing of  $R_{Tot}(L)$  with the  $y$ -axis gives directly the contact resistance ( $2R_C$ ) as it sets  $R_{Ch}$  to 0. The advantages are that it can be done for different gate voltage to study  $R_C(V_G)$  and it gives also extra information on charge injection and transport through the convergence point (crossing of  $R_{Tot}(L)$  of different gate voltage)<sup>118</sup>. It applies to any geometry at the expense of the number of samples to fabricate and measure. Another way would be to use several electrodes with variable spacing on one channel but then there is no more freedom in the geometry. Finally, it doesn't allow to distinguish between the source and drain resistances giving only the sum of both, and the obtained value is only the average of contact resistances of the set of samples.

gFP uses four-probe measurements, *i.e.* two additional electrodes must be patterned between source and drain to provide experimental access to the potential drop within the conductive channel<sup>120,121</sup> (**Figure I.26b**). As no current is flowing in these leads, they probe non-invasively the potential. However, these electrodes must be thin, complicating the fabrication and limiting its suitability for short channels. Nevertheless, one has access to the source and drain resistances separately. The idea is to extrapolate linearly the potential drop between the four-probe leads to the source and the drain contacts. It remains a potential drop on each side that translates into contact resistances. The calculation is as following: first the slope of the potential profile ( $a$ ) have to be determinate by

$$a = \frac{V_2 - V_1}{L_{12}} \quad (1.25)$$

where  $V_1$  and  $V_2$  are the measured potential of electrode 1 and 2, and  $L_{12}$  is the distance between them. Then the y-intercept ( $b$ ) is calculated, which is already almost the source potential drop  $\Delta V_S$ :

$$\Delta V_S = b - V_S = V_2 - aL_2 - V_S = V_1 - aL_1 - V_S \quad (1.26)$$

where  $L_{1,2}$  are the position of the first and second four-probe electrode respectively and  $V_S$  the applied source potential. Finally, the equation of the linear function  $V(x) = ax + b$  enable to find the drain potential drop  $\Delta V_D$ :

$$\Delta V_D = V_D - V(L) = V_D - (aL + b) \quad (1.27)$$

with  $V_D$  the applied drain potential and  $L$  the channel length. By dividing these potential drops by  $I_{SD}$ , the source and drain resistances are recovered. In the latter equations, the pads resistance is assumed negligible.

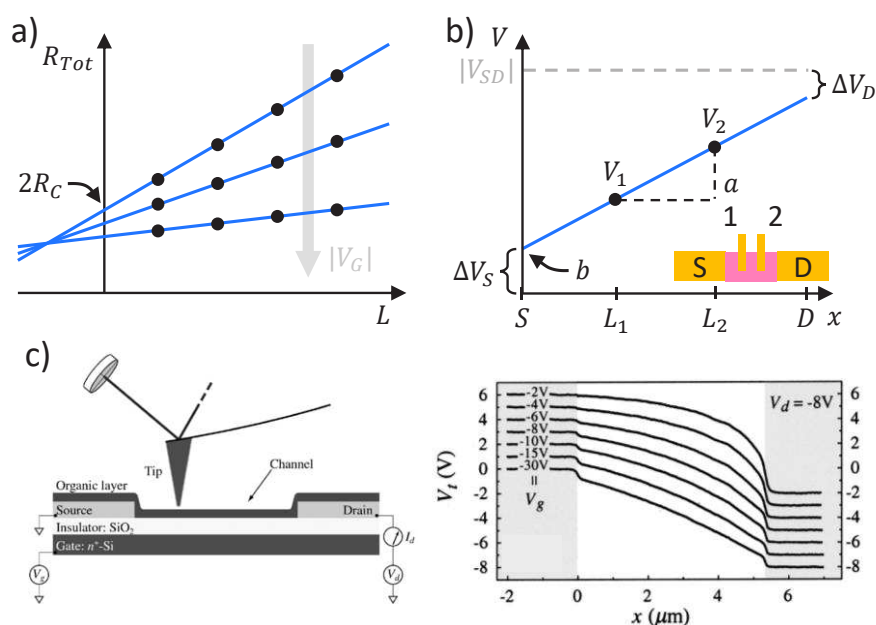


**Figure 1.26** Different extraction methods of the contact resistances. a) Transmission line method: the intercept of the  $R_{Tot}(L)$  curve with the  $y$ -axis is the whole contact resistance. b) Gated four-probe method: two additional electrodes measure the potential drop in the channel (see inset); the extrapolation of the linear function gives the potential drops at source and drain. c) Kelvin probe microscope: the tip of an AFM probes the electrostatic potential along the channel. The setup is schematically shown on the left while the output  $V(x)$  curves are shown on the right. Adapted from Bürgi *et al.*<sup>119</sup>.

It is clear from the assumption of a linear profile that gFP cannot be used in the saturation regime as the pinch-off leads to non-uniformity of the channel (**Figure 1.22d**). Moreover, the presence of metal electrodes within the channel also possibly disturbs the OSC morphology even if there are very thin and protrude only minimally into the channel.

KPM may be the more powerful among the three methods as it is a direct measurement of the potential with high voltage and spatial resolution<sup>122,123</sup>. The principle is to scan the surface of the OSC with a conductive atomic force microscope (AFM) tip that provides directly the electrostatic potential after background subtraction (**Figure I.26c**). However, as it is a surface probing, KPM is not suitable for top-gate geometries. Moreover, this technique is sensitive not only to the surface potential but also to the bulk one up to 100 nm deep, making the results sometimes difficult to analyse.

The KPM called the validity of gFP into question. Indeed, looking carefully to its output, a potential drop near the electrodes is clearly observed in addition to a non-linear behaviour for the lower  $V_G$  (**Figure I.26c**). This sudden drop cannot be seen in the gFP method as the main assumption is a linear profile all along the channel becomes questionable. However, by neglecting the non-linear behaviour, the contact resistance is overestimated. As our objective is to show low  $R_C$ , the amplified values from gFP technique, predominant in the present thesis, gives substance to our claims.

### Typical contact resistances in organic transistors

The typical values of  $R_C W$  reported in the literature for OFETs ranges between tens of k $\Omega$ . cm to M $\Omega$ . cm for various organic and electrode materials, and from different extraction techniques. Natali and Caironi resumed the main results from literature in their survey<sup>54</sup>. The lowest reported is  $\sim 6$  k $\Omega$ . cm for PBTTT with gold contacts on tridecafluorooctyltrichlorosilan (FOTS) functionalized SiO<sub>2</sub><sup>124</sup> in BGTC geometry.

Turning to EGOFETs, the usual values observed is only several  $\Omega$ . cm, much lower than for OFETs.  $R_C W$  as low as 4  $\Omega$ . cm have been reported for poly(3-hexylthiophène) (P3HT)<sup>125</sup> and PBTTT<sup>126</sup> with gold leads and using an ion gel as dielectric. The expected reason of such a decrease may be the enhanced injection through ions introduced by the electrolyte. Sandström *et al.*<sup>127</sup> have shown ion-assisted injection in a light emitting electrochemical cell with an electrolyte and a geometry quit similar to EGOFETs. Ions diffusing near to the contacts may create an additional electric field that help charge injection.

The drastic decrease of contact resistance with electrolyte-gating transistors is of key relevance for this work. Indeed, in order to downscale organic devices, we want to avoid the strong predominance of  $R_C$ . Moreover, how  $R_C$  competes with the channel resistance is key to inject and detect spins in the scope of organic spintronic applications and will be discussed in next chapter. High frequency organic electronics is also dependent on  $R_C$ <sup>128</sup>, but the road remains particularly long as EGOFETs are not suitable for this kind of purposes because limited by the slow motion of gating ions.

## I.5.5. Mobility extraction

As explained in the OFET section, the mobility is usually obtained by the slope of the linear part of the  $I_{SD}(V_G)$  curve (linear regime) or the  $\sqrt{I_{SD}}(V_G)$  curve (saturation regime). However, these curves may exhibit various behavior like S-shape, sublinear bending or superlinear curvature. The extraction of the mobility with such nonlinearities leads to erroneous values<sup>129</sup>. The biases can result from contact resistances (for 2-probe measurements), carrier concentration-

dependent mobility (or  $V_G$ -dependent mobility) or disagreement between source-drain and gate electrical fields (particularly for short-channel). For example, Bittle *et al.*<sup>130</sup> exhibited a mobility overestimation up to one order of magnitude due to the contact resistance dependence on the gate voltage. It is especially true at low  $V_G$  when the device is charge injection limited. Choi *et al.*<sup>129</sup> gave a guideline to follow in order to ensure a relevant calculated mobility:

- The linearity of FET transfer characteristics must extend to a substantial range of gate voltage.
- The mobility should be weakly dependent on the carrier density, especially for high mobility claim.
- The linear regime is preferred because of the non-uniform distribution of charges in the saturation regime (pinch-off).
- Contact effect have to be checked either by 4-probe measurements or TLM, or at least by ensuring the proportionality of  $I_{SD}$  with  $V_{SD}$ .
- Several  $V_G$ -sweep speeds should be tested to address for charge trapping and/or disorder.
- The electrical fields must be calculated to ensure the validity of the gradual channel approximation ( $E_G \gg E_{SD}$ ) and limit the current density to reasonable values.
- Hall-mobility should be given for high mobility materials.

They add also a “reliability factor” ( $r$ ) that quantify how far the device is from the ideal FET and could be used to recover the effective mobility.

The 4-probe geometry, giving access to contact resistance and conductivity, is also imperfect. The choice of the size and the protruding length of 4-probe electrodes need to be minimized in order to reduce the error on the mobility. Overestimation as high as 350% where deduced in a poorly chosen geometry where 4-probe electrodes are large and the channel is long and thin<sup>131</sup>. In our case, we are more interested in conductivity than mobility, but we pay attention to this problem.

### 1.5.6. Downscaling of (EG)OFETs

The downscaling of electronic devices has been the easiest way to increase the electronic performances by increasing the packing density (number of devices per unit area) on chips. The famous Moore’s law predicted the doubling of the number of transistors on integrated circuits about every two years, and it was achieved by reducing the size of transistors. The same is sought for OFETs and EGOFETs in particular because downscaling allows higher frequency operation<sup>10</sup> ( $f \propto L^{-2}$ ,  $L$  being the characteristic size of transistors) and lower bias requirement. Furthermore, the mobility of organic materials being orders of magnitude lower than that of inorganic channels, it is even more important to downscale the channel length of OFETs to keep an adequate drive current for electronic applications.

Various techniques allowed to pattern sub-micrometre channels: photolithography<sup>132</sup>, electron beam lithography<sup>90,133</sup>, angle deposition<sup>134</sup>, nanoimprint lithography<sup>135</sup>, stamping<sup>136</sup>, micro-cutting<sup>137</sup>, silicon etching<sup>138</sup>, mask-free photolithography<sup>139</sup>, inkjet printing<sup>140</sup> and femtosecond laser ablation<sup>141</sup>. However, many of these reports exhibit poor electronic properties with non-

ideal output curves and low  $I_{On}/I_{Off}$  ratio referred as short-channel effects<sup>53,142–145</sup>, following the nomenclature on inorganic electronics. Short-channel effects occur on polymers<sup>135,138,146</sup> as well as small molecules<sup>147</sup> and appear sometimes already for channel of few micrometers long<sup>148</sup>.

The main origin of the change in the behaviour of output curves while downscaling OFETs is the validity of the gradual channel approximation. Upon reducing the size of the channel, the electric field increases between source and drain ( $|\vec{E}_{SD}|$ ) in contrast to the one from the gate ( $|\vec{E}_G|$ ) that is fixed because it depends on the dielectric thickness ( $t$ ) and even decrease when screened by the metallic electrodes. For the gradual channel approximation to hold true, the device should verify:

$$\frac{V_G}{t} = |\vec{E}_G| \gg |\vec{E}_{SD}| = \frac{V_{SD}}{L} \quad (1.28)$$

However, for short-channel transistors,  $L$  compares to  $t$  (and may even be smaller), which results in equations in section 1.5.1 to be inappropriate. Usually, the condition considered is to keep  $L > 10t$ <sup>85</sup> but a factor 4 was already enough in some samples<sup>86</sup>. Anyway, for channel length of several tens of nanometers, the previous condition cannot easily be fulfilled as the dielectric needs a certain thickness to be insulating ( $> 100$  nm for SiO<sub>2</sub>); then the transistor is hardly modulated by the gate voltage.

Shrinking the OFET dimensions may also give more and more importance to the depletion area that would finally occupy the whole channel. While the depletion region becomes a non-negligible fraction of the channel, the required gate voltage to reach inversion diminishes, lowering also the threshold voltage. The shifting of  $V_T$  can be high enough to transform a normally-off device into a normally-on one. In this extreme case,  $V_T$  may pass from positive to negative, turning the transistor current at  $V_G = 0$  V from the off-state into the linear increase of the transfer curve. The subthreshold current in the transfer curve is also increased and depends on  $V_{SD}$ , then the off-state is leaky, leading to poor  $I_{On}/I_{Off}$  ratio. Increasing the source-drain voltage even more, the depletion areas from source and drain come into contact, then SCL current takes place in the whole channel and leads to diode-like output curves. As discussed previously, the contact resistance is also responsible for short-channel effect as it doesn't scale with  $L$ . Under a critical channel length, interface resistance rules the total resistance of the device, and leads to output curves far from the ideal behaviour.

In general, the source-drain voltage becomes the key parameter, first because its electric field is dominant and second because it dictates the effective channel length. As already discussed in the section 1.5.1, when transistors operate above the pinch-off voltage, the channel length reduces and becomes  $V_{SD}$ -dependent, translating into superlinear output curves (as  $I_{SD} \propto L^{-1}$ ) without saturation. Wang *et al.* proposed to add an insulating mesa-structure between source and drain, in order to reduce the longitudinal electric field<sup>133</sup>. They achieved to recover good OFET properties like saturation of the output characteristics and gate-control of the current.

Another successful proposal was to use ultrathin dielectrics to enhance the gate-induced electric field<sup>149</sup>. The latter reminds the EGOFET geometry discussed earlier. Indeed, the dielectric thickness of the double layer between OSC molecules and electrolyte bulk is less than 1 nm thick, and should be perfectly suited to suppress short-channel effect in OFETs through much higher transversal field. Actually, Herlogsson *et al.* studied short-channel EGOFETs and observed nice transistor behaviour<sup>133</sup>.

Organic electronics is still a young and promising field. Improving the understanding of charge transport and injection processes are major steps towards optimized devices for applications. The purpose of organic device may not be the replacement of silicon-based technology but rather an interesting complement to it. The richness of chemical synthesis and its tunability offer unique and infinite possibilities such as biocompatibility or biodegradability. Furthermore, new types of devices such as organic spin-valves could lead to spin transport that aims to reduce the electrical consumption of devices and enhance performances. One step towards spin-based organic transistors is in the scope of this thesis, and the basics of inorganic and organic spin electronics will be reviewed in next chapter.

**Bibliography**

- (1) Heeger, A. J. Semiconducting and Metallic Polymers: The Fourth Generation of Polymeric Materials - Nobel Lecture. *J. Phys. Chem. B* **2001**, *105* (36), 8475–8491.
- (2) Köhler, A.; Bässler, H. *Electronic Processes in Organic Semiconductors: An Introduction*, Wiley-VCH.; 2015.
- (3) Peierls, R. E. *Quantum Theory of Solids*; Oxford University Press, 1955.
- (4) DeLongchamp, D. M.; Kline, R. J.; Lin, E. K.; Fischer, D. A.; Richter, L. J.; Lucas, L. A.; Heeney, M.; McCulloch, I.; Northrup, J. E. High Carrier Mobility Polythiophene Thin Films: Structure Determination by Experiment and Theory. *Adv. Mater.* **2007**, *19* (6), 833–837.
- (5) Biniek, L.; Leclerc, N.; Heiser, T.; Bechara, R.; Brinkmann, M. Large Scale Alignment and Charge Transport Anisotropy of PBTTT Films Oriented by High Temperature Rubbing. *Macromolecules* **2013**, *46* (10), 4014–4023.
- (6) Kang, K.; Watanabe, S.; Broch, K.; Sepe, A.; Brown, A.; Nasrallah, I.; Nikolka, M.; Fei, Z.; Heeney, M.; Matsumoto, D.; et al. 2D Coherent Charge Transport in Highly Ordered Conducting Polymers Doped by Solid State Diffusion. *Nat. Mater.* **2016**, *15* (5), 896–903.
- (7) Delongchamp, D. M.; Kline, R. J.; Jung, Y.; Germack, D. S.; Lin, E. K.; Moad, A. J.; Richter, L. J.; Toney, M. F.; Heeney, M.; Mcculloch, I. Controlling the Orientation of Terraced Nanoscale “Ribbons” of a Poly(Thiophene) Semiconductor. *ACS Nano* **2009**, *3* (4), 780–787.
- (8) Hallam, T.; Lee, M.; Zhao, N.; Nandhakumar, I.; Kemerink, M.; Heeney, M. Local Charge Trapping in Conjugated Polymers Resolved by Scanning Kelvin Probe Microscopy. **2009**, *256803* (December), 1–4.
- (9) Lee, M. J.; Gupta, D.; Zhao, N.; Heeney, M.; Mcculloch, I.; Sirringhaus, H. Anisotropy of Charge Transport in a Uniaxially Aligned and Chain-Extended, High-Mobility, Conjugated Polymer Semiconductor. *Adv. Funct. Mater.* **2011**, *21* (5), 932–940.
- (10) Klauk, H. Organic Thin-Film Transistors. *Chem. Soc. Rev.* **2010**, *39* (7), 2643.
- (11) Paterson, A. F.; Singh, S.; Fallon, K. J.; Hodsdon, T.; Han, Y.; Schroeder, B. C.; Bronstein, H.; Heeney, M.; Mcculloch, I.; Anthopoulos, T. D. Recent Progress in High-Mobility Organic Transistors: A Reality Check. *Adv. Mater.* **2018**, *1801079*, 1–33.
- (12) Bredas, J.; Street, G. Polarons, Bipolarons, and Solitons in Conducting Polymers. *Acc. Chem. Res.* **1985**, *1305* (4), 309–315.
- (13) Bässler, H.; Köhler, A. Charge Transport in Organic Semiconductors. **2011**.
- (14) Austin, I. G. G.; Mott, N. F. F. Polarons in Crystalline and Non-Crystalline Materials. *Adv. Phys.* **2001**, *50* (7), 757–812.
- (15) Coropceanu, V.; Cornil, J.; da Silva Filho, D. A.; Olivier, Y.; Silbey, R.; Brédas, J.-L. Charge Transport in Organic Semiconductors. *Chem. Rev.* **2007**, *107* (4), 926–952.
- (16) Miller, A.; Abrahams, E. Impurity Conduction at Low Concentrations. *Phys. Rev.* **1960**, *120* (3), 745–755.
- (17) Bässler, H. Localized States and Electronic Transport in Single Component Organic Solids with Diagonal Disorder. *Phys. Status Solidi* **1981**, *107* (1), 9–54.
- (18) Arkhipov, V. I.; Emelianova, E. V.; Adriaenssens, G. J. Effective Transport Energy versus

- the Energy of Most Probable Jumps in Disordered Hopping Systems. *Phys. Rev. B* **2001**, *64* (12), 125125.
- (19) Baranovskii, S. D. Theoretical Description of Charge Transport in Disordered Organic Semiconductors. *Phys. Status Solidi Basic Res.* **2014**, *251* (3), 487–525.
- (20) Marcus, R. a. Electron Transfer Reactions in Chemistry: Theory and Experiment (Nobel Lecture). *Angew. Chem. Int. Ed.* **1993**, *32* (8), 1111–1121.
- (21) Kestner, N. R.; Logan, J.; Jortner, J. Thermal Electron Transfer Reactions in Polar Solvents. *J. Phys. Chem.* **1974**, *78* (21), 2148–2166.
- (22) Jortner, J. Temperature Dependent Activation Energy for Electron Transfer between Biological Molecules. *J. Chem. Phys.* **1976**, *64* (12), 4860–4867.
- (23) Lanzani, G. *The Photophysics behind Photovoltaics and Photonics*, 1st edn.; Wiley-VCH Verlag GmbH, Weinheim, 2012.
- (24) Bäessler, H. Charge Transport in Disordered Organic Photoconductors a Monte Carlo Simulation Study. *Phys. Status Solidi* **1993**, *175* (1), 15–56.
- (25) Tanase, C.; Meijer, E. J.; Blom, P. W. M.; de Leeuw, D. M. Unification of the Hole Transport in Polymeric Field-Effect Transistors and Light-Emitting Diodes. *Phys. Rev. Lett.* **2003**, *91* (21), 1–4.
- (26) Hulea, I. N.; Brom, H. B.; Houtepen, A. J.; Vanmaekelbergh, D.; Kelly, J. J.; Meulenkaamp, E. A. Wide Energy-Window View on the Density of States and Hole Mobility in Poly(p-Phenylene Vinylene). *Phys. Rev. Lett.* **2004**, *93* (16), 16–19.
- (27) Movaghar, B.; Grünewald, M.; Ries, B.; Bäessler, H.; Würtz, D. Diffusion and Relaxation of Energy in Disordered Organic and Inorganic Materials. *Phys. Rev. B* **1986**, *33* (8), 5545–5554.
- (28) Movaghar, B.; Ries, B.; Grünewald, M. Diffusion and Relaxation of Energy in Disordered Systems: Departure from Mean-Field Theories. *Phys. Rev. B* **1986**, *34* (8), 5574–5582.
- (29) Hoffmann, S. T.; Bäessler, H.; Koenen, J. M.; Forster, M.; Scherf, U.; Scheler, E.; Strohriegel, P.; Köhler, A. Spectral Diffusion in Poly(Para-Phenylene)-Type Polymers with Different Energetic Disorder. *Phys. Rev. B - Condens. Matter Mater. Phys.* **2010**, *81* (11), 1–8.
- (30) Arkhipov, V. I.; Heremans, P.; Emelianova, E. V.; Bäessler, H. Effect of Doping on the Density-of-States Distribution and Carrier Hopping in Disordered Organic Semiconductors. *Phys. Rev. B - Condens. Matter Mater. Phys.* **2005**, *71* (4), 1–7.
- (31) Panzer, M. J.; Frisbie, C. D. High Carrier Density and Metallic Conductivity in Poly(3-Hexylthiophene) Achieved by Electrostatic Charge Injection. *Adv. Funct. Mater.* **2006**, *16* (8), 1051–1056.
- (32) Zuo, G.; Li, Z.; Andersson, O.; Abdalla, H.; Wang, E.; Kemerink, M. Molecular Doping and Trap Filling in Organic Semiconductor Host-Guest Systems. *J. Phys. Chem. C* **2017**, *121* (14), 7767–7775.
- (33) Gartstein, Y. N.; Conwell, E. M. High-Field Hopping Mobility in Molecular Systems with Spatially Correlated Energetic Disorder. *Chem. Phys. Lett.* **1995**, *245* (4–5), 351–358.
- (34) Novikov, S. V.; Dunlap, D. H.; Kenkre, V. M.; Parris, P. E.; Vannikov, a V. Essential Role of Correlations in Governing Charge Transport in Disordered Organic Materials. *Phys. Rev. Lett.* **1998**, *81* (20), 4472–4475.

- (35) Mott, N. F. Conduction in Glasses Containing Transition Metal Ions. *J. Non. Cryst. Solids* **1968**, *1* (1), 1–17.
- (36) Menon, R.; Yoon, C. O.; Moses, D.; Heeger, A. J.; Cao, Y. Transport in Polyaniline near the Critical Regime of the Metal-Insulator Transition. *Phys. Rev. B* **1993**, *48* (24), 17685–17694.
- (37) Wilson, A. H. The Theory of Electronic Semi-Conductors. *Proc. R. Soc. A Math. Phys. Eng. Sci.* **1931**, *133* (822), 458–491.
- (38) Wilson, A. H. Theory of Electronic Semi-Conductors II. *Proc. R. Soc. A Math. Phys. Eng. Sci.* **1931**, *134* (823), 277–287.
- (39) Mott, N. F.; Davis, E. A. *Electronic Processes in Non-Crystalline Materials*, Clarendon.; Marshall, W., Wilkinson, D. H., Eds.; 1979.
- (40) Shklovskii, B. I.; Efros, A. L. *Electronic Properties of Doped Semiconductors*; 1984.
- (41) Anderson, P. W. Absence of Diffusion in Certain Random Lattices. *Phys. Rev.* **1958**, *109* (5), 1492–1505.
- (42) Mott, N. F. *Metal-Insulator Transitions*, 2nd edn.; Taylor & Francis, 1990.
- (43) Pichard, J. L.; Sarma, G. Finite Size Scaling Approach to Anderson Localisation. *J. Phys. C Solid State Phys.* **1981**, *14* (6), L127–L132.
- (44) Schreiber, M. Numerical Investigation of the Anderson Transition. *J. Non. Cryst. Solids* **1987**, *97–98*, 221–224.
- (45) Mott, N.; Pepper, M.; Pollitt, S.; Wallis, R. H.; Adkins, C. J. The Anderson Transition. *Proc. R. Soc. A Math. Phys. Eng. Sci.* **1975**, *345* (1641), 169–205.
- (46) Sugimoto, A.; Ochi, H.; Fujimura, S.; Yoshida, A.; Miyadera, T.; Tsuchida, M. Flexible OLED Displays Using Plastic Substrates. *IEEE J. Sel. Top. Quantum Electron.* **2004**, *10* (1), 107–114.
- (47) Kim, S.; Kwon, H. J.; Lee, S.; Shim, H.; Chun, Y.; Choi, W.; Kwack, J.; Han, D.; Song, M.; Kim, S.; et al. Low-Power Flexible Organic Light-Emitting Diode Display Device. *Adv. Mater.* **2011**, *23* (31), 3511–3516.
- (48) Yang, S. Y.; Cicoira, F.; Byrne, R.; Benito-Lopez, F.; Diamond, D.; Owens, R. M.; Malliaras, G. G. Electrochemical Transistors with Ionic Liquids for Enzymatic Sensing. *Chem. Commun.* **2010**, *46* (42), 7972–7974.
- (49) Zhang, C.; Chen, P.; Hu, W. Organic Field-Effect Transistor-Based Gas Sensors. *Chem. Soc. Rev.* **2015**, *44* (8), 2087–2107.
- (50) Knupfer, M.; Paasch, G. Origin of the Interface Dipole at Interfaces between Undoped Organic Semiconductors and Metals. *J. Vac. Sci. Technol. A Vacuum, Surfaces, Film.* **2005**, *23* (September 2004), 1072.
- (51) Hwang, J.; Wan, A.; Kahn, A. Energetics of Metal-Organic Interfaces: New Experiments and Assessment of the Field. *Mater. Sci. Eng. R Reports* **2009**, *64* (1–2), 1–31.
- (52) Arkhipov, V. I.; Wolf, U.; Bäessler, H. Current Injection from a Metal to a Disordered Hopping System. II. Comparison between Analytic Theory and Simulation. *Phys. Rev. B* **1999**, *59* (11), 7514–7520.
- (53) Sze, S. M.; Ng, K. K. *Physics of Semiconductor Devices*; John Wiley & Sons, Inc., 2007.

- (54) Natali, D.; Caironi, M. Charge Injection in Solution-Processed Organic Field-Effect Transistors: Physics, Models and Characterization Methods. *Adv. Mater.* **2012**, *24* (11), 1357–1387.
- (55) Fowler, R. H.; Nordheim, L. Electron Emission in Intense Electric Fields. *Proc. R. Soc. A Math. Phys. Eng. Sci.* **1928**, *119* (781), 173–181.
- (56) Simmons, J. G. Richardson-Schottky Effect in Solids. *Phys. Rev. Lett.* **1965**, *15* (25), 967–968.
- (57) Frenkel, J. On Pre-Breakdown Phenomena in Insulators and Electronic Semi-Conductors. *Phys. Rev.* **1938**, *54* (8), 647–648.
- (58) Wolf, U.; Arkhipov, V. I.; Bäessler, H. Current Injection from a Metal to a Disordered Hopping System. I. Monte Carlo Simulation. *Phys. Rev. B* **1999**, *59* (11), 7507–7513.
- (59) Barth, S.; Wolf, U.; Bäessler, H.; Müller, P.; Riel, H.; Vestweber, H.; Seidler, P. F.; Rieß, W. Current Injection from a Metal to a Disordered Hopping System. III. Comparison between Experiment and Monte Carlo Simulation. *Phys. Rev. B - Condens. Matter Mater. Phys.* **1999**, *60* (12), 8791–8797.
- (60) Onsager, L. Initial Recombination of Ions. *Phys. Rev.* **1938**, *54* (8), 554–557.
- (61) Arkhipov, V. I.; Emelianova, E. V.; Tak, Y. H.; Bäessler, H. Charge Injection into Light-Emitting Diodes: Theory and Experiment. *J. Appl. Phys.* **1998**, *84* (2), 848.
- (62) Cheng, X.; Noh, Y. Y.; Wang, J.; Tello, M.; Frisch, J.; Blum, R. P.; Vollmer, A.; Rabe, J. P.; Koch, N.; Sirringhaus, H. Controlling Electron and Hole Charge Injection in Ambipolar Organic Field-Effect Transistors by Self-Assembled Monolayers. *Adv. Funct. Mater.* **2009**, *19* (15), 2407–2415.
- (63) Noh, Y.-Y.; Cheng, X.; Tello, M.; Lee, M.-J.; Sirringhaus, H. Controlling Contact Resistance in Top-Gate Polythiophene-Based Field-Effect Transistors by Molecular Engineering. *Semicond. Sci. Technol.* **2011**, *26* (3), 034003.
- (64) Devillers, S.; Hennart, A.; Delhalle, J.; Mekhalif, Z. 1-Dodecanethiol Self-Assembled Monolayers on Cobalt. *Langmuir* **2011**, *27* (24), 14849–14860.
- (65) Verduci, T.; Yang, C. S.; Bernard, L.; Lee, G.; Boukari, S.; Orgiu, E.; Samorì, P.; Lee, J. O.; Doudin, B. Carbon-Passivated Ni Electrodes for Charge Injection in Organic Semiconductors. *Adv. Mater. Interfaces* **2016**, *3* (6), 1–9.
- (66) Ng, T. N.; Silveira, W. R.; Marohn, J. A. Dependence of Charge Injection on Temperature, Electric Field, and Energetic Disorder in an Organic Semiconductor. *Phys. Rev. Lett.* **2007**, *98* (6), 1–4.
- (67) Hamadani, B. H.; Ding, H.; Gao, Y.; Natelson, D. Doping-Dependent Charge Injection and Band Alignment in Organic Field-Effect Transistors. *Phys. Rev. B - Condens. Matter Mater. Phys.* **2005**, *72* (23), 2–6.
- (68) Rep, D. B. A.; Morpurgo, A. F.; Klapwijk, T. M. Doping-Dependent Charge Injection into Regioregular Poly(3-Hexylthiophene). *Org. Electron. physics, Mater. Appl.* **2003**, *4* (4), 201–207.
- (69) Chiang, C. K.; Fincher, C. R.; Park, Y. W.; Heeger, A. J.; Shirakawa, H.; Louis, E. J.; Gau, S. C.; MacDiarmid, A. G. Electrical Conductivity in Doped Polyacetylene. *Phys. Rev. Lett.* **1977**, *39* (17), 1098–1101.

- (70) Reghu, M.; Cao, Y.; Moses, D.; Heeger, A. J. Counterion-Induced Processibility of Polyaniline: Transport at the Metal-Insulator Boundary. *Phys. Rev. B* **1993**, *47* (4), 1758–1764.
- (71) Kohlman, R. S.; Zibold, A.; Tanner, D. B.; Ihas, G. G.; Ishiguro, T.; Min, Y. G.; MacDiarmid, A. G.; Epstein, A. J. Limits for Metallic Conductivity in Conducting Polymers. *Phys. Rev. Lett.* **1997**, *78* (20), 3915–3918.
- (72) Neoh, K. G.; Pun, M. Y.; Kang, E. T.; Tan, K. L. Polyaniline Treated with Organic Acids: Doping Characteristics and Stability. *Synth. Met.* **1995**, *73* (3), 209–215.
- (73) Ranger, M.; Rondeau, D.; Leclerc, M. New Well-Defined Poly(2,7-Fluorene) Derivatives: Photoluminescence and Base Doping. *Macromolecules* **1997**, *30* (25), 7686–7691.
- (74) Cochran, J. E.; Junk, M. J. N.; Glauddell, A. M.; Miller, P. L.; Cowart, J. S.; Toney, M. F.; Hawker, C. J.; Chmelka, B. F.; Chabynyc, M. L. Molecular Interactions and Ordering in Electrically Doped Polymers: Blends of PBTBT and F4TCNQ. **2014**.
- (75) Zanettini, S.; Dayen, J. F.; Etrillard, C.; Leclerc, N.; Kamalakar, M. V.; Doudin, B. Magnetoconductance Anisotropy of a Polymer Thin Film at the Onset of Metallicity. *Appl. Phys. Lett.* **2015**, *106* (6), 2–6.
- (76) Ito, H.; Harada, T.; Tanaka, H.; Kuroda, S. I. Critical Regime for the Insulator-Metal Transition in Highly Ordered Conjugated Polymers Gated with Ionic Liquid. *Jpn. J. Appl. Phys.* **2016**, *55* (3).
- (77) Yamashita, Y.; Tsurumi, J.; Hinkel, F.; Okada, Y.; Soeda, J.; Zaja, czkowski, W.; Baumgarten, M.; Pisula, W.; Matsui, H.; Müllen, K.; et al. Transition between Band and Hopping Transport in Polymer Field-Effect Transistors. *Adv. Mater.* **2014**, *26* (48), 8169–8173.
- (78) Dhoot, A. S.; Yuen, J. D.; Heeney, M.; McCulloch, I.; Moses, D.; Heeger, A. J. Beyond the Metal-Insulator Transition in Polymer Electrolyte Gated Polymer Field-Effect Transistors. *Proc. Natl. Acad. Sci.* **2006**, *103* (32), 11834–11837.
- (79) White, H. S.; Kittlesen, G. P.; Wrighton, M. S. Chemical Derivatization of an Array of Three Gold Microelectrodes with Polypyrrole: Fabrication of a Molecule-Based Transistor. *J. Am. Chem. Soc.* **1984**, *106* (18), 5375–5377.
- (80) Tsumura, A.; Koezuka, H.; Ando, T. Macromolecular Electronic Device: Field-Effect Transistor with a Polythiophene Thin Film. *Appl. Phys. Lett.* **1986**, *49* (18), 1210–1212.
- (81) Dimitrakopoulos, C. D. Low-Voltage Organic Transistors on Plastic Comprising High-Dielectric Constant Gate Insulators. *Science (80- )*. **1999**, *283* (5403), 822–824.
- (82) Bartic, C.; Jansen, H.; Campitelli, A.; Borghs, S. Ta<sub>2</sub>O<sub>5</sub> as Gate Dielectric Material for Low-Voltage Organic Thin-Film Transistors. *Org. Electron. physics, Mater. Appl.* **2002**, *3* (2), 65–72.
- (83) Zhang, H.-M.; Wang, G.; Demaray, R. E.; Narasimhan, M.; Moses, D.; Heeger, A. J. Poly(3-Hexylthiophene) Field-Effect Transistors with High Dielectric Constant Gate Insulator. *J. Appl. Phys.* **2003**, *95* (1), 316–322.
- (84) Huang, L.; Jia, Z.; Kymissis, L.; O'Brien, S. High K Capacitors and OFET Gate Dielectrics from Self-Assembled BaTiO<sub>3</sub> and (Ba,Sr)TiO<sub>3</sub> Nanocrystals in the Superparaelectric Limit. *Adv. Funct. Mater.* **2010**, *20* (4), 554–560.
- (85) Chua, L.-L.; Ho, P. K. H.; Sirringhaus, H.; Friend, R. H. High-Stability Ultrathin Spin-on Benzocyclobutene Gate Dielectric for Polymer Field-Effect Transistors. *Appl. Phys. Lett.*

- 2004**, *84* (17), 3400–3402.
- (86) Noh, Y. Y.; Zhao, N.; Caironi, M.; Sirringhaus, H. Downscaling of Self-Aligned, All-Printed Polymer Thin-Film Transistors. *Nat. Nanotechnol.* **2007**, *2* (12), 784–789.
- (87) Halik, M.; Klauk, H.; Zschieschang, U.; Schmid, G.; Radlik, W.; Weber, W. Polymer Gate Dielectrics and Conducting-Polymer Contacts for High-Performance Organic Thin-Film Transistors. *Adv. Mater.* **2002**, *14* (23), 1717–1722.
- (88) Noh, Y. Y.; Sirringhaus, H. Ultra-Thin Polymer Gate Dielectrics for Top-Gate Polymer Field-Effect Transistors. *Org. Electron. physics, Mater. Appl.* **2009**, *10* (1), 174–180.
- (89) Park, C. E.; Jeon, H.; Lee, J. W.; Hong, K. P.; Shin, K.; Yang, S. Y.; Kim, S. H. Low-Operating-Voltage Pentacene Field-Effect Transistor with a High-Dielectric-Constant Polymeric Gate Dielectric. *Appl. Phys. Lett.* **2006**, *89* (18), 183516.
- (90) Collet, J.; Tharaud, O.; Chapoton, A.; Vuillaume, D. Low-Voltage, 30 Nm Channel Length, Organic Transistors with a Self-Assembled Monolayer as Gate Insulating Films. *Appl. Phys. Lett.* **2000**, *76* (14), 1941–1943.
- (91) Majewski, L. A.; Schroeder, R.; Grell, M. Low-Voltage, High-Performance Organic Field-Effect Transistors with an Ultra-Thin TiO<sub>2</sub> Layer as Gate Insulator. *Adv. Funct. Mater.* **2005**, *15* (6), 1017–1022.
- (92) Klauk, H.; Zschieschang, U.; Pflaum, J.; Halik, M. Ultralow-Power Organic Complementary Circuits. *Nature* **2007**, *445* (7129), 745–748.
- (93) Wöbkenberg, P. H.; Ball, J.; Kooistra, F. B.; Hummelen, J. C.; De Leeuw, D. M.; Bradley, D. D. C.; Anthopoulos, T. D. Low-Voltage Organic Transistors Based on Solution Processed Semiconductors and Self-Assembled Monolayer Gate Dielectrics. *Appl. Phys. Lett.* **2008**, *93* (1).
- (94) Hallinan, D. T.; Balsara, N. P. *Polymer Electrolytes: Fundamentals and Applications*; Publishing, W., Ed.; 2013; Vol. 43.
- (95) Xie, W.; Liu, F.; Shi, S.; Ruden, P. P.; Frisbie, C. D. Charge Density Dependent Two-Channel Conduction in Organic Electric Double Layer Transistors (EDLTs). *Adv. Mater.* **2014**, *26* (16), 2527–2532.
- (96) Lee, J.; Kaake, L. G.; Cho, J. H.; Zhu, X.-Y.; Lodge, T. P.; Frisbie, C. D. Ion Gel-Gated Polymer Thin-Film Transistors: Operating Mechanism and Characterization of Gate Dielectric Capacitance, Switching Speed, and Stability. *J. Phys. Chem. C* **2009**, *113* (20), 8972–8981.
- (97) Kubo, W.; Murakoshi, K.; Kitamura, T.; Yoshida, S.; Haruki, M.; Hanabusa, K.; Shirai, H.; Wada, Y.; Yanagida, S. Quasi-Solid-State Dye-Sensitized TiO<sub>2</sub> Solar Cells: Effective Charge Transport in Mesoporous Space Filled with Gel Electrolytes Containing Iodide and Iodine. *J. Phys. Chem. B* **2001**, *105* (51), 12809–12815.
- (98) Panzer, M. J.; Frisbie, C. D. Exploiting Ionic Coupling in Electronic Devices: Electrolyte-Gated Organic Field-Effect Transistors. *Adv. Mater.* **2008**, *20* (16), 3176–3180.
- (99) Panzer, M. J.; Frisbie, C. D. High Charge Carrier Densities and Conductance Maxima in Single-Crystal Organic Field-Effect Transistors with a Polymer Electrolyte Gate Dielectric. *Appl. Phys. Lett.* **2006**, *88* (20), 1–4.
- (100) Laiho, A.; Herlogsson, L.; Forchheimer, R.; Crispin, X.; Berggren, M. Controlling the Dimensionality of Charge Transport in Organic Thin-Film Transistors. **2011**, *108* (37).

- (101) Tokuda, H.; Hayamizu, K.; Ishii, K.; Susan, M. A. B. H.; Watanabe, M. Physicochemical Properties and Structures of Room Temperature Ionic Liquids. 1. Variation of Anionic Species. *J. Phys. Chem. B* **2004**, *108* (42), 16593–16600.
- (102) Tokuda, H.; Hayamizu, K.; Ishii, K.; Susan, M. A. B. H.; Watanabe, M. Physicochemical Properties and Structures of Room Temperature Ionic Liquids. 2. Variation of Alkyl Chain Length in Imidazolium Cation. *J. Phys. Chem. B* **2005**, *109* (13), 6103–6110.
- (103) Nketia-Yawson, B.; Kang, S. J.; Tabi, G. D.; Perinot, A.; Caironi, M.; Facchetti, A.; Noh, Y. Y. Ultrahigh Mobility in Solution-Processed Solid-State Electrolyte-Gated Transistors. *Adv. Mater.* **2017**, *29* (16).
- (104) Inal, S.; Rivnay, J.; Suiu, A. O.; Malliaras, G. G.; McCulloch, I. Conjugated Polymers in Bioelectronics. *Acc. Chem. Res.* **2018**, *51* (6), 1368–1376.
- (105) Leger, J.; Berggren, M.; Carter, S. *Iontronics*; Leger, J., Berggren, M., Carter, S., Eds.; CRC Press, 2010.
- (106) Kergoat, L.; Piro, B.; Berggren, M.; Horowitz, G.; Pham, M. C. Advances in Organic Transistor-Based Biosensors: From Organic Electrochemical Transistors to Electrolyte-Gated Organic Field-Effect Transistors. *Anal. Bioanal. Chem.* **2012**, *402* (5), 1813–1826.
- (107) Macchia, E.; Manoli, K.; Holzer, B.; Di Franco, C.; Ghittorelli, M.; Torricelli, F.; Alberga, D.; Mangiatordi, G. F.; Palazzo, G.; Scamarcio, G.; et al. Single-Molecule Detection with a Millimetre-Sized Transistor. *Nat. Commun.* **2018**, *9* (1).
- (108) Zhang, Y. J.; Iwasa, Y.; Arita, R.; Ye, J. T.; Bahramy, M. S.; Akashi, R. Superconducting Dome in a Gate-Tuned Band Insulator. *Science* (80-. ). **2012**, *338* (6111), 1193–1196.
- (109) Bubnova, O.; Berggren, M.; Crispin, X. Tuning the Thermoelectric Properties of Conducting Polymers in an Electrochemical Transistor. *J. Am. Chem. Soc.* **2012**, *134* (40), 16456–16459.
- (110) Scheinert, S.; Paasch, G. Interdependence of Contact Properties and Field- and Density-Dependent Mobility in Organic Field-Effect Transistors. *J. Appl. Phys.* **2009**, *105* (1).
- (111) Necliudov, P. V.; Shur, M. S.; Gundlach, D. J.; Jackson, T. N. Modeling of Organic Thin Film Transistors of Different Designs. *J. Appl. Phys.* **2000**, *88* (11), 6594–6597.
- (112) Seshadri, K.; Frisbie, C. D. Potentiometry of an Operating Organic Semiconductor Field-Effect Transistor. *Appl. Phys. Lett.* **2001**, *78* (7), 993–995.
- (113) Klauk, H.; Schmid, G.; Radlik, W.; Weber, W.; Zhou, L.; Sheraw, C. D.; Nichols, J. A.; Jackson, T. N. Contact Resistance in Organic Thin Film Transistors. *Solid. State. Electron.* **2003**, *47* (2), 297–301.
- (114) Necliudov, P. V.; Shur, M. S.; Gundlach, D. J.; Jackson, T. N. Contact Resistance in Pentacene Thin Film Transistors. *2001 Int. Semicond. Device Res. Symp. ISDRS 2001 - Proc.* **2001**, 345–348.
- (115) Meijer, E. J.; Gelinck, G. H.; van Veenendaal, E.; Huisman, B.-H.; de Leeuw, D. M.; Klapwijk, T. M. Scaling Behavior and Parasitic Series Resistance in Disordered Organic Field-Effect Transistors. *Appl. Phys. Lett.* **2003**, *82* (25), 4576–4578.
- (116) Minari, T.; Miyadera, T.; Tsukagoshi, K.; Aoyagi, Y.; Ito, H. Charge Injection Process in Organic Field-Effect Transistors. *Appl. Phys. Lett.* **2007**, *91* (5).
- (117) Hamadani, B. H.; Natelson, D. Temperature-Dependent Contact Resistances in High-

- Quality Polymer Field-Effect Transistors. *Appl. Phys. Lett.* **2004**, *84* (3), 443–445.
- (118) Liu, C.; Xu, Y.; Ghibaudo, G.; Lu, X.; Minari, T.; Noh, Y. Y. Evaluating Injection and Transport Properties of Organic Field-Effect Transistors by the Convergence Point in Transfer-Length Method. *Appl. Phys. Lett.* **2014**, *104* (1).
- (119) Bürgi, L.; Sirringhaus, H.; Friend, R. H. Noncontact Potentiometry of Polymer Field-Effect Transistors. **2007**, *2913* (2002), 1–4.
- (120) Chesterfield, R. J.; McKeen, J. C.; Newman, C. R.; Frisbie, C. D.; Ewbank, P. C.; Mann, K. R.; Miller, L. L. Variable Temperature Film and Contact Resistance Measurements on Operating n -Channel Organic Thin Film Transistors . *J. Appl. Phys.* **2004**, *95* (11), 6396–6405.
- (121) Pesavento, P. V.; Chesterfield, R. J.; Newman, C. R.; Frisbie, C. D. Gated Four-Probe Measurements on Pentacene Thin-Film Transistors: Contact Resistance as a Function of Gate Voltage and Temperature. *J. Appl. Phys.* **2004**, *96* (12), 7312–7324.
- (122) Puntambekar, K. P.; Pesavento, P. V.; Frisbie, C. D. Surface Potential Profiling and Contact Resistance Measurements on Operating Pentacene Thin-Film Transistors by Kelvin Probe Force Microscopy. *Appl. Phys. Lett.* **2003**, *83* (26), 5539–5541.
- (123) Bürgi, L.; Richards, T. J.; Friend, R. H.; Sirringhaus, H. Close Look at Charge Carrier Injection in Polymer Field-Effect Transistors. *J. Appl. Phys.* **2003**, *94* (9), 6129–6137.
- (124) Umeda, T.; Kumaki, D.; Tokito, S. Surface-Energy-Dependent Field-Effect Mobilities up to 1 Cm<sup>2</sup> /V s for Polymer Thin-Film Transistor. *J. Appl. Phys.* **2009**, *105* (2).
- (125) Braga, D.; Ha, M.; Xie, W.; Frisbie, C. D. Ultralow Contact Resistance in Electrolyte-Gated Organic Thin Film Transistors. *Appl. Phys. Lett.* **2010**, *97* (19).
- (126) Zanettini, S.; Chaumy, G.; Chávez, P.; Leclerc, N.; Etrillard, C.; Leconte, B.; Chevrier, F.; Dayen, J.-F.; Doudin, B. High Conductivity Organic Thin Films for Spintronics: The Interface Resistance Bottleneck. *J. Phys. Condens. Matter* **2015**, *27* (46), 462001.
- (127) Sandström, A.; Matyba, P.; Inganäs, O.; Edman, L. Separating Ion and Electron Transport: The Bilayer Light-Emitting Electrochemical Cell. *J. Am. Chem. Soc.* **2010**, *132* (19), 6646–6647.
- (128) Klauk, H. Will We See Gigahertz Organic Transistors? *Adv. Electron. Mater.* **2018**, *1700474*, 1–8.
- (129) Choi, H. H.; Cho, K.; Frisbie, C. D.; Sirringhaus, H.; Podzorov, V. Critical Assessment of Charge Mobility Extraction in FETs. *Nat. Mater.* **2017**, *17* (1), 2–7.
- (130) Bittle, E. G.; Basham, J. I.; Jackson, T. N.; Jurchescu, O. D.; Gundlach, D. J. Mobility Overestimation Due to Gated Contacts in Organic Field-Effect Transistors. *Nat. Commun.* **2016**, *7*, 10908.
- (131) Choi, H. H.; Rodionov, Y. I.; Paterson, A. F.; Panidi, J.; Saranin, D.; Kharlamov, N.; Didenko, S. I.; Anthopoulos, T. D.; Cho, K.; Podzorov, V. Accurate Extraction of Charge Carrier Mobility in 4-Probe Field-Effect Transistors. *Adv. Funct. Mater.* **2018**, *1707105*, 1–11.
- (132) Di, C. A.; Yu, G.; Liu, Y.; Xu, X.; Song, Y.; Wang, Y.; Sun, Y.; Zhu, D.; Liu, H.; Liu, X.; et al. Noncoplanar Organic Field-Effect Transistor Based on Copper Phthalocyanine. *Appl. Phys. Lett.* **2006**, *88* (12), 4–7.
- (133) Wang, J. Z.; Zheng, Z. H.; Sirringhaus, H. Suppression of Short-Channel Effects in Organic

- Thin-Film Transistors. *Appl. Phys. Lett.* **2006**, *89* (8).
- (134) Dayen, J. F.; Faramarzi, V.; Pauly, M.; Kemp, N. T.; Barbero, M.; Pichon, B. P.; Majjad, H.; Begin-Colin, S.; Doudin, B. Nanotrench for Nano and Microparticle Electrical Interconnects. *Nanotechnology* **2010**, *21* (33).
- (135) Austin, M. D.; Chou, S. Y. Fabrication of 70 Nm Channel Length Polymer Organic Thin-Film Transistors Using Nanoimprint Lithography. *Appl. Phys. Lett.* **2002**, *81* (23), 4431–4433.
- (136) Zaumseil, J.; Someya, T.; Bao, Z.; Loo, Y.-L.; Cirelli, R.; Rogers, J. A. Nanoscale Organic Transistors That Use Source/Drain Electrodes Supported by High Resolution Rubber Stamps. *Appl. Phys. Lett.* **2003**, *82* (5), 793–795.
- (137) Stutzmann, N.; Friend, R. H.; Sirringhaus, H. Self-Aligned, Vertical-Channel, Polymer Field-Effect Transistors. *Science (80-. )*. **2003**, *299* (5614), 1881–1884.
- (138) Chen, Y.; Zhu, W. W.; Xiao, S.; Shih, I. Fabrication of Short Channel Organic Thin Film Transistors by Si-Etching Method. *J. Vac. Sci. Technol. A Vacuum, Surfaces, Film.* **2004**, *22* (3), 768.
- (139) Liu, J.; Herlogsson, L.; Sawatdee, A.; Favia, P.; Sandberg, M.; Crispin, X.; Engquist, I.; Berggren, M. Vertical Polyelectrolyte-Gated Organic Field-Effect Transistors. *Appl. Phys. Lett.* **2010**, *97* (10).
- (140) Cheng, X.; Caironi, M.; Noh, Y. Y.; Newman, C.; Wang, J.; Lee, M. J.; Banger, K.; Di Pietro, R.; Facchetti, A.; Sirringhaus, H. Downscaling of N-Channel Organic Field-Effect Transistors with Inkjet-Printed Electrodes. *Org. Electron. physics, Mater. Appl.* **2012**, *13* (2), 320–328.
- (141) Bucella, S. G.; Nava, G.; Vishunubhatla, K. C.; Caironi, M. High-Resolution Direct-Writing of Metallic Electrodes on Flexible Substrates for High Performance Organic Field Effect Transistors. *Org. Electron. physics, Mater. Appl.* **2013**, *14* (9), 2249–2256.
- (142) Torsi, L.; Dodabalapur, A.; Katz, H. E. An Analytical Model for Short-Channel Organic Thin-Film Transistors. *J. Appl. Phys.* **1995**, *78* (2), 1088–1093.
- (143) Klug, A.; Meingast, A.; Wurzinger, G.; Blümel, A.; Schmoltner, K.; Scherf, U.; List, E. J. W. Organic Field-Effect Transistors: A Combined Study on Short-Channel Effects and the Influence of Substrate Pre-Treatment on Ambient Stability. In *Proceedings of SPIE - The International Society for Optical Engineering*; Shinar, R., Kymissis, I., Eds.; 2011; Vol. 8118, p 811809.
- (144) Herlogsson, L.; Noh, Y.; Zhao, N.; Crispin, X.; Sirringhaus, H.; Berggren, M. Downscaling of Organic Field-Effect Transistors with a Polyelectrolyte Gate Insulator. *Adv. Mater.* **2008**, *20* (24), 4708–4713.
- (145) Haddock, J. N.; Zhang, X.; Zheng, S.; Zhang, Q.; Marder, S. R.; Kippelen, B. A Comprehensive Study of Short Channel Effects in Organic Field-Effect Transistors. *Org. Electron.* **2006**, *7* (1), 45–54.
- (146) Chabiny, M. L.; Lu, J. P.; Street, R. A.; Wu, Y.; Liu, P.; Ong, B. S. Short Channel Effects in Regioregular Poly(Thiophene) Thin Film Transistors. *J. Appl. Phys.* **2004**, *96* (4), 2063–2070.
- (147) Leufgen, M.; Bass, U.; Muck, T.; Borzenko, T.; Schmidt, G.; Geurts, J.; Wagner, V.; Molenkamp, L. W. Optimized Sub-Micron Organic Thin-Film Transistors: The Influence of Contacts and Oxide Thickness. *Synth. Met.* **2004**, *146* (3), 341–345.

- (148) Xu, Y.; Berger, P. R. High Electric-Field Effects on Short-Channel Polythiophene Polymer Field-Effect Transistors. *J. Appl. Phys.* **2004**, *95* (3), 1497–1501.
- (149) Tukagoshi, K.; Fujimori, F.; Minari, T.; Miyadera, T.; Hamano, T.; Aoyagi, Y. Suppression of Short Channel Effect in Organic Thin Film Transistors. *Appl. Phys. Lett.* **2007**, *91* (11), 10–13.

## Chapter II

# Organic spintronics

The research field of spintronics aims to use the spin of electrons to create, transport and store information. Spin-based devices are already widely present in daily life as they are the basic sets of magnetic storage technology of the last 30 years. It starts with the discovery of the giant magnetoresistance (GMR) by Fert & Grünberg<sup>1,2</sup>, owing them the Nobel Prize in 2007. Nowadays, scientific community works on new devices such as magnetoresistive random-access memory (MRAM), possibly working without applied magnetic field by spin torque exchange (STT-MRAM), in order to increase performances and decrease electric consumption of new-generation information storage technology. Organic materials have their own place in the spintronic field because of their ability to keep spin information over long time, in addition to their processability advantages discussed in last chapter.

In the present chapter, basic inorganic spintronic concepts are introduced to move towards spin transport in organic materials. The essential role of interface resistance is also investigated for the spin injection and detection in light of its importance and possible predominance in organic devices.

### II.1. Spintronic concepts

Spintronics aims to use the spin degree of freedom of electrons in addition to their charge for novel applications. The first observation of “spintronic effect” was done by William Thomson (Lord Kelvin) already more than 160 years ago. He measured the variation of the resistance of a piece of iron in a magnetic field by changing its strength and orientation respectively to the channel direction<sup>3</sup>. If at this time the concept of electron’s spin was unknown, it is the first experience that shows an anisotropic magnetoresistance (AMR).

Time passing, Nevil Mott published his two-currents model in 1936 to explain the conductivity of ferromagnetic metals<sup>4</sup>. One example of direct experimental illustration was the work of Tedrow and Meservey<sup>5</sup> in 1971. They exhibited a spin-polarized tunnel effect from nickel to superconductive aluminium, illustrating how the density of states (DOS) at the Fermi level is spin-dependent. Fert and Grünberg presented their works on multi-layer of Fe/Co and Fe/Cr respectively where they observed significant change of resistivity of the heterostructures upon the relative orientation of ferromagnetic layers that is the so-called giant magnetoresistance (GMR). The term giant comes from the much important variation of resistivity of GMR-devices compared to AMR-devices (~80 % compared to the ~1 % respectively). These experiments revealed how scattering involved in materials conductivity depends on the spin of charge carriers, confirming the core hypothesis of Mott' work.

In 1991, IBM commercialized its first MR-based hard disk drive and this technology was predominant for 25 years. Other kind of spin-based devices begin to emerge, like STT-MRAM<sup>6</sup>, spin-transistors<sup>7</sup> and spin-(O)LED<sup>8,9</sup> and pave the way to a bright future to spintronics.

### II.1.1. Magnetic materials

The basic component indicating spin-dependent electric transport in materials is based on two magnetic electrodes separated by a non-magnetic (NM) one, either insulating, then spins tunnel through; or conductive, then spins diffuse inside. In all cases, the choice of the electrode material is crucial for spin-dependent properties.

Magnetization has different origin depending on the type of material. We focus on the transition metals that exhibit magnetization thanks to their  $d$ -states. Each  $d$ -orbital contains five levels able to hold each two electrons of different spin. Moreover, the five levels divided in two groups: three lower energy level ( $t_{2g}$ ) and two higher energy levels ( $e_g$ ) separated by an energy gap. Depending of the size of the gap the  $t_{2g}$ -levels may be fully occupied first before filling the  $e_g$  states. Transitions from one to the other are also possible. When the  $3d$ -orbital is not fully occupied and electrons are not all paired, the unpaired electrons are responsible for the magnetization. These unpaired  $3d$ -electrons are localized enough to have a high exchange coupling that creates an asymmetric DOS (**Figure II.1**).

Applying a magnetic field on transition metals defines the quantum axis to distinguish both spin types. The convention is to ascribe the majority spins to spin up ( $\uparrow$ ), being in the same direction than the magnetic field, and minority spins to spin down ( $\downarrow$ ) that are anti-parallel to the external field. Exchange coupling makes their number very different, which translates into a large magnetization created by the external field. In the band structure of ferromagnetic (FM) transition metals shown in **Figure II.1**, the majority-spin orbital is fully occupied while the minority spin is only partially filled.

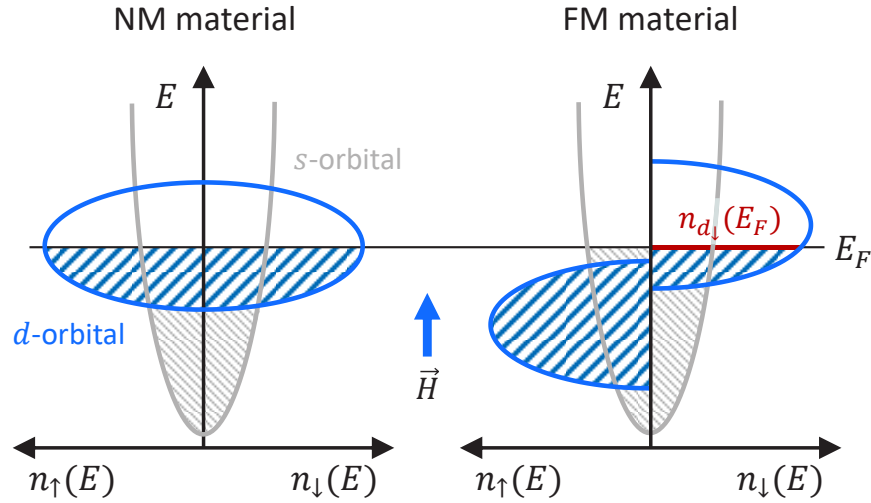


**Figure II.1** Density of states of non-magnetic and ferromagnetic materials. Because of the exchange interaction, the DOS of spin up and spin down are shifted resulting in different density of state at  $E_F$ .

To explain the resistivity of transition metals, Mott presented his two-currents model in 1936. Assuming that scattering events conserve the spin of carriers, charges carrying spin up or spin down can be represented as two separated channels in parallel, with their own resistivity  $\rho_\uparrow$  and  $\rho_\downarrow$ . Resistivities are different because the carriers DOS of both spins is different. Indeed, the resistivity relies on scattering events with phonons and impurities mainly, but also on  $s$ - $d$  scattering that depends on the DOS, which is asymmetric for FM materials. As we assume spin conservation within scattering processes, only  $s_\uparrow \rightarrow d_\uparrow$  and  $s_\downarrow \rightarrow d_\downarrow$  transitions (or reversed) are allowed. However, as the  $d_\uparrow$ -orbital is full, the first process is much rarer than the second, leading to  $\rho_\uparrow < \rho_\downarrow$ .

In the end, the resistivity of transition metals within the two-currents framework writes:

$$\rho = \frac{\rho_\uparrow \rho_\downarrow}{\rho_\uparrow + \rho_\downarrow} \leq \rho_\uparrow, \rho_\downarrow \quad (\text{II.1})$$

If the  $s$ - $d$  scattering of one type of spin is negligible, this channel short-circuits the other and the total resistance decreases. Furthermore, the inequality of  $\rho_\uparrow$  and  $\rho_\downarrow$  in FM metals leads to spin-polarization of carriers, quantified by the (bulk) spin asymmetry coefficient  $\beta$ :

$$\beta = \frac{\rho_\downarrow - \rho_\uparrow}{\rho_\uparrow + \rho_\downarrow} \quad (\text{II.2})$$

that scales the expected amplitude of the spin-dependent signal. The spin-resistivities can be written in term of  $\beta$  as:  $2\rho_{\uparrow,\downarrow} = \rho(1 \mp \beta)$ .

## II.1.2. Magnetoresistances

The magnetoresistance (MR) is the variation of resistance (or resistivity) of materials or devices in an external magnetic field. However, due to the variety of devices and phenomenon involved, different definitions exist to quantify its amplitude. First, the impact of the amplitude and direction versus the current flow of the external magnetic field is investigated on materials. Then, the case of the FM/NM/FM trilayer is discussed in the scope of the understanding of spin-valves.

### Anisotropic magnetoresistance

The resistivity in a magnetic field ( $H$ ) in the positive  $z$  direction can be written in matrix formalism as:

$$\rho(H) = \begin{bmatrix} \rho_{\perp}(H) & -\rho_H(H) & 0 \\ \rho_H(H) & \rho_{\perp}(H) & 0 \\ 0 & 0 & \rho_{\parallel}(H) \end{bmatrix} \quad (II.3)$$

where  $\rho_{\perp(\parallel)}$  is the longitudinal resistivity perpendicular (parallel) to the magnetic field, and  $\rho_H$  is the transverse Hall resistivity. In the case of FM materials, the amplitude of  $\vec{B} = \mu_0(\vec{H} + \vec{M})$  replaces  $H$ ,  $\vec{M}$  being the magnetization and  $\mu_0$  the vacuum permeability. For the following discussion, the current density ( $\vec{J}$ ) is in the positive  $y$ -direction.

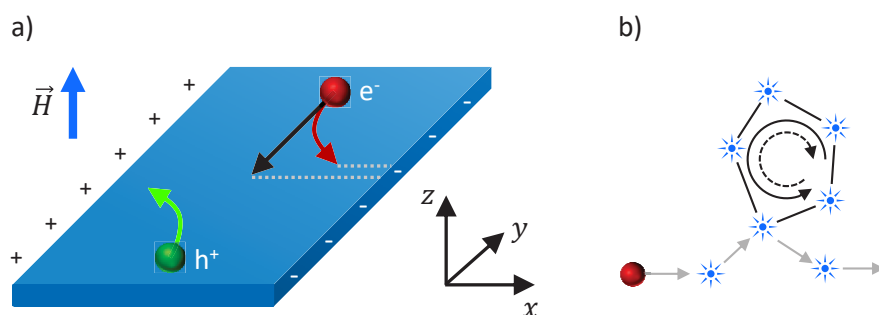


**Figure II.2** a) Schematic representation of the bending of carriers trajectory in a magnetic field. The Lorentz force deflects charge perpendicular to both the current flow and external magnetic field, to the positive or negative  $x$  direction depending on their charge. It involves a reduction of the distance travelled in the current direction before scattering (pointed out by the grey dotted lines), and an electric field in the  $x$ -axis ( $\vec{E}_H$ ). b) Self-closing path leading to weak localization.

The longitudinal resistivity in current direction transverse to the field of materials often increases upon application of an external magnetic field. Indeed, in a classical point of view, the trajectory of charges curves because of the Lorentz force  $\vec{F} = q(\vec{E} + \vec{v} \times \vec{B})$ , where  $q$  is the charge of the carrier,  $\vec{E}$  the electric field and  $\vec{v}$  the velocity of the carrier (**Figure II.2a**). The bending of the pathway of carriers diminishes the  $y$ -component of the distance between two scattering events, and therefore rises the number of scattering processes within the channel. The variation of  $\rho$  is given by the Kohler's rule and is proportional to  $H^2$ . It will be the case of

our organic materials as it will be discussed in the chapter V. In the case of FM materials, Kohler's rule can be generalized accounting for the magnetization such that the variation of resistivity is proportional to  $aH^2 + bM_z^2$ .

For FM materials  $\rho_{\perp} \neq \rho_{\parallel}$ , and in general  $\rho_{\parallel} > \rho_{\perp}$  because of the spin-orbit coupling (SOC). The SOC mixes the up and down states, such that  $s_{\uparrow}$ -electrons are able to scatter into available  $d_{\downarrow}$ -states. In addition,  $d_{\uparrow} \rightarrow s_{\downarrow}$  transitions are also allowed, that creates  $d_{\uparrow}$ -holes, favouring  $s_{\uparrow} \rightarrow d_{\uparrow}$  scattering probability. However, the  $s \rightarrow d$  process occurs only if the momentum of the electron is in the plane of the orbit of the empty  $d$ -state, which is more likely the case when  $\vec{M} \parallel \vec{J}$ <sup>10</sup>. This difference translates into AMR properties.

When the magnetic field is perpendicular to the current, in certain conditions, weak localization arises in disordered systems<sup>11,12</sup>. At low temperatures, when the probability to scatter on phonons becomes low, the resistivity tends to decrease upon the application of perpendicular magnetic field. Indeed, when carriers motion is diffusive, they perform a random walk because of the multiple scattering processes. Therefore, carriers may come back to an already visited site by a self-closing path (**Figure II.2b**). The weak localization tells that the clockwise and anti-clockwise crossing of such close loop interfere constructively, because the lengths are equal, that favour localization. Applying the magnetic field perpendicular to these loops breaks the coherence of these two paths by adding a phase shift that decreases the resistivity. The observation of weak localization is a sign of metallicity in insulating-like materials.

Finally, the off-diagonal terms of the resistivity tensor,  $\pm\rho_H$ , relates to the Hall effect. Again because of the Lorentz force deflecting the charge perpendicular to both the magnetic field and the current flow, charge accumulation takes place on the border of the channel and a difference of potential appears in the  $x$ -direction. In non-magnetic materials, the related electric field is:

$$\vec{E}_H = R_H(\vec{J} \times \mu_0\vec{H}) \quad (II.4)$$

where  $R_H = 1/ne$  is the Hall resistance, from which the Hall resistivity is extracted  $\rho_H = R_H\mu_0H$ . Note that the unit of the Hall variables are not consistent with resistances. The latter definition is known as the ordinary Hall effect because the magnetization is not involved and in the end  $\rho_H \propto H$ .

For FM materials,  $\vec{H}$  has to be replaced by  $\vec{B}$  and the final  $\rho_H$  is the sum of the ordinary Hall resistivity and a second term proportional to  $M_z$ . It becomes then the anomalous Hall effect, where a non-linearity appears for low field increasing rapidly  $\rho_H$ , and tends to the ordinary Hall effect for large field, when the magnetization of the FM material saturates.

The Hall effect is a useful tool to determine the intrinsic mobility of materials. Indeed, it escapes from contact resistance, and is more accurate than the field-effect mobility as it doesn't rely on the uniformity of the channel upon doping.

### Giant magnetoresistance

The most widespread MR nowadays is the giant MR (GMR) pointed out by Fert and Grünberg<sup>1,2</sup>. The changing in resistance arises in their case from the relative orientation of FM

layers in FM/NM/FM heterostructures where NM is a conductive non-magnetic material, defining a so-called spin valve structure. If the spacer is an insulator, charges tunnel through it and it refers to tunnelling magnetoresistance (TMR), detailed later. In both cases, reminders of basic magnetization properties of electrodes are needed.

In most case, spin injection occurs by means of FM electrodes. Their particularity is to present spontaneous magnetization below a critical temperature, the Curie temperature  $T_C$  (**Figure II.3a**). As long as  $T < T_C$ , spin of all electrons points in the same direction thanks to the so-called exchange energy that counterbalanced and surpassed the magnetic dipole-dipole interaction tending to anti-align them. Above  $T_C$ , the thermal agitation is too strong for spins to keep a particular direction and the magnetization is lost: the material turns to paramagnetic and  $M \propto H$ .

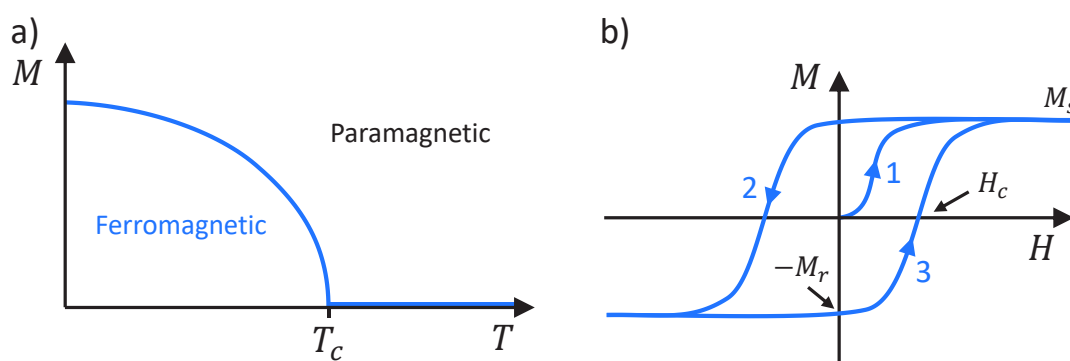


**Figure II.3** a) Magnetization of magnetic material versus temperature. For temperature above the Curie temperature, materials become paramagnetic and present no more macroscopic magnetism. b) Hysteresis cycle of ferromagnetic materials.

One particular feature of FM materials is their hysteresis cycle during applied magnetic field sweep (**Figure II.3b**). The first time an FM material experience an external magnetic field, its magnetization ( $M$ ) begin at 0, and increases until it reaches the saturation magnetization ( $M_S$ ) for high enough magnetic field. However, resetting the magnetic field to 0,  $M$  remains finite at a remanent magnetization ( $M_r$ ) level often on the same order of magnitude than  $M_S$ . Sweeping the field in the opposite direction, the magnetization of the FM layer finally goes to 0 at a given field named coercive field ( $H_c$ ). The amplitude of  $\vec{H}$  increasing, the magnetization of the material reaches again  $M_S$  but in the same direction than the field. Again, a finite magnetization remains when the field come back to 0. Some values of different characteristics for usual materials are given in **Table II.1**.

Material	Saturation magnetization (T)	Curie temperature (K)	Spin polarization (%)
Fe	2,16	1043	~40
Co	1,79	1388	~35
Ni	0,61	627	~23

**Table II.1** Saturation magnetization in Tesla ( $[T] = 4\pi \times 10^{-4} [A \cdot m^{-1}]$ ) and Curie temperature for iron (Fe), cobalt (Co) and nickel (Ni).

The coercive field is an important parameter for applications as it is the field needed to switch the magnetization orientation. FM materials with  $H_c < 10$  Oe ( $\sim 10^{-3}$  T) are magnetically soft materials, useful because their flip requires small energy; whereas hard magnetic materials ( $H_c > 10$  Oe) more likely keep their orientation and serve often as “fixed” magnets in devices. Structure combining hard and soft ferromagnets are the building blocks of hard disk drives as the soft one is addressed independently with a small magnetic field (lower than the coercive field of the hard one) to encode information.

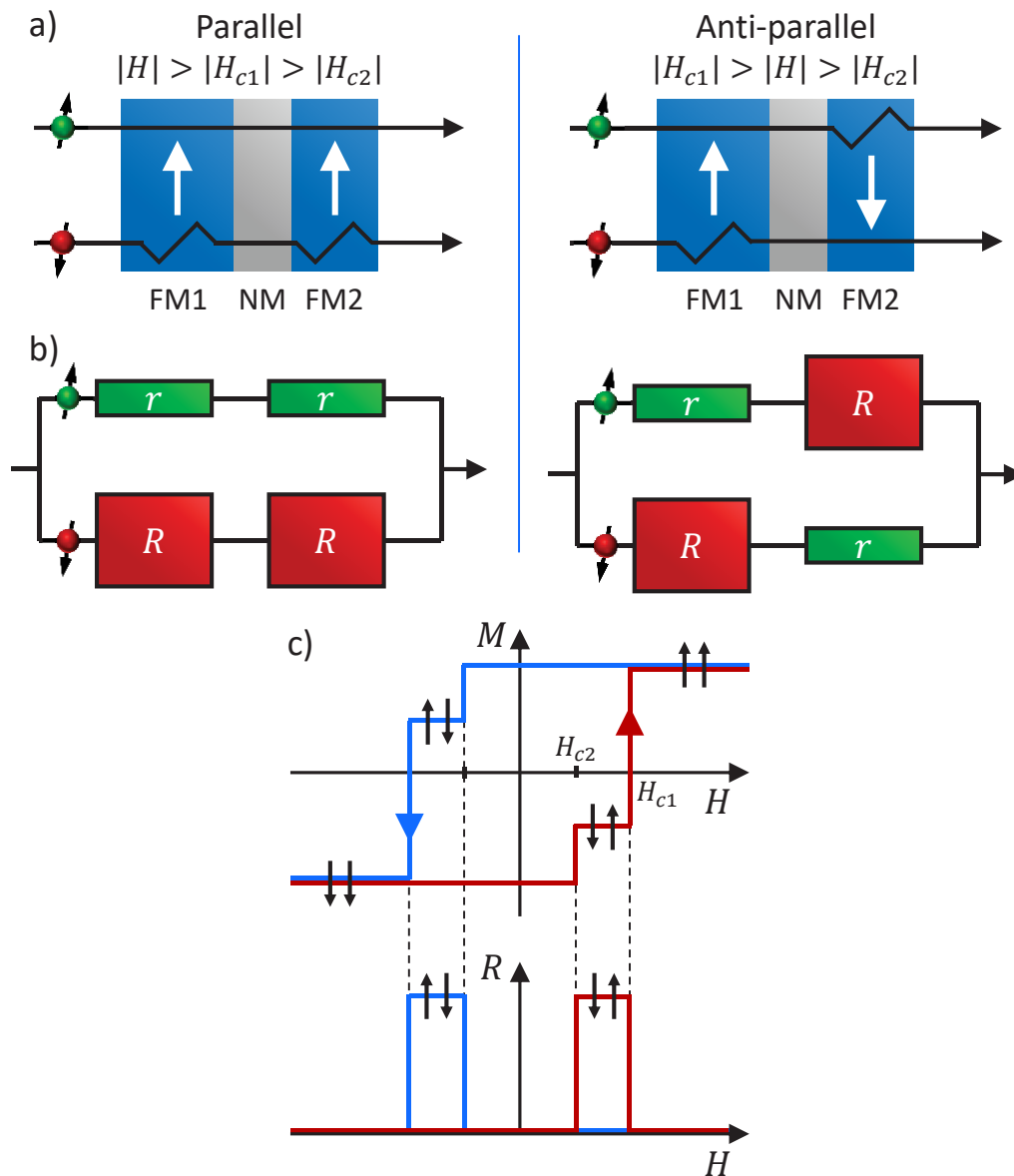


**Figure II.4** a) Parallel (left) and anti-parallel (right) situations. Spins in the opposite orientation than the FM material suffer a lot of scatterings that strongly increases the resistance ( $R$ ). On the other hand, spins parallel to the FM electrode magnetic moment cross easier, with a corresponding lower resistance ( $r$ ). b) The equivalent circuit from the Mott model of two-currents. c) Curves show the magnetization state (top) and the resistance (bottom) variation within an external magnetic field.

The same technique is used in spin-valve devices by patterning two FM electrodes with different size, leading to two different coercive fields, or two different materials, exhibiting a contrast in magnetic properties, in particular the coercivity. Then, upon applying an external magnetic field, the orientation of one layer will turnover before the other and allows the parallel configuration ( $P$ ), where the spin-polarization of electrodes are aligned, and anti-parallel states ( $AP$ ), where the polarization of electrodes are opposite (**Figure II.4a**). The two situations exhibit distinct resistance, that is used for binary encoding.

The difference of resistance between both cases arises easily from the two current model introduced in section II.1.1. The **Figure II.4b** depicts the principle of operation of a metallic spin valve, with the equivalent circuit of the two situations. In the parallel case, when both electrode magnetizations are pointing in the same direction, majority spins experience much fewer scattering events than minority spins in both electrodes. Therefore, the low resistance ( $2r$ ) majority channel shortcuts the high resistance ( $2R$ ) minority one and the resistance is:

$$R_P = \frac{2Rr}{R+r} \quad (II.5)$$

When electrodes polarization is opposite, both up and down spins suffer a lot of scattering in one of the electrodes. Therefore, both channels have the same resistance  $R+r$  and the total resistance in this configuration is:

$$R_{AP} = \frac{R+r}{2} > R_P \quad (II.6)$$

The (G)MR, defined as

$$MR = \frac{R_{AP} - R_P}{R_P} \quad (II.7)$$

is a positive relative value that can reach several tens of percents. Varying the amplitude of the magnetic field, the resistance of the device looks like a rectangular function (**Figure II.4c**). The width of the “gate” function is the difference between the coercive field of FM1 and FM2 as the anti-parallel states remains only between  $|H_{c1}|$  and  $|H_{c2}|$ . The shifting of the high resistance states to the positive or negative side arises because of the hysteresis of the magnetization of magnetic materials.

### Tunnelling magnetoresistance

When the NM spacer of the FM/NM/FM structure is an insulator, spins are tunnelling across it. In this case, the spin-dependent properties of magnetic tunnel junctions originate from the conservation of the spin within the tunnelling process as proposed by Jullière’s model<sup>13</sup>.

The DOS of up and down spins of FM material is asymmetric as explained in section II.1.1. When electrode magnetizations are parallel, the DOSs of both electrodes are similar (**Figure II.5**).

Hence, the number of available states at the Fermi level for each spin is roughly the same in the two electrodes, letting the tunnelling probability relatively unchanged.

In the anti-parallel case, DOSs are different. The detection electrode spin-dependent shifting of the DOS is opposite to the injection electrode one. Using the left electrode as reference, the up-spins DOS is shifted up and the down-spins DOS is shifted down in energy. In consequence, the number of states at the Fermi level is different, as depicted in the bottom of **Figure II.5**. The up-spins from the injector have a large amount of available states in the arrival electrode, but the little amount of up-spin carriers contributes only slightly to the current. However, the large number of down-spins from the left electrodes encounters only a limited number of available sites. Thus, their tunnelling probability is significantly lowered and the resistance in the anti-parallel configuration is higher than in the parallel state.

The TMR signal uses the same definition of the MR and exhibits a similar variation of the resistance upon an external magnetic field than the GMR. However, the process of spin transport is fundamentally different. Note also that the spin-polarization is inverted as the minority spins cross easier the tunnel barrier because they have more available arrival states in the anti-parallel configuration.

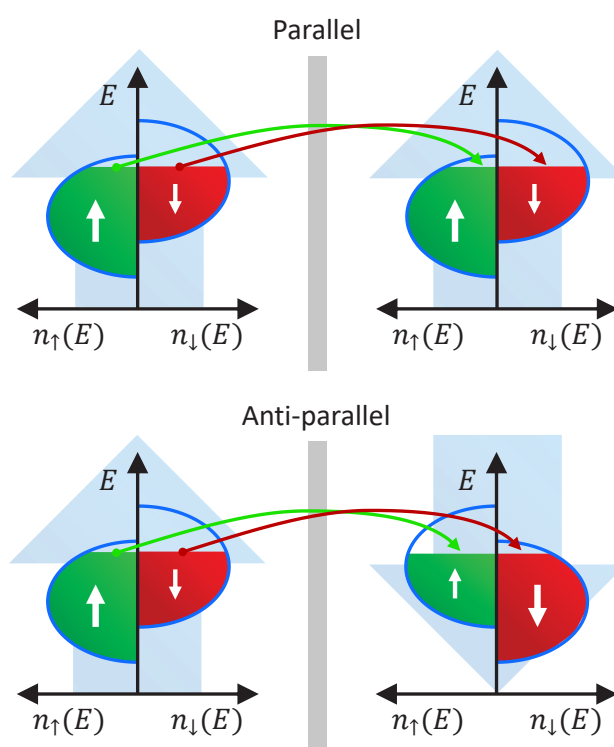


**Figure II.5** Tunnelling process in the parallel (top) and anti-parallel configuration (bottom). The inversed shifting of the DOS in the right panel of the anti-parallel case involves a poor matching of densities of states at the Fermi level of both electrodes.

To give orders of magnitude, Fert and Grünberg measured a GMR around 80 % at 4 K. Presently, MR as high as several hundred percent at room temperature were reported<sup>14,15</sup> with a record 604 % for TMR<sup>16</sup>.

For all spintronics applications, the spin polarization is mandatory. Unfortunately, while the polarization of the bulk is known and appropriate for devices, the surface of magnetic materials is a big issue to overcome. Oxidation of the surface, mainly for 3d-materials, strongly limits the spin injection across interfaces. Sub-nanometer thick oxide layer is already enough to almost extinguish the polarization for tunnelling. The ease of oxidation relates directly to the electronic structure of transition metals and their unpaired electrons. The oxygen being highly reactive, it forms quickly bonds with these lonely electrons and turns the materials into paramagnetic.

To overcome this obstacle, new magnetic materials arise, led by the perovskite LSMO ( $\text{La}_{1-x}\text{Sr}_x\text{MnO}_3$ ,  $x$  is often 0,33) more stable in the air, as it is an oxide. Surface spin polarization of the DOS reaches 95 % in LSMO at low temperature but decreases rapidly when approaching room temperature with a Curie temperature around 320 – 350 K ( $\sim 50 - 80^\circ\text{C}$ ). Consequently, industrial-scale applications are compromised. It is also important to mention that the surface spin polarization is anyway different from the bulk one as atoms reorganized themselves to minimize energy changing the “crystallinity” of the last (few) layer(s), and there is compelling evidence that the surface polarization is quite low. In addition, the surface of LSMO is not that stable and possibly very different of the bulk, impacting significantly the magnetic properties<sup>17</sup>.

Another possibility is to cover the FM electrodes to protect it from the environment. This is of primary concern if the ultra-high vacuum environment (UHV), necessary to prevent oxidation, cannot be maintained when building the device, as is expected for most organic electronics studies, where UHV fabrication studies remain scarce. Coating of organic layers<sup>18,19</sup>, polymers<sup>20,21</sup>, inert metals<sup>22</sup> and SAMs<sup>23,24</sup> have been reported. However, all these methods affect the underlying FM electrode by changing its optical response, electric and thermal conductivities, dimensions and magnetic qualities. Another approach was to grow graphene on top of electrode and is a promising way to keep high quality FM electrodes<sup>25,26</sup>. Finally, a chemical treatment of FM materials with glycolic acid etches the oxide layer<sup>27</sup> (at least the cobalt oxide) and may be an easier way to recover ferromagnetic properties for the following step of the device process when wet chemistry processing is involved.

However, even with well-controlled surfaces, the interface of FM electrodes with other materials is complex and the spin polarization may vary a lot. It is even more true when organic materials are used as they are able to react with the FM electrodes through their  $\pi$ -electrons cloud.

### II.1.3. Spin injection

Key features of spin-valves are the maximisation of the difference between  $R$  and  $r$  through higher spin polarization, and the avoidance of spin memory loss between the magnetic injector and detector electrodes. Looking for GMR, electrons must travel through the FM/NM interface keeping their spin. Indeed, in order to detect a spin-signal, the spin polarization from the FM material needs to remain in the NM until detection. The following spin injection discussion, valid for conductive spacers, relates to a diffusive model of transport based on the Boltzmann equation, know to explain well past experiments.

The two-currents model of Mott involves the spin-dependent resistivities  $\rho_{\uparrow}$  and  $\rho_{\downarrow}$ . It means that there are somehow slow and fast carriers. Therefore, the current density divided also in  $j_{\uparrow}$  and  $j_{\downarrow}$  that defines a current spin polarization as:

$$P = \frac{j_{\uparrow} - j_{\downarrow}}{j_{\uparrow} + j_{\downarrow}} \quad (\text{II.8})$$

NM materials have no spin polarization, that is, spin-up current density ( $j_{\uparrow}$ ) is equivalent to spin-down current ( $j_{\downarrow}$ ) as well as their conductivities (**Figure II.6a**). The  $j_{\uparrow}$  versus  $j_{\downarrow}$  asymmetry in the FM electrode must then transfer into degenerate current densities  $j_{\uparrow} = j_{\downarrow}$  in the NM spacer bulk, away from the interface<sup>28</sup>. For that purpose, spin accumulation takes place around the contact between both materials that splits the chemical potential ( $\mu$ ) of up and down spins ( $\Delta\mu = \mu_{\uparrow} - \mu_{\downarrow}$ ) as shown in **Figure II.6b**. The accumulation area spreads by diffusion on both side of the interface and decreases exponentially away from it with a characteristic length that is the spin diffusion length ( $l_{sf}$ ), *i.e.* the average distance travelled by electrons before their spin flip. That spreading is responsible for the spin injection. It relies on the steady state formed by the incoming/outcoming electrons and the spin flip events, and a spin-polarization appears in the NM material over the distance  $l_{sf}^{NM}$ . Therefore, one of the key parameters to detect spins is the ratio between the channel length ( $L$ ) and  $l_{sf}^{NM}$ , as the spin polarization vanishes exponentially over the length scale  $l_{sf}$ .

Another point to emphasize is the spin-flip rates ( $\Gamma$ ) at the interface. They behave as:

$$\Gamma^{FM,NM} = \frac{1}{\tau_{sf}^{FM,NM}} \propto \frac{\Delta\mu}{r^{FM,NM}} \quad (\text{II.9})$$

where  $\tau_{sf}$  the spin diffusion time and  $r^{FM,NM} = \rho^{FM,NM} l_{sf}^{FM,NM}$  is the spin impedance respectively for the FM and NM materials and  $\rho^{FM,NM}$  is their resistivity. This equation clearly shows that spin-flipping is more favourable in low resistive material such as metal compared to higher resistive materials as semiconductors. Furthermore, the current spin polarization at the interface is:

$$P_{int.} = \frac{j_{\uparrow} - j_{\downarrow}}{j_{\uparrow} + j_{\downarrow}} = \frac{\beta}{1 + \frac{r^{NM}}{r^{FM}}} \quad (\text{II.10})$$

where  $\beta$  is the bulk asymmetry coefficient. Then, in the case of metal/metal interface and  $r^{NM} \sim r^{FM}$ , the spin polarization is only slightly reduced and the spin flipping occurs on both side with the same probability. On the other hand, if the NM material is a semiconductor,  $r^{NM} \gg r^{FM}$  and the polarization drops dramatically near the interface because there will be much more spin-flips in the FM material and the current will already be unpolarized at the interface (**Figure II.6c**). Indeed, the spin accumulation relaxes by diffusion in all directions, that is however much more favourable in low resistivity materials. The later depolarization mechanism is one of the

main obstacles for the efficient spin injection from an FM metal to an NM semiconductor and refers as conductivity mismatch.

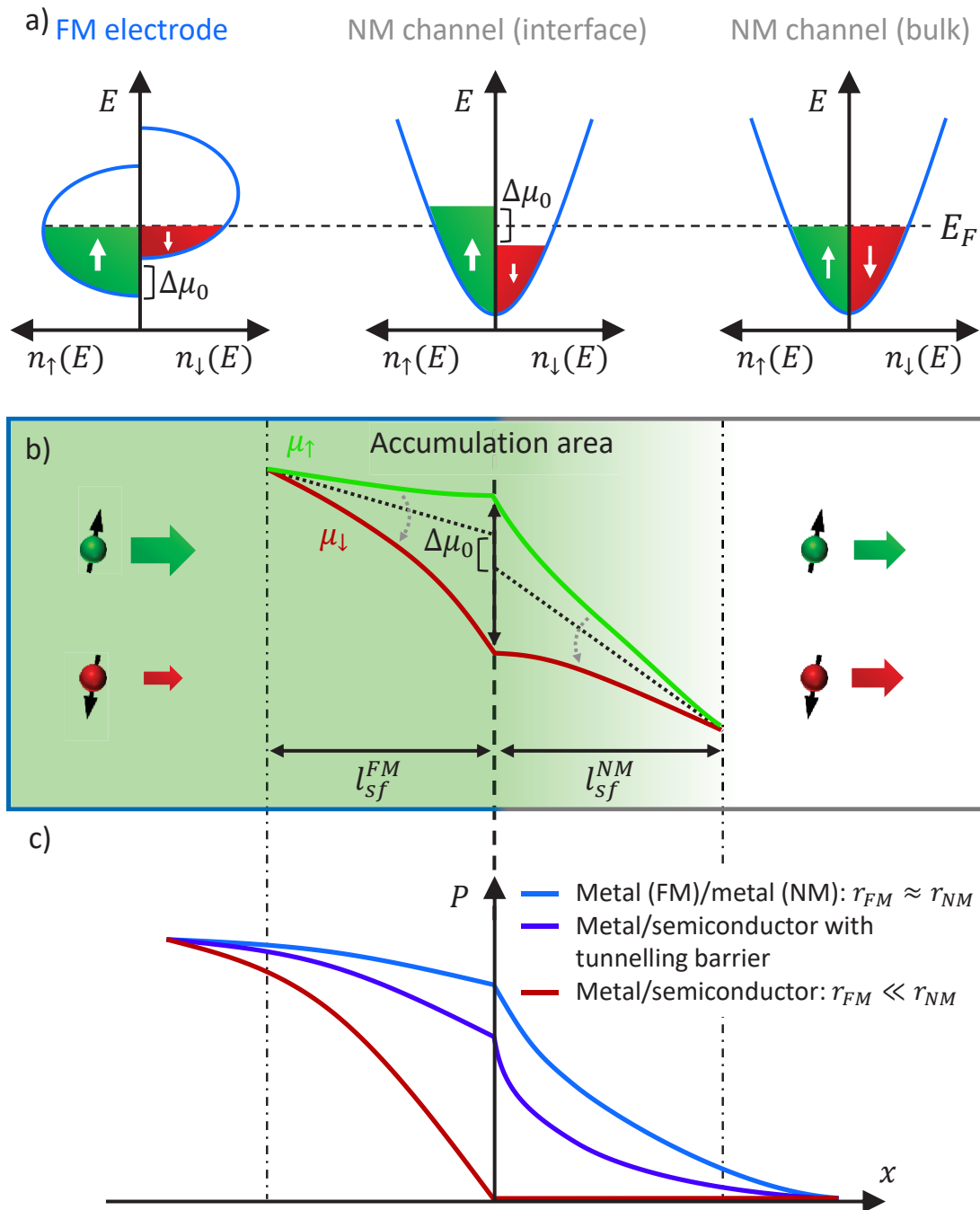


**Figure II.6** a) DOS of each spin for FM material (left) and NM material at the interface (centre) and in its bulk (right). The splitting of up and down spins remains at the interface and vanishes away. b) Chemical potential for both spins in the FM material (left) and in the NM material (right) when no interface resistance is taken into account. The dotted line represents the asymptotic line joined by  $\mu_{\uparrow,\downarrow}$  far from the interface. The grey arrows represent the spin-flipping from the majority to the minority spin channel. The background shows the spin polarization: the greener, the higher the polarization. c) Spin polarization at the interface between FM material and either a NM metal, or a NM semiconductor with and without a tunnelling barrier.

Schmidt *et al.* was the first to find a solution: use an FM semiconductor making possible  $r^{NM} \sim r^{FM}$ <sup>29</sup>. However, these materials have low Curie temperature, much below the room temperature, making applications difficult. The second idea was proposed by Rashba<sup>30</sup> and Fert & Jaffrès<sup>31</sup>. They suggested to add a spin-dependent contact resistance, written  $r_b^*$ , separating the FM and the NM semiconductor. Achieving significantly large  $r_b^*$  translates into the addition of a tunnel barrier (aluminium oxide layer or controlled oxidation of the FM for example). The definition of  $r_b^*$  relies on a new parameter  $\gamma$ , which is the interface spin asymmetry coefficient (in contrast to  $\beta$ , the bulk spin asymmetry coefficient), such as:

$$r_b^* = \frac{r_b}{1 - \gamma^2} \quad (\text{II.11})$$

where  $r_b$  is the interface resistance multiplied by the injection area, or specific interface resistivity. The spin resistivity of the FM injector is now replaced by the metallic one of the electrode (small) in series with the one of the barrier. The latter can be made comparable to the spin resistivity of the NM, and therefore balances the spin current transferred into the NM with the one diffusing back into the FM electrode. The depolarization takes then place also in the semiconductor side and a spin-polarized region exists in the NM material (**Figure II.7**).

From the later discussion, it comes out the condition:

$$r_b^* \geq r^{NM} = \rho^{NM} l_{sf}^{NM} \quad (\text{II.12})$$

in order to ensure that the spin-dependent interface resistance is dominant and increases  $\Delta\mu^{NM}$  significantly. In the limit  $r_b^* \gg r^{NM}$ , the full interface spin polarization of the FM material may be recovered in the NM side ( $P_{int.} = \gamma$ ) and half of it is expected for  $r_b^* = r^{NM}$ , but the total resistance may become too high. More generally, the spin polarization including the tunnelling barrier is:

$$P = \frac{j_{\uparrow} - j_{\downarrow}}{j_{\uparrow} + j_{\downarrow}} = \frac{\beta r^{FM} + \gamma r_b^*}{r^{FM} + r^{NM} + r_b^*} \quad (\text{II.13})$$

The tunnel barrier is a clever and quite easy way to improve spin injection in NM materials. However, these magnetic moments should be detected in the other electrode, that plays the role of analyser, and needs to be included in the model.

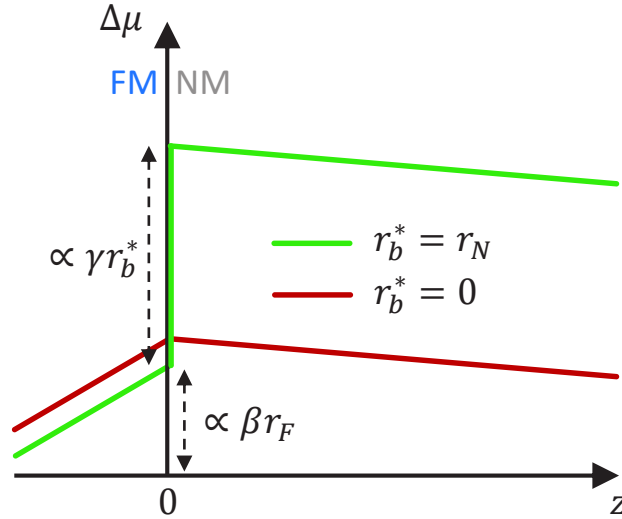


**Figure II.7** Variation of  $\Delta\mu$  across an FM/NM interface with ( $r_b^* = r_N$ ) and without ( $r_b^* = 0$ ) interface resistance. The discontinuous rise of  $\Delta\mu$  when  $r_b^* = r_N$  span over several orders of magnitude ( $\sim 10^6$  in the example of Fert & Jaffrès). Adapted from Fert & Jaffrès.

### II.1.4. Spin detection

In spin-valves, once the spins are injected, they encounter a second interface with the other FM electrode being the detector. Therefore, the successful spin injection is not enough to measure a spin-valve signal, as the spin polarization has to remain until entering the second electrode.

The first condition to detect spins, pointing out directly from the injection discussion, relies on the channel length ( $L$ ). The spin polarization spreads in the NM material over  $l_{sf}^{NM}$ , hence the channel length must be shorter (ideally much shorter) in order to keep the spin polarization until the detection electrode:  $L \leq l_{sf}^{NM}$ . Fert & Jaffrès<sup>31</sup> showed the importance of the ratio  $L/l_{sf}^{NM}$  on the MR amplitude (**Figure II.8**). Basically, it drops as  $\exp(-L/l_{sf}^{NM})$ , i.e.  $l_{sf}^{NM}$  must be longer or at least equal to the channel length to have significant MR signal. Even when  $L = l_{sf}^{NM}$ , the amplitude is already 4 times lower compared to the situation where  $L \ll l_{sf}^{NM}$ , and the MR is diminished by a factor 20 when  $L = 3l_{sf}^{NM}$ . The maximum of MR is only dependent on  $\gamma$  and is reachable for  $L \ll l_{sf}^{NM}$  and  $r_b^* \sim r^{NM}$ :

$$MR_{max} = \left. \frac{\Delta R}{R_P} \right|_{max} = \frac{\gamma^2}{1 - \gamma^2} \quad (\text{II.14})$$

In addition, having two interfaces restrict the efficient contact resistance. Indeed, from the calculation of Fert & Jaffrès on FM/NM/FM configuration, the MR signal exhibits a peak around  $r_b^*/r_N \approx 1$  and decreases for higher and lower values. The rough condition they extracted is:

$$\rho^{NM} L = r^{NM} \frac{L}{l_{sf}^{NM}} = r_1 \ll r_b^* \ll r_2 = r^{NM} \frac{l_{sf}^{NM}}{L} = \rho^{NM} \frac{(l_{sf}^{NM})^2}{L} \quad (\text{II.15})$$

The lower limit  $r_1$  is related to the one mentioned in the previous section (equation II.12), with  $L$  replacing  $l_{sf}^{NM}$  as  $L \leq l_{sf}^{NM}$  is supposed.  $r_1$  is then smaller in this case, giving more freedom to the interface resistance. The second FM electrode helps in this regard as it involved also a spin polarization near its interface with the NM material. Here again, if  $r_b^* < r_1$ ,  $\Delta\mu^{NM}$  is not large enough to drive the depolarization into the semiconductor and no spin polarized current is injected.

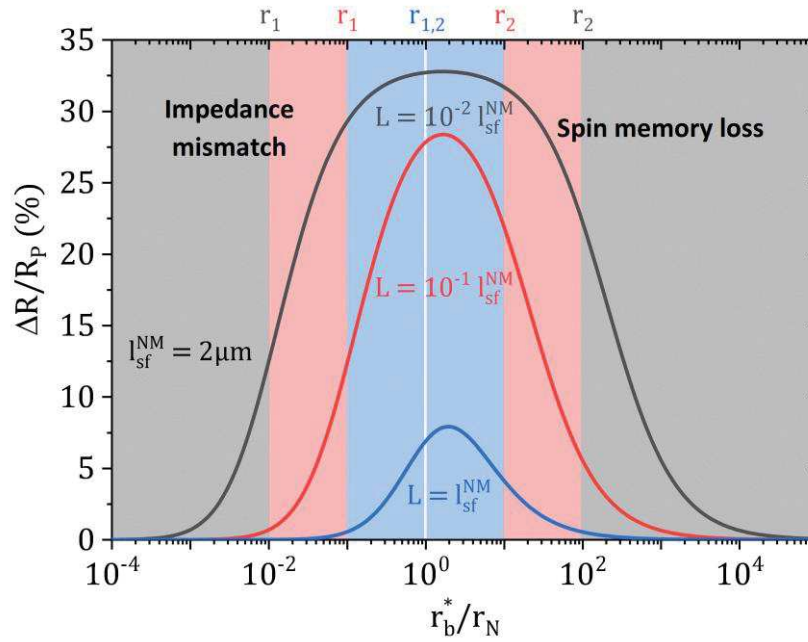


**Figure II.8** Magnetoresistance versus the ratio  $r_b^*/r_N$  from Fert and Jaffrès equations<sup>31</sup> for an FM/NM/FM structure with different channel lengths, scaling with the spin diffusion length. The MR amplitude strongly decreases when  $L$  approaches  $l_{sf}^{NM}$ . The background colours show the impedance mismatch and the spin memory loss regions for each  $L$  (superimposed), with the efficient spin injection and detection between their respective  $r_1$  and  $r_2$ . The white line in the middle represents the limit of Fert and Jaffrès' conditions when  $L = l_{sf}^{NM} \Rightarrow r_1 = r_2$ . Adapted from Fert & Jaffrès<sup>31</sup>.

The upper limit  $r_2$  is the new condition from the addition of the detection electrode. In the situation where spins are successfully injected and transported, they faced the second interface. If the interface resistance is too high, spin carriers backflow into the NM material and the dwell time would be longer than the spin diffusion time, losing the polarization as it was the case for the injection. Therefore, the condition  $r_b^* < r_2$  is needed to detect properly the spin information.

The spin diffusion length is the key for new spintronic applications. The largest  $l_{sf}^{NM}$ , the highest the MR signal and the largest the efficient window of contact resistance. Large  $l_{sf}^{NM}$  relates to a large spin memory time, easing the condition of “short-enough” dwell time

between injection and detection. For this reason, the scientific community began to study OSCs as new type of spacer. It was motivated by the significantly longer spin memory time in organic materials compare to inorganic ones, but their structures, far from the well-ordered inorganic compounds, lead to other issues.

## II.2. Organic materials for spin electronics

The latter section gives the background of spintronics and remains valid when the spacer becomes organic. However, the hopping transport, deeply different from band transport of metals, changes drastically the spin injection and transport in these materials. The relevance of a diffusive model is questionable as transport occurs from tunnelling from site to site, but it provides a proper guideline, especially if we manage the OSC to be diffusive-like.

The long spin diffusion time make organic materials excellent candidates for spintronic applications, but their disordered structure limits their spin diffusion length. The race to the highest mobility helps, but it is still not enough to detect unambiguously spins in organic spin-valves. Indeed, the main limiting factor is the too high contact resistance that hamper injection and detection as discussed in last section.

The interface of organic compounds with metals is also more complicated. The presence of organic molecules may affect strongly the spin polarization of the FM electrode interface and may even reverse it<sup>32</sup>.

### II.2.1. Relevance of organic materials and their drawbacks

In the scope of organic spintronics, the main asset of organic materials is the particularly long spin memory time ( $\tau_s$ ), *i.e.* the average time electrons keep their spin before flipping.  $\tau_s$  between  $10^{-6}$  and  $10^{-3}$  s is reported<sup>33,34</sup>, that is several orders of magnitude larger than inorganic materials one, generally of the order of the nanosecond. This huge difference between organic and inorganic materials comes from spin-orbit coupling (SOC) and hyperfine interaction (HFI), which are the two main spin relaxation processes, that are much weaker in organic compounds.

SOC results from the interaction of the orbital magnetic moment with the spin moment of electrons. Indeed, in the point of view of the electron, it is the nucleus that turns around it which creates a coupling. The strength of the SOC is highly dependent on the atomic number ( $Z$ ) since it is proportional to  $Z^4$ <sup>35</sup>. Looking to the composition of materials used in spintronics, it is straightforward to note that organic SOC is much weaker from their majority of carbon atom ( $Z(C) = 6$ ) in contrast with inorganic case where heavier atoms are consider ( $Z(Si) = 14$  or  $Z(Cu) = 29$ ). Taking the example of carbon and silicon the SOC is already  $\sim 30$  times stronger for the second one.

Elliot & Yafet<sup>36,37</sup> and D'yakonov & Perel<sup>38</sup> investigated spin relaxation mechanisms from SOC and two models arose named after them: the Elliot-Yafet (EY) and the D'yakonov-Perel (DP) theories. EY model is based on a weak connection between up and down spins. The SOC gives a

down (up) component to up- (down-) states. When the carrier meets a scattering centre (impurities, phonons...) it has a finite probability to switch spin because of the additional opposite spin component. DP model relies on the splitting of up and down bands because of SOC in materials without inversion symmetry (typically materials where there is two distinct atoms in the Bravais lattice). It acts on spins as if there was a random internal magnetic field, what make them flip randomly quite efficiently especially at higher temperatures because the spin bands splitting becomes weak compared to the thermal energy.

The HFI is the interaction of the electron spin with the magnetic moment of surrounding nucleus. In organic materials, carbon nuclei ( $^{12}\text{C}$ ) are not participating to the HFI, as they don't have any magnetic moment. It remains mainly hydrogen atoms creating HFI from their  $1/2$  nuclear spin. It acts on spin carrier like a local and randomly oriented magnetic field of the order of  $10^{-2} - 10^{-3}$  T that cause depolarization.

HFI in organic materials is low not only because carbon nuclear spin is 0, the large number of hydrogen atoms would not lead to such small HFI. It is also due to the  $\pi$ -hybridation of molecular orbitals. As electrons lay generally in  $p_z$ -orbital, they don't overlap the nucleus as  $p_z$ -wavefunction amplitude vanishes in the molecular plane<sup>39</sup>. However, even if HFI is small compare to inorganic materials, Nguyen *et al.* showed that it remains an important depolarization process in organic devices by observing higher MR signal by changing  $^1\text{H}$  into  $^2\text{H}$  atoms having lower HFI<sup>40</sup>.

HFI is also responsible for the organic magnetoresistance (OMAR), which is also a variation of resistance upon application of external magnetic field. It occurs at rather small applied field (in the range of millitesla, in order to overcome the HFI), which makes it easy to differentiate form other types of MR. The OMAR amplitude reaches 10 – 20 % and is highly interesting for applications due to the low magnetic field involved<sup>41</sup>.

The long  $\tau_s$  originating from the latter low magnitude mechanisms is the main advantages of organic materials for spintronics. However, the relevant quantity is the spin diffusion length  $l_{sf}^{NM}$  introduced in the general spintronic section. It writes as:

$$l_{sf}^{NM} = \sqrt{D\tau_s} = \sqrt{\frac{\mu k_B T}{e} \tau_s} \quad (\text{II.16})$$

*i.e.* the length over which the spin is kept is directly related to the mobility of carrier. In the latter equation,  $D$  is the Einstein diffusion coefficient assume to hold true in disordered semiconductors<sup>42</sup>. Therefore, even with very long  $\tau_s$ ,  $l_{sf}^{NM}$  is short because of the poor mobility of OSCs from hopping transport. Typical values around 60 nm are reported these last years<sup>43–47</sup>, to compare with spin diffusion length exceeding 1  $\mu\text{m}$  in gallium-arsenide<sup>48</sup>, germanium<sup>49</sup> or silicon<sup>50</sup>, and tens of micrometres in graphene<sup>51,52</sup>. The spin injection is also more difficult in organic devices as the charge injection into OSCs is a multiple hopping process that makes the spin flipping probability increase.

The choice of material, already important for electronic devices, is crucial for spintronic applications. To hope for spin-valve signal, high conductivity OSCs are excellent candidates, as

they should exhibit longer spin diffusion length and low contact resistance with the appropriate metal and the suitable geometry.

## II.2.2. Organic spin-valves

The geometry of organic spin-valves (OSVs) is the same than the inorganic spin-valve one discussed in section II.1.2. The only difference is the organic nature of the spacer, either small molecules or polymers.

The first spin-based organic device dates from 2002 after the work of Dediu *et al.*<sup>53</sup>. They fabricated a lateral OSV with LSMO electrodes and sexithiophene (6T), a  $\pi$ -conjugated oligomer, as channel (**Figure II.9a**). They managed to measure a MR between 30 and 7 % for channel lengths in the range 70 – 200 nm at room temperature, the MR decreasing with the distance between FM electrodes (**Figure II.9b**). For longer channel, no MR was observed, eliminating the possible interface origin of the signal. They gave also a rough estimation of  $l_{sf}^{NM}$ , expected to be about 200 nm and deduced also  $\tau_s \sim 10^{-6}$  s. However, both electrodes had the same geometry and thus the same coercive field, hampering to have the parallel and anti-parallel configurations. Despite this, they assigned the MR to spin transport in the organic spacer, but a more direct proof was required.

Two years later, Xiong *et al.* published their results on the first real OSV with electrodes having different coercive field<sup>43</sup>. They used a vertical geometry, with LSMO as bottom FM electrodes over which they evaporated a small  $\pi$ -conjugated molecule: 8-hydroxy-quinoline aluminium (Alq<sub>3</sub>, thickness above 100 nm). The top FM electrode was made of few nanometers cobalt (in contact with the Alq<sub>3</sub>) covered with aluminium (**Figure II.9c**). Their structure allowed to reach almost 40 % of MR with a clear spin-valve-like signal at 11 K (**Figure II.9d**), and vanishing above 200 K and for channel longer than 240 nm. However, some questions arose from this paper. First, the MR is negative, *i.e.* the resistance in the parallel case is higher than in the anti-parallel case, which is unexpected. A negative spin polarization, because of higher minority spin density of states at the Fermi level, was expected in cobalt and claimed to be the reason of the inversion<sup>54</sup>. Furthermore, it is quite astonishing to have such high MR while the extracted spin diffusion length is not even halfway to the channel length ( $l_{sf}^{NM} = 45$  nm).

### Vertical OSVs

One has to be careful about the structure of the samples. The vertical geometry chosen by Xiong and his co-worker is useful to have sub-micrometer channels, essential to measure a spin signal as  $l_{sf}^{NM} < 1$   $\mu$ m. However, the evaporation of metal on top of organic material is often detrimental: metal atoms may penetrate and diffuse into the OSC<sup>55</sup> and even react with it, radiation may damage the OSC<sup>56</sup> or magnetic inclusions may occur<sup>57</sup>. In all cases, the interface between the top FM electrode and the organic layer is poorly defined.

The worst case is the “ill-defined” layers where high energy metal atoms protrude into the OSC until they reach the bottom electrode and create a bridge (**Figure II.10e**) or a reduction of the layer thickness (**Figure II.10c**). It was actually already proposed by Xiong *et al.* in their paper<sup>43</sup>. The idea is to model the channel as two sub-layers: one “ill-defined” containing pinholes

and cobalt inclusions up to 100 nm deep, and one “clean” organic layer. It ended to poorly defined organic channel, with hot points where current flows. The channel may be simply shortened, but short-cuts with charge transfer occurring without transit through the organic spacer is possible.

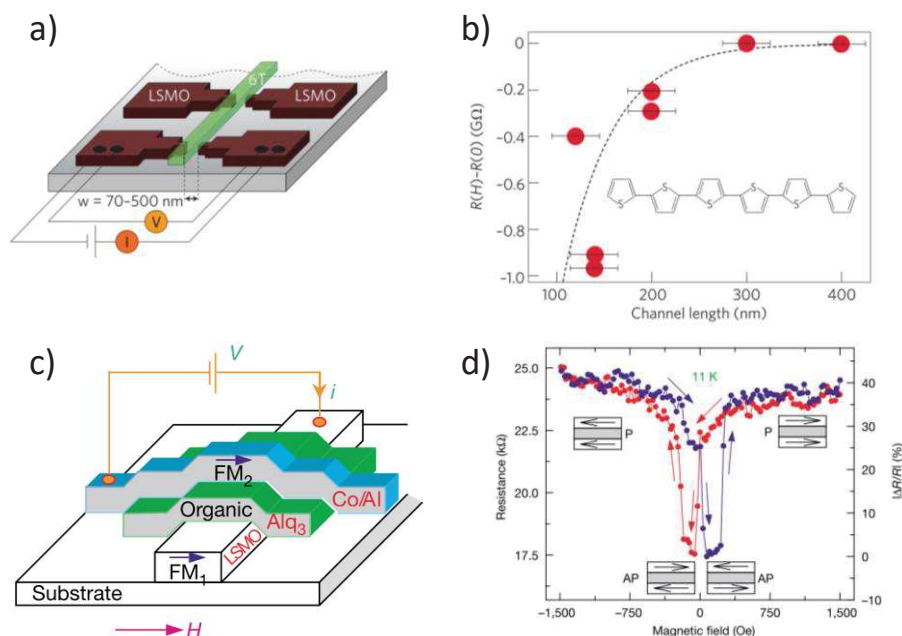


**Figure II.9** a-b) Schematic of the lateral LSMO/6T/LSMO device (a) and its MR response for different channel lengths at room temperature (b) from the work of Dediu *et al.*<sup>53</sup>. c-d) Structure of the vertical LSMO/Alq<sub>3</sub>/Co device (c) and its MR response passing from parallel to anti-parallel state at 11 K (d). Adapted from Xiong *et al.*<sup>43</sup>.

Precisely, Galbiati *et al.* showed that small cross-section short-cuts, not involving organic species, mimic oddly the MR from spin transport through organic materials<sup>58</sup>. They proceeded to a rigorous comparison of three samples: one whole inorganic reference sample (Co/Al<sub>2</sub>O<sub>3</sub>/Co) and two organic magnetic junctions (Co/Al<sub>2</sub>O<sub>3</sub>/Alq<sub>3</sub>/Co), samples 1 and 2 (Figure II.10a, c and e). As first statement, they pointed out that their MRs – from 8 to 20 % – and their resistances – of the order of 10<sup>7</sup> – 10<sup>8</sup> Ω – are similar (Figure II.10b, d and f). In principle, a MR signal is the proof of spin polarized current into the organic channel, and such high resistance eliminate the possibility of short-cuts. However, using inelastic electron tunnelling spectroscopy (IETS), they were able to demonstrate that the current was not flowing within the organic channel in one of their two organic devices. IETS reveals molecular vibrations from the second derivative of the current ( $d^2I/dV^2$ ) via lock-in measurements. Peaks in the latter signal are labelled according to infrared and Raman spectra and are a fingerprint of inelastic tunnelling through the Alq<sub>3</sub> layer. Looking at IETS signal, it was clearly shown that the sample 2 spectrum is almost flat and corresponds well to the reference sample with no signature of Alq<sub>3</sub> vibrations (Figure II.10g). On the contrary, sample 1 presents the typical peaks assigned to Alq<sub>3</sub>, meaning that some of the current is indeed flowing through the organic channel. The essential conclusion of this article is that well-defined and short-circuited samples are hardly distinguishable with only their

magnetic response. Moreover, small cross-section short-cuts keep the devices resistance very high usually ascribed as working device, but where the transport is purely inorganic.

The vertical geometry relies also in general to ultra-high vacuum (UHV) deposition of OSCs that has the advantage of purity of the ferromagnetic layer, but however limits the number of available materials. Indeed, part of OSCs cannot handle the high temperature needed for evaporation. Moreover, the size of OSC molecules leads often to rough surface. Thus the metal deposition on top of organic films forms inevitably rough interface, very detrimental for interface magnetic properties governing the spin injection<sup>57</sup>.

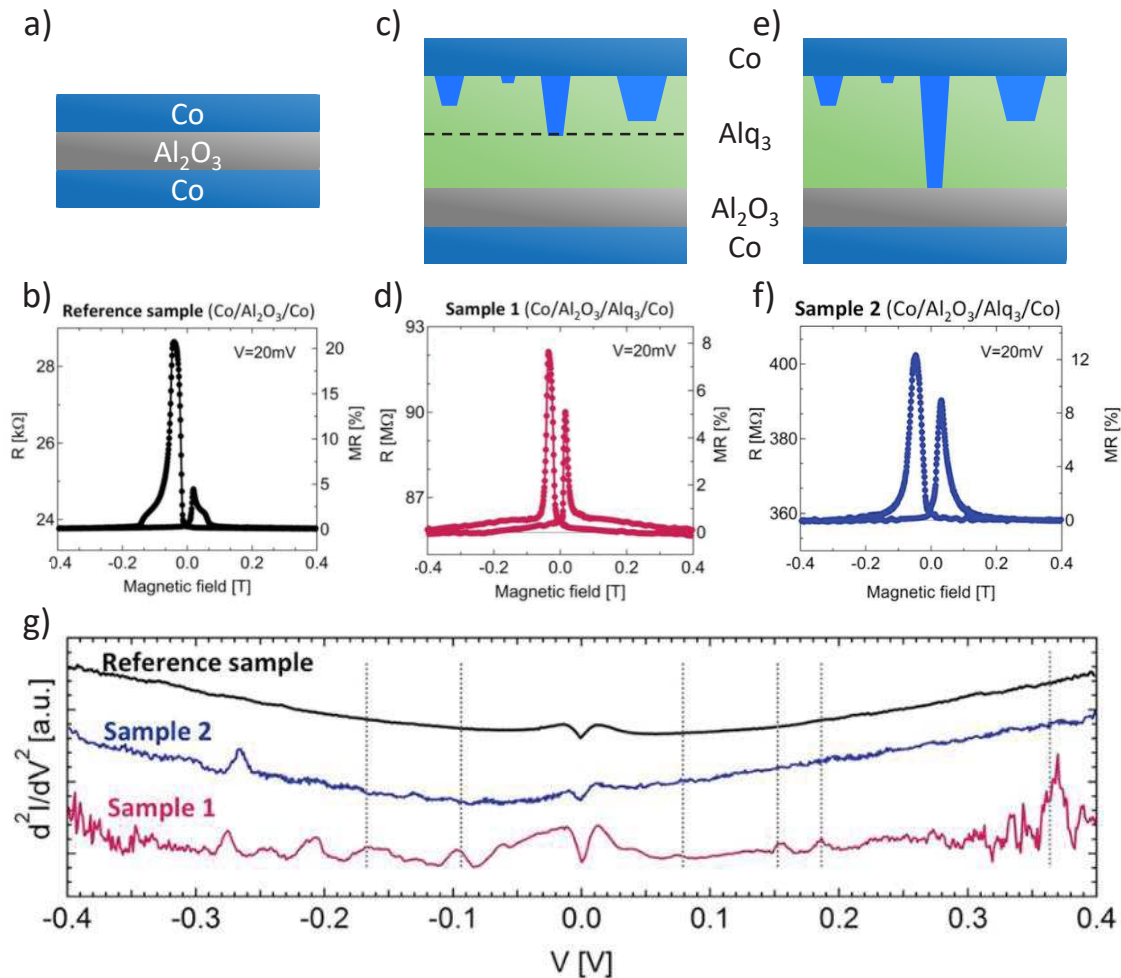


Figure II.10 Device schematics and corresponding MRs of reference sample (a-b), sample 1 (c-d) and sample 2 (e-f). There is no organic channel in the reference sample, while the cobalt deposition protrudes half of the  $\text{Alq}_3$  layer in sample 1 and spans the entire thickness in sample 2 (respectively a, c and e). No significant differences are visible on the MR measurements (b, d, and f). IETS however points out the vibrational levels of  $\text{Alq}_3$  when the current is flowing through it (g). The characteristic peaks of  $\text{Alq}_3$  appear only in sample 1, meaning that the similar MR signal of sample 2 is coming from an all-inorganic channel.

For all the outlined reasons, the reliability of claimed spin transport through an organic channel in vertical geometry is still debated and more robust proofs are needed<sup>59–62</sup>.

## Lateral OSVs

One way to avoid the latter interface issues is to study lateral devices, where injection and detection electrodes are patterned on a substrate, and the OSC is deposited afterwards. In this case, the difficulty is mainly to fabricate such structure with a spacing between electrodes short enough to obey to  $L \leq l_{sf}^{NM}$ . Spacing from hundreds of nanometers down to tens of nanometers were achieved with different techniques such as e-beam lithography, angle deposition or etching<sup>63–66</sup>.

In lateral geometry, the device parameters like channel length or roughness of electrodes are more easily controlled and/or probed. There is also no real limitation on the material choice as the deposition method of OSCs can occur by evaporating, spin-coating, drop-casting or printing on electrodes, which is one of the main advantage of OSCs for industrial purposes.

The possibility to interact with external stimuli on the organic channel like light, chemical doping, pressure or transverse electrical field with a third top or bottom electrode is also particularly relevant for fundamental study. Indeed, the mobility and/or conductivity is then tunable and the magnetic response could possibly be optimized. Furthermore, the accessibility to both electrode surfaces before the OSC deposition, allows special treatment as oxide etching, optimization with self-assembled monolayers or simply roughness and cleanliness control.

Concerning the measurement methods, lateral geometry lets the possibility to add extra contacts for 4-probes (nevertheless difficult for sub-micrometre channels) or non-local measurements much more accurate and reliable for fundamental studies. Non-local measurements are particularly relevant in spintronics, as pure spin current (no charge transport) through diffusion from an accumulation area is the best indicator of spin transport and an accurate way to determine the spin diffusion length.

Despite the many advantages of lateral structure, only few experiments have been reported in the literature and the conclusions are often disappointing<sup>67–69</sup> or results difficult to interpret<sup>70</sup>. Non-local measurements were also tried, but the Hanle effect – precession of spins in a rotating magnetic field – was not observed<sup>71</sup> indicating a lack of spin transport. LSMO electrodes seem nevertheless promising but complicate the device fabrication<sup>72,73</sup>.

These failures may come from the carrier nature in OSCs. Indeed, as explained in the first chapter, charge carriers are polarons. In order to increase the mobility, doping process occurs generally in lateral OSVs, either chemical or from transverse electrostatic field. Doing that, the current may be more likely carried by spinless bipolarons, ruining the spin polarization in the OSC. Moreover, if doping implies surely carrier density rise, it may also increase scattering centre density<sup>74</sup>. In the other hand, doping affects also the HFI and possibly enhances spin diffusion<sup>75</sup>.

The variation of the spin diffusion length with dopant concentration is still not clear. It has been shown very recently by Wang *et al.*<sup>76</sup> that high carrier density may be the key for spintronic devices. They based their arguments on the concepts of Yu<sup>77–80</sup> who proposed exchange coupling between localized polarons to be the main mechanism of spin transport in organic materials. In this case, charge and spin transport are decoupled, the latter being more efficient while the carrier density increases as the distance between polarons reduces ( $\propto n^{-3}$ ). Wang and co-worker managed to measure a spin diffusion length above 1  $\mu\text{m}$  in doped pBTTT by injecting pure spin current from ferromagnetic permalloy in an external magnetic field, driven into

ferromagnetic resonance by an applied microwave field. The spin current is then detected by a nearby narrow platinum wire and convert into an electromotive force through the inverse spin Hall effect (ISHE).  $l_{sf}^{NM}$  is deduced from the exponential decay of the ISHE-induced voltage with the length of the channel. This article gives hope to the future of organic spin-valves as  $l_{sf}^{NM}$  seems to scale almost linearly with the conductivity and high spin relaxation length was also achieved in Poly(3-hexylthiophene-2,5-diyl) (P3HT). The plentiful additional measurements ensure also that the flow in the organic channel is pure spin current, and the extracted ISHE-voltage match with the expected behaviour. The advantage of injecting 'pure spin currents' is that the resistance mismatch issue is not a limiting issue. However, these experiments rely on (non-local) voltage measurements and require the absence of charge (drift) currents.

They explained these interestingly long spin diffusion lengths by the exchange-mediated coupling between neighbouring spins. Indeed, they decoupled the diffusion coefficient into a hopping and an exchange term:  $D = D_{hop} + D_{exc}$ . The hopping diffusion ( $D_{hop}$ ) is the classical Einstein coefficient. They exhibit the domination of  $D_{exc}$  at sufficiently high carrier density, roughly  $n > 3 \times 10^{19} \text{ cm}^{-3}$ , often reached in organic electronic materials. They pointed out also a maximal related spin relaxation length ( $l_{sf}^{NM} = \sqrt{D\tau_s}$ ) versus the carrier density followed by a smooth decay for high densities. Therefore, tunable carrier density would be an important parameter for spin transport study.

Their discovery stimulates us in the scope of successful spin transport and detection, following the strategy to make organic channel having higher conductivity in EGOFETs geometry, with a controlled carrier density, reaching possibly larger concentration than in the cited paper. However, FM metal-organic interface remains difficult to grasp. Several articles emphasize how spin-based applications can rely on huge variations of interface spin-polarization of metals in contact with organic molecules, the so-called spinterface<sup>81</sup>.

### II.2.3. Spinterfaces

Spin-dependent charge transfer through interfaces is a key ingredient of the two-channels model of the GMR (section II.1.2). The poor efficiency of spin injection and the changing of MR sign from sample to sample having the same materials was a strong limitation on the road for spin-based organic devices. In 2010, Barraud *et al.*<sup>32</sup> proposed that the spin state of metal-organic interfaces is the main point to explore. They carefully characterized nanoscale magnetic tunnel junctions (MTJs) of LSMO/Alq<sub>3</sub>/Co and suggested presence of spin-hybridization-induced polarized states (SHIPs) at the interface.

The model they build is based on the strength of the coupling between the magnetic metal and the organic molecule. When the metal/organic interaction is weak, the spin-dependent broadening due to hybridization of the organic molecule orbitals with metal ones is negligible (**Figure II.11a**). On the contrary, when the coupling is strong, the energy levels of the molecular states broaden significantly. Under the hypothesis that the broadening may be much more pronounced in one spin channel than in the other, the DOS at the Fermi level is able to be inverted compare to the magnetic metal with  $n_{\downarrow}(E_F)$  becoming larger than  $n_{\uparrow}(E_F)$  (**Figure II.11b**). In this case, the MR signal resulting from a tunnelling-type model would be negative as it is sometimes reported<sup>82,83</sup>. It is also possible that organic spin-DOSs shift when brought into

contact with the FM material in a spin-dependent manner as well (**Figure II.11c**). Therefore, the majority spin-DOS may dominate again at  $E_F$ , if the variation matches, and positive MR would then be recovered, explaining the positive MR also reported in the literature for the same materials<sup>32,83</sup>.

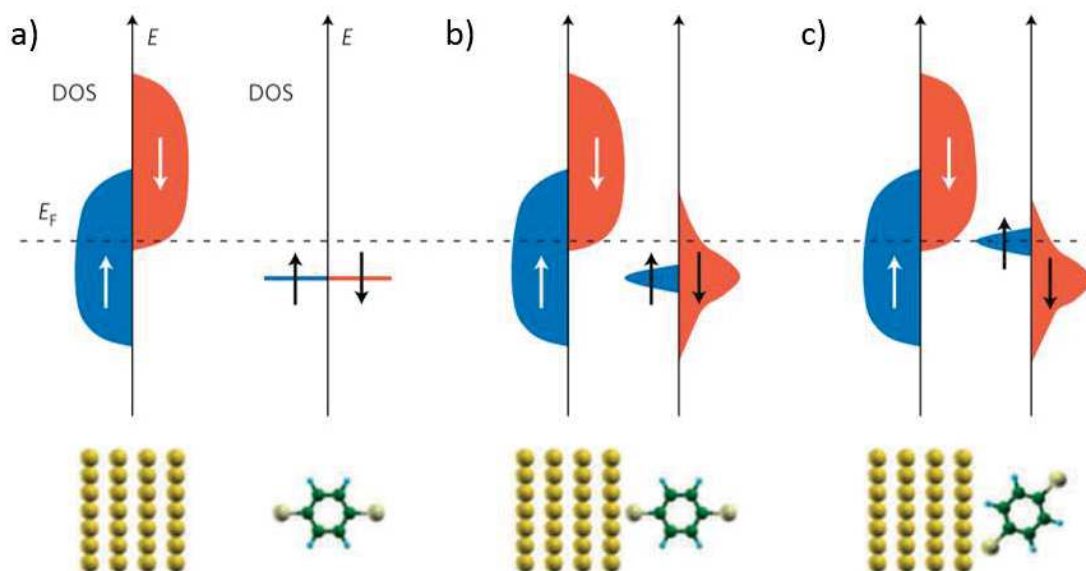


**Figure II.11** Schematic of the energy landscape of an inorganic FM material and an organic molecule. a) Both components are far away and the energy levels are the same than each part isolated. The magnetic metal broad DOS shifts upward for minority spins and downwards for majority ones while the organic molecule has discrete levels (only HOMO shown here). b-c) The molecule and the FM material are brought into contact leading to broadening (b-c) and shifting (c) of the HOMO level of the organic part. Then the spin polarization of the injected current is determined by this new interfacial DOS at  $E_F$  able to reverse the magnetic orientation of the injection electrode, as it is the case in b). Reprinted from Sanvito<sup>81</sup>.

The main difficulty provided by spinterfaces is their non-reproducibility. As the hybridization between organic and inorganic materials enters into account, it will be strongly dependent on the choice of these materials and the particular binding site of the molecule-metal contact. Moreover, even with well described organic/metal coupling, it changes to a certain extent from sample to sample because of different roughness, impurities or geometries. Barraud and colleagues also pointed out that the size of the MTJs matter, as large-scale junctions average out nanoscale effects coming for example from hot point in the spacer.

Despite this additional obstacle for spin injection, spinterface gives ideas for new kind of devices. Cinchetti *et al.*<sup>84</sup> presented the working principle of a device based on an active-controlled molecular interface. They propose to tune the hybridization between the magnetic material and the molecular layer using gating. By changing the number of carriers through it, the coupling varied and the coercive field of the magnetic layer changes. If the latter magnetic electrode is the top electrode of a vertical spin-valve, one would be able to go from parallel to anti-parallel state via the electric field provided by the gate in a magnetic field. Of course, the present state-of-the-art mastery of spinterface is not enough, but it opens the door to new and original hybrid spin-based devices in the future.

## II.2.4. Fringe-field issues in organic spintronics

The notion of fringe-field refers to the magnetic field emanating from a ferromagnet because of its multi-domain structure if the magnetization is perpendicular to the surface, like cobalt films for instance. At the border of two magnetic domains, the magnetic field diverges (**Figure II.12a**) and creates a non-negligible local field within a characteristic length around 50 nm (**Figure II.12b**)<sup>85</sup>. The magnitude of the variation of the residual magnetic field is close to 100 mT at 12 nm away from the surface (**Figure II.12c**) and decreases with the distance as expected.

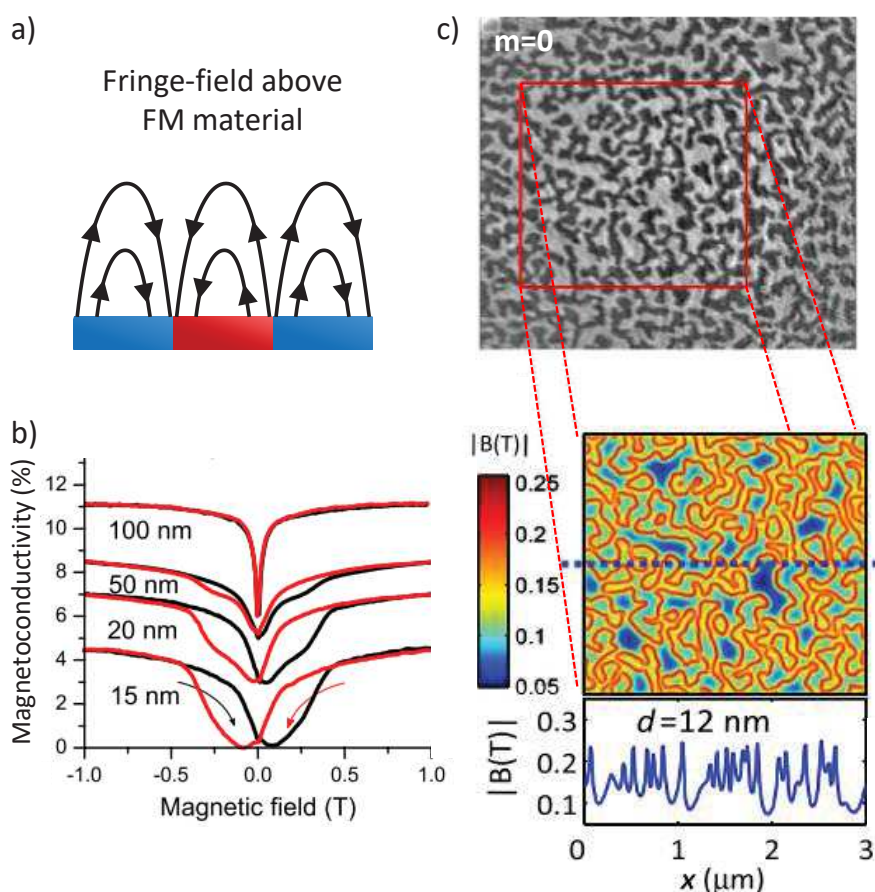


**Figure II.12** a) Illustration of magnetic field lines above different magnetic domains, *i.e.* the fringe-field. b) Dependence of the magnetoconductivity on the thickness of the spacer (PEDOT) between the organic channel ( $\text{Alq}_3$ ) where the current flows and the underlying ferromagnetic electrode presenting the latter fringe-field. The external field is perpendicular to the surface. c) Top: X-ray microscopy image of the surface of the magnetic electrode when the magnetization is zero. Bottom: Calculated Fringe-field on the surface. The variation of magnetic field reaches  $\pm 70$  mT with respect to the mean value. Reprinted from Wang *et al.*<sup>85</sup>.

The team of Michael Flatté dedicated few articles on this topic since organic spintronics comes out because of the possible strong sensitivity of organic materials on magnetic field (OMAR). Indeed, they focused more onto issues for OMAR study, as the local field created by the fringe-field is of the same order of magnitude than the external applied field in this kind of systems. Thus, it is difficult to distinguish the phenomenon at the origin of the magnetic signal. Particularly, they were able to reproduce the MR signal of a semi-spin-valve. They measured the

magnetoconductivity of  $\text{Alq}_3$  on top of a typical fringe-field from cobalt, but without any electrical contact (**Figure II.12b**). The magnetic interaction of the underlying FM layer is the main condition to keep the external field lower than the fringe-field amplitude.

Again, it does not make the study of spin-based organic devices easier, but a proposal was to pattern the domains in order to engineer the magnetic curves<sup>86,87</sup>. The main advantage of such device would be the large magnitude of the magnetic field locally near the interface without any applied field.

The very recent observation of long spin diffusion length in highly doped pBTTT, in a diffusive transport regime, is the indication that the transport within the organic channel may not be the main limiting factor. Instead, the spin injection is an important issue to solve but is still ambiguous and its probing quite delicate. The difficulty to understand it properly may arise from the charge transfer description clearly oversimplified in a single tunnelling event.

The previous two chapters give an idea of the challenges the scientific community had to overcome over the years to understand organic electronics and, more recently, organic spintronics. Even though organic spintronics is more than 15 years old, no consensus exists, and there are no unambiguous indications that an organic spin-valve can be reliably made.

Nowadays, organic electronics reaches industrial-scale applications particularly as OLED devices. However, plenty of outcome remains in the medical sphere for example. Among possibilities belong organic spintronics where the known issues from organic electronics are exacerbated and limits its development. The main difficulty to overcome now is the metal-organic interface overviewed in the second chapter. The following experimental work try to move one step forward in the understanding of such interfaces by temperature, doping and magnetic studies over different transistor scales.

**Bibliography**

- (1) Baibich, M. N.; Broto, J. M.; Fert, A.; Van Dau, F. N.; Petroff, F.; Eitenne, P.; Creuzet, G.; Friederich, A.; Chazelas, J. Giant Magnetoresistance of (001)Fe/(001)Cr Magnetic Superlattices. *Phys. Rev. Lett.* **1988**, *61* (21), 2472–2475.
- (2) Grünberg, P.; Schreiber, R.; Pang, Y.; Brodsky, M.; Sowers, H. Layered Magnetic Structures: Evidence for Antiferromagnetic Coupling. *Phys. Rev. Lett.* **1986**, *57* (19), 2442–2445.
- (3) Thomson, W. On the Electro-Dynamic Qualities of Metals:—Effects of Magnetization on the Electric Conductivity of Nickel and of Iron. *Proc. R. Soc. London* **1857**, *8*, 546–550.
- (4) Mott, N. The Electrical Conductivity of Transition Metals. *Proc. R. Soc. London. Ser. A - Math. Phys. Sci.* **1936**, *153* (880), 699–717.
- (5) Tedrow, P. M.; Meservey, R. Spin-Dependent Tunneling into Ferromagnetic Nickel. *Phys. Rev. Lett.* **1971**, *26* (4), 192–195.
- (6) Huai, Y. Spin-Transfer Torque MRAM (STT-MRAM): Challenges and Prospects. *AAPPS Bull.* **2008**, *18* (6), 33–40.
- (7) Datta, S.; Das, B. Electronic Analog of the Electro-optic Modulator. *Appl. Phys. Lett.* **1990**, *56* (7), 665–667.
- (8) Elasticity, R. M.; Escape, A.; Fiederling, R.; Keim, M.; Reuscher, G.; Ossau, W.; Schmidt, G.; Waag, A.; Molenkamp, L. W. Injection and Detection of a Spin-Polarized Current in a Light-Emitting Diode. *Nature* **1999**, *402* (6763), 787–790.
- (9) Nguyen, T. D.; Ehrenfreund, E.; Vardeny, Z. V. Spin-Polarized Light-Emitting Diode Based on an Organic Bipolar Spin Valve. *Science (80-. )*. **2012**, *337* (6091), 204–209.
- (10) O’Handley, R. C. *Modern Magnetic Materials: Principles and Applications*, 2nd ed.; 1999.
- (11) Lee, P. A.; Ramakrishnan, T. V. Disordered Electronic Systems. *Rev. Mod. Phys.* **1985**, *57* (2), 287–337.
- (12) Aleshin, A. N. Charge Carrier Transport in Conducting Polymers on the Metal Side of the Metal-Insulator Transition: A Review. *Phys. Solid State* **2010**, *52* (11), 2307–2332.
- (13) Jullière, M. Tunneling between Ferromagnetic Films. *Phys. Lett. A* **1975**, *54* (3), 225–226.
- (14) Yuasa, S.; Nagahama, T.; Fukushima, A.; Suzuki, Y.; Ando, K. Giant Room-Temperature Magnetoresistance in Single-Crystal Fe/MgO/Fe Magnetic Tunnel Junctions. *Nat. Mater.* **2004**, *3* (12), 868–871.
- (15) Parkin, S. S. P.; Kaiser, C.; Panchula, A.; Rice, P. M.; Hughes, B.; Samant, M.; Yang, S. H. Giant Tunneling Magnetoresistance at Room Temperature with MgO (100) Tunnel Barriers. *Nat. Mater.* **2004**, *3* (12), 862–867.
- (16) Ikeda, S.; Hayakawa, J.; Ashizawa, Y.; Lee, Y. M.; Miura, K.; Hasegawa, H.; Tsunoda, M.; Matsukura, F.; Ohno, H. Tunnel Magnetoresistance of 604% at 300 K by Suppression of Ta Diffusion in CoFeBMgOCoFeB Pseudo-Spin-Valves Annealed at High Temperature. *Appl. Phys. Lett.* **2008**, *93* (8), 67–70.
- (17) Dulli, H.; Dowben, P. A.; Liou, S.-H.; Plummer, E. W. Surface Segregation and Restructuring of Colossal-Magnetoresistant Manganese Perovskites LSMO. *Phys. Rev. B*

- 2000**, 62 (22), R14629–R14632.
- (18) Stratmann, M.; Feser, R.; Leng, A. Corrosion Protection by Organic Films. *Electrochim. Acta* **1994**, 39 (8–9), 1207–1214.
- (19) Gray, J. E.; Luan, B. Protective Coatings on Magnesium and Its Alloys - A Critical Review. *J. Alloys Compd.* **2002**, 336 (1–2), 88–113.
- (20) Tallman, D. E.; Spinks, G.; Dominis, A.; Wallace, G. G. Electroactive Conducting Polymers for Corrosion Control. *J. Solid State Electrochem.* **2002**, 6 (2), 73–84.
- (21) Redondo, M. I.; Breslin, C. B. Polypyrrole Electrodeposited on Copper from an Aqueous Phosphate Solution: Corrosion Protection Properties. *Corros. Sci.* **2007**, 49 (4), 1765–1776.
- (22) Pushpavanam, M.; Raman, V.; Shenoi, B. A. Rhodium — Electrodeposition and Applications. *Surf. Technol.* **1981**, 12 (4), 351–360.
- (23) Lusk, A. T.; Jennings, G. K. Characterization of Self-Assembled Monolayers Formed from Sodium S-Alkyl Thiosulfates on Copper. *Langmuir* **2001**, 17 (25), 7830–7836.
- (24) Appa Rao, B. V.; Yakub Iqbal, M.; Sreedhar, B. Self-Assembled Monolayer of 2-(Octadecylthio)Benzothiazole for Corrosion Protection of Copper. *Corros. Sci.* **2009**, 51 (6), 1441–1452.
- (25) Chen, S.; Brown, L.; Levendoff, M.; Cai, W.; Ju, S. Y.; Edgeworth, J.; Li, X.; Magnuson, C. W.; Velamakanni, A.; Piner, R. D.; et al. Oxidation Resistance of Graphene-Coated Cu and Cu/Ni Alloy. *ACS Nano* **2011**, 5 (2), 1321–1327.
- (26) Verduci, T.; Yang, C. S.; Bernard, L.; Lee, G.; Boukari, S.; Orgiu, E.; Samorì, P.; Lee, J. O.; Doudin, B. Carbon-Passivated Ni Electrodes for Charge Injection in Organic Semiconductors. *Adv. Mater. Interfaces* **2016**, 3 (6), 1–9.
- (27) Galbiati, M.; Delprat, S.; Mattera, M.; Ma??as-Valero, S.; Forment-Aliaga, A.; Tatay, S.; Deranlot, C.; Seneor, P.; Mattana, R.; Petroff, F. Recovering Ferromagnetic Metal Surfaces to Fully Exploit Chemistry in Molecular Spintronics. *AIP Adv.* **2015**, 5 (5), 0–8.
- (28) Fert, A.; George, J.-M.; Jaffres, H.; Mattana, R. Semiconductors Between Spin-Polarized Sources and Drains. *IEEE Trans. Electron Devices* **2007**, 54 (5), 921–932.
- (29) Schmidt, G.; Ferrand, D.; Molenkamp, L.; Filip, A.; van Wees, B. Fundamental Obstacle for Electrical Spin Injection from a Ferromagnetic Metal into a Diffusive Semiconductor. *Phys. Rev. B - Condens. Matter Mater. Phys.* **2000**, 62 (8), R4790–R4793.
- (30) Rashba, E. I. Theory of Electrical Spin Injection: Tunnel Contacts as a Solution of the Conductivity Mismatch Problem. *Phys. Rev. B* **2000**, 62 (24), R16267–R16270.
- (31) Fert, A.; Jaffrès, H. Conditions for Efficient Spin Injection from a Ferromagnetic Metal into a Semiconductor. *Phys. Rev. B* **2001**, 64 (18), 184420.
- (32) Barraud, C.; Seneor, P.; Mattana, R.; Fusil, S.; Bouzehouane, K.; Deranlot, C.; Graziosi, P.; Hueso, L.; Bergenti, I.; Dediu, V.; et al. Unravelling the Role of the Interface for Spin Injection into Organic Semiconductors. *Nat. Phys.* **2010**, 6 (8), 615–620.
- (33) Szulcowski, G.; Sanvito, S.; Coey, M. A Spin of Their Own. *Nat. Mater.* **2009**, 8 (9), 693–695.
- (34) Watanabe, S.; Ando, K.; Kang, K.; Mooser, S.; Vaynzof, Y.; Kurebayashi, H.; Saitoh, E.; Siringhaus, H. Polaron Spin Current Transport in Organic Semiconductors. *Nat. Phys.*

- 2014**, *10* (4), 308–313.
- (35) McClure, D. S. Spin-Orbit Interaction in Aromatic Molecules. *J. Chem. Phys.* **1952**, *20* (4), 682.
- (36) Elliott, R. J. Theory of the Effect of Spin-Orbit Coupling on Magnetic Resonance in Some Semiconductors. *Phys. Rev.* **1954**, *96* (2), 266–279.
- (37) Yafet, Y. Conduction Electron Spin Relaxation in the Superconducting State. *Phys. Lett. A* **1983**, *98* (5–6), 287–290.
- (38) Dyakonov, M. I.; Perel', V. I. Spin Relaxation of Conduction Electrons in Noncentrosymmetric Semiconductors. *Sov. Phys. Solid State, Ussr* **1972**, *13* (12), 3023–3026.
- (39) Naber, W. J. M.; Faez, S.; van der Wiel, W. G.; Wiel, W. G. Van Der. Organic Spintronics. *J. Phys. D. Appl. Phys.* **2007**, *40* (12), R205–R228.
- (40) Nguyen, T. D.; Hukic-Markosian, G.; Wang, F.; Wojcik, L.; Li, X.-G.; Ehrenfreund, E.; Vardeny, Z. V. Isotope Effect in Spin Response of Pi-Conjugated Polymer Films and Devices. *Nat. Mater.* **2010**, *9* (4), 345–352.
- (41) Koopmans, B.; Wagemans, W.; Bloom, F. L.; Bobbert, P. A.; Kemerink, M.; Wohlgenannt, M. Spin in Organics: A New Route to Spintronics. *Philos. Trans. R. Soc. A Math. Phys. Eng. Sci.* **2011**, *369* (1951), 3602–3616.
- (42) Wetzelaer, G. A. H.; Koster, L. J. A.; Blom, P. W. M. Validity of the Einstein Relation in Disordered Organic Semiconductors. *Phys. Rev. Lett.* **2011**, *107* (6), 1–4.
- (43) Xiong, Z. H.; Wu, D.; Vardeny, Z. V.; Shi, J. Giant Magnetoresistance in Organic Spin-Valves. *Nature* **2004**, *427* (6977), 821–824.
- (44) Shim, J. H.; Raman, K. V.; Park, Y. J.; Santos, T. S.; Miao, G. X.; Satpati, B.; Moodera, J. S. Large Spin Diffusion Length in an Amorphous Organic Semiconductor. *Phys. Rev. Lett.* **2008**, *100* (22), 1–4.
- (45) Morley, N. A.; Rao, A.; Dhandapani, D.; Gibbs, M. R. J.; Grell, M.; Richardson, T. Room Temperature Organic Spintronics. *J. Appl. Phys.* **2008**, *103* (7), 5–8.
- (46) Jiang, S. W.; Wang, P.; Chen, B. B.; Zhou, Y.; Ding, H. F.; Wu, D. Tuning Carrier Mobility without Spin Transport Degrading in Copper-Phthalocyanine. *Appl. Phys. Lett.* **2015**, *107* (4), 042407.
- (47) Li, F.; Li, T.; Chen, F.; Zhang, F. Excellent Spin Transport in Spin Valves Based on the Conjugated Polymer with High Carrier Mobility. *Sci. Rep.* **2015**, *5*, 1–7.
- (48) Lou, X.; Adelman, C.; Crooker, S. A.; Garlid, E. S.; Zhang, J.; Reddy, K. S. M.; Flexner, S. D.; Palmstrøm, C. J.; Crowell, P. A. Electrical Detection of Spin Transport in Lateral Ferromagnet–Semiconductor Devices. *Nat. Phys.* **2007**, *3* (3), 197–202.
- (49) Jain, A.; Rojas-Sanchez, J. C.; Cubukcu, M.; Peiro, J.; Le Breton, J. C.; Prestat, E.; Vergnaud, C.; Louahadj, L.; Portemont, C.; Ducruet, C.; et al. Crossover from Spin Accumulation into Interface States to Spin Injection in the Germanium Conduction Band. *Phys. Rev. Lett.* **2012**, *109* (10), 1–5.
- (50) Sasaki, T.; Oikawa, T.; Suzuki, T.; Shiraishi, M.; Suzuki, Y.; Noguchi, K. Temperature Dependence of Spin Diffusion Length in Silicon by Hanle-Type Spin Precession. *Appl. Phys. Lett.* **2010**, *96* (12), 1–4.

- (51) Yan, W.; Phillips, L. C.; Barbone, M.; Hämmäläinen, S. J.; Lombardo, A.; Ghidini, M.; Moya, X.; MacCherozzi, F.; Van Dijken, S.; Dhesi, S. S.; et al. Long Spin Diffusion Length in Few-Layer Graphene Flakes. *Phys. Rev. Lett.* **2016**, *117* (14), 1–6.
- (52) Drögeler, M.; Franzen, C.; Volmer, F.; Pohlmann, T.; Banszerus, L.; Wolter, M.; Watanabe, K.; Taniguchi, T.; Stampfer, C.; Beschoten, B. Spin Lifetimes Exceeding 12 Ns in Graphene Nonlocal Spin Valve Devices. *Nano Lett.* **2016**, *16* (6), 3533–3539.
- (53) Dediu, V.; Murgia, M.; Maticotta, F. C.; Taliani, C.; Barbanera, S. Room Temperature Spin Polarized Injection in Organic Semiconductor. *Solid State Commun.* **2002**, *122* (3–4), 181–184.
- (54) De Teresa, J. M.; Barthélémy, A.; Fert, A.; Contour, J. P.; Lyonnet, R.; Montaigne, F.; Seneor, P.; Vaurès, A. Inverse Tunnel Magnetoresistance in Co/SrTiO<sub>3</sub>/La<sub>0.7</sub>Sr<sub>0.3</sub>MnO<sub>3</sub> : New Ideas on Spin-Polarized Tunneling. *Phys. Rev. Lett.* **1999**, *82* (21), 4288–4291.
- (55) Wang, F. J.; Xiong, Z. H.; Wu, D.; Shi, J.; Vardeny, Z. V. Organic Spintronics: The Case of Fe/Alq<sub>3</sub>/Co Spin-Valve Devices. *Synth. Met.* **2005**, *155* (1), 172–175.
- (56) Rybicki, J.; Lin, R.; Wang, F.; Wohlgenannt, M.; He, C.; Sanders, T.; Suzuki, Y. Tuning the Performance of Organic Spintronic Devices Using X-Ray Generated Traps. *Phys. Rev. Lett.* **2012**, *109* (7), 1–5.
- (57) Chan, Y. L.; Hung, Y. J.; Wang, C. H.; Lin, Y. C.; Chiu, C. Y.; Lai, Y. L.; Chang, H. T.; Lee, C. H.; Hsu, Y. J.; Wei, D. H. Magnetic Response of an Ultrathin Cobalt Film in Contact with an Organic Pentacene Layer. *Phys. Rev. Lett.* **2010**, *104* (17), 1–4.
- (58) Galbiati, M.; Tatay, S.; Delprat, S.; Khanh, H. Le; Servet, B.; Deranlot, C.; Collin, S.; Seneor, P.; Mattana, R.; Petroff, F. Is Spin Transport through Molecules Really Occurring in Organic Spin Valves? A Combined Magnetoresistance and Inelastic Electron Tunnelling Spectroscopy Study. *Appl. Phys. Lett.* **2015**, *106* (8), 10–14.
- (59) Jiang, J. S.; Pearson, J. E.; Bader, S. D. Absence of Spin Transport in the Organic Semiconductor Al Q<sub>3</sub>. *Phys. Rev. B - Condens. Matter Mater. Phys.* **2008**, *77* (3), 1–7.
- (60) Schoonus, J. J. H. M.; Lumens, P. G. E.; Wagemans, W.; Kohlhepp, J. T.; Bobbert, P. A.; Swagten, H. J. M.; Koopmans, B. Magnetoresistance in Hybrid Organic Spin Valves at the Onset of Multiple-Step Tunneling. *Phys. Rev. Lett.* **2009**, *103* (14), 1–4.
- (61) Yoo, J. W.; Jang, H. W.; Prigodin, V. N.; Kao, C.; Eom, C. B.; Epstein, A. J. Tunneling vs. Giant Magnetoresistance in Organic Spin Valve. *Synth. Met.* **2010**, *160* (3–4), 216–222.
- (62) Tran, T. L. A.; Le, T. Q.; Sanderink, J. G. M.; Van Der Wiel, W. G.; De Jong, M. P. The Multistep Tunneling Analogue of Conductivity Mismatch in Organic Spin Valves. *Adv. Funct. Mater.* **2012**, *22* (6), 1180–1189.
- (63) Collet, J.; Tharaud, O.; Chapoton, A.; Vuillaume, D. Low-Voltage, 30 Nm Channel Length, Organic Transistors with a Self-Assembled Monolayer as Gate Insulating Films. *Appl. Phys. Lett.* **2000**, *76* (14), 1941–1943.
- (64) Wang, J. Z.; Zheng, Z. H.; Siringhaus, H. Suppression of Short-Channel Effects in Organic Thin-Film Transistors. *Appl. Phys. Lett.* **2006**, *89* (8).
- (65) Chen, Y.; Zhu, W. W.; Xiao, S.; Shih, I. Fabrication of Short Channel Organic Thin Film Transistors by Si-Etching Method. *J. Vac. Sci. Technol. A Vacuum, Surfaces, Film.* **2004**, *22* (3), 768.
- (66) Dayen, J. F.; Faramarzi, V.; Pauly, M.; Kemp, N. T.; Barbero, M.; Pichon, B. P.; Majjad, H.;

- Begin-Colin, S.; Doudin, B. Nanotrench for Nano and Microparticle Electrical Interconnects. *Nanotechnology* **2010**, *21* (33).
- (67) Alborghetti, S.; Coey, J. M. D.; Stamenov, P. Electron and Spin Transport Studies of Gated Lateral Organic Devices. *J. Appl. Phys.* **2012**, *112* (12).
- (68) Kawasugi, Y.; Ara, M.; Ushirokita, H.; Kamiya, T.; Tada, H. Preparation of Lateral Spin-Valve Structure Using Doped Conducting Polymer Poly(3,4-Ethylenedioxythiophene) Poly(Styrenesulfonate). *Org. Electron. physics, Mater. Appl.* **2013**, *14* (7), 1869–1873.
- (69) de Oliveira, T. V. A. G.; Gobbi, M.; Porro, J. M. J. M.; Hueso, L. E.; Bittner, A. M. Charge and Spin Transport in PEDOT:PSS Nanoscale Lateral Devices. *Nanotechnology* **2013**, *24* (47), 475201.
- (70) Grünewald, M.; Kleinlein, J.; Syrowatka, F.; Würthner, F.; Molenkamp, L. W.; Schmidt, G. Large Room-Temperature Magnetoresistance in Lateral Organic Spin Valves Fabricated by in Situ Shadow Evaporation. *Org. Electron. physics, Mater. Appl.* **2013**, *14* (8), 2082–2086.
- (71) Riminucci, A.; Prezioso, M.; Pernechele, C.; Graziosi, P.; Bergenti, I.; Cecchini, R.; Calbucci, M.; Solzi, M.; Alek Dediu, V. Hanle Effect Missing in a Prototypical Organic Spintronic Device. *Appl. Phys. Lett.* **2013**, *102* (9), 0–4.
- (72) Ikegami, T.; Kawayama, I.; Tonouchi, M.; Nakao, S.; Yamashita, Y.; Tada, H. Planar-Type Spin Valves Based on Low-Molecular-Weight Organic Materials with La<sub>0.67</sub>Sr<sub>0.33</sub>MnO<sub>3</sub> Electrodes. *Appl. Phys. Lett.* **2008**, *92* (2008), 153304.
- (73) Ozbay, A.; Nowak, E. R.; Yu, Z. G.; Chu, W.; Shi, Y.; Krishnamurthy, S.; Tang, Z.; Newman, N. Large Magnetoresistance of Thick Polymer Devices Having La<sub>0.67</sub> Sr<sub>0.33</sub> MnO<sub>3</sub> Electrodes. *Appl. Phys. Lett.* **2009**, *95* (23), 19–22.
- (74) Rakheja, S.; Naeemi, A. Roles of Doping, Temperature, and Electric Field on Spin Transport Through Semiconducting Channels in Spin Valves. *IEEE Trans. Nanotechnol.* **2013**, *12* (5), 796–805.
- (75) Teferi, M. Y.; Ogle, J.; Joshi, G.; Malissa, H.; Jamali, S.; Baird, D. L.; Lupton, J. M.; Whittaker Brooks, L.; Boehme, C. Tuning Effective Hyperfine Fields in PEDOT:PSS Thin Films by Doping. *Phys. Rev. B* **2018**, *98* (24), 1–5.
- (76) Wang, S.-J.; Venkateshvaran, D.; Mahani, M. R.; Chopra, U.; McNellis, E. R.; Di Pietro, R.; Schott, S.; Wittmann, A.; Schweicher, G.; Cubukcu, M.; et al. Long Spin Diffusion Lengths in Doped Conjugated Polymers Due to Enhanced Exchange Coupling. *Nat. Electron.* **2019**, *2* (3), 98–107.
- (77) Yu, Z. G. Spin-Orbit Coupling, Spin Relaxation, and Spin Diffusion in Organic Solids. *Phys. Rev. Lett.* **2011**, *106* (10), 1–4.
- (78) Yu, Z. G. Suppression of the Hanle Effect in Organic Spintronic Devices. *Phys. Rev. Lett.* **2013**, *111* (1), 1–5.
- (79) Yu, Z. G. Impurity-Band Transport in Organic Spin Valves. *Nat. Commun.* **2014**, *5*.
- (80) Yu, Z. G. Spin Transport and the Hanle Effect in Organic Spintronics. *Nanoelectron. Spintron* **2015**, *1*, 1–18.
- (81) Sanvito, S. Molecular Spintronics: The Rise of Spinterface Science. *Nat. Phys.* **2010**, *6* (8), 562–564.

- 
- (82) Dediu, V.; Hueso, L. E.; Bergenti, I.; Riminucci, A.; Borgatti, F.; Graziosi, P.; Newby, C.; Casoli, F.; De Jong, M. P.; Taliani, C.; et al. Room-Temperature Spintronic Effects in Alq<sub>3</sub>-Based Hybrid Devices. *Phys. Rev. B - Condens. Matter Mater. Phys.* **2008**, *78* (11), 1–6.
- (83) Vinzelberg, H.; Schumann, J.; Elefant, D.; Gangineni, R. B.; Thomas, J.; Büchner, B. Low Temperature Tunneling Magnetoresistance on (La,Sr) Mn O<sub>3</sub> Co Junctions with Organic Spacer Layers. *J. Appl. Phys.* **2008**, *103* (9), 0–5.
- (84) Cinchetti, M.; Dediu, V. A.; Hueso, L. E. Activating the Molecular Spinterface. *Nat. Mater.* **2017**, *16* (5), 507–515.
- (85) Wang, F.; Macià, F.; Wohlgenannt, M.; Kent, A. D.; Flatté, M. E. Magnetic Fringe-Field Control of Electronic Transport in an Organic Film. *Phys. Rev. X* **2012**, *2* (2), 021013.
- (86) Wohlgenannt, M.; Flatté, M. E.; Harmon, N. J.; Wang, F.; Kent, A. D.; Macià, F.; Fischer, P.; Im, M.-Y. A New Twist on Organic Spintronics: Controlling Transport in Organic Sandwich Devices Using Fringe Fields from Ferromagnetic Films. *Spintron. VI* **2013**, *8813* (April 2015), 881300.
- (87) Harmon, N. J.; Wohlgenannt, M.; Flatté, M. E. The Effect of Fringe Fields from Patterned Magnetic Domains on the Electroluminescence of Organic Light-Emitting Diodes. *Spintron. IX* **2016**, *9931*, 993102.



# **PART 2**

## **NUMERICAL COMPUTATION AND EXPERIMENTAL WORK**



## Chapter III

# Current crowding effect

In planar devices, current crowding effects in staggered structures imply a charge injection away from the electrodes edges. A resulting non-uniform current in the active channel involves an increase of the charge carrier pathways in the organic channel. The first reference to this effect dates from the end of the 70's and was considered to calculate more accurately resistances of silicon devices and explore their contact properties<sup>1,2</sup>. Recently, it was pointed out again by Richards and Sirringhaus to model the contact resistance of organic transistors<sup>3</sup>.

In this chapter, the consequences of the current crowding on the injection/detection areas are discussed in order to provide designing rules and analysis guidance for lateral organic devices. In addition, the impact of the extended channel length on the contact resistance and spin signal is investigated through numerical simulations. The outcomes will reveal the roadmap of the experiments performed during this thesis.

### III.1. Extended injection/detection interfaces

The large metal-organic contact resistance is nowadays a major issue to overcome for large-scale organic device production. The understanding of metal-organic interfaces is then of key relevance for the improvement of charge injection. Here, we are interested in defining more precisely the geometric parameter of the injection and detection electrodes.

In staggered configuration, OFET and EGOFET gate electrodes often overlap the source and drain contacts over a large area. Thus, the polymer encapsulated by the two metallic layers is as doped as the organic channel between the source and drain electrodes. More generally, if the organic layer has uniform conductivity and also overlaps with source and drain electrodes, these resulting additional regions also participate to the current flow, and the injection and detection

interfaces spread over the top surface of source and drain (**Figure III.1**). The extension of these injection and detection areas is the current crowding effect.

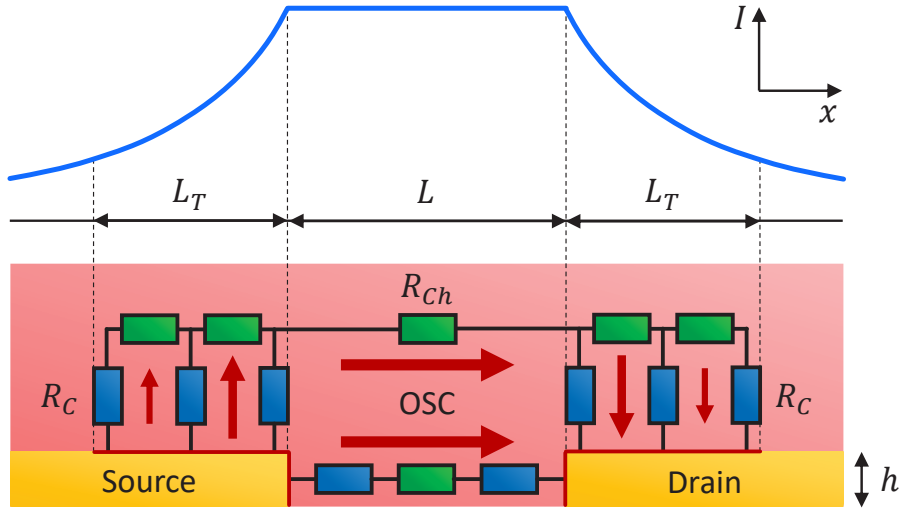


**Figure III.1** Drawing of the current crowding effect. The current amplitude decays exponentially over the electrodes, with a characteristic length  $L_T$  (blue line on top). Therefore, injection and detection occur from the top of electrodes in addition to their edges (Red line on electrodes). The effective channel length is then elongated by  $2L_T$  compared to the distance between the two electrode edges ( $L$ ). Red arrows show the current flow, the larger the higher the current. The green and blue rectangles represent the channel and the contact resistances respectively. The top-gate electrode is not represented for clarity.

As depicted in the **Figure III.1**, the current crowding can be modelled by a network circuit, where the contact resistances ( $R_C$ ) are in parallel all over the electrodes. Charge transport passing through this array of resistance join then the channel. Under the hypothesis of uniform resistance values, circuit analysis reveals that the current is decaying exponentially from the edge of the electrodes with a characteristic length called the transfer length ( $L_T$ ). Assuming that metallic wires are much more conductive than the organic semiconductor,  $L_T$  reflects the balance between the contact resistance and the channel resistance. Using a transmission line analysis, under the hypothesis of ohmic contacts, the transfer length writes<sup>4</sup>:

$$L_T = \sqrt{\frac{r_b}{R_{Sheet}}} \quad (\text{III.1})$$

where  $r_b$  is the interface contact resistance normalized by the injection area ( $\Omega \cdot \text{cm}^2$ ), or specific contact resistivity, similarly to the one defined in the previous chapter.  $R_{Sheet} = 1/\sigma h_{OSC}$  is the sheet resistance (resistance of a square slice of the channel parallel to the current flow), with  $\sigma$  the conductivity and  $h_{OSC}$  the thickness of the organic layer.  $r_b$  is an intrinsic property of the system, depending only on the materials composing the hybrid junction.  $R_{Sheet}$  depends on the thickness of the channel but can also be considered as intrinsic, as  $h_{OSC}$  is fixed.

It is worth noting that equation III.1 is self-consistent as the calculation of  $r_b$  includes the injection area, that is modified by the crowding effect in the case of EGOFETs. Indeed, the current flows in the entire volume of the channel as the doping is three-dimensional. Hence, the active interface can be considered as made of the height of the electrode plus its top, up to  $L_T$ :

$$r_b = R_C^{L_T} W (h + L_T) \quad (\text{III.2})$$

where  $W$  is the channel width. In the latter equation,  $R_C^{L_T}$  refers to the average contact resistance evaluated by considering the extended injection/detection areas as indicated by the  $L_T$  exponent. One could define source and drain transfer length, but we avoid it in the next discussions for simplicity purposes. It is worth noting that this definition gives indeed  $r_b$ , not  $r_b^{L_T}$ . As  $r_b$  is an intrinsic property, the latter definition is only a better definition of the normalization area of the contact resistance for a more proper determination of  $r_b$ .

A simple definition of the average interface resistance is:

$$R_C^{L_T} = \frac{1}{2} [R_{Sample} - R_{Ch}^{L_T}] = \frac{1}{2} \left[ R_{Sample} - \frac{L + 2L_T}{\sigma W h_{OSC}} \right] \quad (\text{III.3})$$

where the channel length has been elongated by the transfer length on each side. It is straightforward that the crowding effect reduces the interface resistance of devices. In other words, for a given  $R_{Sample}$ , we always have  $R_C^{L_T} < R_C$ . The longer  $L_T$ , the lower  $R_C^{L_T}$ , hence the transfer length is a tool to control the contact resistance. It is particularly interesting as  $L_T$  is tunable through the conductivity of the organic channel, *i.e.* by the gate voltage, under the approximation that  $r_b$  doesn't vary with it. Indeed, increasing  $\sigma$ , or equivalently reducing  $R_{Sheet}$ , rises the transfer length (equation III.1).

If we neglect  $h$  versus  $L_T$ , often realized experimentally, the calculation of the transfer length becomes no more self-consistent by combining equations III.1, III.2 and III.3:

$$L_T = \frac{1}{4} \left[ \frac{R_{Sample}}{R_{Sheet}} W - L \right] \quad (\text{III.4})$$

For our experimental conditions, we found that equation III.4 is a very good approximation (within 10 %) of the original definition of  $L_T$ .

The last relation holds true as long as more current flows from the top of electrodes than from edges. Recent experimental results on top-gated OFETs exhibit transfer lengths of the same order of magnitude than the channel length, following roughly  $4L_T = L$  for micrometer-scale transistors<sup>5,6</sup>. Another work on nano-scale devices present a constant  $L_T = 600$  nm for sub-micrometer OFETs down to 100 nm<sup>7</sup>. Reminding that the transfer length takes place on both source and drain electrodes, the effective channel length is possibly much longer than the physical separation between electrodes. Therefore, attention must be given to the design of samples to either take advantage of the crowding effect or to minimize it. For comparison with inorganic devices,  $L_T \sim 2$   $\mu\text{m}$  in silicon channels for  $L = 50$   $\mu\text{m}$ <sup>4</sup>. On another note, the quite large values

reported in the literature give robustness to the approximation we have done to obtain equation III.4.

Another way to limit the crowding is to limit the length of electrodes (in the  $x$ -direction of **Figure III.1**). While increasing the injection/detection areas is key for functioning sub-micrometric OFETs, the question of miniaturization arises if infinitely long electrodes are needed. In their article, Xu and co-workers looked for the best compromise between downscaling and needed charge injection/detection areas for the optimal performance per unit area of the device<sup>7</sup>. They extracted the transfer length this way, and found the best compromise for  $L_T = 600$  nm, that sets then their smallest possible device.

Another point to emphasize from the work on nano-scale OFETs is the comparison between the channel length and  $L_T$ . For the shortest devices, the transfer length is fully dominant for the charge injection and detection such that finally the initial channel length ( $L$ ) is negligible. By using the hypothesis  $L_T \gg L$ , previous equations imply that:

$$2R_C^{L_T} = R_{Ch}^{L_T} = \frac{1}{2}R_{Sample} \quad (\text{III.5})$$

This equality is key for the understanding of charge injection in sub-micrometer transistors. It shows simply that the transfer length adapts in order to balance the contact and the channel resistances. If the channel conductivity increases, via doping for example, and  $r_b$  is not changed,  $L_T$  increases such that  $R_{Ch}^{L_T} = (L + 2L_T)/\sigma h_{OSC}W$  equilibrates the interface resistance ( $R_C^{L_T}$ ) – that changes as well. In other words, gating the device changes its size.

In conclusion, the current crowding effect modifies the effective channel length and the estimate of  $r_b$ . It has the advantage to reduce the contact resistance by increasing the interface area. The resulting extended travel path of charges also has important consequences for spintronic applications.

## III.2. Outcomes for organic electronics and spintronics

From previous section, two key outcomes for spintronics emerges. First, the effective channel length is much longer than the physical distance between electrodes. How it compares to the spin diffusion length ( $l_{sf}^{NM}$ ) is key for spin-preserving charge transfer through organic materials. This may be a major limitation as  $L + 2L_T$  can be larger than  $l_{sf}^{NM}$  while  $L$  isn't. Second, as in general  $2R_C^{L_T} \sim R_{Ch}^{L_T}$ , a magnetoresistance (MR) signal could be observed without the need of spin information transfer between source and drain. This possibly shines new light on previous finding of spin-valve behaviour.

### III.2.1. Tuning of the channel length

The equivalence exhibited between the contact and the channel resistances in equation III.5 provides opportunity to study more deeply how crowding effects impact the effective length of the channel ( $L_{eff}$ ). From an arbitrary initial state (**Figure III.2a**), two cases may occur:

- 1) Let's assume that only the intrinsic specific interface resistivity increases such that  $r_b' > r_b$ . As indicated by the equation III.1, the transfer length rises as well, meaning that the channel resistance  $R_{Ch}^{LT}$  also increases (**Figure III.2b**). As it builds half the total resistance,  $R_{Sample}$  increases. The same effect happens if the sheet resistance decreases (higher conductivity), with both cases resulting in an **increase of the effective length of the sample**.
- 2) Let's assume that only the sheet resistance increases, *i.e.* the conductivity decreases, such that  $R_{Sheet}' > R_{Sheet}$ . In contrast to the first hypothesis,  $L_T$  diminishes, that also reduces  $R_{Ch}^{LT}$ , counterbalancing partially the conductivity drop (**Figure III.2c**). As both interface and channel resistance contribute equally to the sample resistance,  $R_{Sample}$  decreases. The same reasoning applies to a specific interface resistivity increase, both leading to a **decrease of the effective length of the sample**.

A quantitative approximation, based on equation III.5 and neglecting again  $h$  versus  $L_T$  (thus  $r_b = R_C^{LT} W L_T$ ), expresses the total resistance as:

$$R_{Sample} = \frac{4}{W} \sqrt{r_b R_{Sheet}} \quad (III.6)$$

In general, one expects a linear change of the sample resistance with both  $r_b$  and  $R_{Sheet}$ :  $R_{Sample} W = R_{Sheet} L + 2 r_b / h$ . The very unusual and key relationship of equation III.6 between the interface resistance and the sheet resistance (resistivity) comes from the variation of the length of the channel because of the current crowding effect. Therefore, the reduction of the resistivity of the channel by a factor 4 for instance, would reduce the total resistance only by a factor 2 because it involves in the same time the rise of the interface resistance. Note also that in addition to a square root behaviour, it is no more the addition of both resistances but their multiplication that determines the total resistance. For MR purposes, if  $r_b$  or  $R_{Sheet}$  changes under magnetic field, the whole sample resistance also exhibits an MR-like signal. This should be kept in mind when looking for MR studies, in particular if the specific interface resistivity depends on the magnetic orientation of the electrode.

Assuming a weak MR amplitude, *i.e.* the resistance variation is small, the MR of the total sample could be written in the formalism of uncertainty at the first order approximation, leading to:

$$MR(R_{Sample}) \cong \frac{1}{2} MR(r_b) + \frac{1}{2} MR(R_{Sheet}) \quad (III.7)$$

Equation III.7 provides an easy method to determine the MR of interfaces, if the condition of small  $R_{Sample}$  modulation is fulfilled.

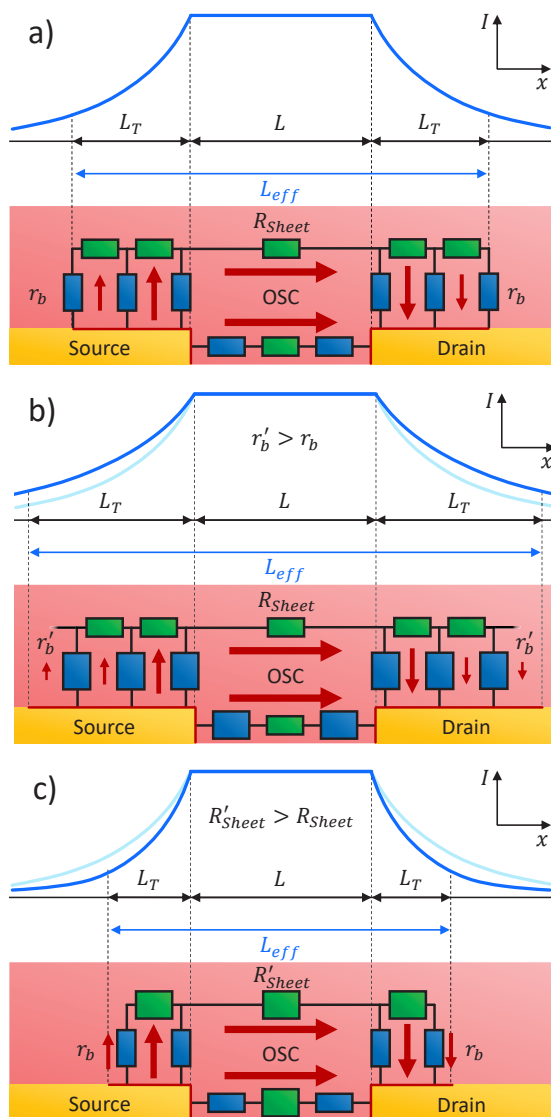


**Figure III.2** Drawing of the current crowding effect at the initial state (a), when  $r_b$  increases (b) and when  $R_{Sheet}$  rises (c). The effective channel length ( $L_{eff} = L + 2L_T$ ) modulates with the variation of both variables, increasing with the rise of  $r_b$  and decreasing with the rise of  $R_{Sheet}$ .

### III.2.2. How current crowding impacts the MR of spin-valves

As already discussed in the second chapter, the spin diffusion length ( $l_{sf}^{NM}$ ) is the characteristic distance of spintronic devices. For efficient spin injection and detection, the channel length must be shorter than  $l_{sf}^{NM}$ , expected to reach around 200 nm in best organic materials<sup>8</sup>. For this reason, nano-scale devices are needed. However, current crowding effect is inevitable in staggered lateral geometry. It leads to an elongation of the effective channel length possibly resulting in an average distance travelled by carriers that exceeds the spin diffusion length. This issue may be an explanation for the lack of experimental success in spin-valve signal detection.

To investigate quantitatively the importance of the crowding effect on the expected MR signal, we performed a numerical computation based on Fert & Jaffrès' article on the efficiency of

spin injection and detection<sup>9</sup>. The objective is to quantify the loss of MR amplitude when the channel length is no more  $L$  but  $L_{eff} = L + 2L_T$ .

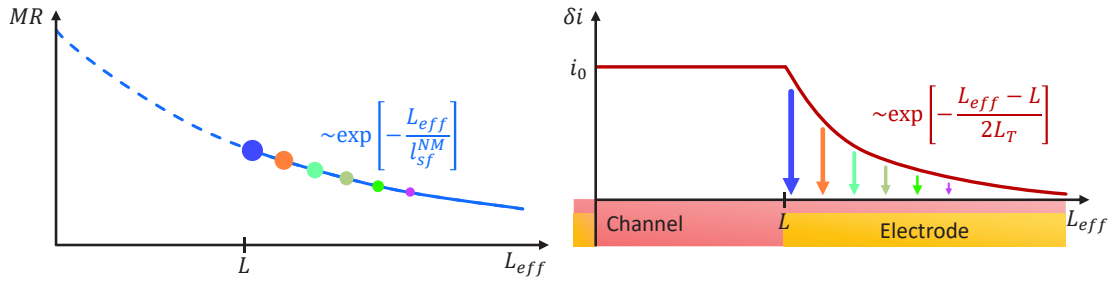


**Figure III.3** Left: Valet-Fert MR for a channel length equal to  $L_{eff} > L$ . Right: partial current  $\delta i$  distribution above the detection electrode.  $\delta i$  weighted the MR for the consideration of the crowding effect as depicted by the colour coding of arrows and dots.

The Valet-Fert expression for the resistance of two magnetic electrodes separated by a non-magnetic spacer when their magnetization are parallel ( $R_P$ ) and antiparallel ( $R_{AP}$ ) are<sup>10</sup>:

$$R_P = 2(1 - \beta^2)r_F + r_N \frac{L}{l_{sf}^{NM}} + 2(1 - \gamma^2)r_b^* + 2 \frac{(\beta - \gamma)^2 r_F r_b^* + r_N (\beta^2 r_F + \gamma^2 r_b^*) \tanh\left(\frac{L}{2l_{sf}^{NM}}\right)}{r_F + r_b^* + r_N \tanh\left(\frac{L}{2l_{sf}^{NM}}\right)}$$

$$\Delta R = R_{AP} - R_P = \frac{2(\beta r_F + \gamma r_b^*)^2}{(r_F + r_b^*) \cosh\left(\frac{L}{l_{sf}^{NM}}\right) + \frac{r_N}{2} \left[1 + \left(\frac{r_b^*}{r_N}\right)^2\right] \sinh\left(\frac{L}{l_{sf}^{NM}}\right)}$$

$$MR^{V-F} = \frac{\Delta R}{R_P}$$

(III.8)

with the variables being:

$\beta$ : bulk spin asymmetry of the electrode.

$\gamma$ : interface spin asymmetry of the electrode.

$l_{sf}^{NM}$ : spin diffusion length of the non-magnetic channel.

$L$ : channel length. It replaces  $t_N$  in the paper of Valet-Fert.

$r_F$ : "spin resistivity" of the electrode,  $r_F = \rho_F l_{sf}^{FM}$ .

$r_N$ : "spin resistivity" of the non-magnetic channel,  $r_N = \rho_N l_{sf}^{NM}$ .

$r_b^*$ : spin-dependent specific contact resistance (see chapter II).

$R_{AP}$ : resistance in the anti-parallel configuration.

$R_P$ : resistance in the parallel configuration.

for numerical applications:

$\beta = 0,46$

$\gamma = 0,5$

$l_{sf}^{NM} = 200 \text{ nm}$

$L = 20 \text{ nm}$

$r_F = 4,5 \times 10^{-15} \Omega \cdot \text{m}^2$

$\rho_N = 2 \times 10^{-3} \Omega \cdot \text{m}$

The choice of parameters values relates to cobalt as electrode material ( $\beta$ ,  $\gamma$  and  $r_F$ ), in correspondence with our experimental choice. For easier comparison with Fert & Jaffrès' calculations, we keep also  $\rho_N = 2 \times 10^{-3} \Omega \cdot \text{m}$  used in their paper even if our polymer is significantly more

conductive ( $\rho \sim 2 \times 10^{-5} \Omega \cdot \text{m}$ ). The spin diffusion length is adapted to the expectation of organic material we are using in experiments ( $\rho\text{BTTP}^8$ ). This MR decay with the elongation of the channel is very close to an exponential decay with  $l_{sf}^{NM}$  as characteristic length (**Figure III.3**, left panel).

In order to consider the current crowding effect, we implemented the non-uniformity of the current shown in the right schematic of **Figure III.3**. A current ( $i_0$ ) is flowing in the channel of length  $L_{eff} = L + 2L_T$ . Above the collection electrode, the local current at each point ( $\delta i(L_{eff})$ ) diminishes exponentially from the total current ( $i_0$ ) with the transfer length as characteristic length:

$$\delta i(L_{eff}) = i_0 \exp\left[-\frac{L_{eff} - L}{2L_T}\right] \quad (\text{III.9})$$

If there is no current crowding effect,  $L_{eff} = L$  such that  $\delta i(L_{eff} = L) = i_0$ , meaning that all the current is passing through the electrodes edges.

The relative change of resistance in the Valet-Fert model can be thought as a relative change of conductance and therefore a relative change of current. The MR taking into account the current crowding ( $MR^{LT}$ ) is taken as the weighted average of the MR of the small current  $\delta i$  summing up to  $i_0$  (**Figure III.3**):

$$MR^{LT}(L) = \frac{\int_L^\infty MR^{V-F}(L_{eff}) \delta i(L_{eff}) dL_{eff}}{\int_L^\infty \delta i(L_{eff}) dL_{eff}} = \frac{1}{2L_T} \int_L^\infty MR^{V-F}(L_{eff}) \exp\left[-\frac{L_{eff} - L}{2L_T}\right] dL_{eff} \quad (\text{III.10})$$

The value of the transfer length ranges between 0 (reference) and  $4l_{sf}^{NM}$ , the order of magnitude extracted on short-channel organic transistors by Xu and co-workers<sup>7</sup>. The channel length and the spin diffusion length are also parameters we work on.

The figure 3 of Fert and Jaffrès' article is adapted in **Figure III.4**. It shows how MR in a spin-valve has maximum amplitude when  $r_b^* \sim r_N$  (thin blue line). When taking into account the transfer length, the MR is significantly reduced already for the lowest  $L_T$ . Note that all tilded variables are in  $l_{sf}^{NM}$  unit. We choose a quite short channel of 20 nm ( $\tilde{L} = 0,1$ ) to emphasize the impact of the crowding effect by keeping a short enough channel, where significant MR signal is expected.

Basically, the MR decreases of one order of magnitude when  $L_T$  reaches  $4l_{sf}^{NM} = 800$  nm ( $\tilde{L}_T = 4$ ), which is expected for sub-micrometer devices. As a reminder, the transfer length reported in the literature for nano-scale OFETs is 600 nm using pentacene as organic channel. Therefore, by combining a maximum spin diffusion length of 200 nm and  $L_T \geq 600$  nm, the previous simulation tells us that the measure of any spin-valve signal in lateral geometry is challenging and probably limited to few percents. In addition, here we keep relatively high bulk and interface spin asymmetries ( $\beta$  and  $\gamma$ ), that are not easily achieved experimentally. Note however that EGOFETs we study experimentally in the following chapters can exhibit very shorter transfer length down a few tens of nanometers.

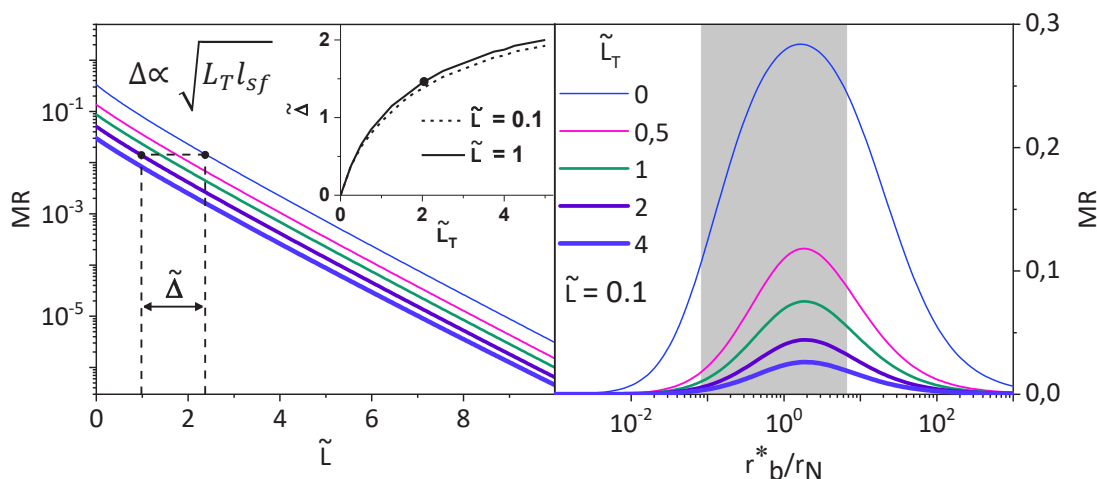


**Figure III.4** Magnetoresistance versus the channel length (left) and the normalized contact resistance (right). Tilded variables are in  $l_{sf}^{NM}$  unit that is set to **200 nm** as expected in suitable organic materials. On the left panel, no change in slope of the curve  $MR(L)$  is observed by considering the crowding effect. The only impact is the decay in amplitude. In the end, the transfer length acts as if the channel length were elongated by  $\Delta$ . On the right side, a dramatic decrease of the MR signal is exhibited by taking into account the transfer length. From  $L_T > 4l_{sf}^{NM}$ , the MR loses roughly one order of magnitude.

Another aspect of the simulation is the decrease of the MR with the channel length. The usual manner to determinate the spin diffusion length is to extract the MR of a set of devices with various channel lengths. However, as the transfer length elongates the effective channel, we were curious to see if the crowding effect leads to an error on  $l_{sf}^{NM}$  by this method. For that, the same equations were used, but instead of varying  $r_b^*$ , we investigated MR as a function of  $L$  and  $L_T$ . The value of  $r_b^*$  was calculated such as it is the optimal interface resistance for each case (maximum value of curves in the right panel of **Figure III.4**).

The calculation shows that the MR keeps its exponential decay with the channel length – for  $L > l_{sf}^{NM}$  – as expected from classical Valet-Fert equations. The crowding effect modifies the MR amplitude, but doesn't affect the slope, needed for the determination of the spin diffusion length. An interesting feature is the equivalence between the MR with and without the crowding effect. As all  $MR^{L_T}(L)$  are parallel, the amplitude of the MR considering  $L_T$  behaves as if there was no crowding effect but for a channel elongated by  $\Delta$ . The value of  $\Delta$  is not  $2L_T$  but approximates the geometrical mean value  $\Delta \sim \sqrt{l_{sf}^{NM} L_T}$ .

The crowding effect is a useful tool to decrease the contact resistance in lateral (EG)OFETs. The participation of the top surface of electrodes extends the injection and detection areas that reduces the interface resistance. Nevertheless, our simulation reveals that the spin injection will be very challenging precisely because of the transfer length which strongly limits the probability to detect injected spins.

In the following chapters, the electrical characterisations, mainly focused on contact resistance, and magnetic responses of our EGOFETs are presented. The conductivity of sub-micrometer channels is required to explore the previous hypothesis and outputs. To achieve accurate analysis, the conductivity is deduced from 4-probe measurements on micrometer size EGOFETs and applied to nano-scale transistors. Therefore, the first step is the comparison of performance between both scales, as short-channel effects often occur. Afterwards, the same devices are realized using magnetic electrodes for spin-dependent properties investigation.

**Bibliography**

- (1) Kennedy, D. P.; Murley, P. C. A Two-Dimensional Mathematical Analysis of the Diffused Semiconductor Resistor. *IBM J. Res. Dev.* **1968**, *12* (3), 242–250.
- (2) Murrmann, H.; Widmann, D. Current Crowding on Metal Contacts to Planar Devices. *IEEE Trans. Electron Devices* **1969**, *16* (12), 1022–1024.
- (3) Richards, T. J.; Sirringhaus, H. Analysis of the Contact Resistance in Staggered, Top-Gate Organic Field-Effect Transistors. *J. Appl. Phys.* **2007**, *102* (9), 1–6.
- (4) Chiang, C. S.; Martin, S.; Kanicki, J.; Ugai, Y.; Yukawa, T.; Takeuchi, S. Top-Gate Staggered Amorphous Silicon Thin-Film Transistors: Series Resistance and Nitride Thickness Effects. *Japanese J. Appl. Physics, Part 1 Regul. Pap. Short Notes Rev. Pap.* **1998**, *37* (11), 5914–5920.
- (5) Wang, S. D.; Yan, Y.; Tsukagoshi, K. Understanding Contact Behavior in Organic Thin Film Transistors. *Appl. Phys. Lett.* **2010**, *97* (6), 63305–63308.
- (6) Natali, D.; Chen, J.; Maddalena, F.; García Ferré, F.; Di Fonzo, F.; Caironi, M. Injection Length in Staggered Organic Thin Film Transistors: Assessment and Implications for Device Downscaling. *Adv. Electron. Mater.* **2016**, *2* (8), 1600097.
- (7) Xu, Y.; Liu, C.; Scheideler, W.; Darmawan, P.; Li, S.; Balestra, F.; Ghibaudo, G.; Tsukagoshi, K. How Small the Contacts Could Be Optimal for Nanoscale Organic Transistors? *Org. Electron. physics, Mater. Appl.* **2013**, *14* (7), 1797–1804.
- (8) Watanabe, S.; Ando, K.; Kang, K.; Mooser, S.; Vaynzof, Y.; Kurebayashi, H.; Saitoh, E.; Sirringhaus, H. Polaron Spin Current Transport in Organic Semiconductors. *Nat. Phys.* **2014**, *10* (4), 308–313.
- (9) Fert, A.; Jaffrès, H. Conditions for Efficient Spin Injection from a Ferromagnetic Metal into a Semiconductor. *Phys. Rev. B* **2001**, *64* (18), 184420.
- (10) Valet, T.; Fert, A. Theory of the Perpendicular Magnetoresistance in Magnetic Multilayers. *Phys. Rev. B* **1993**, *48* (10), 7099–7113.



## Chapter IV

# Interface resistance of EGOFETs

The reduction of transistors size is mandatory to improve performance of devices. However, while downscaling electric circuits, the potential drop across interfaces takes over the one within the organic channel. Devices become then contact limited because electrodes are not able to provide enough current to the channel. From there, further reduction of the system size is useless as the interface properties won't enhance and continue to dominate the whole electric behaviour. For organic electronic semiconductor devices, the critical channel length is few micrometers in size, thus being much larger than the state-of-the-art inorganic transistors size. Therefore, an important enhancement of the interface resistance is needed to overcome this key major issue for miniaturization. In addition, the magnitude of resistance interfaces values is key for spin information transfer as only a limited range of values is allowed in order to inject and detect spins properly.

In this fourth chapter, the interestingly low contact resistance of electrolyte-gated organic field-effect transistors (EGOFETs) is pointed out. First, the properties of the polymer are investigated to justify its choice. Then, we analyse the interface resistance upon doping, temperature sweeping and scaling down to the tens of nanometer scale. The injection area is also carefully discussed because of the current crowding effect – the elongation of the effective channel length due to the participation of the top of electrodes to the current (see chapter III). The consequences of the extended active area are investigated, with the support simulation and discussions from the previous chapter.

### IV.1. PBTTT thin film

Among the wide library of organic semiconductors we choose to focus on the poly(2,5-bis(3-tetradecylthiophen-2-yl)thieno(3,2-b)thiophene) (pBTTT) synthesized the first time by McCulloch and co-workers in 2006<sup>1</sup>. This polymer remains nowadays a first choice material because it is a

polymer forming semicrystalline structures, easy to process from solution, showing relevant mobility for applications ( $\mu \sim 1 \text{ cm}^2 \cdot \text{V}^{-1} \cdot \text{s}^{-1}$ ). PBTTT was previously studied in our laboratory, and conductivities above  $3000 \text{ S} \cdot \text{cm}^{-1}$  were found<sup>2</sup>, with indications of metal-insulator transition<sup>3</sup>, and interestingly low contact resistance with gold<sup>4</sup>. The group of Siringhaus in Cambridge also extensively worked on it and was able to reveal metallicity through Hall effect measurements at room temperature in another geometry<sup>5</sup>. Moreover, the spin diffusion length is expected to be around 200 nm in undoped pBTTT<sup>6</sup> and possibly above 1  $\mu\text{m}$  when highly doped<sup>7</sup>. All mentioned features of pBTTT make it an excellent candidate for our purpose, the realization of spin-based transistors.

PBTTT belongs to the wide polythiophene family. Its synthesis was motivated by the success of the regioregular poly(3-hexylthiophene) (RR-P3HT, **Figure IV.1a**) versus the regiorandom one (RRa-P3HT, **Figure IV.1b**) that proves the importance of alkyl chains for highly ordered thin film. McCulloch managed to keep RR-P3HT advantages and strongly reduced its drawbacks by lowering the alkyl side-chain density, fusing two thiophene rings to form a longer monomer (**Figure IV.1c**). By limiting the number of carbonated side-chains, pBTTT interdigitates better and regio-irregularities are less frequent. Therefore, the packing and ordering of pBTTT is enhanced compared to RR-P3HT. The thieno-rings are perpendicular to the dielectric substrate and lamellar structures were demonstrated<sup>8</sup>. The bicyclic thienothiophene in the middle of the monomer endows rigidity to the backbone and more importantly increases the ionization potential, leading to better oxidation stability. Thus, pBTTT is more crystalline and more stable than RR-P3HT, that translates into better transport performance with a mobility reaching almost  $2 \text{ cm}^2 \cdot \text{V}^{-1} \cdot \text{s}^{-1}$  in optimized devices<sup>5</sup> versus top value of  $0,1 \text{ cm}^2 \cdot \text{V}^{-1} \cdot \text{s}^{-1}$  for RR-P3HT<sup>9</sup>.

The ease of charge transport in pBTTT has been deeply examined by Liu and Troisi<sup>10</sup>. By density functional theory, they pointed out 3 main origins:

- The mobility edge is close to the valence band. The delocalization requires then only a little amount of energy to occur, easily provided by phonons.
- The conjugation length is long ( $\sim 10 \text{ nm}$ ). It means also that the coherence stays over a long distance, favouring efficient transport over tens of nanometres.
- The thermal fluctuations may be sufficient to detrap carriers. Traps from local distortions of the chain have a lifetime shorter than 0,1 ns, revealing that simple conformation changes may involve charge release.

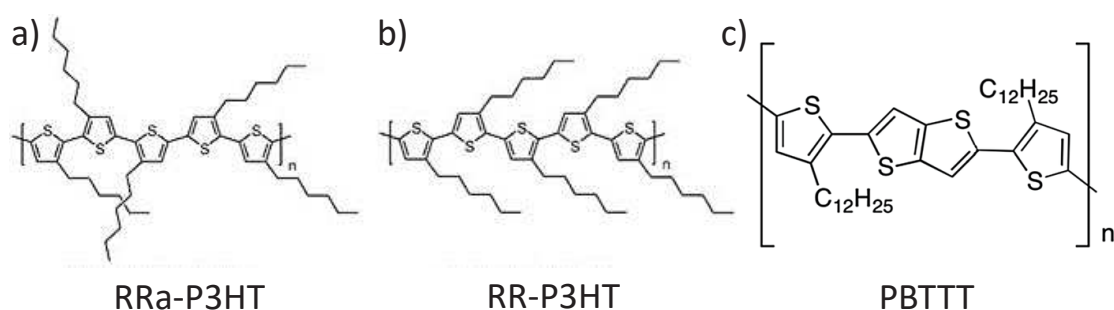


**Figure IV.1** Chemical structure of regiorandom P3HT-C6 (a), regioregular P3HT-C6 (b) and pBTTT-C12 (c).

As already detailed in the first chapter, thermal annealing of the deposited pBTTT thin film allows to change its morphology to obtain a polycrystalline structure with grains reaching 200 nm in size. Such large crystalline regions open the possibility to fabricate organic single-crystal transistors through electronic lithography for example. However, in our work we limit ourselves to a more disordered nodule-like phase. This choice is motivated by the study we want to perform: we compare large-scale transistors ( $L = 20 \mu\text{m}$ ,  $W = 1 \text{ mm}$ ) with nano-scale transistors ( $L \sim 100 \text{ nm}$ ,  $W \sim 40 \mu\text{m}$ ). Therefore, it would be possible to probe one single crystal in the nano-scale case, but not in the large-scale transistors as the channel length is way too large compared to the domain size. It is then more relevant to keep a “less crystalline” morphology for better electric properties comparison of both scales, as it depends on the polymer morphology.

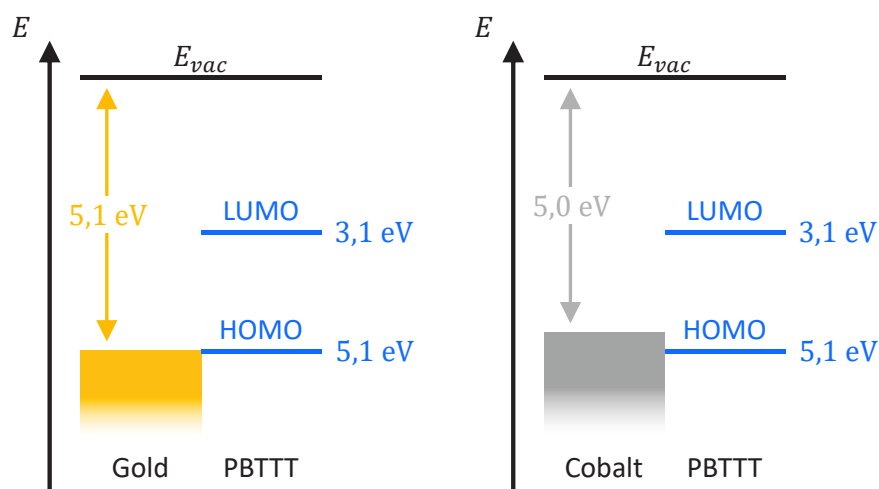


**Figure IV.2** Energy levels diagram of pBTTT-gold and pBTTT-cobalt junctions. For illustration, values given here are simply the energies from materials in vacuum.

The energy levels of pBTTT are 5,1 eV away from the vacuum level for the highest occupied molecular orbital (HOMO) and 3,1 eV for the lowest unoccupied molecular orbital (LUMO), it is thus a *p*-type semiconductor<sup>11</sup>. HOMO matches perfectly with gold as its work function ( $W_f$ ) is 5,1 eV and nicely also with cobalt where  $W_f = 5,0 \text{ eV}$  (**Figure IV.2**). We prefer cobalt as magnetic electrode even if nickel ( $W_f = 4,8 \text{ eV}$ ) was already studied in our group<sup>12</sup> because its better energy fitting is expected to optimize the contact resistance, and the spin polarization of cobalt is higher than nickel ( $\sim 23 \%$  vs.  $\sim 35 \%$ ), and should therefore increase the magnitude of spin signals.

One main issue of pBTTT for industrial purposes is its poor stability in ambient air. The rise of ionization potential limits its oxidation but it remains sensitive to moisture. The mobility typically drops by a factor 4 within 5 days after deposition if exposed to 50 % humidity. For that reason, the polymer deposition and room temperature measurements were performed in  $\text{N}_2$ -filled glove box ( $\text{H}_2\text{O}$  and  $\text{O}_2 < 3 \text{ ppm}$ ), and low temperature as well as magnetic studies were performed under primary vacuum ( $10^{-2} - 10^{-3} \text{ mbar}$ ).

The pBTTT used in this thesis was synthesized by Dr. Nicolas Leclerc from Institut de Chimie et Procédés pour l'Énergie, l'Environnement et la Santé (ICPEES) in Strasbourg. He followed the

recipe from McCulloch and ended up with a molecular weight of  $\sim 27$  kDa and a good polydispersity index (PDI) of 1,7. The PDI defines the heterogeneity of molecule size by the ratio  $M_W/M_n$ , where  $M_W$  is the mass-average molar mass and  $M_n$  is the number-average molar mass. Hence, if the PDI is 1 the chemical substance is perfectly homogenous, and value below 2 are indicative of good sample homogeneity. The backbone chain length is between 50 and 60 nm corresponding to roughly 40 monomers. The alkyl chains, helping for the stacking, are composed of 12 carbon atoms (pBTTT-C12).

The thin film deposition process is detailed in annex A, while basic electrical measurements such as output curves and transfer curves versus the temperature and dopant concentration are available in annex B. The main outcomes are optimized transistor behaviour, with high conductivity, large  $I_{On}/I_{Off}$  ratio and Ohmic contacts at room temperature over a wide range of source-drain voltage for gold and cobalt electrodes.

## IV.2. The low contact resistance of EGOFETs

First, we will review the way we extract the contact resistance ( $R_C$ ) on millimeter-scale (mT) and nano-scale (nT) transistors. Then, the interface resistances of mT and nT are investigated as a function of gate voltage and temperature.

The typical sample studied in this thesis is presented in **Figure IV.3**. On each chip, one or two mTs and three or four nTs are patterned. The typical dimensions are:  $L = 20 \mu\text{m}$ ,  $W = 0,1 \text{ mm}$  for mTs and  $L = 80 \text{ nm}$ ,  $W = 40 \mu\text{m}$  for nTs both sharing the same channel thickness  $h = 20 \text{ nm}$ . The transfer curve ( $I_{SD}(V_G)$ ) shows the high  $I_{On}/I_{Off}$  ratio of the order of  $10^5$ , reaching  $10^7$  on best samples, with a current approaching the milliampere for a source-drain voltage of  $-100 \text{ mV}$ . The output curve ( $I_{SD}(V_{SD})$ ) is ohmic for the highest doping level in the selected  $V_{SD}$  range but is slightly non-linear for lowest gate voltage and below 10 K. More detailed measurements are available in annex B.

Other geometries were investigated, in the scope of the realization of organic spin-valves, that are presented in the annex C. However, the high conductivity polymer we achieved in the EGOFET structure leads to geometric issues, highlighted in the annex, that we didn't manage to overcome. For this reason, the classical spin-valve design is not presented in the core of the manuscript.

### IV.2.1. Contact resistance extrapolation

#### Large-scale transistors

For mTs, we determine the contact resistance from the gated-4-probe method (gFP) already introduced in the first chapter. This technique allows to discriminate the source and drain potential drops by assuming a linear decrease of the potential along the pBTTT channel (**Figure IV.4**). Measuring the potential on two points ( $V_1$  and  $V_2$ ) within the channel, at known distance

from the source ( $L_1$  and  $L_2$ ), we deduce simply the slope ( $a$ ) and the intercept ( $b$ ). Then, the potential drops ( $\Delta V_S$  and  $\Delta V_D$ ) are:

$$\begin{aligned}\Delta V_S &= b - V_S \\ \Delta V_D &= V_D - V(L) = V_D - (aL + b)\end{aligned}\tag{IV.1}$$

where  $V_S$  is the potential applied to the source ( $V_S = 0$  V in our case),  $V_D$  the one on the drain ( $V_D = -100$  mV usually) and  $L$  is the channel length. However, when the pBTTT is highly doped, its resistance in our geometry ( $W/L = 50$ ) compares to the gold pads resistance, that are very long. It is even more true with cobalt electrodes as  $\rho_{cobalt} > \rho_{gold}$ . Therefore, the effective voltage applied to the organic semiconductor (OSC) is reduced by the voltage drop across leads ( $\Delta V_{pad}$ ). To subtract the latter parasitic decrease, we use the pseudo-4-probe measurements on nTs as we will see later. Once we obtain the potential drops, we directly get the contact resistance by dividing them by the current flowing in the transistor ( $R_{S,D} = \Delta V_{S,D}/I_{SD}$ ). It is worth noting that the potential difference between the two 4-probe electrodes is not enough to calculate the contact resistances of source and drain. The “absolute” potential values  $V_1$  and  $V_2$  are required, by probing them independently versus the source potential, to calculate  $\Delta V_S$  and  $\Delta V_D$ .

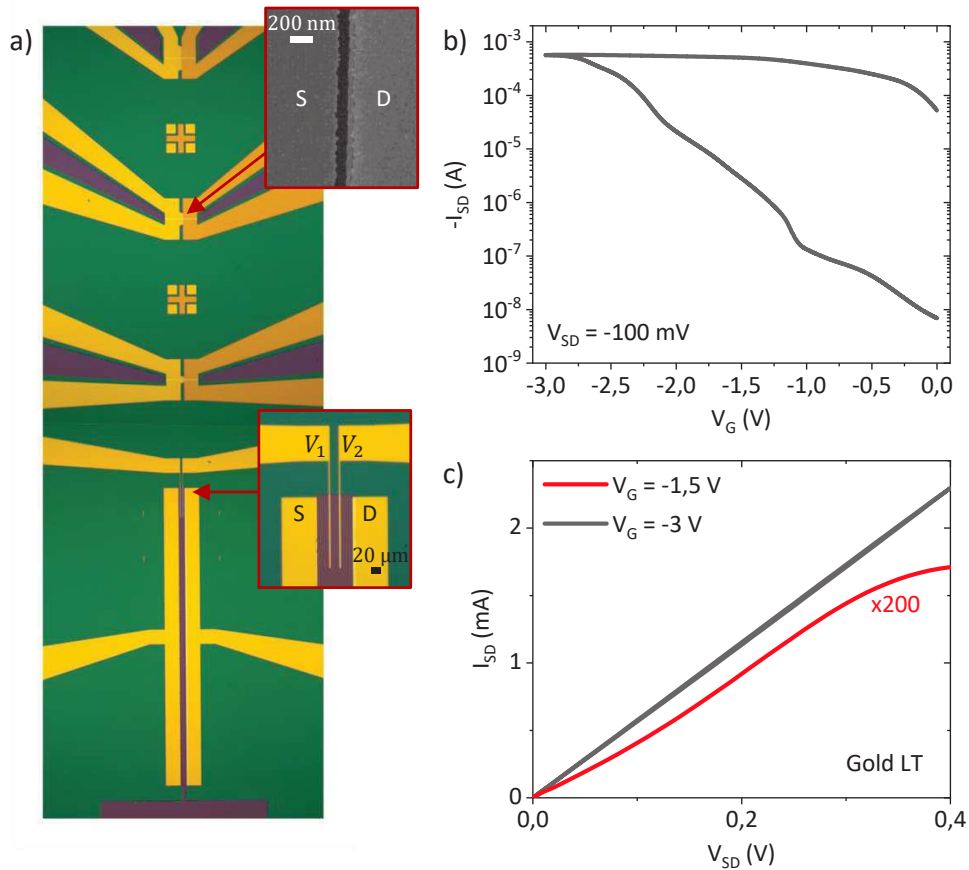


**Figure IV.3** a) Optical microscope image of a typical sample. Insets show electronic microscope image of one nano-gap (top) and a picture of 4-probe electrodes (bottom). The two steps are slightly visible on nTs, the right side being darker than the left side gold electrodes, corresponding to different thicknesses. The green colour

comes from the additional SiO<sub>2</sub> layer. b) Transfer curve of a gold mT. c) Output curves for two different gate voltages:  $V_G = -1,5$  V and  $-3$  V. The curve for low doping is scaled up by a factor 200 for clarity and show its slight non-linearity.

An important remark is the probable overestimation of the contact resistance using the gFP method. Indeed, a more pronounced potential decrease is expected close to the electrodes<sup>13</sup>, that is not taken into account by the gFP technique. It means that the very low values of interface resistances we will present may not be very accurate, but is an upper estimate, giving consistency to our claim of making devices with very low contact resistance.

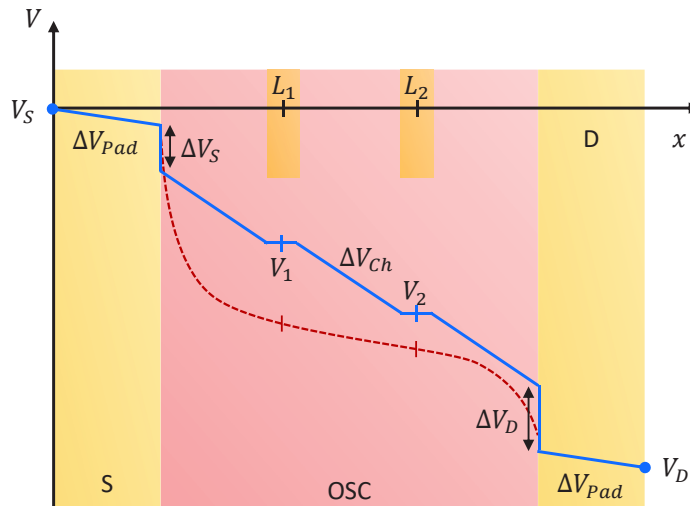


**Figure IV.4** Draw of the potential profile along the whole device. The blue line is the linear extrapolation used in the gFP method. The red dotted line is the shape of an alternative potential landscape with a faster decrease near the electrodes. Note that the extracted potential drop between the 4-probes electrodes could be very different in the two different cases, leading to a possibly large variation of the extracted contact resistance.

### Nano-scale transistors

In the case of nano-scale EGOFETs, the gFP method is not suitable as it would be very challenging to pattern two electrodes inserted between source and drain spaced by only tens or hundreds of nanometers. For that reason, we opted for pseudo-4-probe measurements where the voltmeter is connected onto the source and drain electrodes, the closest to the organic channel (**Figure IV.5**). The potential is thus probed at the end of source and drain wires that eliminates the pad resistances. The real potential applied is therefore  $|V_2 - V_1| < |V_{SD}|$ . The remaining metallic interconnect (the vertical leads on **Figure IV.5**) has been patterned in order to ensure that their resistances are below 0,2  $\Omega$  for gold and 0,4  $\Omega$  for cobalt.

Finally, in order to distinguish  $R_{Ch}$  from  $R_C$ , we use the conductivity inferred from the 4-probe measurements on the mT ( $\sigma$ ):

$$R_C = \frac{1}{2} [R_{Sample} - R_{Ch}] = \frac{1}{2} \left[ \frac{V_2 - V_1}{I_{SD}} - \frac{L^{nT}}{hW^{nT}\sigma} \right] \quad (IV.2)$$

Therefore, the presence of mT while probing nTs is mandatory, otherwise we could not separate the contact from the channel resistance. There is however uncertainty on the relevance of assuming conductivity values identical at the nano-scale and micrometer-/millimeter-scale as it supposes good reproducibility and similar material structures in the 100 nm and 20  $\mu\text{m}$  length scales. We will see that our conclusion of low contact resistance remains robust versus the conductivity values hypothesis. It is worth noting that nTs measurements do not allow to distinguish between source and drain resistance. We have only access to  $2R_C = R_S + R_D$ .

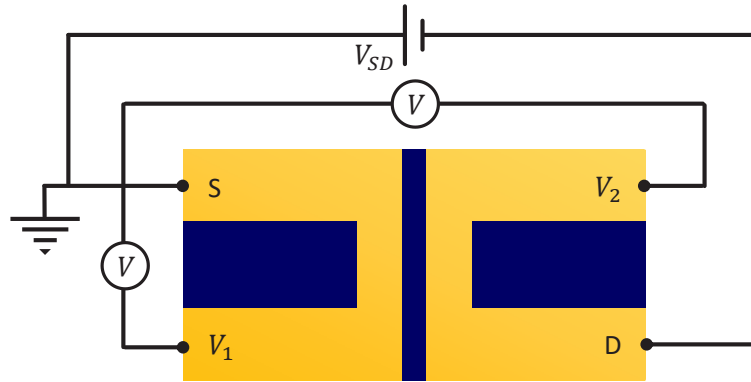


**Figure IV.5** Drawing of the electric connections on nTs. The potentials  $V_1$  and  $V_2$  correspond to the end of the metallic wires.

Our “U-shape” geometry also provides information on the resistivity of the metal pads. Indeed, we know the potential we apply on one side of wires, and we measure the potential on its other side. As we know perfectly the design of our samples, we know the length, width and thickness of the leads, thus we have all information we need to calculate the resistivity of the metal. It is useful for the calculation of the pads resistance on mTs as previously mentioned. Moreover, as the latter measurements is anyway performed to study the nTs, we are able to determine the variation of resistivity of metals within the temperature and/or magnetic field sweeps. This technique is then an efficient way to subtract the parasitic pad resistance values. For room temperature in glovebox (see next section), we lack multiple cabling necessary for simultaneous measurements of the pad resistance and mT properties. Thus, the resistivity of leads is first probe on these “U-shape” devices and used for the calculation of the resistance of mT pads, with their corresponding geometry. The uncertainty on the extracted pad resistance is estimated better than 5 %.

To give an order of magnitude, the wire resistances is usually  $> 20 \Omega$  on each side, while the channel resistance at the highest doping level is generally  $> 25 \Omega$  for mTs and can reach values down to few  $\Omega$  for nTs at room temperature. The low value on nTs is coming from the high aspect ratio  $W/L > 100$ . Note that reducing the aspect ratio to increase the channel resistance would not lead to  $R_{Ch} \gg R_{Pad}$ . Indeed, as we need  $L \sim 100$  nm, the only parameter we can tune is the width. However, downscaling  $W$  would accordingly raise the pad resistance, such that in the end  $R_{Pad}$  remains comparable to  $R_{Ch}$ . Taking into account the pads resistances remains therefore essential.

In the following, the interface resistance will mainly be discussed as specific contact resistivity  $r_b$  that is the area-normalized contact resistance. As mentioned in the chapter III, the area nearly scales with the transfer length  $L_T$ . The two methods presented above to determine the contact

resistance  $R_C$ , are not taking into account the current crowding effect. The contact resistance  $R_C$  we extract is the contact resistance when taking into account the crowding in series with the channel resistance due to the partial currents on top of the electrode, over the length  $L_T$ :

$$R_C = R_C^{L_T} + R_{Ch}(L_T) = \frac{r_b}{W(h + L_T)} + \frac{L_T}{\sigma W h} \quad (IV.3)$$

By replacing  $L_T$  with equation III.1 and neglecting  $h$  versus  $L_T$ , the specific contact resistivity that takes crowding into account writes:

$$r_b = \left( \frac{R_C W}{2} \right)^2 \sigma h \quad (IV.4)$$

It has the advantage to not assume  $L_T \gg L$  compared to equation III.3. Indeed, it is important for mT where the latter condition is often not fulfilled as we will see later. In the case of nT, equation III.3 and IV.4 lead to the same result as in general  $L_T$  is longer than the channel length.

Equation IV.4 also allows us to distinguish the source from the drain specific contact resistivity and transfer length, as we only have to replace  $R_C$  by  $R_S$  and  $R_D$  to obtain  $r_{b,S}$  and  $r_{b,D}$  and corresponding  $L_{T,S}$  and  $L_{T,D}$ .

### IV.2.2. Gate-dependent contact resistance

The interface resistance is known to be low in EGOFETs since its first investigation in such system by Braga and co-workers<sup>14</sup>. They demonstrated specific contact resistance of the order of 10  $\Omega \cdot \text{cm}$ , at least 500 times lower than classical doping method of OFETs. The impressive interface property seems to be related to the ion penetration in the polymer. By changing the active polymer, they observed no significant variation of contact resistance, whereas an important difference in classical bottom-gate structure was shown<sup>15</sup>. Therefore, the choice of the polymer is not responsible for the very weak  $R_C$ . It is plausible that ions at the OSC-metal interface create an additional electric field driving charge injection.

We first checked how the interface resistance changes versus the gate voltage, *i.e.* the doping level. The electrical property measurements were performed with a Keithley 2636A series SourceMeter and a Keithley 2182 nanovoltmeter connected to the 4-probe electrodes. For better comparison of the contact resistance with the literature, it is usual to refer to **specific contact resistance** ( $R_C W$ ), given in  $\Omega \cdot \text{cm}$ . This definition makes the interface resistance independent on the width of injection as doubling of width would divide  $R_C$  by two – as there is two times more injection area – letting  $R_C W$  unchanged. This variable was introduced in the scope of bottom-gate bottom contacts OFETs, where the accumulation channel thickness is only about few nanometres and is not expected to change significantly with the thickness of the organic layer or the injection -detection electrodes. Therefore, the injection/detection areas are close to a line. However, the physical quantity is the **specific contact resistivity**  $r_b = R_C A$ , where  $A$  is the involved area for injecting or detecting carriers. In the case of staggered geometries (bottom gate top electrodes OFETs, EGOFETs), the injection/detection areas are larger and generally assumed

equal to the edge of the electrodes ( $A = Wh$ , where  $h$  is the electrodes thickness). However, because of the crowding effect, the effective area involved in current transport is larger, and finally  $A = W(h + L_T)$ . In the following, only the latter injection/detection areas are considered, and the specific contact resistivity refers to  $r_b = R_C^{L_T} W(h + L_T)$ . As a reminder, mTs are 0,1 cm wide and  $h = 20$  nm.

In this chapter, the black curves refer to measure on gold electrodes, whereas blue ones are related to cobalt wires (section IV.3). In addition, all contact resistances include the crowding effect unless stated otherwise, but the exponent " $L_T$ " is omitted for clearer notation  $R_C^{L_T} \rightarrow R_C$ . As a rule of thumb, taking into account the current crowding results in dividing the (specific) interface resistance by a factor two. We emphasize again here that it can however modifies more drastically the interface contact resistivity  $r_b$ , which is the physical quantity intrinsic to an interface, of interest.

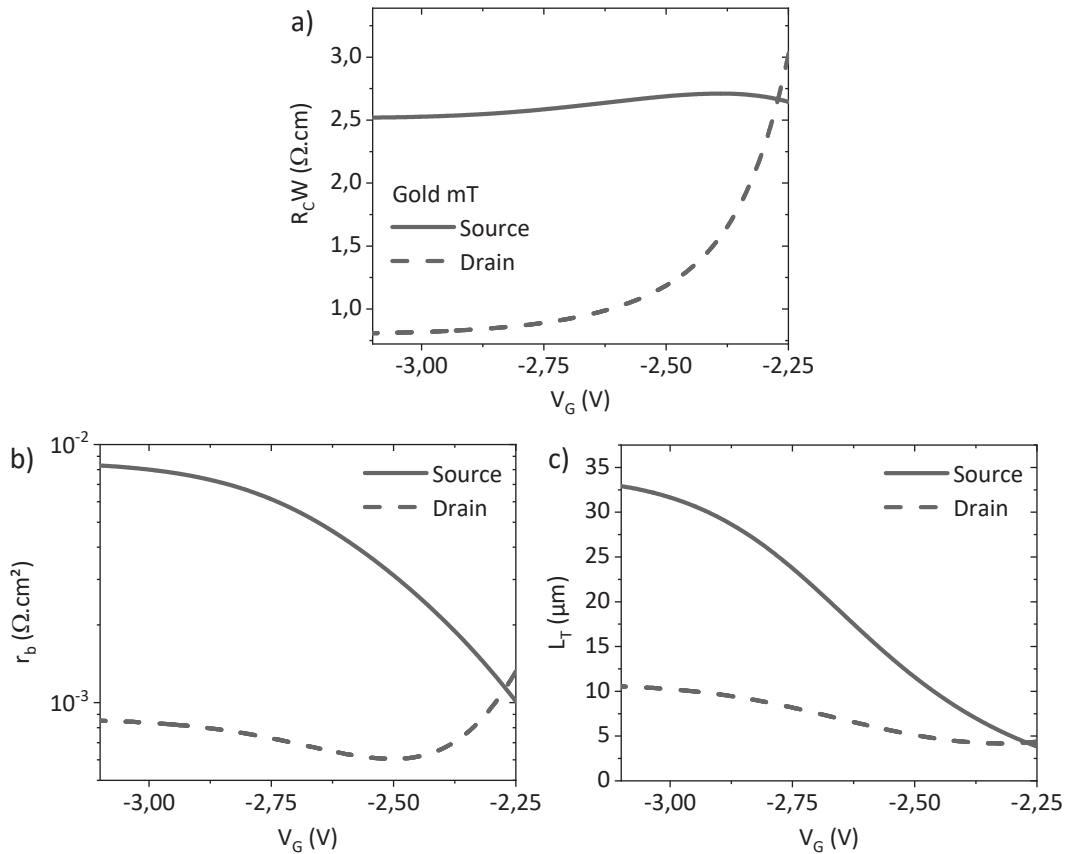


**Figure IV.6** Specific contact resistance (a) and resistivity (b) and related transfer lengths (c) of source and drain mT versus the gate voltage.

An average specific contact resistance  $R_C W < 2 \Omega \cdot \text{cm}$  is found at the highest doping level (**Figure IV.6a**). The low value obtained on gold is very interesting as it is the lowest reported to our knowledge in organic devices<sup>16</sup>. However, the crowding effect is not included in the major part of contact resistance studies. Assuming that the simple division by 2 we observed on our devices hold true,  $R_C W$  is comparable with the work of Braga and co-workers on electrolyte-

gated transistors<sup>14</sup>. The very long transfer length (**Figure IV.6c**), the longest we measured, comes partially from the particularly high conductivity of our sample, reaching more than  $650 \text{ S. cm}^{-1}$ .

We note also a different behaviour of source and drain resistances upon gate voltage rise.  $R_S$  is almost flat within the selected range whereas  $R_D$  is decreasing. The doping mechanism of EGOFETs is likely its origin. The first step of the doping process is the extraction of one electron, to create a positive charge, compensated afterwards by an anion from the electrolyte. It is then rational to imagine an easier doping close to the source – where electrons are extracted – reducing the contact resistance sooner in the  $V_G$  ramp. Then, the dopants spread uniformly within the organic channel and finally the polymer is uniformly doped, and the drain resistance also reaches its minimum value.

The intrinsic quantity to a hybrid metal-organic interface is  $r_b$ , found to reach  $\sim 5 \times 10^{-3} \text{ } \Omega. \text{ cm}^2$  in our sample in **Figure IV.6b**. Note that this data, designed to emphasize the role of the crowding, shows the largest values we observed in our samples (see **Figure IV.19** at the end of the chapter summarizing all data). We will see later that much smaller values can be observed in our devices. Nevertheless, our quoted maximum observed value remains smaller than those found for electrostatically gated OFETs. To our knowledge, the smallest  $R_C W$  values were reported by Umeda *et al.*<sup>17</sup>. They reported  $6,5 \times 10^3 \text{ } \Omega. \text{ cm}$ , while typical values for standard OFETs are larger, spanning the range  $10^4 - 10^6 \text{ } \Omega. \text{ cm}$ <sup>16</sup>. Umeda *et al.* compared top-contact (TC) OFETs, where current crowding is possible, and bottom-contact (BC) OFETs, where the crowding effect doesn't occur. We extracted  $r_b \approx 0,5 \text{ } \Omega. \text{ cm}^2$  and  $r_b \approx 1,2 \times 10^{-2} \text{ } \Omega. \text{ cm}^2$  respectively for TC and BC, with  $h = 3 \text{ nm}$  for BC (charge accumulation) and a transfer length for the TC estimated to  $3,6 \text{ } \mu\text{m}$ . Our finding confirms the claim of Braga *et al.*<sup>14</sup> who investigated EGOFETs. At high doping level on P3HT we approximate that they report  $r_b \approx 10^{-3} \text{ } \Omega. \text{ cm}^2$ . However, these values are estimates, deduced from the data on total resistance and interface resistance values, with large uncertainty related to the lack of information on the conductivity values and absence of discussion of crowding length in their devices. In summary, for our largest reported values and the lowest values reported by Braga, the difference in specific contact resistivity between EGOFETs and OFETs is typically one order of magnitude when we compare the proper physical quantities, namely  $r_b$ .

The choice of this sample exhibiting  $L_T > 20 \text{ } \mu\text{m}$  was motivated to pointed out how large the transfer length could be. In this case, it triples the effective channel length, but more importantly it impacts very significantly  $r_b$ . Indeed, the effective injection/detection surfaces can increase by up to three orders of magnitude by considering  $L_T$ , that scales linearly  $r_b$ . Therefore, only  $r_b$  that takes into account the transfer length will be discussed in the following.

### IV.2.3. Temperature-dependent contact resistance

Spin injection, transport and detection is much more efficient a low temperature, generally below 50 K. Indeed, by decreasing the temperature, the probability to scatter on phonons is weaker as their number diminishes exponentially with the temperature. Therefore, we investigated the temperature-dependence of contact resistance in EGOFETs down to 1,5 K. Again, basic electric properties at low temperature are provided in annex B. All measures of this chapter are performed at the highest doping level ( $V_G = -3 \pm 0,1 \text{ V}$ ) except stated otherwise.

$r_b$  and  $\sigma$  are plotted against the temperature in **Figure IV.7**. The specific contact resistivity remains very small, never exceeding  $4 \times 10^{-4} \Omega \cdot \text{cm}^2$ . The source transfer length decreases by a factor 5 over the temperature range with a maximum value of  $\sim 2 \mu\text{m}$  at 200 K. The very low specific contact resistivity and corresponding transfer length observed on drain electrode have to be carefully considered because the related  $R_C$  is smaller than the uncertainty on the pad resistance. Its behaviour is indeed similar to the pad resistance over a wide range of temperature ( $\sim 60 - 200 \text{ K}$ ). Nevertheless, it means that the drain  $r_b$  is smaller than the source one. The peak presents around  $3 - 5 \text{ K}$  is an experimental artefact coming from an abrupt heating of the sample at this temperature range in our cryostat.

The subtraction of the pads resistance is sometimes an issue for the calculation of source and drain contact resistances. Indeed, with the gFP method, a small error on the potential slope within the channel translates possibly into significant uncertainty on both contact resistances. Adding the uncertainty of the pads resistance, it happened that the extracted interface resistances were negative. It pointed out how important is the accuracy of all parameters of the device.

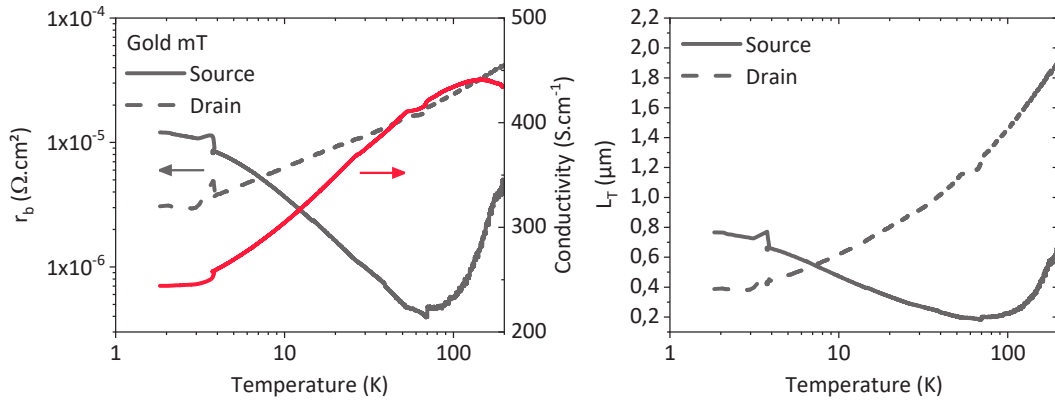


**Figure IV.7** Specific contact resistivities of source and drain (left) and the related transfer length (right) versus the temperature. The corresponding channel conductivity is also shown in the left panel.

The combination of temperature and gate voltage dependence is exhibited in **Figure IV.8**. For lower gate voltage, *i.e.* weaker doping level, both  $r_b$  diverge below 6 K likely because the potential profile becomes highly non-linear. The tuning of the interface resistance through the dopant concentration hence needs careful analysis and the gFP method may not be suitable for too low carrier density. In addition, values below 10 K are doubtful (for both doping level) because the applied source-drain voltage ( $V_{SD} = -100 \text{ mV}$ ) is not in the linear part of the output curve (annex B). We should therefore take with some care the difference between source and drain interfaces deduced in this section. From now, we will consider the average of the two values as the quantity of interest, as it is an experimental outcome that we found reproducibly, and less sensitive to series circuit resistance corrections.

The scale of transistors studied until now is far too large for spin detection. Indeed, the channel length has to be shorter than the spin diffusion length ( $\sim 200 \text{ nm}$ ) in order to detect spins. Thus, the downscaling of EGOFETs to the 100 nm-size is required.

### IV.2.4. Scaling of the contact resistance

The previous results are encouraging, confirmed by their record low value of interface resistance of metal-organic interfaces. However, spin injection over tens of micrometers is unrealistic as the spin of electrons is kept only over some tens or few hundreds nanometers in organic materials. Therefore, we studied how the interface resistance evolves when downscaling the device, in the same EGOFET structure, going down to channel lengths matching the requirement of spintronics. However, at the nanometer-scale, short channel effects introduced in chapter I become an issue for applications.

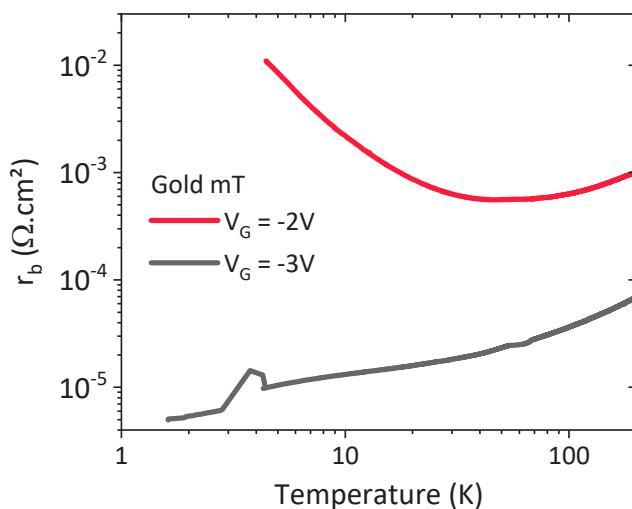


**Figure IV.8** Specific contact resistivity of mT versus temperature for two doping levels measured on the same sample.

To our knowledge, only one article presents nano-scale organic transistors without severe short-channel effects<sup>18</sup>. Herlogsson *et al.* achieved high transverse electric field using electrolyte gating that recovers the saturation of output curves. However, their  $I_{On}/I_{Off}$  ratio was limited to 25. This work was actually an important starting point in our group. Unfortunately, the contact resistance was not described in their article.

Channel lengths of  $80 \text{ nm} < L < 600 \text{ nm}$  were then patterned by shadow-edge evaporation or focused ion beam cutting as explained in annex A, with typical width of  $40 \mu\text{m}$ . Transistor performances, reported in annex B, are very close to mT, with no signs of short-channel effects. The  $I_{On}/I_{Off}$  ratio remains large, exceeding  $10^5$ , and the output curves saturate. This is already an achievement on its own, as short-channel issues was often pointed out even for micrometer-long channel<sup>19,20</sup>, and we obtained data clearly improving the poor  $I_{On}/I_{Off}$  ratio reported by Herlogsson and co-workers.

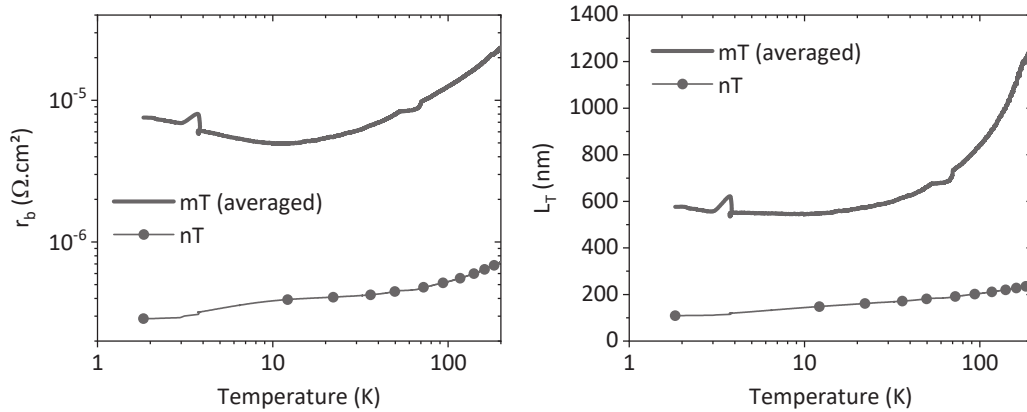


**Figure IV.9** Specific contact resistivity of mT and nT (left) and related transfer lengths (right) versus the temperature.

**Figure IV.9** presents the specific contact resistivity of nT ( $L = 80$  nm) compared to mT, and their respective transfer lengths. The main outcome is the spectacular decrease of the specific contact resistivity by 2 – 3 orders of magnitude by downscaling transistors to the nanometer-scale, becoming the lowest reported to our knowledge. Values ranging from  $10^{-7}$   $\Omega \cdot \text{cm}^2$  to  $10^{-6}$   $\Omega \cdot \text{cm}^2$  are very reproducible on nTs, over several samples and for various channel widths (**Figure IV.10**). Moreover, the  $L_T$  extracted from nT is roughly 100 nm at 1,5 K and slightly larger than 200 nm at 200 K. As expected from  $r_b$ , the transfer length is very short compared to the mT and the literature. The contrast between the  $L_T$  on large- and nano-scale transistors shows also that the crowding effect is mainly a matter of precision gain for mTs, as the channel elongated by only  $\sim 10$  %, but is of paramount importance for nTs as the effective channel length is in the end much longer than the nominal channel length  $L$ . The lowest transfer length measured during the project was  $\sim 40$  nm at 200 K, that already doubled the charges journey in the organic channel in our nTs.

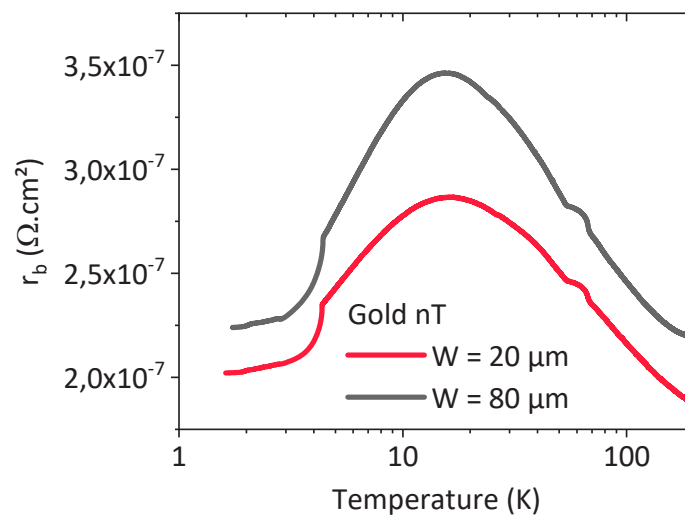


**Figure IV.10** Specific contact resistivities of 20  $\mu\text{m}$ - and 80  $\mu\text{m}$ -width nTs on the same chip ( $L = 80$  nm). The difference is negligible.

It is worth noting that the particularly low specific contact resistivity remains a rather robust claim versus the possible unknown conductivity of the polymer. Indeed, the assumption of equal conductivity of mTs and nTs is questionable as there is no real proof that the polymer transport charges with the same efficiency on both scales. For example, based on the sample from **Figure IV.9**, if we multiply the conductivity by 10,  $r_b$  remains around  $6 \times 10^{-6} \Omega \cdot \text{cm}^2$ . On the other hand, if we suppose that the nT specific interface resistance is the same as the one found on large scale devices, let's say of  $10^{-5} \Omega \cdot \text{cm}^2$ , the conductivity should then be multiplied by a factor  $\sim 15$ , reaching values  $> 6000 \text{ S} \cdot \text{cm}^{-1}$ . As the lowest  $r_b$  values are found for the highest conductivities (see **Figure IV.19**), the hypothesis of  $r_b$  not changing with the device length scale, while the conductivity is enhanced when downsizing, results in remarkably high conductivity values. This trend in **Figure IV.19** makes this hypothesis unlikely.

The spin diffusion length expected around 200 nm given from the beginning of this report was in fact demonstrated for the pBTtT by Watanabe and co-workers<sup>6</sup>. Using a trilayer structure of  $\text{Ni}_{80}\text{Fe}_{20}/\text{pBTtT}/\text{Pt}$ , they injected spin current in the polymer by spin pumping through ferromagnetic resonance of the  $\text{Ni}_{80}\text{Fe}_{20}$  magnetic layer. Reaching the platinum layer, the spin current converts into an electric field orthogonal to both the current and the spin polarization due to the spin-orbit coupling (inverse spin Hall effect). The spin polarization coming out of the pBTtT is thus directly related to the potential difference measured on the Pt layer. Moreover, the very recent work of Wang *et al.* pointed out a possible longer  $l_{sf}$  for highly doped pBTtT that may exceed  $1 \mu\text{m}$ <sup>7</sup>.

The transfer length exhibited on nano-scale EGOFETs in addition to their low  $r_b$  and their high conductivity make our devices excellent candidates for spin injection and detection as  $r_b/r_N$  has reasonable values (**Figure IV.11**). Reporting the values of  $r_b$  on the expected MR that consider the crowding effect (from the simulation of chapter III), an MR signal should be possible. However, these very interesting results apply for gold. The electrical properties must now be tested on magnetic electrodes for spin-valves fabrication.

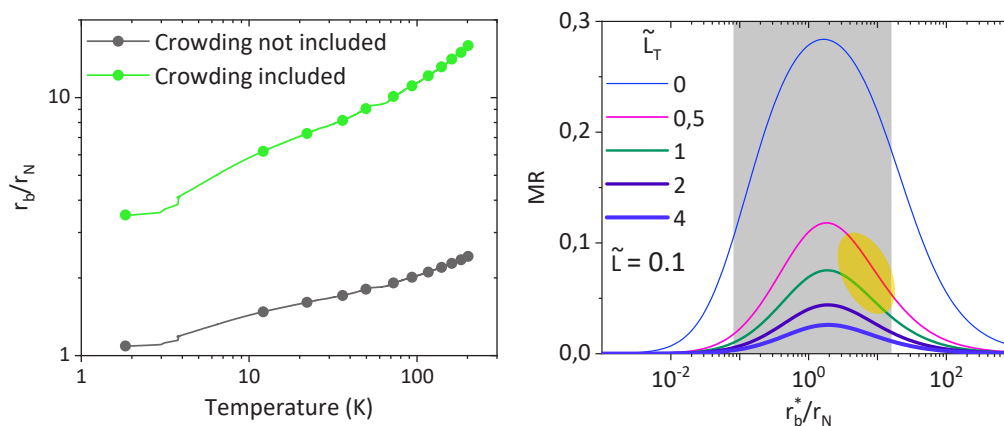


**Figure IV.11** The plots on the left presents the  $r_b/r_N$  ratio for the nT when the crowding effect is included or not. On the right is shown again the calculation of the MR amplitude by adding the transfer length (see chapter III). The yellow region points out the area in which the latter sample would be among the temperature

variation. The grey area underneath is the range of usual  $r_b/r_N$  measured on the same structure since our group is interested in.

### IV.3. Magnetic electrodes for spin injection

To go further towards spin-based transistors, the gold electrodes were changed to cobalt electrodes. The choice of cobalt results from its work function very similar to gold (difference of 0,1 eV), its high spin-polarization ( $\sim 35\%$ ) and, to a less extent, our experience in fabricating cobalt thin film of good quality. The fabrication process and basic electrical characterization are shown in annexes A and B.

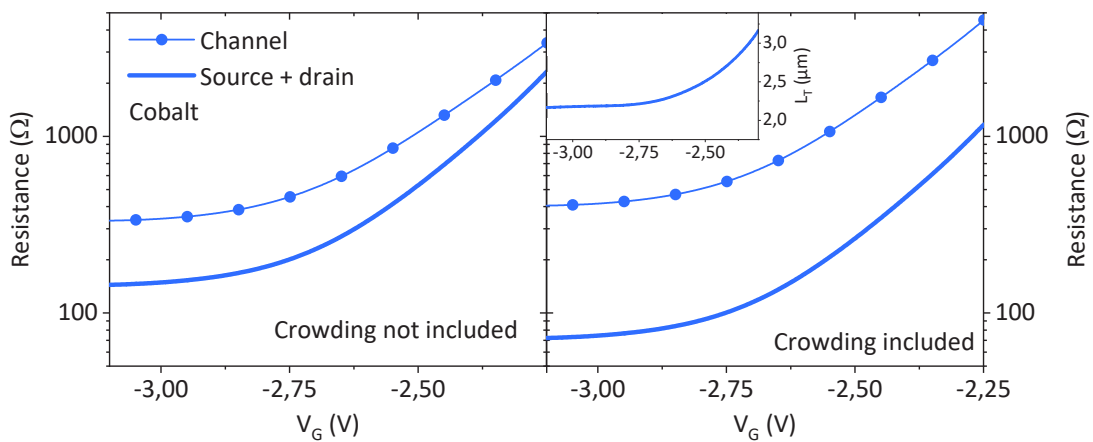


**Figure IV.12** Comparison of the average contact resistance with the channel resistance, without considering crowding effect (left) and when taking it into account (right).

The dependence of channel and total contact resistance on the gate voltage is illustrated in **Figure IV.12**. Again, the impact of the current crowding is pointed out. The device is not contact limited, the crowding being included or not. We generally observed that the conductivity significantly reduced for cobalt electrodes when compared to gold, with an approximate factor 10 reduction. We attribute this to the differences in samples preparation. Indeed, as no UV-ozone cleaning can be performed on cobalt, the surface of the substrate may suffer of impurities or bad wettability of the polymer solution during the spin-coating (annex A). Moreover, the acid glycolic treatment performed to etch the cobalt oxide could also be responsible for poor conductivity.

Organic materials are well known for their bad reproducibility. Thus, in order to verify that the difference between gold and cobalt is not coming from a more or less ordered polymer on different chips, we also fabricated heterogeneous mTs with one electrode made of gold and the other of cobalt, with the same treatment than the cobalt samples. By separating source from drain resistance, we recover values close to the previous ones with respect to the material (**Figure IV.13**). The figure depicted two different gate sweeps, by changing the source-drain polarization (once the cobalt is the source and once the drain) on the sample with the maximum

conductivity. The extracted specific contact resistivities are indeed robust against source and drain exchange. The gold  $r_b$  is more than one order of magnitude below the cobalt one, for almost the same conductivity (400 S. cm<sup>-1</sup> versus 500 S. cm<sup>-1</sup>).

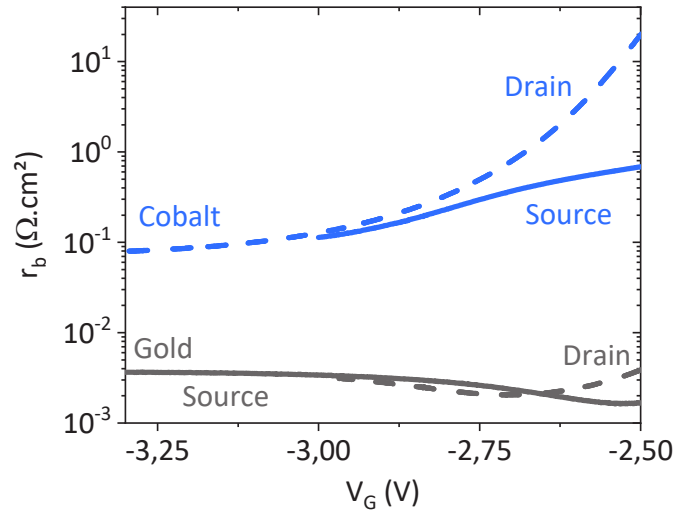


**Figure IV.13** Specific contact resistivities of source and drain on a heterogeneous mT versus the gate voltage. Two sweeps are shown for different source-drain polarization. The conductivities are slightly different, around 500 S. cm<sup>-1</sup> for the transfer curve reaching  $V_G = -3,3$  V and 400 S. cm<sup>-1</sup> for the other at their respective highest doping level. It may explain the small shift of  $r_b$ .

The maximum gate voltage is slightly different because it is usually easier to dope the polymer a second time. The organic channel reorganizes upon the penetration of ions and keeps some memory after the un-doping procedure that facilitates further doping process. The second  $V_G$  ramp, the cobalt being the source, was stopped at the appearance of negative transconductance (with source-drain current decreasing when increasing further the gate voltage, not shown), indicative of the maximum doping achievable.

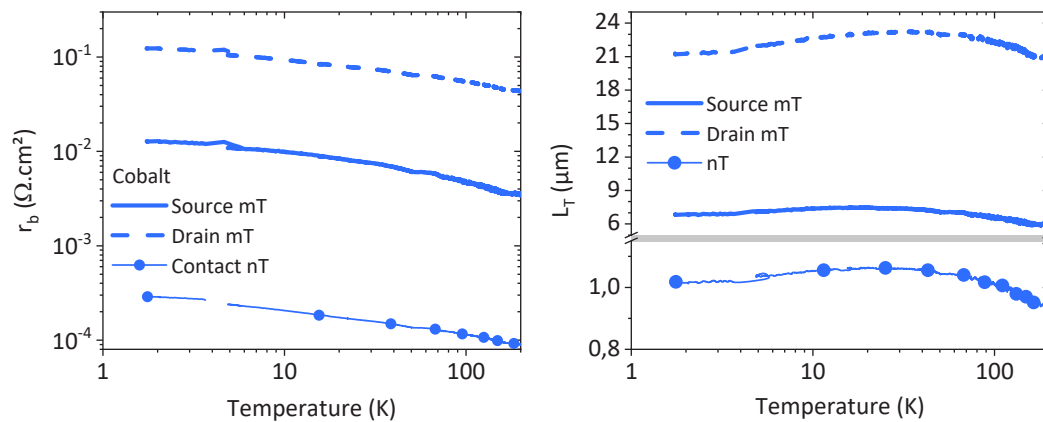


**Figure IV.14** Specific contact resistivity (left) and related transfer lengths (right) versus the temperature.  $r_b$  of mT and nT are compared on the left panel. The nT specific

contact resistivity is well below the mT one, but it is much larger than in the case of gold electrodes;  $L_T$  is thus longer.

The specific contact resistivity of mT and nT during a temperature ramp is shown in **Figure IV.14**. The  $r_b$  values are much larger than in the previous sample made of gold electrodes. Both mTs and nT  $r_b$  are roughly three orders of magnitude larger over the whole temperature range for cobalt than for gold. Moreover, the behaviour while cooling is different, with the specific contact resistivity while diminishing the temperature. It follows thermally activated processes, which is expected from the difference of energy between the Fermi energy of the metal and the HOMO of the polymer (**Figure IV.2**). The conductivity drops exponentially as it was the case in previous gold samples as demonstrated in the annex B. The transfer lengths are longer compared to gold-based devices as a result of the larger  $r_b$ , that is not enough counterbalanced by the reduction of conductivity ( $L_T = \sqrt{r_b \sigma h}$ ). Such elongation of the nT by  $\sim 1 \mu\text{m}$  is critical for spin injection/detection as the effective channel length becomes much longer than the spin diffusion length. Thus, achieving spin information transfer, when the average distance between injection and detection points exceed 2 microns, is unlikely, with the related spin-valve signal expected to be very small.

In fact, the rise of  $L_T$  is more detrimental for spin signal than the increase of  $R_c W$  as it results in a much larger  $r_b$  in addition to a severe drop of the MR. Finally, the ratio  $r_b^*/r_N$  related to the previous sample is no more suitable for efficient spin injection when the injection area is clearly defined (**Figure IV.15**).  $r_b^*/r_N$  behaves the same way than the transfer length, as  $L_T$  dominates the device.

In conclusion, the preliminary analysis of gold-pBTTT interface was highly motivating for the realization of organic spin-valves. EGOFETs with an appropriate effective channel length ( $L + 2L_T \leq 200 \text{ nm}$ ) were fabricated exhibiting outstanding specific contact resistivity 100 times smaller than the lowest reported in the literature. However, for FM electrodes,  $r_b$  increases significantly that implies a huge elongation of the effective channel length such that  $L + 2L_T \gg l_{sf}^{NM}$ . Therefore, the current crowding critically limits the spin-dependent properties in EGOFETs as well as in majority OFET structures.

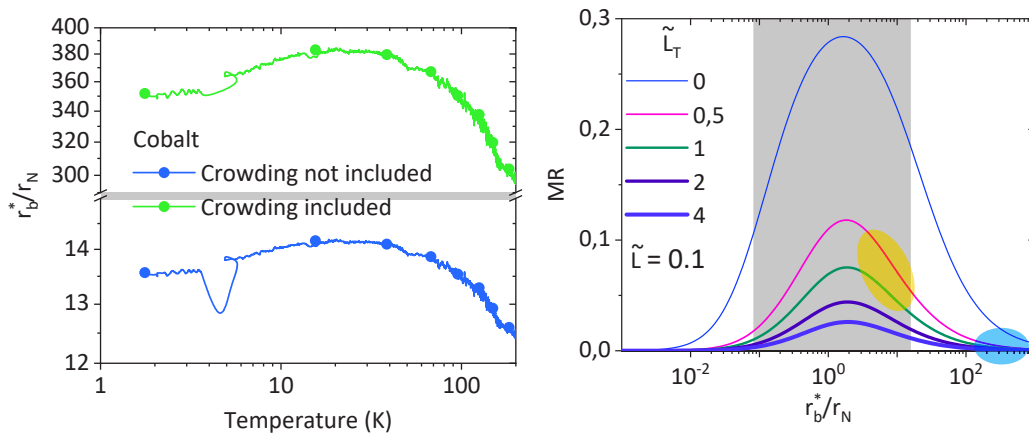


**Figure IV.15** The plots on the left presents the  $r_b^*/r_N$  ratio for the nT when the crowding effect is included or not. On the right is shown again the calculation of the

MR amplitude by adding the transfer length (see chapter III). The blue region on the right highlights the typical values obtained on sample with cobalt.

## IV.4. Limiting the transfer length influence

$r_b$  is sensitive to  $L_T$ , that can be varies if the conductivity hypothesis is changed (see discussion in previous section). Better confidence in our small  $r_b$  values can be gained by avoiding crowding. This is also essential for spintronics, and in particular for our estimate of  $r_b/r_N$ . If  $r_b$  is underestimated, namely the crowding length is larger, this relates to a better conductivity, and therefore a smaller  $r_N$ . The ratio  $r_b/r_N$  is therefore highly sensitive to the conductivity value hypothesis when analysing our results. Therefore, the best way around this issue, and the best check for or ultra-small  $r_b$  findings, is to design EGOFETs exempt of crowding. One possibility is to diminish the size of the source and drain electrodes, with an injection/detection area limited by the electrode's sizes. This involves challenging fabrication of sub-100 nm size electrodes, in addition to severe issues of series resistance due to the small electrodes, making possible non-uniform applied voltages on source and drain contacts. A more attractive alternative is to cover the source-drain electrodes with an insulating layer, leaving only their side capable of injecting and detecting carriers. We found impractical to use lift-off lithography techniques for making metal-insulator electrodes (necessity of two separate evaporation chambers, difficulties in lifting the rather thick dielectric). We therefore patterned metal electrodes making a continuous electrode for defining the source and drains, initially shorted. After covering the whole sample with SiO<sub>2</sub>, focused ion beam (FIB) was used to cut the metal-SiO<sub>2</sub> structure and create the nano-gaps (see annex A). In the end, only the cut in the metallic wires can inject and detect the current (**Figure IV.16**). This method was performed on gold leads. In addition, it provides the freedom to vary the channel length as the cut area can be set when milling. This is an advantage to samples fabricated by the shadow-edge technique that exhibits nTs on a chip having all the same separation.



**Figure IV.16** Staggered structure for the suppression of the crowding effect. The SiO<sub>2</sub> layer covers the whole top surface of source and drain. The injection and detection areas are pointed out with the dark red lines.

The possibility to analyse the contact resistance versus the channel length is very interesting in order to understand the origin of the drop of  $R_C$  with the downscaling of the device. Therefore, nanogaps in the range of  $\sim 70$  nm to  $\sim 300$  nm are etched, while keeping the mT of  $20 \mu\text{m}$ . As multiple temperature ramps may damage the polymer, the conductivity on mT is always probed together with the electric properties of each nT, as only 2 transistors can be measured

for a given temperature sweep because of the limited number of connections. As shown in **Figure IV.17**, the conductivity is quite well reproducible under repeated temperature sweeps.

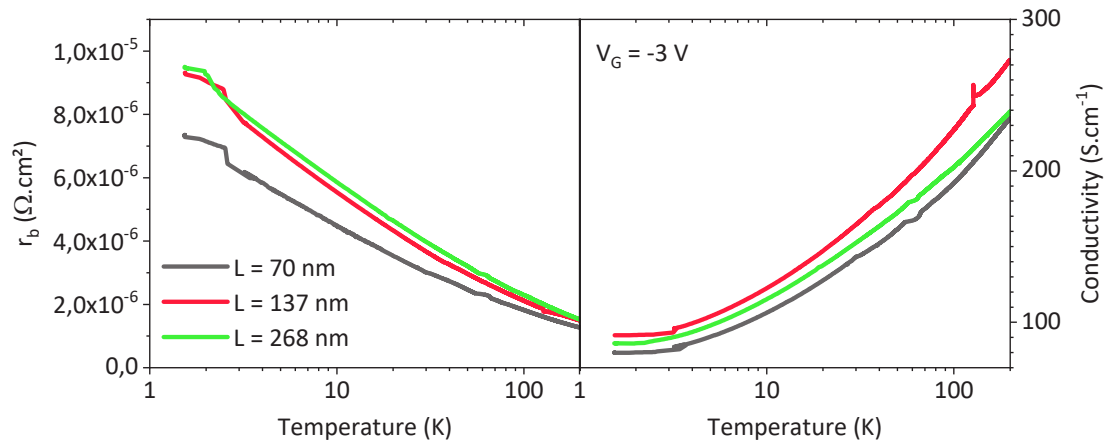


**Figure IV.17** Specific contact resistivity (left) and conductivity (right) versus the temperature for various nT lengths. The three curves of conductivity were measured through 4-point measurements on mT on the same chip than nTs, with the colour coding indicating the temperature sweep corresponding to the measured nT.

As the crowding effect is prohibited,  $r_b$  keeps its original definition:  $r_b = R_c Wh$ . The specific interface resistances extracted on these devices are 10 times larger than the previous gold-base nTs but remain lower than mTs. The results confirm the small value of  $r_b$  that was inferred from the previous section on gold nTs and the importance of considering crowding effects when analysing the value of  $r_b$  of our nano-scale lateral EGOFETs. It emphasizes also that the contact resistance could be tuned via the geometry of samples, by letting or not the top surface in touch with the channel, or either limiting the allowed transfer length with an insulator. However, the specific contact resistivity doesn't significantly change with the channel length and indicates that a broader range of investigated channel lengths should be used to explain the difference between mTs and nTs contact resistance.

**Figure IV.18** exhibits the calculated  $r_b/r_N$  ratios which are of the same order of magnitude as the ones extracted in section IV.2.4. However, the slope is inverted,  $r_b/r_N$  becoming here larger when cooling down the sample. The lack of transfer length may be the reason, as it tends to dominate the evaluation of  $r_b$  and decreases with the temperature.

The latter outcomes give robustness to the crowding effect as interface resistance is reduced due to the increase of area for injecting and detecting carriers. It however elongates too much the effective channel length for the injection and detection of spins. Nevertheless, by suppressing the current crowding, it may be possible to keep a reasonable  $r_b$  on gold, but the cobalt specific contact resistivity, reported here 100 to 1000 times larger, will likely remain an issue.

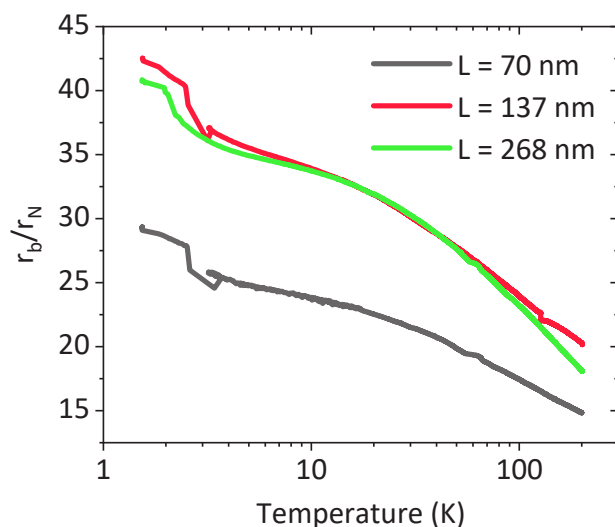


**Figure IV.18** Ratio  $r_b/r_N$  for the three different lengths versus the temperature when no current crowding is allowed.

As a summarizing figure of this chapter, the interface resistance of EGOFETs with gold and cobalt electrodes at micrometre and nanometre scales are depicted in **Figure IV.19** for most of the samples measured during the thesis, plus few from previous work in the group: filled square in the nT panel, IIDDT-based EGOFETs<sup>a</sup> (triangle) and transistors made of nickel electrodes in pink<sup>b</sup>.  $r_b$  is plotted versus the conductivity of the device, and it tends clearly to diminish with increasing conductivity. It confirms also a similar variation of gold and cobalt junctions on both scales, with a systematic larger value for cobalt than gold. The grey dashed line is mainly a guide for the eye from the initial definition of  $L_T$  ( $r_b = L_T^2/\sigma h$ ), for a sample having a transfer length of 1  $\mu\text{m}$  and 200 nm respectively for mTs and nTs. It translates into  $r_b = c\sigma^{-1}$  where  $c(\text{mT}) = 5 \times 10^{-3}$  cm and  $c(\text{nT}) = 2 \times 10^{-4}$  cm. We note that the majority of highly conductive gold-nTs is below the grey line, meaning that  $L_T$  is shorter than 200 nm. The very nice matching of samples with silicon oxide limiting the transfer length (half-filled symbols) with the grey line indicates that the method to account for the current crowding in the calculation of  $r_b$ , on sample needing it, is relevant.

Cobalt contact resistances are sparser and larger than their gold counterpart and the trend is not that clear, with however the nTs specific contact resistivity smaller than the mTs ones. It is also very interesting to see that samples made with nickel electrodes covered with graphene RTA places in between the cobalt and gold  $r_b$ . The specific interface resistance of samples less doped (encircled in red and green) are also added to the graph and is surprisingly not out of range despite the probable poor linearity of the potential drop along the channel.

<sup>a</sup>Poly[1,1'-bis(4-decyltetradecyl)-6-methyl-6'-(5'-methyl-[2,2'-bithiophen]-5-yl)-[3,3'-biindolinylidene]-2,2'-dione] (IIDDT-C3) is an isoindigo-based conjugated polymer with electric properties close to pBTTT and more stable in air<sup>21</sup>.

<sup>b</sup>Nickel is covered with graphene on one sample, grown with the rapid thermal annealing (RTA) method<sup>22,23</sup>.

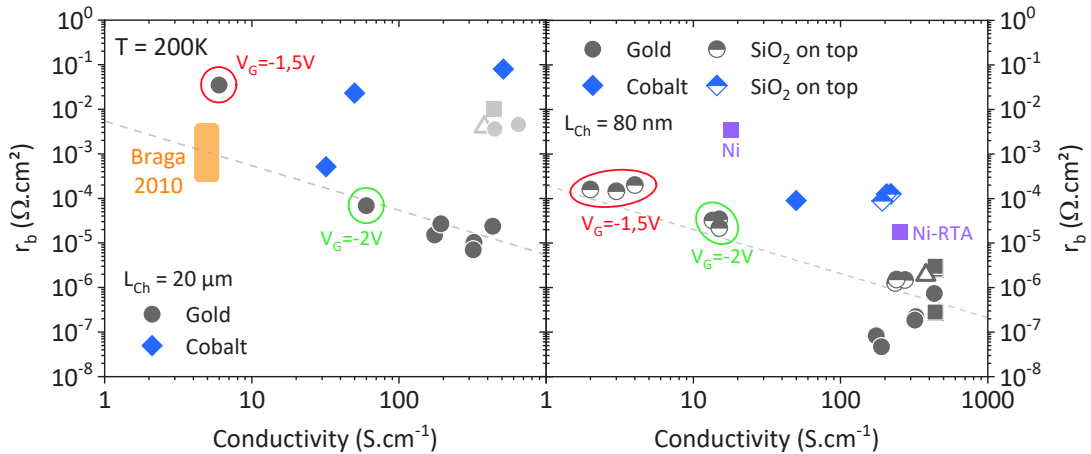


**Figure IV.19** Specific contact resistivity at 200 K versus the conductivity for nTs and mTs, with gold and cobalt electrodes and with or without an SiO<sub>2</sub> layer on top. For comparison, samples with nickel and nickel covered by graphene RTA electrodes are added (pink square), as well as EGOFETs with IIDDT instead of pBTTT (triangle). Black squares are value of previous work in the group on similar devices than presented in this thesis. The value of Braga *et al.* is also depicted.

An important point that would need further investigation concerns the values of gold-based mT in the top right corner of the corresponding panel. The grey dots were measured on sample where cobalt electrodes were also present on the chip and hence endure the same dipping in glycolic acid. It seems that the acid affects significantly the interface of gold and may also explain the generally higher  $r_b$  on cobalt electrodes. The other value in the same corner (also in grey) comes from a previous work where the pad resistances were not subtracted from the interface resistance, being likely the reason of the large  $r_b$  reported.

In the next chapter, an external magnetic field is applied on samples perpendicular and parallel to the current flow. For the sample made of gold electrodes, it will provide insight into the transport properties of the polymer, in particular for revealing possible transition to metallic-like behaviour. Investigating the magnetoresistance properties of the interface resistance, to our knowledge not reported in the literature, is also key for understanding how the total resistance changes under magnetic field. For cobalt electrodes, the magnetic field will switch the magnetization of the thin ferromagnetic layer to possibly reveal for spin-valve signal.

## Bibliography

- (1) McCulloch, I.; Heeney, M.; Bailey, C.; Genevicius, K.; MacDonald, I.; Shkunov, M.; Sparrowe, D.; Tierney, S.; Wagner, R.; Zhang, W.; et al. Liquid-Crystalline Semiconducting Polymers with High Charge-Carrier Mobility. *Nat. Mater.* **2006**, *5* (4), 328–333.
- (2) Zanettini, S.; Chaumy, G.; Chávez, P.; Leclerc, N.; Etrillard, C.; Leconte, B.; Chevrier, F.; Dayen, J.-F.; Doudin, B. High Conductivity Organic Thin Films for Spintronics: The Interface Resistance Bottleneck. *J. Phys. Condens. Matter* **2015**, *27* (46), 462001.
- (3) Zanettini, S.; Dayen, J. F.; Etrillard, C.; Leclerc, N.; Kamalakar, M. V.; Doudin, B. Magnetoconductance Anisotropy of a Polymer Thin Film at the Onset of Metallicity. *Appl. Phys. Lett.* **2015**, *106* (6), 2–6.
- (4) Verduci, T.; Chaumy, G.; Dayen, J. F.; Leclerc, N.; Devaux, E.; Stoeckel, M. A.; Orgiu, E.; Samori, P.; Doudin, B. Current Crowding Issues on Nanoscale Planar Organic Transistors for Spintronic Applications. *Nanotechnology* **2018**, *29* (36).
- (5) Kang, K.; Watanabe, S.; Broch, K.; Sepe, A.; Brown, A.; Nasrallah, I.; Nikolka, M.; Fei, Z.; Heeney, M.; Matsumoto, D.; et al. 2D Coherent Charge Transport in Highly Ordered Conducting Polymers Doped by Solid State Diffusion. *Nat. Mater.* **2016**, *15* (5), 896–903.
- (6) Watanabe, S.; Ando, K.; Kang, K.; Mooser, S.; Vaynzof, Y.; Kurebayashi, H.; Saitoh, E.; Sirringhaus, H. Polaron Spin Current Transport in Organic Semiconductors. *Nat. Phys.* **2014**, *10* (4), 308–313.
- (7) Wang, S.-J.; Venkateshvaran, D.; Mahani, M. R.; Chopra, U.; McNellis, E. R.; Di Pietro, R.; Schott, S.; Wittmann, A.; Schweicher, G.; Cubukcu, M.; et al. Long Spin Diffusion Lengths in Doped Conjugated Polymers Due to Enhanced Exchange Coupling. *Nat. Electron.* **2019**, *2* (3), 98–107.
- (8) Schuettfort, T.; Watts, B.; Thomsen, L.; Lee, M.; Sirringhaus, H.; McNeill, C. R. Microstructure of Polycrystalline PBTTT Films: Domain Mapping and Structure Formation. *ACS Nano* **2012**, *6* (2), 1849–1864.
- (9) Sirringhaus, H. Integrated Optoelectronic Devices Based on Conjugated Polymers. *Science (80-. )*. **1998**, *280* (5370), 1741–1744.
- (10) Liu, T.; Troisi, A. Understanding the Microscopic Origin of the Very High Charge Mobility in PBTTT: Tolerance of Thermal Disorder. *Adv. Funct. Mater.* **2014**, *24* (7), 925–933.
- (11) Gludell, A. M.; Cochran, J. E.; Patel, S. N.; Chabinyk, M. L. Impact of the Doping Method on Conductivity and Thermopower in Semiconducting Polythiophenes. *Adv. Energy Mater.* **2014**, *5* (4), 1401072.
- (12) Verduci, T.; Yang, C. S.; Bernard, L.; Lee, G.; Boukari, S.; Orgiu, E.; Samorì, P.; Lee, J. O.; Doudin, B. Carbon-Passivated Ni Electrodes for Charge Injection in Organic Semiconductors. *Adv. Mater. Interfaces* **2016**, *3* (6), 1–9.
- (13) Bürgi, L.; Sirringhaus, H.; Friend, R. H. Noncontact Potentiometry of Polymer Field-Effect Transistors. *2007*, *2913* (2002), 1–4.
- (14) Braga, D.; Ha, M.; Xie, W.; Frisbie, C. D. Ultralow Contact Resistance in Electrolyte-Gated Organic Thin Film Transistors. *Appl. Phys. Lett.* **2010**, *97* (19).
- (15) Bürgi, L.; Richards, T. J.; Friend, R. H.; Sirringhaus, H. Close Look at Charge Carrier Injection in Polymer Field-Effect Transistors. *J. Appl. Phys.* **2003**, *94* (9), 6129–6137.

- 
- (16) Natali, D.; Caironi, M. Charge Injection in Solution-Processed Organic Field-Effect Transistors: Physics, Models and Characterization Methods. *Adv. Mater.* **2012**, *24* (11), 1357–1387.
- (17) Umeda, T.; Kumaki, D.; Tokito, S. Surface-Energy-Dependent Field-Effect Mobilities up to  $1 \text{ cm}^2/\text{V s}$  for Polymer Thin-Film Transistor. *J. Appl. Phys.* **2009**, *105* (2).
- (18) Herlogsson, L.; Noh, Y.; Zhao, N.; Crispin, X.; Siringhaus, H.; Berggren, M. Downscaling of Organic Field-Effect Transistors with a Polyelectrolyte Gate Insulator. *Adv. Mater.* **2008**, *20* (24), 4708–4713.
- (19) Xu, Y.; Berger, P. R. High Electric-Field Effects on Short-Channel Polythiophene Polymer Field-Effect Transistors. *J. Appl. Phys.* **2004**, *95* (3), 1497–1501.
- (20) Chabynyc, M. L.; Lu, J. P.; Street, R. A.; Wu, Y.; Liu, P.; Ong, B. S. Short Channel Effects in Regioregular Poly(Thiophene) Thin Film Transistors. *J. Appl. Phys.* **2004**, *96* (4), 2063–2070.
- (21) Lei, T.; Cao, Y.; Fan, Y.; Liu, C. J.; Yuan, S. C.; Pei, J. High-Performance Air-Stable Organic Field-Effect Transistors: Isoindigo-Based Conjugated Polymers. *J. Am. Chem. Soc.* **2011**, *133* (16), 6099–6101.
- (22) Sun, Z.; Yan, Z.; Yao, J.; Beitler, E.; Zhu, Y.; Tour, J. M. Growth of Graphene from Solid Carbon Sources. *Nature* **2010**, *468* (7323), 549–552.
- (23) Peng, Z.; Yan, Z.; Sun, Z.; Tour, J. M. Direct Growth of Bilayer Graphene on  $\text{SiO}_2$  Substrates by Carbon Diffusion through Nickel. *ACS Nano* **2011**, *5* (10), 8241–8247.



## Chapter V

# EGOFETs in a magnetic field

The application of an external magnetic field to conductive materials is a way to gain better insight into its charge transport mechanisms. We therefore investigated the variation of resistance of electrolyte-gated organic field-effect transistors (EGOFETs) under magnetic field and detail how it can reveal the occurrence of metallic-type transport. In addition, we analyse the specific magnetoresistivity of interfaces to estimate in which extent it impacts the total magnetoresistance of the sample. Furthermore, in the case of cobalt-based EGO-FETs, the magnetic field experienced by the conducting polymer also involves the stray field created by the ferromagnetic electrodes, also dependent on the applied external field. We discuss how it can result in a magnetoresistance signal and analyse it in the light of the influence of the crowding effect.

### V.1. Magnetotransport

Investigation of the variation of resistivity of materials upon application of an external magnetic field provides information about the transport mechanisms. In chapter II, we already discussed the anisotropy of the magnetoresistance (MR) and the breaking of the weak localization. The former leads to a different MR behaviour depending if the magnetic field is parallel or perpendicular to the current flow, and the latter refers to a decrease of the resistivity in diffusive materials because of the decoherence of self-closing paths due to the field normal to the conductive plane. We have to emphasize that measurements are time consuming (commonly reaching three weeks per sample), essentially because of the needed room-temperature very slow gating or ungating process, and the required temperature sweeps when measuring the samples under different conditions. Because of the non-uniformity of organic thin film and the expected weak MR signals, results are often noisy and lack reproducibility. The need to change the magnetic field orientation requires either a cryogenic sample rotation setup that limits the

size of the sample under study, or heating/cooling procedure that is time consuming and might impact the reproducibility of the experiments. In the following, we restrict the presented data where stable and reproducible behaviours were observed, and comparisons relies as much as possible between measurements on EGOFETs on the same chip.

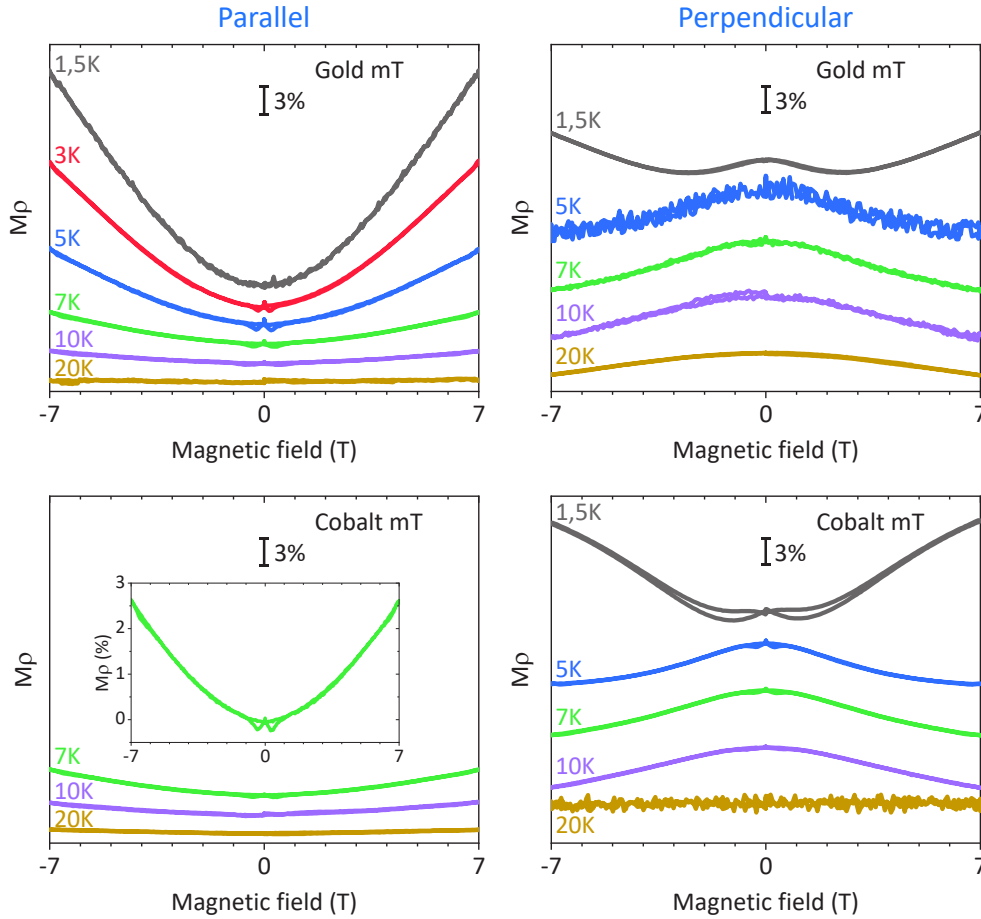


**Figure V.1** Magnetoresistivity of gold- (top) and cobalt-based (bottom) mT, in the parallel (left) and perpendicular (right) configurations. Curves are vertically shifted for clarity. Missing curves (3 K in perpendicular configuration and 1,5 K, 3 K and 5 K for the cobalt sample in parallel) were excluded because too noisy for interpretations. The resistivity on the cobalt transistor is one order of magnitude larger compared to the gold device ( $\rho_{Co} \approx 10\rho_{Au} \sim 0,13 \Omega \cdot \text{cm}$ ).

We first explored the magnetic response of the previously presented electrolyte-gated organic field-effect transistors (EGOFETs) to search for the metallic-like diffusive transport of the most doped channel, more specifically those where indications of metallicity occurred through the conductivity plateau while cooling the sample to 1,5 K (annex B). The applied field ( $H$ ) is swept from  $-7$  T to  $+7$  T, in both parallel,  $H$  is colinear to the current, and perpendicular,  $H$  is orthogonal to the current and the substrate, configurations. Note that the perpendicular configuration is orthogonal to the current, but also to the substrate plane. Despite the non-linearity of the output curve, measurements were performed at a bias voltage of  $V_{SD} = -100$  mV like the previous studies. Some measurements have also been carried out sourcing current ( $I_{SD} = -200$   $\mu\text{A}$ ), in the linear regime of the output curve, but no relevant difference was observed in MR properties. In the following, we will analyse the variation of the resistivity ( $\rho$ ) of the channel

deduced from 4-probe measurements, referred to magnetoresistivity ( $M\rho$ ) to avoid confusion with the change of contact and sample resistances in the next section. The magnetoresistivity in percent is defined as:

$$M\rho = \frac{\rho(H) - \rho(0)}{\rho(0)} \times 100 \quad (\text{V.1})$$

**Figure V.1** shows the magnetoresistivity of EGOFETs with gold and cobalt electrodes **on the same chip**, for the magnetic field parallel and perpendicular to the current. The main outcome is the opposite variation of the resistivity in the perpendicular versus parallel configuration, with a positive  $M\rho$  when  $\vec{H} \parallel \vec{j}$ , and a transition from negative to positive  $M\rho$  when  $\vec{H} \perp \vec{j}$  below 5 K. We emphasize that the deviations from a parabolic shape (dips in the data of typically 0,2 % amplitude) observed around  $\pm 500$  mT, particularly apparent in the parallel case, comes likely from a change of range of the superconducting magnet power supply, and are categorized as experimental artefacts. We found that the signal became noisy around the liquid helium temperature, possibly related to the excess of liquid helium in the sample space, and therefore possibly another experimental artefact.

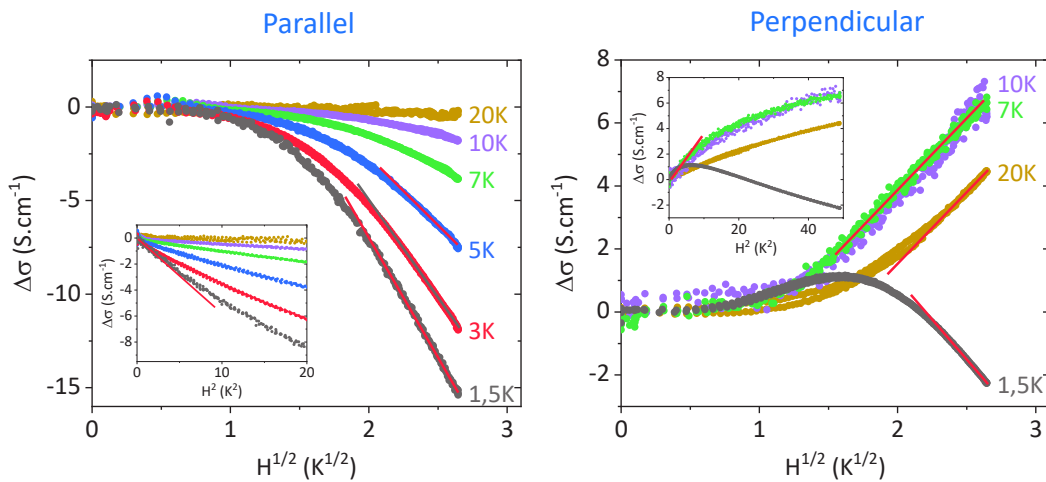


**Figure V.2** Variation of conductivity of the organic channel versus  $\sqrt{H}$  and  $H^2$  (in-sets) in the parallel (left) and perpendicular (right) configurations at different temperatures. The straight lines exhibit the linear behaviours.

In the parallel case, the amplitude of the variation is large at 1,5 K for the gold-based EGOFET reaching +22 % at  $\pm 7$  T and goes almost down to 0 % at 20 K. Unfortunately, the sample broke for the three last measurements on the EGOFET made of cobalt and the  $M\rho$  at 1,5 K could not be determined. The increase of the resistivity at 1,5 K is assigned to electron-electron interactions, highlighted by the reduction of electron-phonon scattering probability by cooling the sample. The magnetic field splits the spin-up and spin-down bands by  $\mp g\mu_B H$  (Zeeman effect), where  $g$  is the Landé factor considered equal to 2 and  $\mu_B$  the Bohr magneton, and the variation of conductivity at fixed temperature is then<sup>1,2</sup>:

$$\Delta\sigma(H) \propto \begin{cases} -H^2 & g\mu_B H \ll k_B T \\ -\sqrt{H} & g\mu_B H \gg k_B T \end{cases} \quad (\text{V.2})$$

To verify the hypothesis of electron-electron interactions responsible for the rise of resistivity, we analysed the variation of conductivity versus  $H^2$  and  $\sqrt{H}$  (**Figure V.2**). Indeed, for the three lowest temperatures, in the parallel situation,  $\Delta\sigma$  is linear with  $\sqrt{H}$  at high field and linear with  $H^2$  at low field. It is worth noting that “high” and “low” fields refer to the comparison with the thermal energy. For example, at 1,5 K,  $g\mu_B H$  overpasses the thermal energy around 1,1 T, consistent with the onset of the drop of  $\Delta\sigma$ . Electron-electron interactions and related positive MR were already exhibited for doped polyaniline<sup>3</sup> and poly(3,4-ethylenedioxythiophene)<sup>4</sup> below 4,2 K.

As the origin of the increase of resistivity when  $\vec{H} \parallel \vec{j}$  can be attributed to the Zeeman splitting, it happens also in the perpendicular situation. However, as depicted in **Figure V.1**,  $\rho$  tends to decrease until 7 K, and then, from 5 K, a mixing of negative and positive  $M\rho$  appears, at low and high field respectively. The negative magnetoresistivity in the perpendicular situation is likely due to disruption of the weak localization, introduced in chapter II. By suppressing the constructive interference of clockwise and anticlockwise path along a self-closing trajectory, carriers become less localized that reduces the resistivity. This effect is more pronounced at low temperature when the probability to scatter inelastically on phonons becomes small enough such that carriers are able to travel along the self-closed path coherently, and less important for high resistive materials as scattering events are more probable. In our sample, variations of resistivity due to weak localization extinguishment were no more observed above  $\sim 30$  K.

The absence of negative  $M\rho$  in the parallel configuration as well as its occurrence in a limited range of temperature support the weak localization disruption as origin of the reduction of resistivity. In addition, the model of Hikami-Larkin-Nagaoka suggests  $\Delta\sigma \propto \sqrt{H}$  at high field and  $\Delta\sigma \propto H^2$  at low field<sup>5,6</sup>. Analysing **Figure V.2** (right panel), we find indeed a linear variation of  $\Delta\sigma$  with the square root of the field. The observation of weak localization is a second signature of metallic-like transport. Further support for this transport mechanisms is given in annex D that describes the occurrence of a Hall voltage detected in the maximum doped EGOFETs structures.

Cooling down to 1,5 K, the magnetoresistivity changes drastically (**Figure V.1**) with a positive  $M\rho$  for high fields superposed to the weak localization disruption for lower fields ( $H < 3$  T). The increase of the resistivity is due to the electron-electron interactions as in the parallel case with a reduced amplitude due to the contribution of the weak localization. Again **Figure V.2** confirm the carrier-carrier interactions at 1,5 K with  $\Delta\sigma \propto -\sqrt{H}$  for large magnetic field.

Weak localization were also independently reported in pBTTT doped by solid state diffusion in a wide range of temperature (35 – 290 K)<sup>7</sup>, as well as previously observed on chemically doped poly(p-phenylenevinylene)<sup>6</sup>. In the former work, the variation of conductance ( $\Delta G$ ) they exhibited is very small ( $\Delta G \sim 40 - 600$  nS within their temperature range), about three orders of magnitude lower than presented in our sample at 20 K ( $\Delta G \sim 400$   $\mu$ S). The weak localization signal at higher temperature would then possibly be hidden in the larger noise of our measurements, estimated of few  $\mu$ S.

## V.2. Interface versus bulk magnetoresistance

To explore further the issue of interface resistance in organic electronics and particularly organic spintronics, we studied the change of specific contact resistivity ( $Mr_b$ ) and compared it to  $M\rho$  and the modulation of the total sample resistance ( $MR_{Sample}$ ) on both millimetre-scale (mT) and nanometer-scale (nT) EGOFETs, with gold and cobalt electrodes. We are not aware of previous MR studies on contact resistance in organic transistors. The change of the contact resistance ( $MR_C$ ) is also analysed to emphasize again the importance of the current crowding effect. As usually  $R_C^{LT}$  is proportional to  $R_C$ , considering or not the transfer length would not change the MR amplitude of the contact resistance. However,  $Mr_b$  takes into account the transfer length and is therefore expected to behave differently than  $MR_C$ . Taking advantage of the 4-probe method, the source and drain  $r_b$  are decoupled for the mTs. As highlighted in the previous chapter, we subtracted the pads resistance for more accurate determination of  $R_{Sample}$  and both interface terms  $R_C$  and  $r_b$ .

**Figure V.3** and **Figure V.4** show the four different magnetoresistances for gold- and cobalt-based millimeter-scale EGOFETs respectively at 1,5 K and in the parallel and perpendicular cases. Focusing first on the gold sample, we observed a similar variation of  $MR_{Sample}$  and  $M\rho$  in each configuration with the parabola shape when the magnetic field is parallel to the sample and the mixing or positive and negative slopes in the perpendicular case, which mirrors the properties of  $M\rho$  discussed in the previous section.

In the parallel case, the modulation of the contact resistances is also close to  $M\rho$ , with a roughly halved amplitude. The drain resistance is however more linear versus the external field and exhibits an abrupt increase at very low field ( $|\mu_0 H| < 30$  mT), also significantly present on the drain  $Mr_b$ , and very slightly in  $MR_{Sample}$  possibly arising from organic magnetoresistance (OMAR)<sup>8</sup>. It is worth noting this is not found for the bulk conductivity of the sample, for which OMAR is usually reported in the literature. Both source ( $Mr_{b,S}$ ) and drain ( $Mr_{b,D}$ ) specific contact resistivity behave very differently from  $R_C$ :  $Mr_{b,D}$  reaches a plateau while  $Mr_{b,S}$  becomes negative at high field, and their amplitude is reduced. Indeed, as the resistivity rises, the transfer length ( $L_T$ ) decreases according to equation III.1, and therefore reduces  $r_b$  and counterbalances the increase of  $R_C$ .

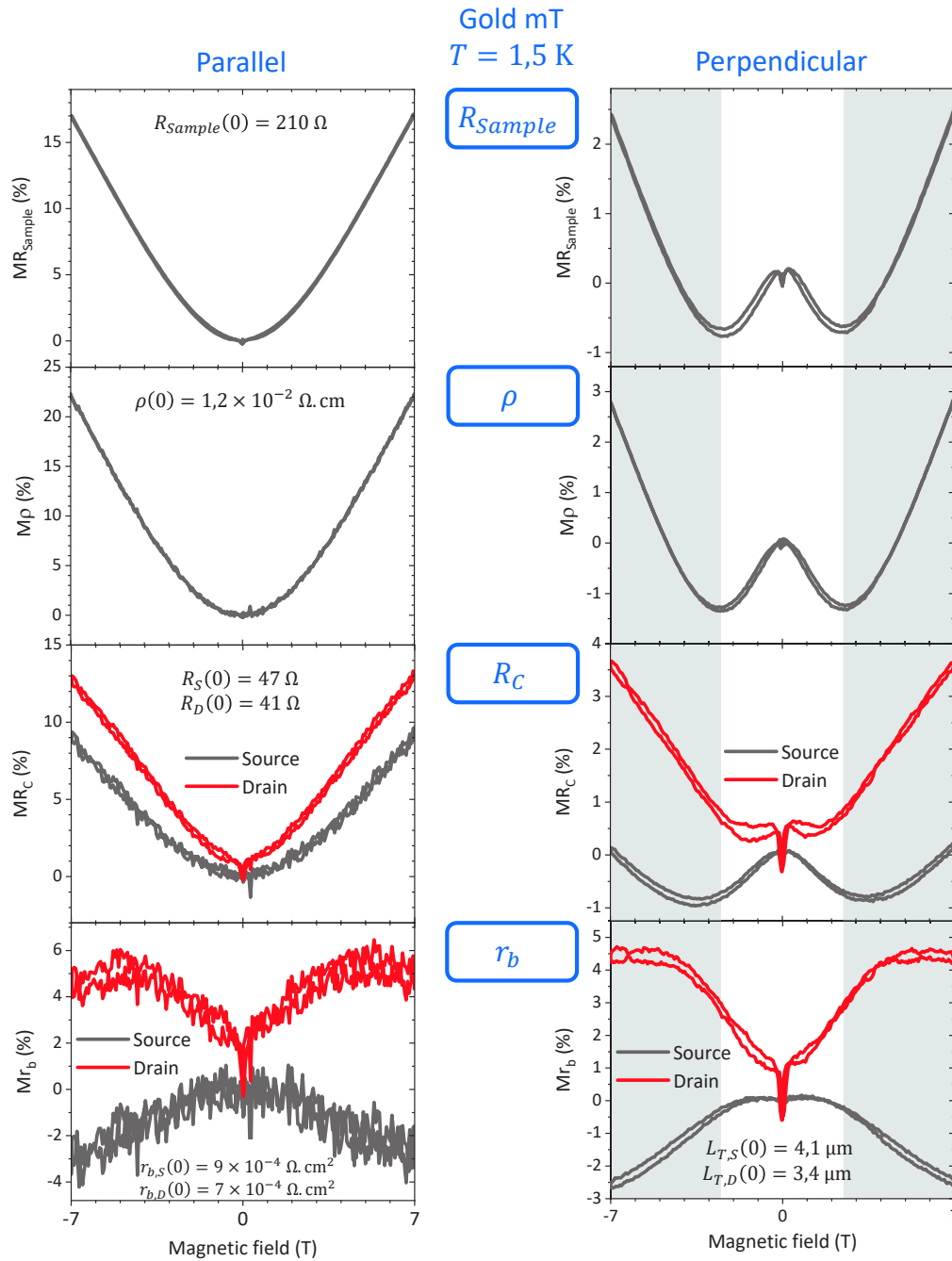


**Figure V.3** Modulation of sample resistance, resistivity, contact resistance and specific contact resistivity versus the applied magnetic field of the millimeter-scale EGOFET with gold electrodes. The parallel configuration is depicted on the left and the perpendicular case on the right. The grey areas in the perpendicular situation point out the domination of the electron-electron interactions against the weak localization. Indicated numbers give the initial value of each property at zero-field, very close in both orientations.

Equation III.6, tells us that  $R_{Sample} \propto \sqrt{r_b \rho}$  if  $L_T$  is larger than the thickness of electrodes. However, even if the condition is fulfilled ( $L_T = 3 - 4 \mu\text{m}$ ),  $MR_{Sample} \neq \sqrt{Mr_b \cdot M\rho}$  but surprisingly  $MR_{Sample} \approx \sqrt{MR_C \cdot M\rho}$  for both parallel and perpendicular cases. Note that because of the square dependence of  $r_b$  on  $R_C$  (equation IV.4),  $Mr_b$  is not simply the average of  $Mr_{b,S}$

and  $Mr_{b,D}$ , while it is valid for  $MR_C$ . The proper average  $r_b$  has been used for the previous checking of the square root law. The deviation from equation III.6 may originate from the limitation of the crowding effect. Indeed, we defined a window in the protecting  $\text{SiO}_2$  layer, leaving only  $3 \mu\text{m}$  free over the electrodes. It is plausible than the device would require longer transfer length if it were possible, supported by the calculated  $L_T$  exceeding the allowed  $3 \mu\text{m}$ . It involves then an error on  $r_b$  as we account for longer  $L_T$  than physically possible. However, by imposing  $L_T = 3 \mu\text{m}$  for the calculation of both  $r_{b,S}$  and  $r_{b,D}$ , no significative shape change was observed with only a reduction of  $Mr_{b,S}$  amplitude by roughly a factor two. In addition, investigation of the contact resistance versus channel resistance values considering the crowding effect carried out that we don't reach the equality  $R_{Ch}^{L_T} = 2R_C^{L_T}$ , suggesting again restricted transfer length.

The last interesting outcome of **Figure V.3** is the change of behaviour of both  $R_C$  and  $r_b$  in the same time than the negative to positive slope transition of  $MR_{Sample}$  and  $M\rho$ . The source magnetoresistance slope changes its sign concomitantly to  $MR_{Sample}$  and  $M\rho$ , while the drain one turns from a plateau to a linear increase when electron-electron interactions dominate the MR signal. Interestingly,  $r_{b,D}$  is symmetric to its corresponding contact resistance going from a linear rise to a plateau at high field, while the drain  $R_C$  shows a plateau at low field and then increases linearly.

Focusing now on EGOFETs with cobalt electrodes (**Figure V.4**), the MRs for all contributions to the sample resistance are quite similar. We emphasize that results of both orientations were not measured on the same sample because of reproducibility issues, explaining the significative different values. The parabolic increase of resistances in the parallel case is reproduced also on the interface properties of the device, and amplitude of the four different MRs are equal. The shapes of the MRs curves are also similar when the magnetic field is perpendicular to the sample and show little difference from the parallel case. Furthermore, in addition to the previous MR effect showed on gold-based EGOFET, an hysteresis is observed within  $\pm 3 \text{ T}$ . We attribute this hysteresis to the stray field effect due to the magnetization of the cobalt electrodes. We recall here that the effective field experience by the carriers is the sum of the one created by the solenoid magnet, of amplitude corresponding to the  $x$ -axis of the plots, added to the field created by the magnetic electrodes. Indeed, in between magnetic wires, the magnetic lines are opposite to the external field direction, that diminishes locally its strength (**Figure V.5**). In contrast, the local magnetic field is enhanced by around 20% near the top surfaces of the electrodes. The analysis of the data in **Figure V.4** is further complicated by a MR which appears as a superposition of the double-minimum structure of **Figure V.3** and the contribution of the cobalt stray field. This effect will likely be more important on nTs because of the very short channel, but it may explain also why the hysteresis extend to larger field than the one of bar cobalt ( $\pm 1,8 \text{ T}$ ), as a portion of the channel feels a reduced effective magnetic field. The simulation showed in **Figure V.5** for a nT exhibit a lowering of almost 1 T in the channel, close to electrodes, compared to the external magnetic field.

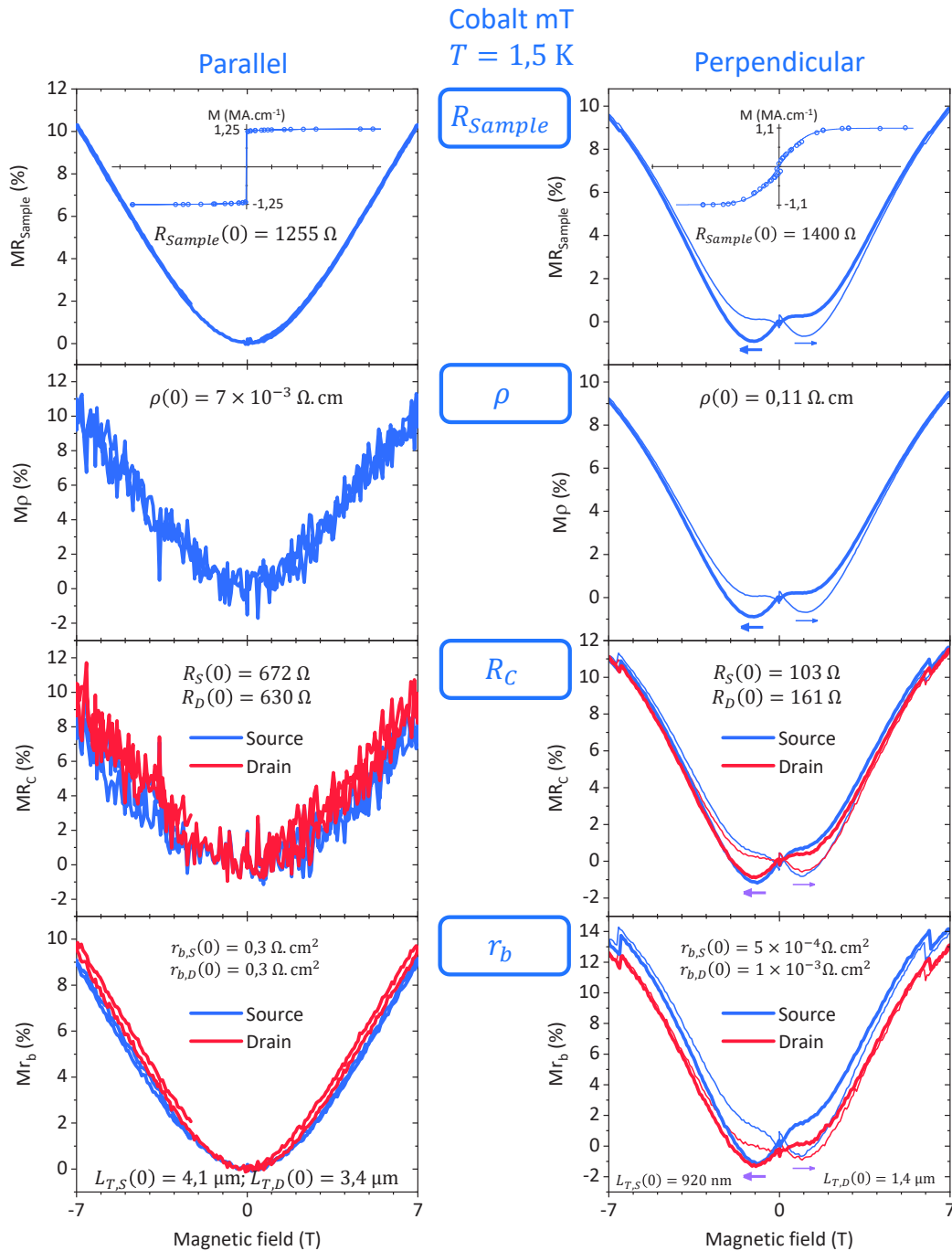


**Figure V.4** Modulation of sample resistance, resistivity, contact resistance and specific contact resistivity versus the applied magnetic field of the millimeter-scale EGOFET with cobalt electrodes. The parallel configuration is depicted on the left and the perpendicular case on the right, with the magnetization curves of the cobalt in the corresponding orientation of the field as inset in the  $MR_{Sample}$  plots. The results of both orientations came from different sample, explaining the variation of values at zero-field.

However, as shown in the insets of the **Figure V.4**, cobalt electrodes have a coercive field close to 0 and the magnetization curve of the insets cannot be used to explain the hysteresis behaviour. The non-reproducibility of the back and forth magnetic field possibly takes its origin

in a different magnetization property of the bulk cobalt electrodes compared to their interface because of the interaction with the polymer molecules (spinterface, see section II.2.3).

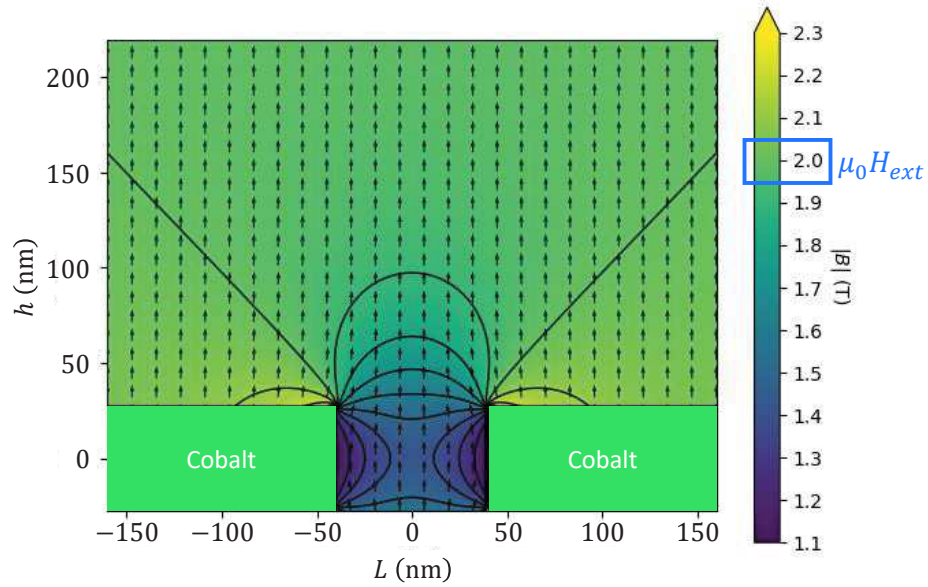


**Figure V.5** Effective magnetic field around two cobalt electrodes separated by 80 nm in an external magnetic field of 2 T pointing up. Lines are isovalues of the total magnetic field  $B = \mu_0(H_{ext} + M_z)$  where  $\mu_0$  is the vacuum permeability and  $M_z$  the magnetization of the cobalt electrodes.

One should also have in mind that the weak localization should also be present here in perpendicular case, which results into a very complex system with various contribution to the MR, difficult to decouple. To check that the hysteresis is not an artefact, we also investigated an heterogenous mT with one electrode made of gold and the other of cobalt. By looking at the variation of the specific contact resistivity on each electrode, we recover the hysteresis loop on the cobalt contact only, being the source or the drain electrode (**Figure V.6**). We also note here different  $Mr_b$  amplitudes, as if the injection electrode is more sensitive to the magnetic field.

As we aim to inject, transport and detect spins in hybrid devices, the channel length must be shorter than the spin diffusion length. Therefore, we explore also the effect of the external magnetic field on nT with gold and cobalt electrodes depicted in **Figure V.7** and **Figure V.8**.

The gold nT exhibit surprisingly large negative  $MR_{Sample}$  in the parallel case with a non-negligible value of 12 % at  $\pm 7$  T ,while  $M\rho$  , measured on the nearby mT device, is positive. By analysing the interface properties, we pointed out a significative variation of  $r_b$  whose (absolute) amplitude exceeds  $M\rho$  and dominates the total MR of the device. However,  $MR_{Sample}$  is still not proportional to  $\sqrt{Mr_b \cdot M\rho}$  and  $R_{Ch}^{L_T} \neq 2R_C^{L_T}$  likely because of the very short  $L_T$  ( $\sim 100$  nm) making the conditions  $L_T \gg h$  and  $L_T \gg h, L$  not fulfilled.

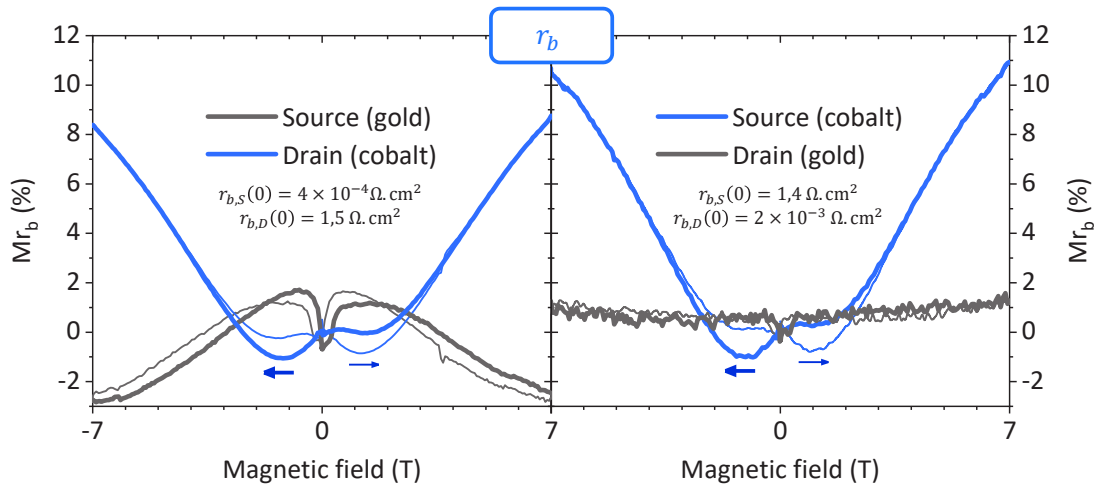


**Figure V.6** Specific contact magnetoresistivity versus the external field applied perpendicularly to the substrate on a heterogeneous mT. The left panel shows the variation of  $Mr_{b,S}$  and  $Mr_{b,D}$  when the gold electrode is the source and the cobalt is the drain. The right panel presents the same measure by inverting both electrodes. The resistivity is almost the same for both measurements. The resistivity is the same in both cases ( $\rho \sim 4,3 \times 10^{-2} \Omega \cdot \text{cm}$ ).

The perpendicular case is not depicted because all MRs are negligible ( $< 1\%$ ) and MRs in the negative field are too noisy for interpretation. As the definitions of perpendicular and parallel orientations are questionable, any outcome would be very doubtful.

For cobalt nT (**Figure V.8**), we observe a reasonable channel/contact resistances equality due to micrometer-scale transfer lengths, translating into very similar  $MR_{\text{sample}}$  and  $MR_C$  as  $4R_C = R_{\text{sample}}$ . This sample was voluntarily not fully covered with  $\text{SiO}_2$  to let the transfer length being as long as needed, but we still evaporated an insulating layer to avoid shortcuts and define properly the width of the channel. In this favourable condition where  $L_T$  is much longer than  $h$  and  $L$  we confirm our model of chapter III and  $MR_{\text{sample}} = \sqrt{Mr_b \cdot M\rho}$  for both parallel and perpendicular cases. A hysteresis seems also present when the magnetic field is perpendicular to the sample, but the noise and the shifting of MRs at zero-field after the magnetic ramp makes difficult the analysis of the data.

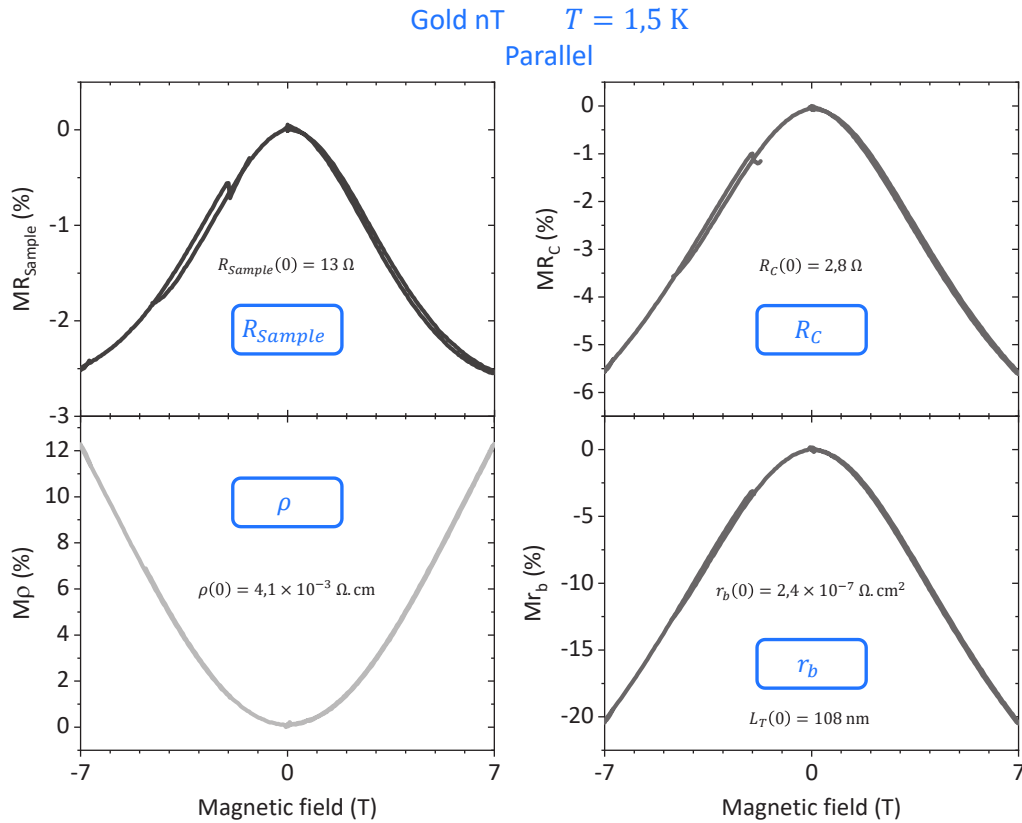


**Figure V.7** Modulation of sample resistance, resistivity, contact resistance and specific contact resistivity versus a parallel magnetic field of the nanometer-scale EGOFET with gold electrodes. Different grey levels are used to emphasize that  $M\rho$  (light grey) comes from a nearby mT and allows the determination of  $MR_C$  and  $Mr_b$ . Only  $MR_{Sample}$  is a pure value of nT. The resistivity is around  $4,3 \times 10^{-2} \Omega \cdot \text{cm}$ .

In summary, in this chapter we observed weak localization in highly doped pBTTT, that is an important evidence of diffusive transport. We also pointed out an eventual lower effective magnetic field in nano-scale devices with magnetic electrodes that must be considered when analysing the magnetoresistance for magnetic field in the range of the coercive field of wires. Investigation of the specific contact magnetoresistivity, not reported in the literature to our knowledge, unfortunately doesn't lead to a clear picture of the impact of the contact resistance on the total sample resistance upon application of a magnetic field within the current crowding framework. Nevertheless, when conditions are optimal (cobalt nT), *i.e.* when  $L_T$  is not limited by the geometry of the sample and the channel resistance equilibrates the contact resistance ( $R_{Ch}^{L_T} = 2R_C^{L_T}$ ) we were able to confirm the model developed in the chapter III. For more robust validation, more data are needed with a better reproducibility of properties between the two orientations.

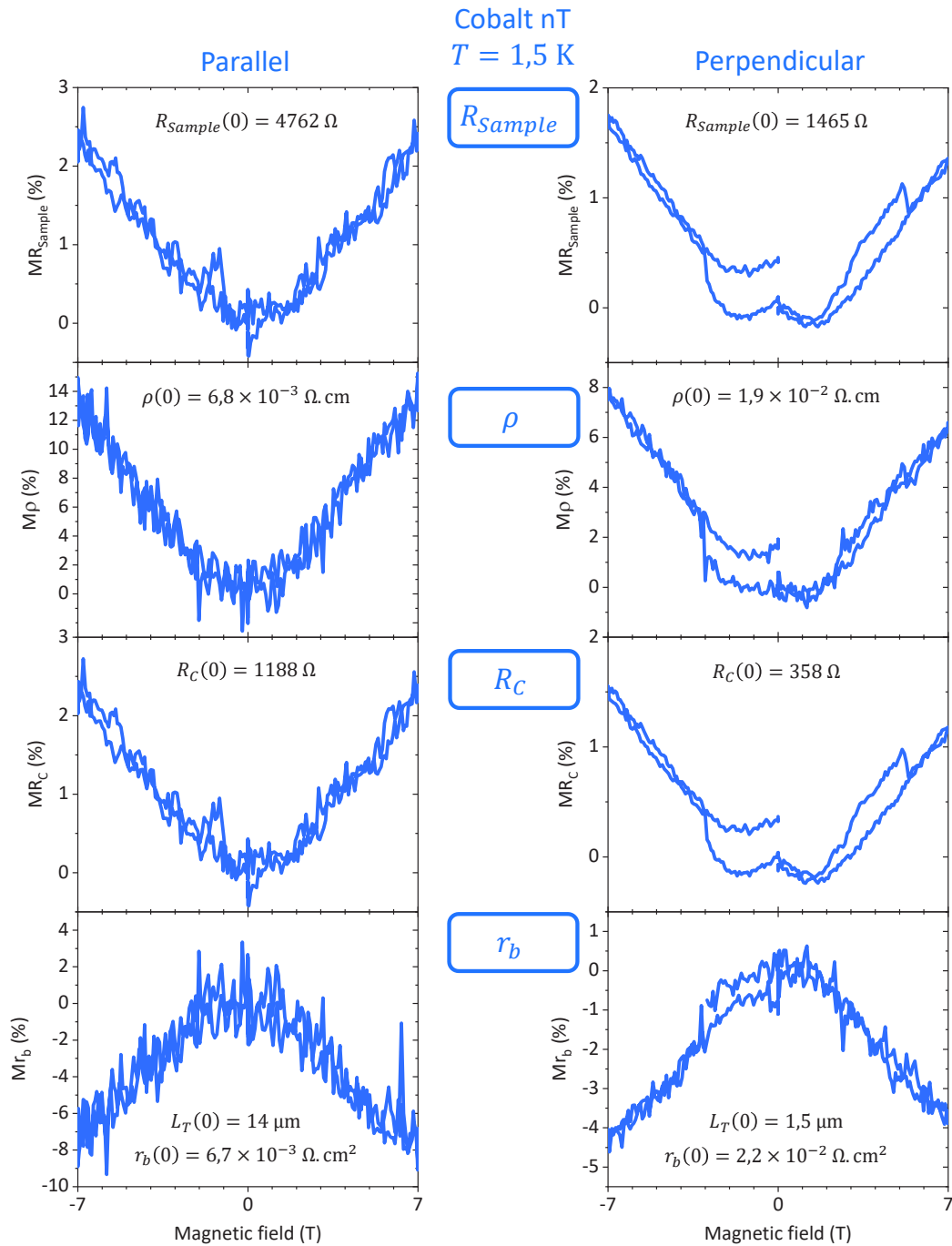


**Figure V.8** Modulation of sample resistance, resistivity, contact resistance and specific contact resistivity versus the applied magnetic field of the nanometer-scale EGOFET with cobalt electrodes. The parallel configuration is depicted on the left and the perpendicular case on the right. The resistivity drops by turning the sample from parallel to perpendicular ( $\rho_{\parallel} \sim 3\rho_{\perp} \sim 6,9 \times 10^{-3} \Omega \cdot \text{cm}$ ).

**Bibliography**

- (1) Lee, P. A.; Ramakrishnan, T. V. Disordered Electronic Systems. *Rev. Mod. Phys.* **1985**, *57* (2), 287–337.
- (2) Dai, P.; Zhang, Y.; Sarachik, M. P. Magnetoconductance of Metallic Si:B near the Metal-Insulator Transition. *Phys. Rev. B* **1992**, *46* (11), 6724–6731.
- (3) Menon, R.; Yoon, C. O.; Moses, D.; Heeger, A. J.; Cao, Y. Transport in Polyaniline near the Critical Regime of the Metal-Insulator Transition. *Phys. Rev. B* **1993**, *48* (24), 17685–17694.
- (4) Aleshin, A.; Kiebooms, R.; Menon, R.; Wudl, F.; Heeger, A. Metallic Conductivity at Low Temperatures in Poly(3,4-Ethylenedioxythiophene) Doped With. *Phys. Rev. B - Condens. Matter Mater. Phys.* **1997**, *56* (7), 3659–3663.
- (5) Hikami, S.; Larkin, A. I.; Nagaoka, Y. Spin-Orbit Interaction and Magnetoresistance in the Two Dimensional Random System. *Prog. Theor. Phys.* **1980**, *63* (2), 707–710.
- (6) Ahlskog, M.; Reghu, M.; Heeger, A.; Noguchi, T.; Ohnishi, T. Electronic Transport in the Metallic State of Oriented Poly(p-Phenylenevinylene). *Phys. Rev. B - Condens. Matter Mater. Phys.* **1996**, *53* (23), 15529–15537.
- (7) Kang, K.; Watanabe, S.; Broch, K.; Sepe, A.; Brown, A.; Nasrallah, I.; Nikolka, M.; Fei, Z.; Heeney, M.; Matsumoto, D.; et al. 2D Coherent Charge Transport in Highly Ordered Conducting Polymers Doped by Solid State Diffusion. *Nat. Mater.* **2016**, *15* (5), 896–903.
- (8) Francis, T. L.; Mermer, Ö.; Veeraraghavan, G.; Wohlgenannt, M. Large Magnetoresistance at Room Temperature in Semiconducting Polymer Sandwich Devices. *New J. Phys.* **2004**, *6*, 185–185.



## Conclusion and perspectives

The ultimate goal of this project was the realization of organic spin-valves. In order to achieve injection, transport and detection of spins, we reminded the two key conditions to fulfil: the spin diffusion length must be significantly larger than the channel length for the conservation of the spin information; and the contact resistance needs to obey Fert & Jaffrès' rules for efficient spin injection and detection<sup>1</sup>.

The first condition could be solved by working on vertical geometry where the organic channel could easily reach length down to few nanometers. However, as it was highlighted in the second chapter, vertical structures lead possibly to wrong measurements because of eventual shortcuts hard to unravel. Therefore, lateral geometry is preferred, but the fabrication of suitable channel length is not that easy. Indeed, the expected spin diffusion length of organic materials is only of several tens of nanometers, requiring sub-100 nm planar devices. In the same time, working on highly conductive organic material is also key as a longer spin diffusion length is expected for higher conductivities, where band-like transport starts to appear.

The second condition implies that the specific contact resistivity ( $r_b^*$ ) should be close to the spin impedance of the non-magnetic organic spacer ( $r_N$ ). If  $r_b^* \ll r_N$ , no spin injection occurs, *i.e.* the purely diffusive spin current generated at the interface flow back in the injection electrode and does not enter the semiconductor spacer. If  $r_b^*$  is too large compared to  $r_N$ , the spin detection is compromised and spins take too much time to escape from the spacer. This last condition appears the most challenging for organic-inorganic interfaces, known to exhibit very high contact resistances, orders of magnitude larger than the higher limit of Fert and Jaffrès' conditions for efficient spin injection and detection.

To overcome these difficulties, we focused our efforts on lateral electrolyte-gated organic field-effect transistors (EGOFETs). The pBTTT used as active polymer is known for its high mobility and accordingly, a rather long spin diffusion length ( $l_{sf}$ ) of 200 nm is expected<sup>2</sup>. To further increase its transport capability, the EGOFET geometry generates electrochemical doping that enhances significantly the pBTTT conductivity, observed among the highest

reported in the literature<sup>3</sup>. Signs of metallicity were also pointed out, with occurrence of conductivity plateau and weak localization at low temperature, in combination with Hall voltage detection. The findings highlight the emergence of diffusive transport, with an estimate of the mobility of the doped pBTTT possibly reaching  $20 \text{ cm}^2 \cdot \text{V}^{-1} \cdot \text{s}^{-1}$ , among the largest reported in the literature for polymers.

In addition, probably because of the injection of ions of the electrolyte, the contact resistance ( $R_C$ ) is several orders of magnitude smaller than those found on more classical organic field-effect transistors (OFETs), a key finding providing hopes to solve the second outlined issue. It was even more motivating to further investigate EGOFET devices as we found further reduction of the interface resistance by downscaling the system to sub-100 nm size.

In this work, we focused on the specific contact resistivity  $r_b$ , the area-normalization of the contact resistance  $R_C$ , which is the physical quantity intrinsic to the materials defining the interface and is the relevant quantity for spin injection and detection modelling. We emphasized the generally underestimated active area for injecting and collecting carriers. Current crowding that occurs in lateral stacked geometry devices makes the top surface of electrodes contribute to charge injection and collection, over the so-called transfer length ( $L_T$ ) distance. The effective area participating to transport could hence be much larger than the edge of electrodes and impacts significantly the calculation of  $r_b$ . By considering properly the interfaces, we systematically calculated the transfer length and confirmed an ultralow specific contact resistivity, especially in the case of nano-scale channels, reaching values three orders of magnitude lower than reported in the literature for EGOFETs<sup>4</sup> and at least five orders of magnitude lower than in best OFETs<sup>5</sup> for gold electrodes. Using magnetic cobalt wires,  $r_b$  rises significantly but remains within the window of values needed for observing a non-negligible spin valve effect.

Further study of the current crowding effect provides us a very simple relationship between the total sample resistance ( $R_{Sample}$ ) with  $r_b$  and its resistivity ( $\rho$ ) that follows a square root law such that  $R_{Sample} \propto \sqrt{r_b \rho}$ . This equation, never specified in the literature (to our knowledge) holds true as long as  $L_T$  is larger than the thickness of the electrodes, condition most of the time verified both in this project and in the literature. It arises because of the modulation of the effective channel length that writes  $L_{eff} = L + 2L_T$ , where  $L$  is the physical distance between the electrodes. Therefore, if the resistivity of the channel increases for instance,  $L_{eff}$  diminishes because the transfer length reduces as  $L_T \propto \sqrt{r_b / \rho}$ .

The variation of the distance travelled by charge and spin carriers is also key for a spin-valve signal. Indeed, even though the physical spacing between spin injection and detection electrodes is patterned shorter than  $l_{sf}$ , the crowding effect possibly elongates the effective channel such that in the end  $L_{eff} > l_{sf}$ . The simulation we performed points out an important decrease of the magnetoresistance (MR) because of the transfer length. Indeed, the longer the carrier path in the non-magnetic spacer, the higher the probability to lose the spin information before detection. The more accurate determination of the specific contact resistivity helps also to better estimate the amplitude of the MR signal as it shows a maximum value for  $r_b^* \sim r_N$  with  $r_b^* \propto r_b$  and accounts the spin asymmetry. The results of the modified Fert and Jaffrès' model we proposed are relatively pessimistic for the realization of lateral organic spin-valve where

current crowding occurs, as even with the very low specific contact resistivity of our samples, the expected MR do not exceed the percent range. For the purpose of avoiding crowding effects, we then grew an insulator on top of electrodes, and used focused-ion beam cutting to define short lateral distance between electrodes. We found that such samples exhibited similar  $r_b$  values, adding confidence to our implementation of the crowding model.

Finally, we took advantages of the 4-probe geometry of our millimeter-scale EGFETs to explore the source and drain specific contact magnetoresistivities ( $Mr_{b,S}$  and  $Mr_{b,D}$ ) as well as their deduced average values for nanometer-scale devices. The underlying physics is still unclear, but we observed  $Mr_{b,S}$  and  $Mr_{b,D}$  possibly independent of the orientation of the magnetic field versus the sample, and confirmation of our square root equation of the total resistance in suitable conditions. We highlighted also the problem to define the perpendicular and parallel configurations as the current injected from the top surface of electrodes because of the crowding effect is perpendicular to the current flow within the channel. Moreover, in the case of magnetic wires, the extra stray field from the electrodes leads to non-uniform magnetic field, stronger over magnetized electrodes and weaker in the channel. The interpretation of data is therefore difficult and need deeper analysis.

For further work on lateral organic spin-valves, we believe that limit the transfer length the shorter possible is the most relevant geometry, as it implies no decrease of the MR signal through  $L_T$ . Controlling the allowed transfer length, by patterning thin electrodes for example, may also be useful to optimize device properties. EGFETs seems nevertheless a required geometry as they exhibit very low specific contact resistivities and high conductivity, and properties are tunable through the doping level, the temperature and the device scale.

More robust confirmation of the relation  $R_{Sample} \propto \sqrt{r_b \rho}$  is necessary for eventual novel applications based on the crowding effect. As figure of merit, we imagined various systems in which we could vary the interface resistance and decouple it from the resistivity:

- Functionalization of gold electrodes with photo-switching molecules: for example, azobenzene molecules are optically switchable from *trans* to *cis* conformation that modulates the interface resistance<sup>6</sup>. Preliminary study was performed but more work is needed for conclusion mainly because the geometry is different (top-gated OFET) and the insulation leads also to parasitic photocurrent that needs to be subtracted.
- Spin-crossover materials: spin transition materials are interesting alternatives to photo-switching molecules. Their change from high spin to low spin state can be triggered by light, pressure or temperature. If we use them to cover the (Au) metal electrodes, one can imagine to modulate the interface resistance when the state of the spin transition molecules changes. We are currently testing nano-particles and thin film spin-crossover systems are currently processed.

The current crowding effect may also shine light on previous results of the literature. Let assume that electrodes of an OFET are made of a ferromagnetic bilayer, separated by a spin-dependent tunnelling junction (**Figure I.1**). As most of the current is expected to come from the top surface of electrodes because of crowding effect, a significant portion of carriers has to

cross the tunnel barrier. It translates into an interface resistance dependent on the relative orientation of the ferromagnetic materials, possibly looking like a spin-valve signal. As  $R_{Sample} \propto \sqrt{\tau_b \rho}$  in the picture of the current crowding effect, the total resistance of the sample would also behave like a spin-valve in a magnetic field (**Figure I.1**). The latter system could possibly apply to LSMO electrodes, having an interface showing different properties than the bulk, and showing a large variation upon application of a magnetic field. The formation of spinterface could also be in the same framework, therefore the crowding effect may explain some of MR detection reported in the literature without the need of a model of spin injection/detection.

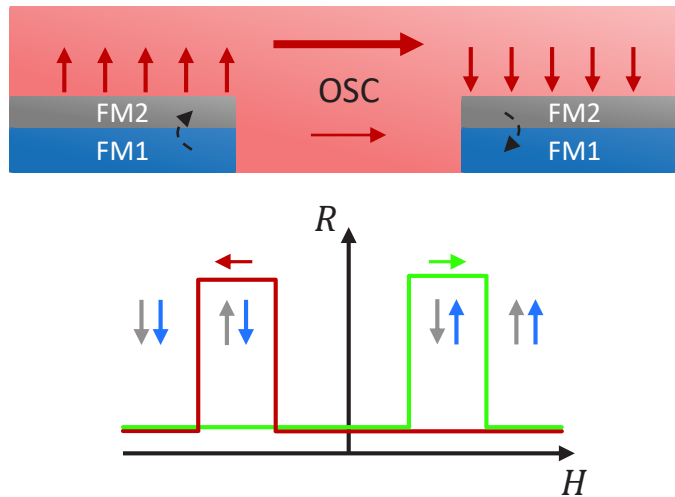


**Figure I.1** Top: hypothetic sample with ferromagnetic bilayers as electrodes where the transfer length is long. Bottom: resistance of the depicted sample in a magnetic field originating from the variation of the contact resistance between the two magnetic layers.

The transfer length could also be used to activate device functionalities by the elongation of the channel. **Figure I.2** for example presents electrodes that are partially ferromagnetic. By increasing the transfer length, through resistivity increase, the magnetic part of electrodes activates and spins could be injected. However, as we exhibited difficult spin injection/detection in this project, and the contribution of the current away from edges being weak, the realization of such device would be challenging. It gives nevertheless an idea of possible systems taking advantage of current crowding.



**Figure I.2** Example of an OFET with heterogenous electrodes.

Our results, discussions and modelling make very unlikely to success of organic semiconductors as spacers for spin valve effects. We however think that lateral structures, with controlled and variable effective length under externa stimuli, could open new

possibilities for devices design and intertwined properties between neighbour cells in more complicated planar structures. The issue of current crowding has been largely downplayed in the community of hybrid and organic electronics and could interestingly be taken advantage of.

## Bibliography

- (1) Fert, A.; Jaffrès, H. Conditions for Efficient Spin Injection from a Ferromagnetic Metal into a Semiconductor. *Phys. Rev. B* **2001**, *64* (18), 184420.
- (2) Watanabe, S.; Ando, K.; Kang, K.; Mooser, S.; Vaynzof, Y.; Kurebayashi, H.; Saitoh, E.; Siringhaus, H. Polaron Spin Current Transport in Organic Semiconductors. *Nat. Phys.* **2014**, *10* (4), 308–313.
- (3) Zanettini, S.; Dayen, J. F.; Etrillard, C.; Leclerc, N.; Kamalakar, M. V.; Doudin, B. Magnetoconductance Anisotropy of a Polymer Thin Film at the Onset of Metallicity. *Appl. Phys. Lett.* **2015**, *106* (6), 2–6.
- (4) Braga, D.; Ha, M.; Xie, W.; Frisbie, C. D. Ultralow Contact Resistance in Electrolyte-Gated Organic Thin Film Transistors. *Appl. Phys. Lett.* **2010**, *97* (19).
- (5) Umeda, T.; Kumaki, D.; Tokito, S. Surface-Energy-Dependent Field-Effect Mobilities up to 1 Cm<sup>2</sup>/V s for Polymer Thin-Film Transistor. *J. Appl. Phys.* **2009**, *105* (2).
- (6) Crivillers, N.; Orgiu, E.; Reinders, F.; Mayor, M.; Samorì, P. Optical Modulation of the Charge Injection in an Organic Field-Effect Transistor Based on Photochromic Self-Assembled-Monolayer-Functionalized Electrodes. *Adv. Mater.* **2011**, *23* (12), 1447–1452.

# Annex A

## Device fabrication

The following chapter is dedicated to the fabrication process of the samples realized during the thesis. Electrodes patterning, polymer deposition and ion gel preparation are explained for the electrolyte-gated organic field-effect transistors fabrication.

### A.1. Electrodes patterning

The substrate we are using is *p*-doped silicon wafer covered with 500 nm thick silicon oxide (SiO<sub>2</sub>). This widespread substrate is suitable for organic electronics as the roughness is sub-nanometric and it lets the possibility to perform bottom-gate measurements. The design of electrodes is depicted in **Figure A.1a**. To achieve such geometry, two steps are needed: the first for the micrometer-scale transistor (mT), the gate electrode (not shown) and one side of nano-scale transistors (nTs), and the second for the other side of nTs. In order to make channel length shorter than 100 nm we choose the shadow-edge method<sup>1</sup> that is much easier than electronic lithography and is very efficient.

The first lithography step is realized using reversed AZ5214 resist with laser lithography as it will be the case for main electrode patterning. The inversion process helps for the lift-off thanks to the inward trapezoid shape of the resist after development. It avoids extra-material deposition and let a direct access to the resist during the lift-off in acetone. Once the pattern is drawn on the resist, 6 nm of adhesion titanium layer (deposition rate 0,1 nm. s<sup>-1</sup>) followed by 54 nm of gold (deposition rate 0,2 nm. s<sup>-1</sup>) are evaporated in an electron-beam evaporator. The sample is then immersed in remover AZ at 60 °C for 2 to 4 hours. Ultrasonic bath is avoided as much as feasible to keep the edges of electrodes as sharp as possible. It is anyway important for the interface study but even more here as we will use the first layer as “shadow mask” for the next step of nTs.

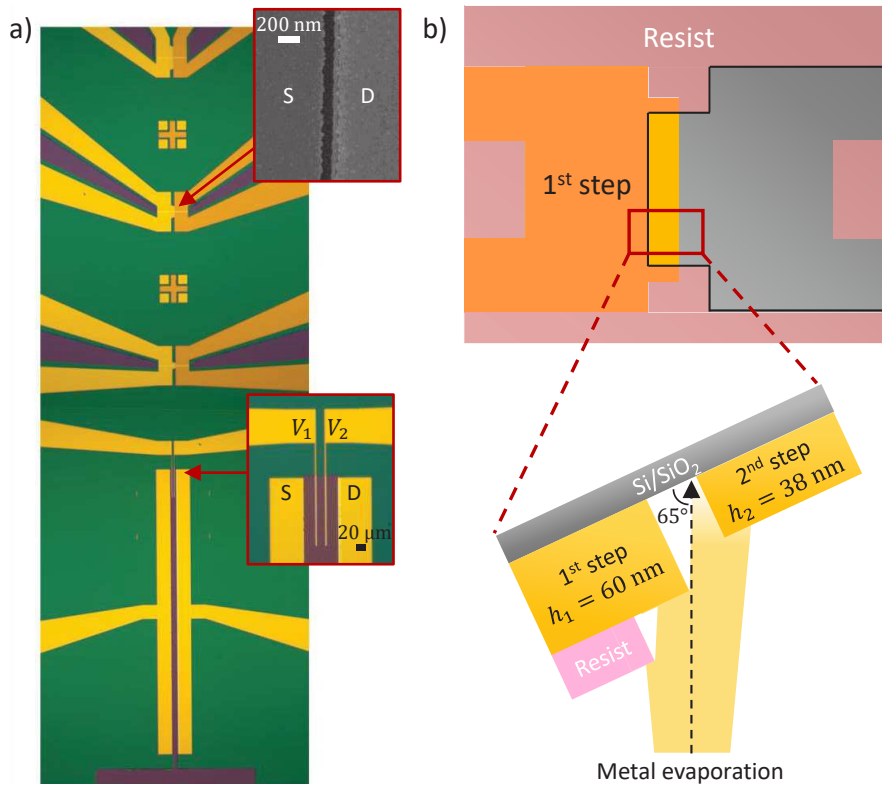


**Figure A.1** a) Optical microscope image of a typical sample. Insets show electronic microscope image of one nano-gap (top) and a picture of 4-probe electrodes (bottom). The two steps are slightly visible on nTs, the right side being darker than the left side gold electrodes, corresponding to different thicknesses. b) Developed resist after the second step lithography. The grey area is the substrate and the pink the remaining resist. c) Schematic sample during the evaporation. The sample is tilted to  $\theta = 65^\circ$  with respect to the sublimated atoms beam.

The geometry of mT is designed to perform 4-probe measurements to determine precisely the conductivity of the polymer channel. It allows also the source and drain contact resistances with the gated-4-probe (gFP) method (see chapter I). The high aspect ratio ( $W/L = 50$ ) is a way to ensure that the main part of the current flows in between the two electrodes without channel enlargement (point effect).

The second step consists in adding the missing side of nTs. To create gaps of tens of nanometer, the electrodes already present hide a part of the substrate by shadowing the metallic source during evaporation, following the so-called shadow-edge method (**Figure A.1b**). The length of the gap ( $L$ ) depends on the height of the first layer ( $h_1$ ) and the angle between the substrate and the beam of evaporated material ( $\theta$ ) such as:

$$L = h_1 \tan \theta$$

The height of the second electrode ( $h_2$ ) is also reduced compare to the nominal metal deposition ( $h_0$ ):

$$h_2 = h_0 \cos \theta$$

In other word, to get 38 nm-high electrodes (as second step) with a gap of 80 nm, the second evaporation is set to 10 nm of titanium and 80 nm of gold with an angle of 65°. Usually, the lithography is here positive using the resist AZ1505. The nTs shape is then fully dependent on the sharpness and the cleanliness of the first layer. After the lift-off, eventual shortcuts are always checked by measuring the resistance from one side of nTs to the other. Electronic imaging is also performed on one sample in a batch to have a look on the edges of nTs.

The design chosen for nTs is optimized for pseudo-4-probe measurements. As the realization of 4-probe electrodes within a sub-100 nm channel is at best challenging, we use this double “U-shape” in order to eliminate the major part of the wires and gold pads resistance. The pBTTT in our EGOFET geometry reaches high conductivity such as the channel resistance becomes of the order of even lower than the metallic leads. It is therefore mandatory to suppress this parasitic resistance, done here by the probing of the potential the closest possible to the organic channel as explain in chapter IV.

Finally, a protecting SiO<sub>2</sub> layer is generally added to well define the current path and avoid any shortcut through the forthcoming high conductive polymer. Thanks to the high alignment resolution of the laser lithography, the window without oxide lets only 3 μm free over the electrodes. This step was a big issue for several months because the silicon oxide layer didn't stick on gold whatever the precautions taken for the lithography and lift-off. Even water was able to infiltrate in between the gold and the SiO<sub>2</sub> layer. We suspect a higher concentration of carbon in the gold source than usual, as this issue was solved after a new batch of gold in the evaporator, and strange white marks appear on the “bad” gold electrodes afterwards.

For cobalt electrodes, the later process remains globally the same, except than the lift-off must be in acetone because the hot remover AZ dissolves the cobalt with an insidious efficiency. The cobalt layer doesn't need any adhesion material underneath, thus the first and second step are simply 60 nm and 90 nm (with 65° tilting) of cobalt respectively. However, the larger grain size of cobalt and the general worse layer (regarding the roughness or the edges cleanness) leads to poorly define nTs with zig-zag shape edges and frequent shortcuts (**Figure A.2**). For this reason, we decided to use focused ion beam (FIB) for the fabrication of nTs. One step lithography was then enough as we basically pattern shortcuts that are then cut with FIB. For comparison, gold nTs was also done to ensure no difference between shadow-edge and FIB techniques. The FIB gaps are much proper (**Figure A.2**), but the depth of the etching is hard to determine that involves a possible underestimation in the thickness of the thin film. As shown in chapter IV, FIB cutting provides also the freedom to change the channel length of nTs on the same substrate – impossible with shadow-edge method – that is particularly relevant to understand the scaling of EGOFETs. The FIB cutting has been performed in Institut de Science et d'Ingénierie Supramoléculaires (ISIS) by Éloïse Devaux within the electronic microscope enclosure equipped with gallium ion beam.

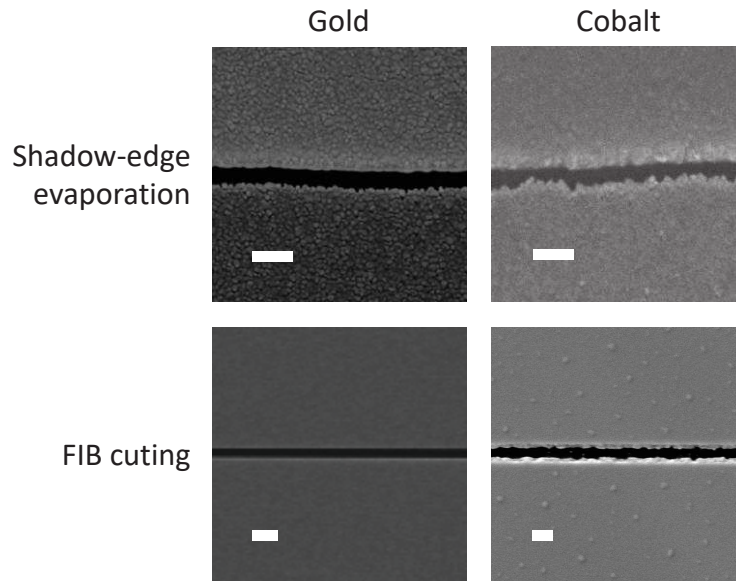


**Figure A.2** Electron microscope image of gold and cobalt nano-gaps fabricate through the shadow-edge method and FIB cutting. Cobalt gaps are generally less sharp than gold, likely due to larger grain size. The white line represent 200 nm according to the scale of the image.

In all cases, mTs refer to large-scale transistors with channel length  $L = 20 \mu\text{m}$  and width  $W = 1 \text{ mm}$  unless stated otherwise and nTs refer to nano-scale transistors with  $L = 80 - 500 \text{ nm}$  and  $W = 20 - 80 \mu\text{m}$  whatever the way they are processed.

## A.2. PBTTT deposition

The polymer is spin-coated on the samples in a  $\text{N}_2$ -filled glove box to avoid any detrimental interactions with water or oxygen from ambient air. If this condition is not fulfilled, it translates generally into bad off-state of transistors, the encapsulate  $\text{H}_2\text{O}$  molecules acting as charge traps and  $\text{O}_2$  oxidizing the polymer.

In order to ensure proper surface, gold-samples are first clean with acetone and isopropanol and put in an UV-ozone cleaner for 30 min (5 min under UV light followed by 25 min in the subsequent ozone environment). This treatment eliminates all organic compounds at the interface and changes the surface potential to enhance the wettability of the polymer solution. Its effect last only few minutes then the deposition must be done immediately. We didn't perform any further surface functionalization as we are interested by the metal-organic interface, that would be affected by such treatment.

It is worth noting that UV-ozone is not suitable for cobalt electrode as it would strongly oxidize the interface, therefore we skip this step. However, even without UV-ozone, cobalt is anyway oxidized (to a less extent) that is strongly limiting the expected spin injection. We choose then to follow the paper of Galbiati *et al.* to recover the bare cobalt by chemical etching<sup>2</sup>. They

demonstrate that glycolic acid in ethanol dissolve cobalt oxide at a rate of  $0,5 \text{ nm} \cdot \text{min}^{-1}$ , relatively independent on the acid concentration, in glove box environment. We reproduce the latter etching before the pBTTT spin-coating by immersing the cobalt-sample 10 min in such a solution ( $1 \text{ mg} \cdot \text{mL}^{-1}$ ) and rinsing it with pure ethanol.

The pBTTT is dissolved in 1,2-dichlorobenzene with a concentration of  $4 \text{ mg} \cdot \text{mL}^{-1}$  by agitating and heating the solution at  $150 \text{ }^\circ\text{C}$  for 30 min. Then, the polymer is spin-coated on the prepared samples in two steps: 1000 RPM for 120 s followed by 2000 RPM during 60 s. The layer is further dried on a hot plate 30 min at  $150 \text{ }^\circ\text{C}$  that serves also as quick annealing of the polymer thin film.

Finally, the contact pads far from the active region, the gate electrode and the back and edges of the substrate are cleaned with solvent-wet cotton bud. It is especially important to avoid any direct contact between the polymer and the gate electrode, otherwise the leakage current (from source to gate electrode) would be dominant because the electric field from the gate voltage is superior to the source-drain one.

From this moment, the samples need to be store in glove box (or under vacuum) to keep reasonable transistor performances over time.

### A.3. Electrolyte gel

The final step of EGOFETs fabrication is the addition of the electrolyte on top of the polymer. We choose the “cut and stick” technique introduced by Lee and co-workers to add the top-gate on our samples<sup>3</sup>. The principle is to turn an ionic liquid into an ion gel, cut the gel to the appropriate size and drop it on the OFET. It is a very convenient method because we prepare large-size ion gel at once that is used for several samples. This step is then very quick and easy to set up and is suitable for different ionic compounds. The main issue of gel is its freezing during temperature ramp (around 200 K) because it tends to flow away from the sample. It can then be easily replaced but the underneath polymer channel may be damage by the pull-out of the electrolyte.

The ion gal was prepared by dissolving the ionic liquid 1-butyl-3-methylimidazolium ( $[\text{BMIM}]^+[\text{PF}_6]^-$ ) and the polymer poly(vinylidene fluoridecohexafluoropropylene) (P(VDF-HFP)) in acetone. The ionic liquid afforded the ion for the doping and the polymer gels the ionic liquid. The jellifying polymer is in pellet form and need to be firstly ground into powder for better dissolution in acetone. The weight ratio between P(VDF-HFP),  $[\text{BMIM}]^+[\text{PF}_6]^-$  and acetone is 1: 4: 7. The solution is then drop casted on a glass slide previously cleaned with acetone, ethanol and isopropanol and putted in a plasma-oxygen cleaner for 20 min. Finally, the still liquid ion gel is dried in a vacuum oven at  $70 \text{ }^\circ\text{C}$  for 24 h. The thickness of the layer is roughly  $500 \text{ }\mu\text{m}$ .

The ion gel is simply cut with a razor blade and transferred onto the sample with a tweezer in order to bridge the active polymer channel and the gate electrode (**Figure A.3**). The obtained electrolyte is sensitive to humidity and has also to be kept in glove box. The EGOFET is then ready for measurements.

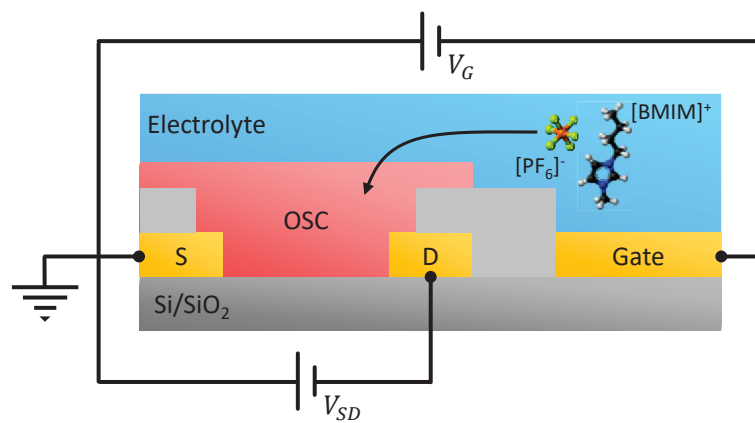


Figure A.3 Schematic of the final lateral EGOFET structure.

**Bibliography**

- (1) Dayen, J. F.; Faramarzi, V.; Pauly, M.; Kemp, N. T.; Barbero, M.; Pichon, B. P.; Majjad, H.; Begin-Colin, S.; Doudin, B. Nanotrench for Nano and Microparticle Electrical Interconnects. *Nanotechnology* **2010**, *21* (33).
- (2) Galbiati, M.; Delprat, S.; Mattera, M.; Mañas-Valero, S.; Forment-Aliaga, A.; Tatay, S.; Deranlot, C.; Seneor, P.; Mattana, R.; Petroff, F. Recovering Ferromagnetic Metal Surfaces to Fully Exploit Chemistry in Molecular Spintronics. *AIP Adv.* **2015**, *5* (5), 0–8.
- (3) Lee, K. H.; Kang, M. S.; Zhang, S.; Gu, Y.; Lodge, T. P.; Frisbie, C. D. “Cut and Stick” Rubbery Ion Gels as High Capacitance Gate Dielectrics. *Adv. Mater.* **2012**, *24* (32), 4457–4462.



## Annex B

# PBTTT-based EGOFETs

**B**asic electrical characterisations of electrolyte-gated organic field effect transistors (EGOFETs), fabricated following the recipe from annex A, are presented in this second annex. Output curves and transfer curves for different scales, doping levels and materials are investigated to support the discussion of the core chapters. An estimation of the mobility and the carrier density is also calculated, and conduction properties at low temperature for different doping levels revealing the onset of insulator to metal transition is also presented.

### B.1. Room temperature electrical characterization

At room temperature, samples are measured on a probe station inside a glove box. We perform output curves and transfer curves to study the quality of the electronic transport and interfaces before more systematic temperature and magnetic field analysis in our cryostat. However, the figure of merit of a good organic channel is its mobility ( $\mu$ ), that is not accurately available in our top-gate EGOFET devices. The easiest way to obtain  $\mu$  is the deduction from the slope of the linear part of the transfer curve (see section I.5.1). In the case of EGOFETs, there is a continuous transition from electrostatic to electrochemical doping (see chapter I) that hamper the latter method. In addition, the leakage current is usually quite high in top-gate geometry, then the extracted mobility is doubtful. To circumvent the problem, we prepare – at the same time than our home-made sample – one commercial Fraunhofer substrate often used in the organic electronic community for polymer characterization. We perform mobility measurements on these purchased test substrates in bottom-gate geometry that are well known for their excellent SiO<sub>2</sub> quality translating into very low leakage current (< 100 nA) even for voltage overpassing 80 V (**Figure B.1a**). The typical mobility we get is around 0,05 cm<sup>2</sup>. V<sup>-1</sup>. s<sup>-1</sup> (**Figure B.1b**). The transport efficiency is relatively low compared to literature because we are not operating any surface functionalization such as octadecyltrichlorosilane (OTS) nor high temperature

annealing ( $> 180$  °K). Moreover, the reliability factor of Choi and co-workers<sup>1</sup>, introduced in **section I.5.5**, is around 0,5, meaning a possibly overestimation of 50 % of the effective mobility. Nevertheless, the aim of this thesis is not to improve further the mobility, we need high conductivity ( $\sigma$ ) and we achieve it through the rise of carrier density ( $n$ ) as  $\sigma = en\mu$  – where  $e$  is the electric charge – by the electrochemical doping.

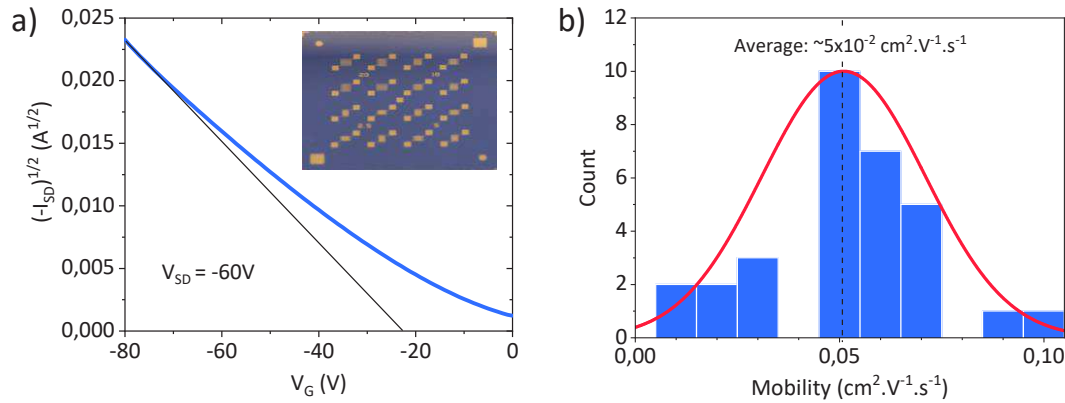


**Figure B.1** a) Square root of  $-I_{SD}$  versus  $V_G$  of pBTTT on Fraunhofer substrate at  $V_{SD} = -60$  V. The inset shows the device geometry (picture from Fraunhofer's website) and the black line is the linear fitting to determine the slope and then the mobility of carrier in the polymer. b) Histogram of the extracted mobility of a set of 31 transistors. The average value is around  $5 \times 10^{-2} \text{ cm}^2 \cdot \text{V}^{-1} \cdot \text{s}^{-1}$ .

### B.1.1. Gold-electrode EGOFETs

Transistors with gold electrodes was widely study in our group as well as in the literature. Gold Fermi energy (see **Figure IV.2**) and chemical stability make it very suitable for our pBTTT-EGOFETs.

Output curves are operated in order to determine the regime in which the transistor is working, according to the applied source-drain voltage. As explain in chapter I, we want it to run in the linear regime such that the gated-4-probe (gFP, section I.5.4) method is valid. From **Figure B.2**, we observed linear output curves for  $V_G \geq 2,5$  V until  $\pm 400$  mV for both mT and nT. At lower doping levels, the output curves are non-linear in the selected  $V_{SD}$  range, saturation occurring from  $V_{SD} \sim \pm 300$  mV for  $V_G = -2$  V. In the experimental part, the applied  $V_{SD}$  will be generally  $-100$  mV: the value must be high enough to avoid the low source-drain voltage non-linearity (generally below 20 mV), but also small enough to keep uniform doping within the channel, *i.e.* to prevent mismatch with the gate electric field. The saturation of nT is also presented in **Figure B.2**, occurring at large source-drain voltage and reaching the milliampere range. The negative sign keeps the source electrode as source of carrier as pBTTT is a *p*-type polymer.

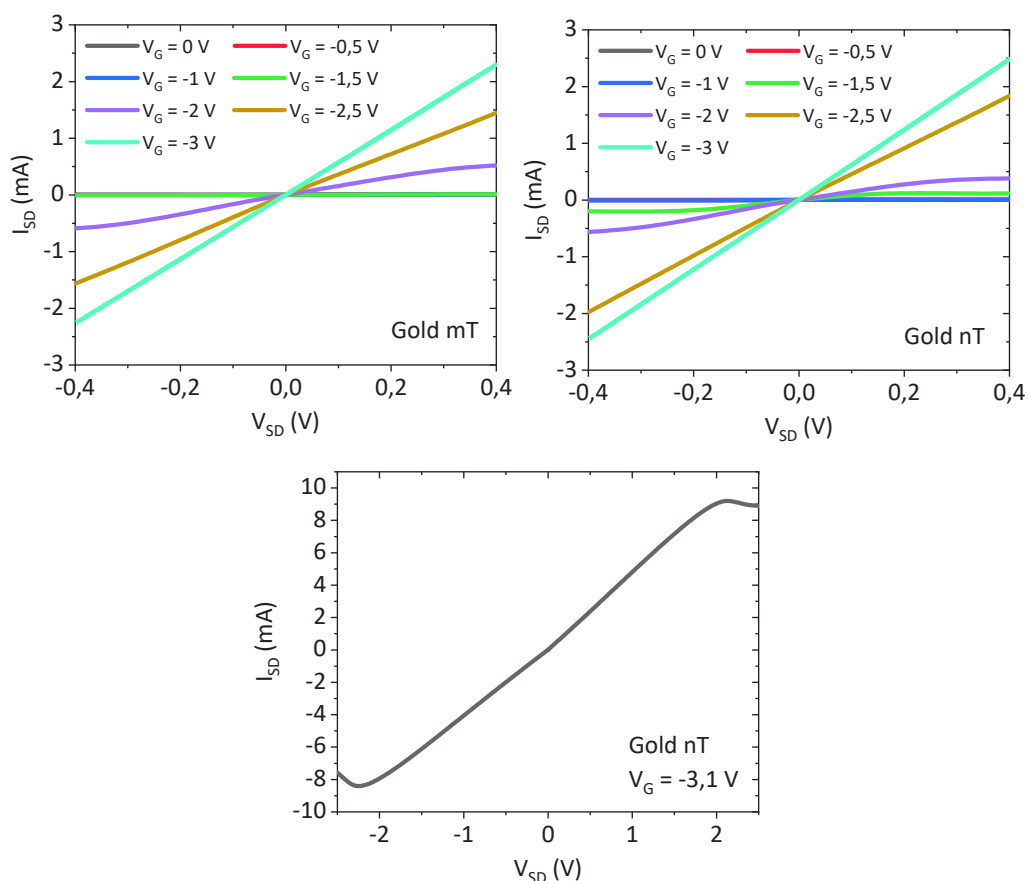


**Figure B.2** Top: output curves for both EGOFET scales with gold electrodes, for various gate voltage from 0 V to  $-3$  V with a step of 0,5 V. Bottom: saturation of the nT at the maximum doping level.

The migration of ions is slow, therefore it is important to let the system reach equilibrium at each gate voltage before performing the output curves. Accordingly, we first apply the chosen gate voltage while monitoring  $I_{SD}$  and  $I_G$  versus time. When both currents stabilize, the output curve measurement is performed. The stabilization is fast for low gate voltage as ions stay in the electrolyte (tens of seconds) but lasts tens of minutes for the highest doping levels when ions must penetrate inside the polymer.

Transfer curves are also performed on both mTs and nTs (**Figure B.3a-b**). In EGOFET devices, the maximum gate voltage is around 3 V. If  $V_G$  is too large, chemical reactions driven by the high potential may occur, making the system unknown. As an indicator, negative transconductance appears with the current significantly decreasing while  $V_G$  continue to rise. The latter phenomenon generalizes on all electrolyte-gated organic materials but is not yet fully understood. Different explanation are reported as bipolaron formation<sup>2</sup>, carrier-carrier interactions<sup>3</sup> or band filling<sup>4</sup>. To hold  $V_G$  in the appropriate range, we keep an eye on  $I_{SD}$  during the sweeps. When it saturates, we stop the increase of gate voltage and make it slowly come back to 0.

In EGOFETs, huge hysteresis is very usual because of the slow motion of ions. The current at the end of the transfer curve (when  $V_G$  sets back to 0 V) remains relatively high because ions need more time to come back in the electrolyte, despite slow gate voltage sweeping speed of

either  $1 \text{ mV} \cdot \text{s}^{-1}$  or even  $0,5 \text{ mV} \cdot \text{s}^{-1}$ . The semi-log scale (black curves) helps to see the shoulder in the current rise, around  $V_G = -1 \text{ V}$ , assigned to the transition from electrostatic to electrochemical doping. The latter transition is also supported by the much smaller hysteresis when the transfer curve is stopped at lower gate voltage as depicted in **Figure B.4**. When the gate voltage stops to  $-1 \text{ V}$ , the back and forth currents are close to each other. If  $V_G$  reaches  $-1,5 \text{ V}$ , signs of electrochemical doping appear with an S-shape current and a sort of “inertia” of  $I_{SD}$  that continue slightly to increase while the gate voltage is already returning to  $0 \text{ V}$ . Finally, from  $V_G = -2 \text{ V}$ , the hysteresis becomes very large.

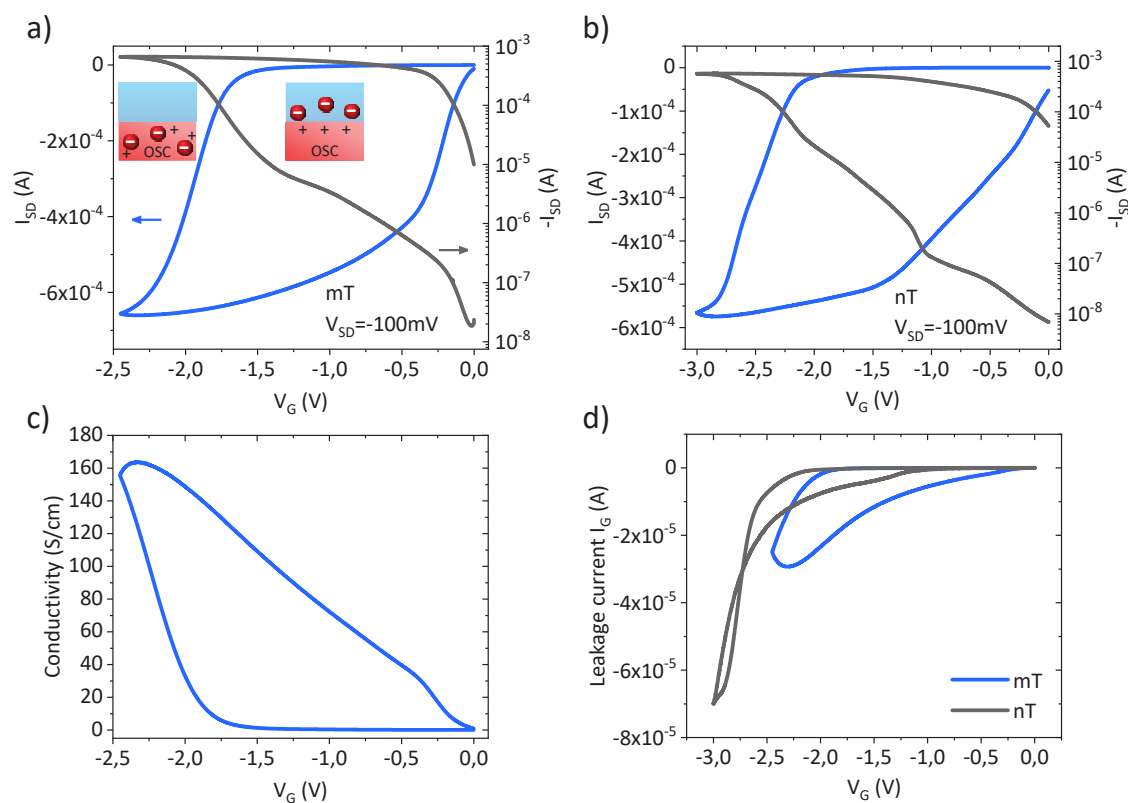


**Figure B.3** a-b) Transfer curves of an mT (a) and an nT (b) in linear (blue) and logarithmic scale (black). The insets in figure a) show the doping regime: electrostatic (right) or electrochemical (left). c) Conductivity versus gate voltage corresponding to the above transfer curve. The conductivity is extracted from 4-probe measurements. d) Leakage current ( $I_G$ ) measured during the transfer curves of the mT (a) and the nT (b).

To recover from the relatively high current at maximum applied gate voltage values (here  $\sim 10^{-5} \text{ A}$  for the mT) down to its initial value prior to applying the gate voltage, an undoping step is needed by putting  $V_G$  to zero while keeping the source-drain voltage. The undoping lasts between tens of minutes to whole night depending on the sample, relating for instance on the electrolyte/gate electrode area versus the electrolyte/polymer interface area.

The usual polymer conductivity at maximum doping with gold leads is around  $400 \text{ S} \cdot \text{cm}^{-1}$  and reaches sometimes higher values close to  $600 \text{ S} \cdot \text{cm}^{-1}$  (**Figure B.3c**). Such conductive semiconductor polymer is not common, even for better process films with mobility one or two order

of magnitude larger. Another important point to emphasize is the very similar transistor behaviour of nT compared to mT. No short-channel effects has been reported on our nano-scale EGFETs. The high capacitance from the electrolyte and the low  $V_{SD}$  seems to keep the transverse electric field larger than the one between source and drain. This is already an important result as it opens the door to nano-size device for organic electronics applications.

Finally, in order to ensure that the current is indeed flowing in the organic channel, the leakage source-gate current ( $I_G$ ) is checked (**Figure B.3d**). The leaking is always much larger in top-gate than in bottom-gate geometry, but we manage to limit it at least one order of magnitude lower than  $I_{SD}$ . Samples showing too high leakage current are not further studied. It will not be a major issue later on, as main experimental studies operated at low temperature. The cooling suppresses the leakage current by freezing the electrolyte gel such that ions become nearly motionless.

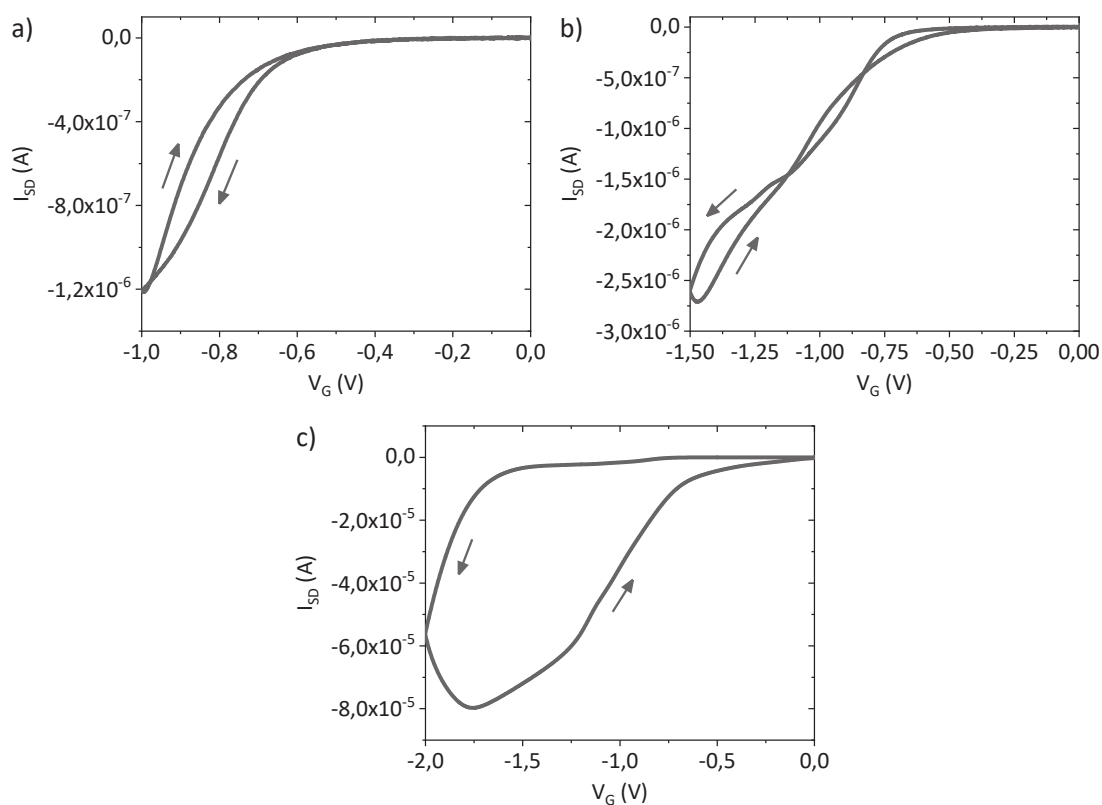


**Figure B.4** Transfer curve limited to a maximum gate voltage of  $-1$  V (a),  $-1,5$  V (b) and  $-2$  V (c).

The source-gate current gives also information on the doping as this current is carried by the dopant ions. By applying suddenly the maximum  $V_G$ , the leakage current exhibits a large peak (negative as we apply a negative gate voltage) and relaxes with time ( $t$ ) until it reaches a new equilibrium (**Figure B.5**). By integrating  $I_G$  over time – and subtracting the intrinsic leakage value ( $I_{offset}$ ) – the carrier density ( $p$ ) estimation is given by:

$$p = \frac{1}{ehA} \int (I_G - I_{offset}) dt$$

where  $h$  is the channel thickness and  $A$  is the coverage area of the electrolyte above the polymer. Typical values we extracted are above  $10^{21} \text{ cm}^{-3}$ , corresponding to an astonishing number of holes per monomer larger than 2, assuming a uniform doping in the whole pBTTT volume. From the plot of **Figure B.5** for example, the deduced density is  $\sim 4 \times 10^{21} \text{ cm}^{-3}$ . The area chosen for the calculation considers the whole electrolyte/organic semiconductor area, thus it should be the minimal density of dopants injected into the organic layer, that is already surprisingly high.

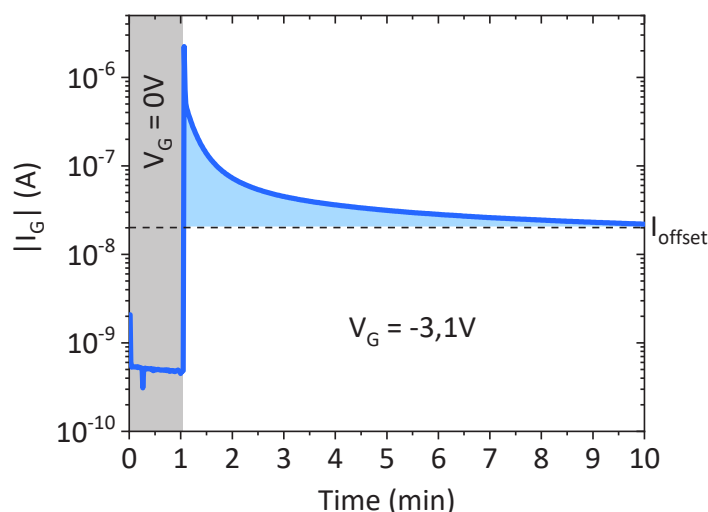


**Figure B.5** Leakage current versus time when turning on the gate voltage abruptly from zero (grey zone) to its maximum value. The area under the curve (blue) is proportional to the number of ions entering the polymer.

In addition to the uncertainty on the area to consider for the determination of the carrier density, the capacity formed by the staggered structure is not uniform because of the presence of electrodes. It may therefore lead to non-uniform doping within the channel. Moreover, the polymer is likely highly doped under the electrolyte, but the uncovered pBTTT may also be doped by the diffusion of ions within the polymer. Finally, it is impossible to distinguish the portion of ions entering in the polymer versus the ones staying inside the electrolyte, at the interface, that participate also to  $I_G$ . It may however be partially suppressed by the subtraction of  $I_{offset}$  as they are likely responsible for the increase of the relaxed leakage current.

The accurate knowledge of the carrier density is useful to determine the mobility of carrier in the polymer, following  $\sigma = ep\mu$ . In our case, considering the average conductivity of  $400 \text{ S}\cdot\text{cm}^{-1}$ , the carrier concentration from **Figure B.5** would translate into  $\mu \approx 0,6 \text{ cm}^2\cdot\text{V}^{-1}\cdot\text{s}^{-1}$ .

### B.1.2. Cobalt-electrodes EGOFETs

The output curves of EGOFETs with cobalt wire are very similar to the previous one on samples with gold (**Figure B.6**). The main difference is the lower intensities and a more important gap between  $V_G = -2 \text{ V}$  and  $V_G = -2,5 \text{ V}$ , coming from a larger threshold voltage (**Figure B.7a-**

b). For the highest doping levels, the curves become linear which is suitable for the gFP method used in the chapter IV for contact resistances calculation.

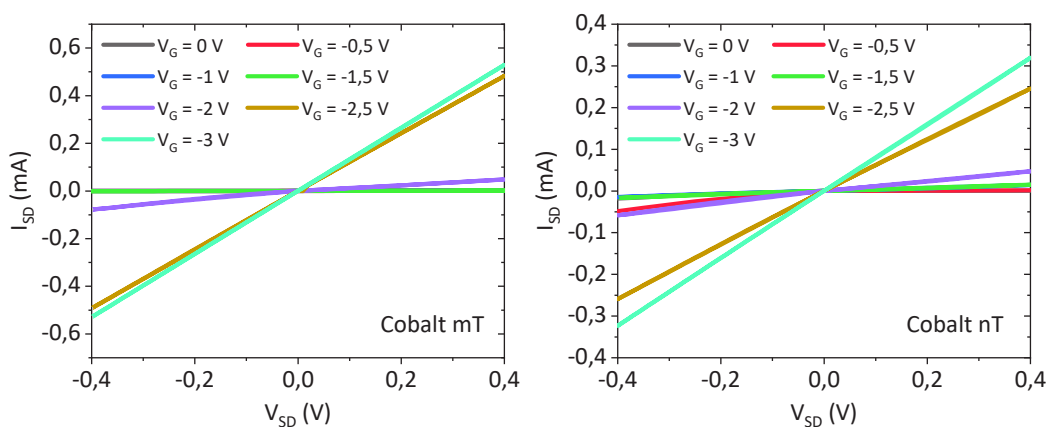


**Figure B.6** Output curves for both EGOFET scales with cobalt electrodes, for various gate voltage from 0 V to  $-3$  V with a step of 0,5 V.

Transfer curves are displayed in **Figure B.7a-b**. We observe again nice transistor behaviours of both scales with high on/off ratio and significant current at maximum doping. The conductivity is however usually lower by a factor 10 (**Figure B.7c**) compared to samples with gold electrodes, likely as a result of the lack of UV-ozone cleaning and alternative chemical treatment before the polymer deposition as mentioned in annex A. Again, the leakage current is high but remains at least one order of magnitude lower than  $I_{SD}$ . There is also no sign of short-channel effects on nTs.

## B.2. Low temperature electrical characterization

To further investigate EGOFETs, samples were inserted in a cryostat to cool them down to 1,5 K. The cryostat is an isolated liquid helium reservoir, with a variable temperature insert (VTI) in which samples are introduced. The liquid  $^4\text{He}$  basis temperature is 4,2 K, and a needle valve is available to blow helium gas to achieve 1,5 K.

It is important to remind that the ion gel freezes around 200 – 220 K. Therefore, doping is no more possible when the temperature is below because ions cannot move anymore. As we are interested in highly doped pBTTT, the doping process must be done at higher temperature before cooling down. Within the enclosure of the VTI, a heater warms up the sample to 300 K. The gate voltage is not continuously increased in this case. Rather,  $V_G$  is slowly incremented with steps of  $-0,5$  V (**Figure B.8**). At each level, the stabilization of  $I_{SD}$  and  $I_G$  is awaited before rising the gate voltage one step further. After each incrementation, a peak appears in the leakage current, as ions are more and more pushed towards the polymer. In this way, we ensure the maximal doping level of the polymer. The maximum  $V_G$  is known from the previous room temperature characterization. The main drawback is the time duration that ranges from 8 h to 24 h.

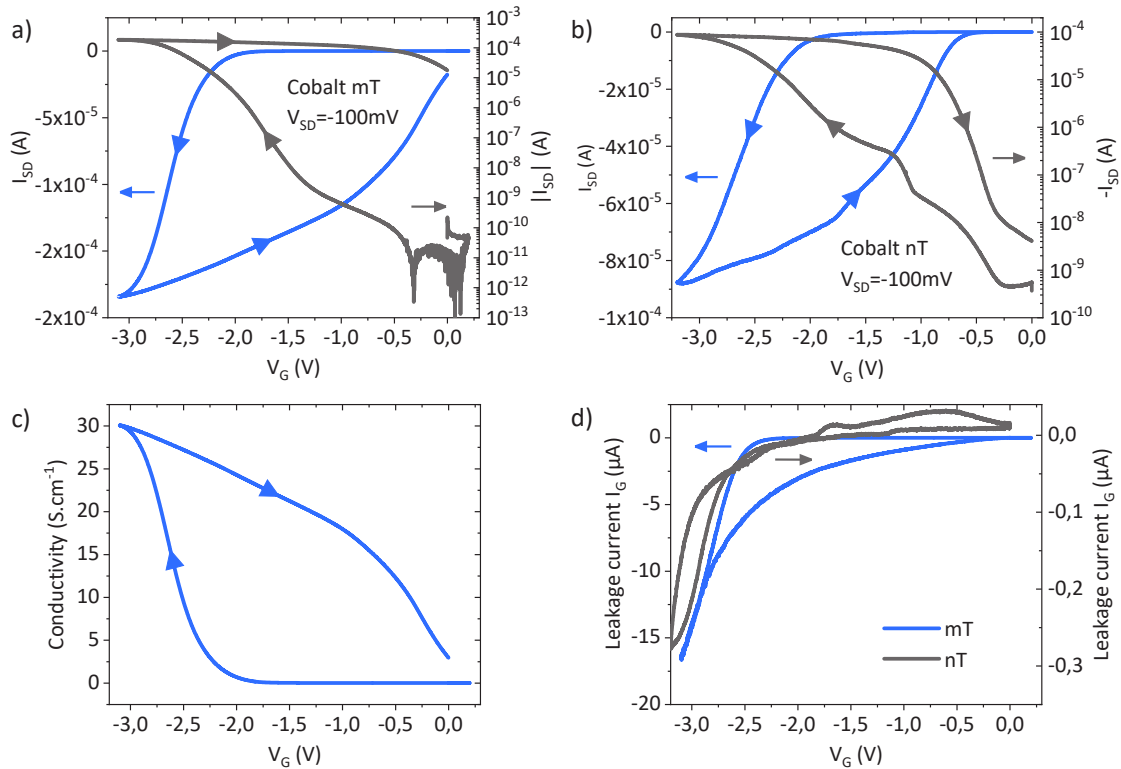


**Figure B.7** a-b) Transfer curves of an mT(a) and an nT (b) in linear (blue) and logarithmic scale (black). c) Conductivity versus gate voltage corresponding to the above transfer curve. d) Leakage current ( $I_G$ ) measured during the transfer curves of the mT (a) and the nT (b).

Once the desired doping level is obtained, the sample is slowly cooled down under constant  $V_G$  until the leakage current becomes negligible, sign of the freezing of the ion gel. From that point, and as long as the sample is not heated above 200 K, the sample is safe regarding the doping level. The doping procedure shown below belong to an mT with gold electrodes, but the same behaviour is obtained for mTs and nTs made of gold and cobalt.

As already mentioned, the doping is reversible by stopping the gate voltage until the source-drain current comes more or less back to its initial value of the undoped pBTTT. However, the freezing of the ion gel makes it very fragile, and it usually breaks and detaches when heating up. Then, the only way to study another doping level is to take out the sample, put another ion gel and insert it again. This is often harmful to the channel because the organic channel had to spend time again in the air. In addition, some polymer may be stick on the ion gel that was removed, leading to an ill-define thin film. When this operation is done, current at the new doping level with the new ion gel is compared to the current at the same  $V_G$  with the former electrolyte. If there is no matching, the sample is not further examined.

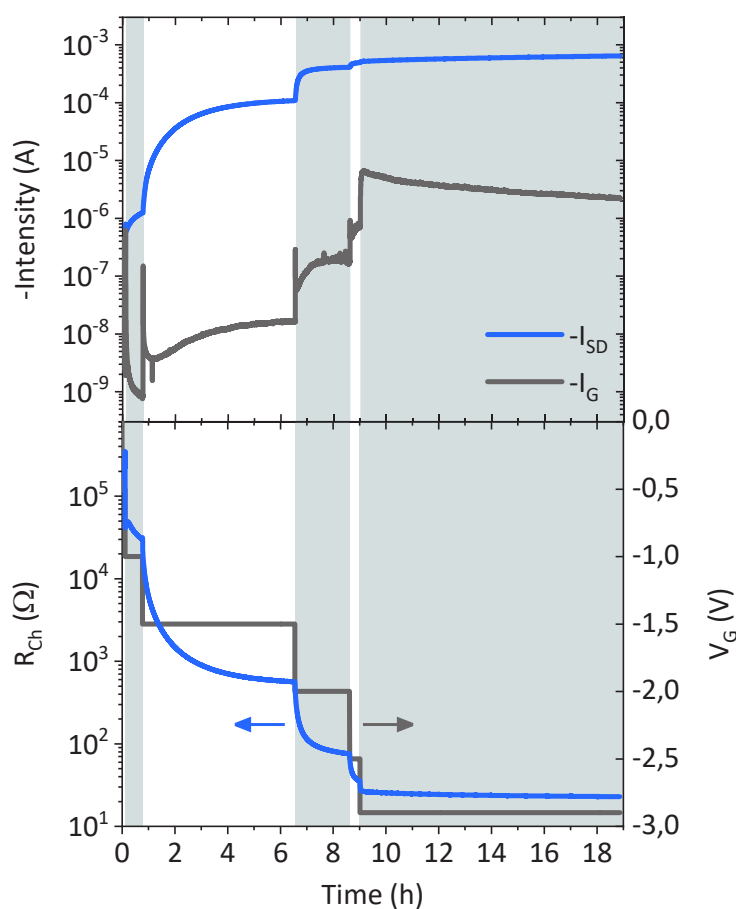


**Figure B.8** Doping procedure at 300 K. The two first steps stabilizes very fast (few minutes). The following steps are much longer particularly from the moment ions penetrate the pBTTT ( $|V_G| \geq 1,5$  V).

### B.2.1. Insulator- to metallic-like transition

A very nice feature of pBTTT-based EGOFETs is the transition from bad conductor to the onset of metallicity by tuning the gate voltage by a few volts only. Looking at the temperature dependence of the conductivity for three doping level (corresponding to  $V_G = -1,5$ ;  $-2$ ;  $-3$  V), a clear changeover takes place (**Figure B.9**). The conductivity of the less doped channel decreases drastically by cooling down the sample and was hardly measurable under 20 K. By decreasing  $V_G$  by only 0,5 V, the organic channel keeps a reasonable transport capability until 1,5 K. However, the slope of the curve indicates a faster decay the lower the temperature leading to a probably negligible conductivity when the temperature tends to 0. Finally, on the highest doped polymer ( $V_G = -3$  V), the conductivity exhibits a plateau below 4 K that is a sign of metallic-like behaviour. This onset of metallicity was more in details considered by Zanettini *et al.* from our group, on the same EGOFET structure<sup>5</sup>.

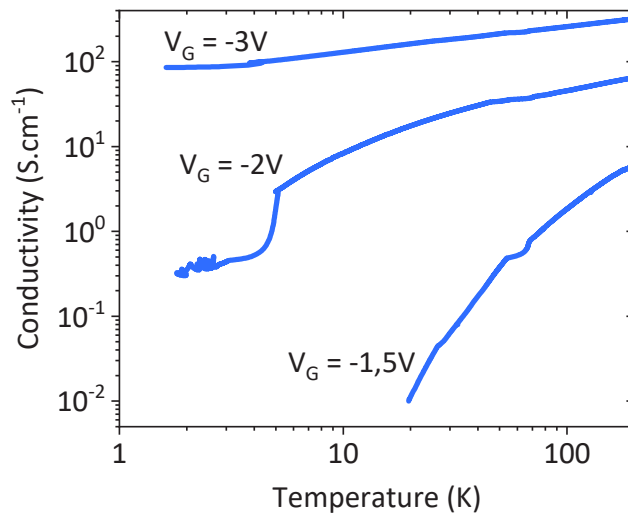


**Figure B.9** Conductivity from 4-probe measurements on mT for various doping levels. A transition from insulator- (no conduction at 0 K) to metallic-like (finite conductivity at 0 K) behaviour is observed.

Observing the sample resistances ( $R_{Sample} = R_{Ch} + 2R_C$ ) of mT and nT, they operate the same way except for the lowest doping (**Figure B.10**). The resistance diverges for the long channel but saturated on nT. The quite different aspect ratio is likely the origin of the contrast.

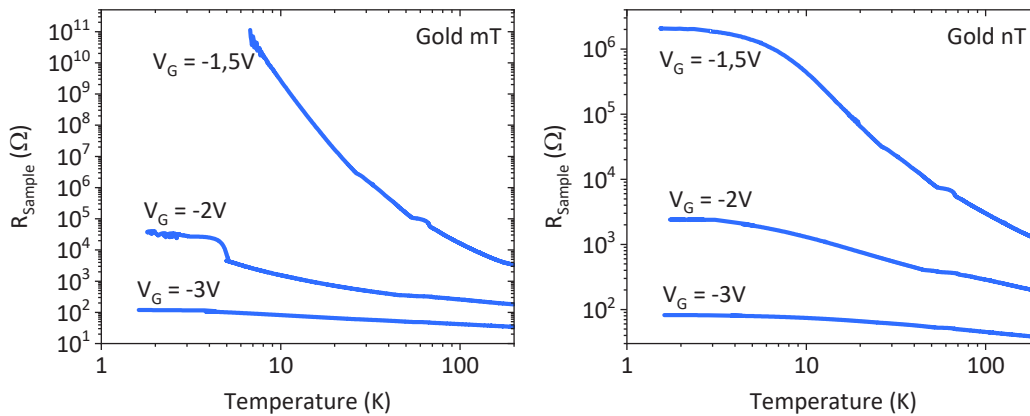


**Figure B.10** Sample resistance of gold mT (left) and nT (right) for three doping levels.

Output curves were also performed on both scales and for the highest and lowest doping levels (**Figure B.11**). Significant non-linearities appear only at 1,5 K on the mT while there are already present at 50 K on the nT for both doping levels shown. The early non-Ohmic output curves of nT suggests a notable interface barrier.

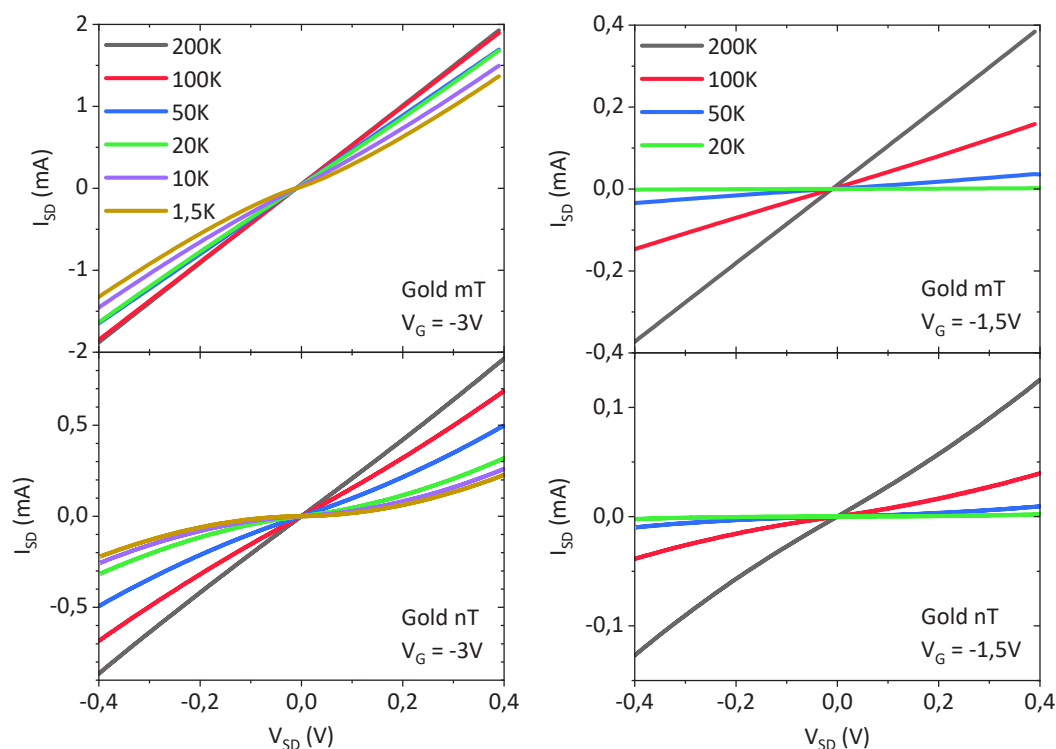


**Figure B.11** Output curves of gold mT (top) and nT (bottom) for the highest (left) and lowest (right) doping level investigated.

### B.2.2. Comparison of gold and cobalt electrodes

In order to compare performances of transistors with gold and cobalt electrodes in the same experimental conditions, both types were patterned on the same chip. mT and nT of both metals are deposited with the same techniques than explained in annex A. The main discrepancy is the number of fabrication steps, as two evaporations are required per nanogap per material. In this way, we ensure the closest polymer morphology on both kinds of device and the most similar doping of the channel.

Output curves of cobalt samples are again very similar to gold ones, with the appearance of significant non-linearities only at 1,5 K for the mT and already at 50 K for the nT (**Figure B.12**).

Electrical properties of gold and cobalt mT and nT are summarized in **Figure B.13**. The channel resistance of all devices is depicted.  $R_{Ch}$  of mT is deduced from 4-probe measurements and the extracted conductivity is used to calculate the channel resistance of the nT. Therefore, on the same material, both  $R_{Ch}$  are proportional. Focusing first on mT, the transport properties exhibit an exponential decay over a wide range of temperature corresponding to activated carrier motion, but seems to reach a plateau at low temperature.

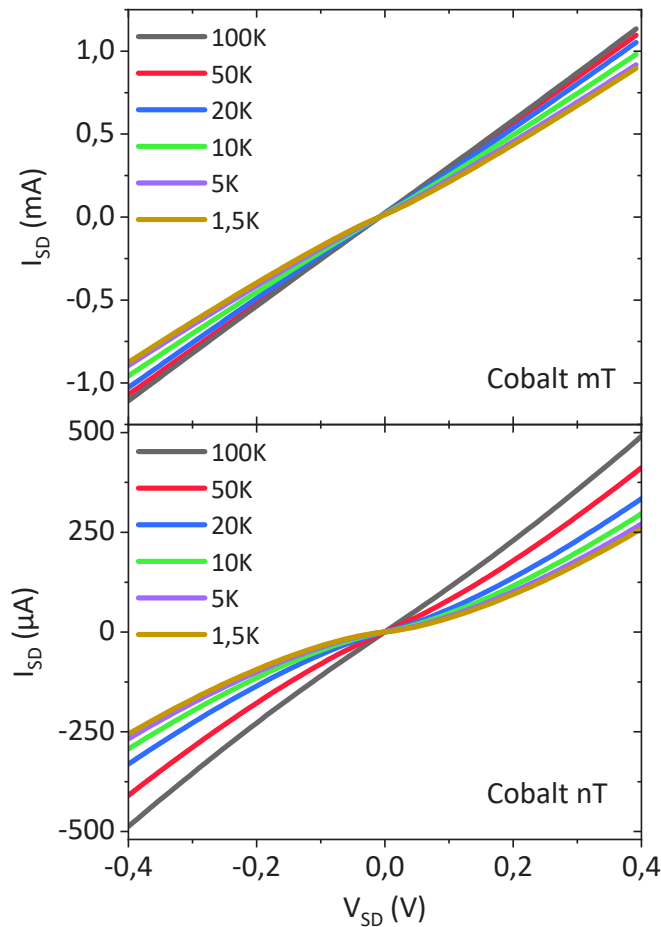


**Figure B.12** Output curves of cobalt mT (top) and nT (bottom) for the highest doping level investigated.

The conductivity of nT being unknown, the sample resistance is also plotted. By comparison of  $R_{Ch}$  and  $R_{Sample}$ , the transistors seem indeed contact limited as  $R_{Ch}$  is at least on order of magnitude lower than  $R_{Sample}$ . Even more annoying is the very high sample resistance versus channel resistance of the cobalt-based nano-scale EGOFET that announces large contact resistance.

The fabrication of EGOFETs with gold and cobalt electrodes with proper transistor characteristics were demonstrated on micro- and nano-scale. The tuning of the doping level through the voltage applied to the electrolyte is an easy tool to study the properties of charge transport in an organic channel, from almost insulator to the onset of metallicity. The plateau of the conductivity, reached at very low temperature, is of particular interest for spin detection. However, the preliminary results on devices with cobalt electrodes suggests a much poorer interface with pBTTT that might severely hamper spin injection or detection. The contact resistance is more thoroughly investigated in the chapter IV.

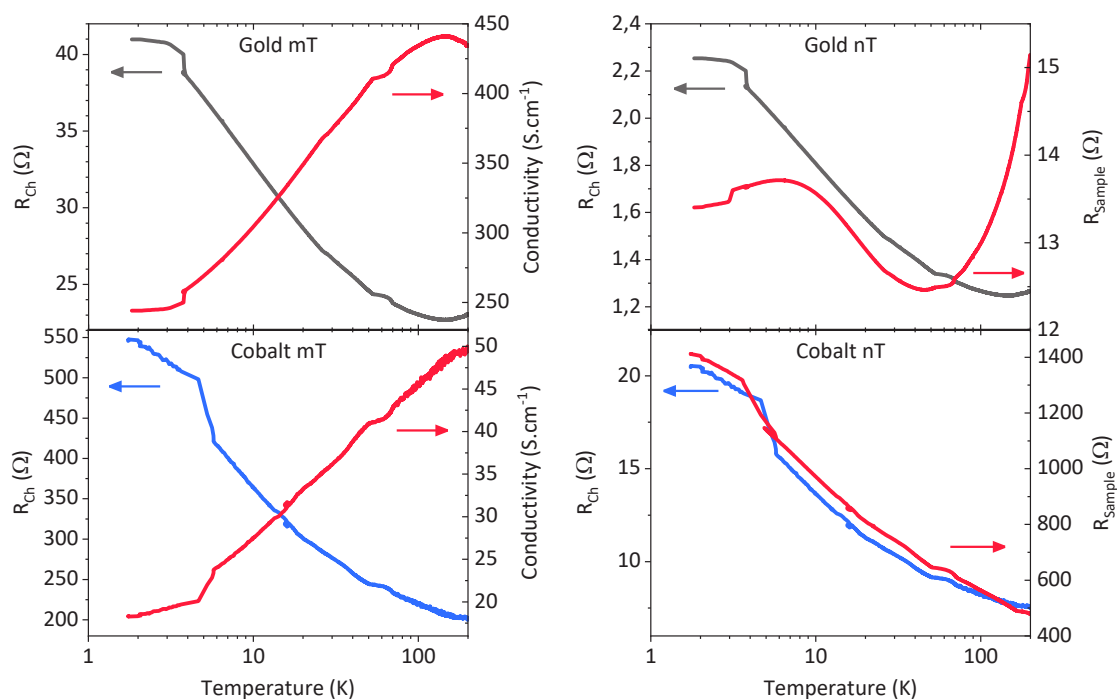


**Figure B.13** Right: channel resistance and conductivity of mT made of gold (top) and cobalt (bottom) electrodes. Left: channel resistance and total resistance of nT made of gold (top) and cobalt (bottom) electrodes.

### Bibliography

- (1) Choi, H. H.; Cho, K.; Frisbie, C. D.; Siringhaus, H.; Podzorov, V. Critical Assessment of Charge Mobility Extraction in FETs. *Nat. Mater.* **2017**, *17* (1), 2–7.
- (2) Street, R.; Salleo, a.; Chabinyo, M. Bipolaron Mechanism for Bias-Stress Effects in Polymer Transistors. *Phys. Rev. B* **2003**, *68* (8), 1–7.
- (3) Xia, Y.; Cho, J.; Paulsen, B.; Frisbie, C. D.; Renn, M. J. Correlation of On-State Conductance with Referenced Electrochemical Potential in Ion Gel Gated Polymer Transistors. *Appl. Phys. Lett.* **2009**, *94* (1).
- (4) Paulsen, B. D.; Frisbie, C. D. Dependence of Conductivity on Charge Density and Electrochemical Potential in Polymer Semiconductors Gated with Ionic Liquids. *J. Phys. Chem. C* **2012**, *116* (4), 3132–3141.
- (5) Zanettini, S.; Dayen, J. F.; Etrillard, C.; Leclerc, N.; Kamalakar, M. V.; Doudin, B. Magnetoconductance Anisotropy of a Polymer Thin Film at the Onset of Metallicity. *Appl. Phys. Lett.* **2015**, *106* (6), 2–6.

## Annex C

# Design issues for planar devices involving high-conductivity organics

The research of the optimal design of EGOFETs for spin injection, detection and transport leads to the search of optimal geometry design, for magnetism and charge transport. We pointed out here the difficulty encountered in few structures.

### C.1. Point effect

To ensure the best reproducibility between micrometer- and nanometer-scale transistors, we tried to pattern both scale on the same organic thin film. We designed an organic channel in the 100  $\mu\text{m}$ -range and added couples of transverse electrodes, with 150 nm to 500 nm distance between wires of a pair (**Figure C.1b**) through electronic lithography. These leads, perpendicular to the current flow, aim to both measure the potential (for 4-probe measurements) and inject and detect current at the nanometer-scale.

First, we chose a low aspect ratio ( $W = 5 \mu\text{m}$  and  $L = 100 \mu\text{m}$ ) to increase the intrinsic resistance of the channel (aspect ratio of **Figure C.1a**). Preliminary results on such geometry leads to spectacular conductivities reaching  $100\,000 \text{ S}\cdot\text{cm}^{-1}$  at the highest doping level, 100 times larger than the higher reported in the literature. To understand this surprising transport capability, we performed a simplified simulation on Comsol Multiphysics. It considers two gold electrodes in contact with a large area conductive material having the typical conductivity of pBTTT reported in this project, *i.e.*  $400 \text{ S}\cdot\text{cm}^{-1}$ . The analysis of the current density, depicted in **Figure C.1a**, carried out a highly non-uniform distribution of the current, because of the so-called point effect. At the edge of electrodes, charges accumulate and create a large local electric field that leads to poorly know effective channel geometry.

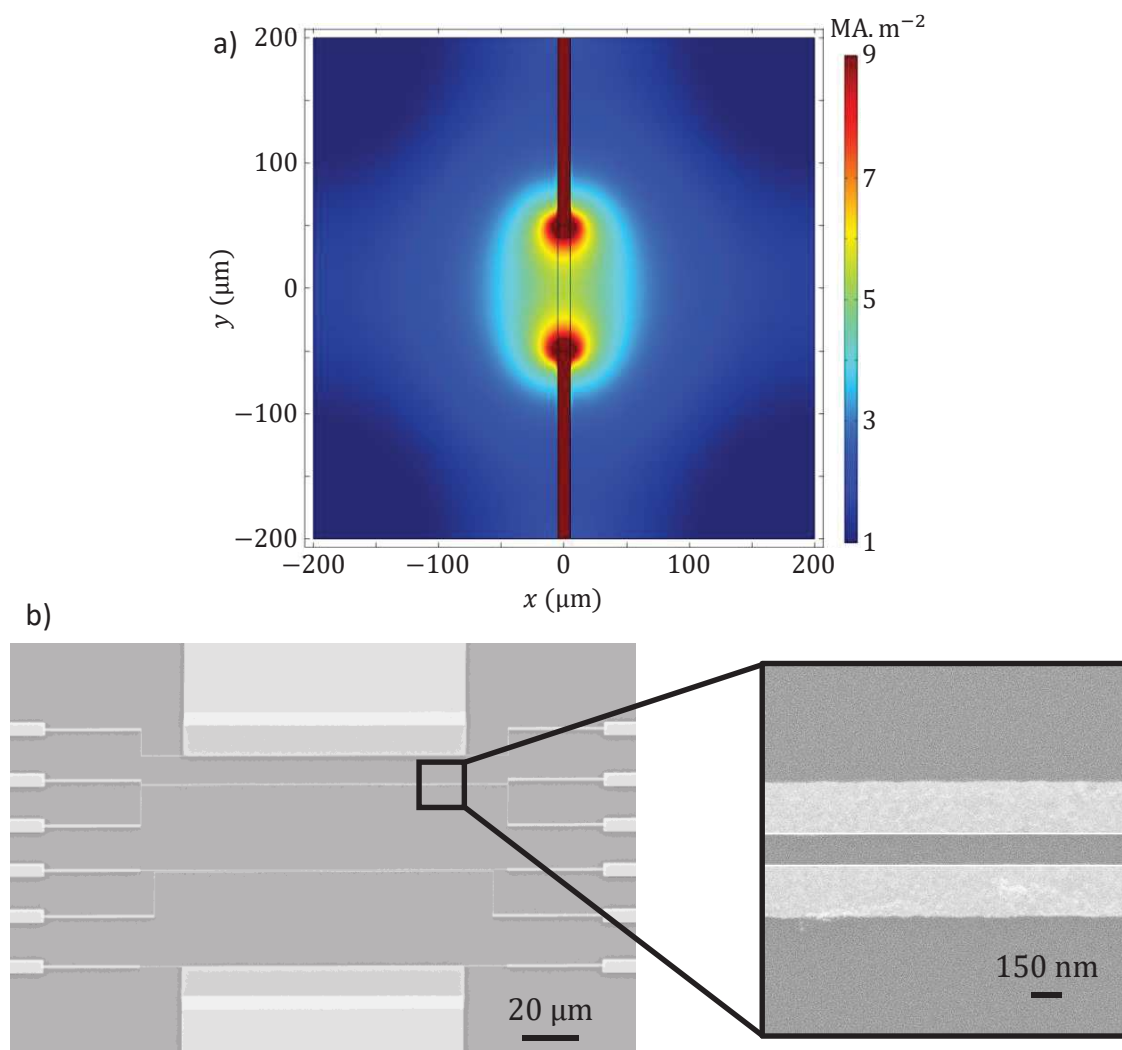


**Figure C.1** a) Simulation of the current density in an organic channel with low aspect ratio. The appearance of a large red dot on the edges of electrodes is due to the point effect and changes the effective width of the channel. b) Electron microscope image of the larger sample.

We therefore increase the width of the channel to 100 μm to approach an aspect ratio of 1 (**Figure C.1b**). Results of the micrometer-scale device was then close to the one reported in annex B. However, investigating the nanometer-scale EGOFETs, values were scattered and extracted contact resistance often negative. Again, we performed a numerical computation on Comsol Multiphysics that exhibited a drastic potential drop along the long and thin electrodes. The current is in fact injected over the first few micrometers and the channel is hence extremely non-uniform, involving a large uncertainty on extracted parameters.

## C.2. Channel broadening

The classical design for spin-valve is depicted in the left panel of **Figure C.2**. In the previous section we discussed the point effect that broads the channel in the case of thin electrodes.

However, it happens also when the aspect ratio is large as shown in the figure. On the right side of electrodes, the current spreads out of the patterned transistors. It could be a negligible part of the current, but we remind that the whole current passing in the positive  $x$  half surface of the picture has to be integrated, and results into a significant portion of the total current. Here again, it is a simplified situation where the contact resistance (and therefore current crowding) is not considered. By adding these two effects, the price to pay to pass “out of the transistor” becomes much lower that could translate into large uncertainty when inferring the properties.

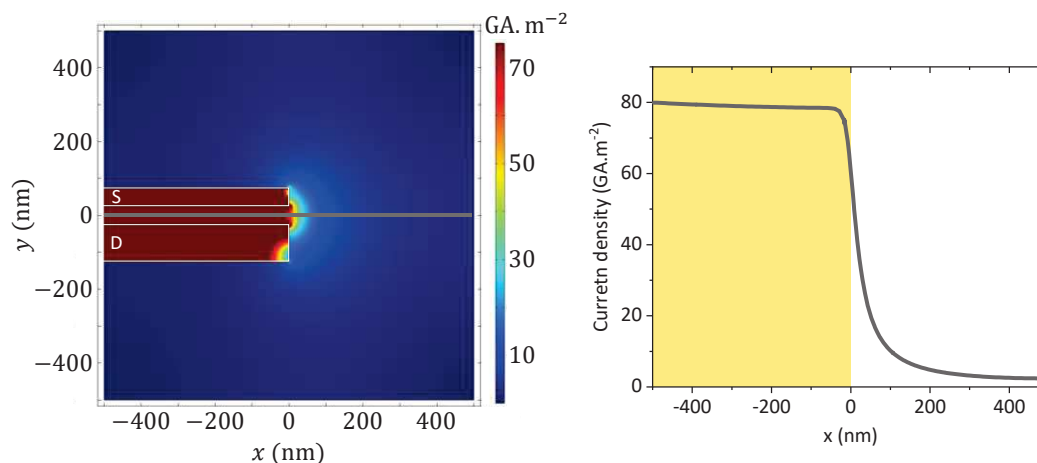


**Figure C.2** Left: simulation of the current density in a spin-valve geometry. Right: current density amplitude along the grey line of the left panel. The yellow region represents the region in between electrodes. The current flow extends also away from the electrode edges.

These geometrical issues, in addition to the eventual dominance of the pads resistance versus the channel one, was not accurately predictable because of the poor reproducibility of electric properties from sample to sample. Therefore, and because of the relatively bad preliminary results, we didn't focus further on spin-valve structures.



## Annex D

# Hall measurements on EGOFETs

**H**all effect investigation was carried out to indicate eventual diffusive band-like transport. Ordinary Hall effect relies on the deflection of charges in an external magnetic field ( $\vec{H}$ ), perpendicularly to the current flow and  $\vec{H}$  because of the Lorentz force. In a simplified picture, carriers in hopping transport regime should be only slightly sensitive to the Lorentz force as no classical velocity can be defined. The Hall potential ( $V_H$ ) is the transverse potential drop created by the deflected delocalized charges and writes:

$$V_H = R_H \frac{IH}{h}$$

where  $R_H$  is the Hall coefficient,  $I$  the current and  $h$  the thickness of the channel. The Hall coefficient  $R_H$  relates to the density of free carrier ( $n$ ) as:

$$R_H = \frac{1}{en}$$

where  $e$  is the elementary charge. In addition to point out delocalized transport, Hall measurements allowed to calculate the density of charges, and then the intrinsic mobility as  $\sigma = en\mu_H$ .

Hall effect in semiconductor polymer thin films was reported in several articles, but its amplitude is often lower than expected<sup>2,3</sup>. The weak Hall signal is generally assigned to lack of current uniformity and its disruption by the transverse electrodes. Nevertheless, significant Hall voltage has been measured recently referring to delocalized transport in organic materials<sup>4-6</sup>. The cited works of Wang *et al.* and Kang and co-workers are of particular interest for us as the former investigates electrochemically doped polymer while the second explores the properties of pBTTT.

In order to unravel if diffusive transport occurs in our EGOFET structure, we fabricated Hall bar (**Figure D.1a**) and measured the transverse potential upon the application of an external magnetic field, perpendicular to the organic thin film ( $V_{xy} \leftrightarrow V_H$ ). The amplitude of the field was

swept from  $-7$  T to  $7$  T, and Hall potential was indeed detected, in the microvolt range at  $10$  K (**Figure D.1b**). It is worth noting that the raw data presents an asymmetric parabolic shape likely due to the detection of residual  $V_{xx}$  exhibiting a parabolic variation with the field because of non-uniformity of the channel or no perfect alignment of Hall electrodes. Therefore, we subtracted the symmetric contribution to the data to recover the Hall signal.

From the slope of **Figure D.1b** we extracted  $R_H \sim 6 \times 10^{-8} \text{ m}^3 \cdot \text{C}^{-1}$  leading to a carrier density of  $1 \times 10^{20} \text{ cm}^{-3}$ . Then, knowing the conductivity ( $\sim 450 \text{ S} \cdot \text{cm}^{-1}$ ), we estimate the Hall mobility ( $\mu_H$ ) to  $\sim 25 \text{ cm}^2 \cdot \text{V}^{-1} \cdot \text{s}^{-1}$  that is one order of magnitude larger than previously reported in best doped pBTTT thin film<sup>6</sup>. However, the carrier concentration from Hall measurement is not consistent with the one determined in the annex B through the leakage current. With the latter method, the deduced carrier density is 40 times larger and the mobility ( $\mu_G$ ) is then around  $0,6 \text{ cm}^2 \cdot \text{V}^{-1} \cdot \text{s}^{-1}$  at room temperature. The Hall signal being very noisy, that could involve a significant uncertainty on  $R_H$ , the mobility would remain close to  $20 \text{ cm}^2 \cdot \text{V}^{-1} \cdot \text{s}^{-1}$  even by considering the smallest possible slope for the presented data. The origin of weak Hall signal is also accredited to contact resistance in the literature, that should not be a major issue as we pointed out in the previous chapters particularly low interface resistance in our samples. Furthermore, the charges counting from the leakage current analysis is likely overestimated, as only a part of carriers are indeed involved in the current transport. Therefore, the mobility  $\mu_G$  may be underestimated. In the end, it seems reasonable to assign both methods as upper and lower limits of the effective mobility ( $\mu_{eff}$ ) and then  $\sim 1 \text{ cm}^2 \cdot \text{V}^{-1} \cdot \text{s}^{-1} < \mu_{eff} < \sim 20 \text{ cm}^2 \cdot \text{V}^{-1} \cdot \text{s}^{-1}$ .

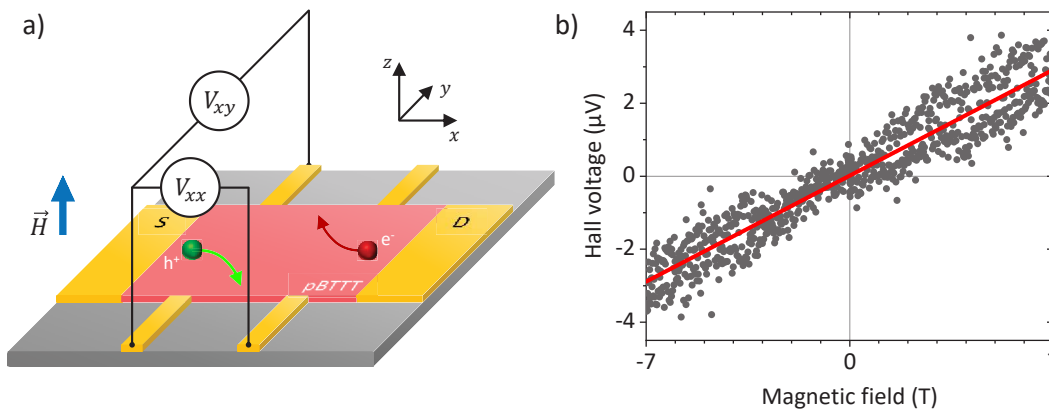


**Figure D.1** a) Hall bar geometry with the current flowing in the positive  $x$ -direction and the magnetic field pointing up in the  $z$ -direction. The channel length is  $400 \mu\text{m}$ , its width is  $150 \mu\text{m}$  and the thickness is  $25 \text{ nm}$ . b) Hall voltage after the subtraction of the symmetric contribution from  $V_{xx}$ . A clear linear dependence on the magnetic field is observed.

The mobility in electrolyte-gated pBTTT remains hard to determine, but the Hall voltage detection is already an important outcome as it is another sign of metallic-like transport in the organic channel. These results are reported in the paper<sup>7</sup>. More measurements, by reversing the source-drain voltage for instance would be necessary to confirm this result.

**Bibliography**

- (1) Dayen, J. F.; Faramarzi, V.; Pauly, M.; Kemp, N. T.; Barbero, M.; Pichon, B. P.; Majjad, H.; Begin-Colin, S.; Doudin, B. Nanotrench for Nano and Microparticle Electrical Interconnects. *Nanotechnology* **2010**, *21* (33).
- (2) Seeger, K.; Gill, W. D.; Clarke, T. C.; Street, G. B. Conductivity and Hall Effect Measurements in Doped Polyacetylene. *Solid State Commun.* **1978**, *28* (10), 873–878.
- (3) Yamashita, Y.; Tsurumi, J.; Hinkel, F.; Okada, Y.; Soeda, J.; Zaja, czkowski, W.; Baumgarten, M.; Pisula, W.; Matsui, H.; Müllen, K.; et al. Transition between Band and Hopping Transport in Polymer Field-Effect Transistors. *Adv. Mater.* **2014**, *26* (48), 8169–8173.
- (4) Wang, S.; Ha, M.; Manno, M.; Daniel Frisbie, C.; Leighton, C. Hopping Transport and the Hall Effect near the Insulator-Metal Transition in Electrochemically Gated Poly(3-Hexylthiophene) Transistors. *Nat. Commun.* **2012**, *3*, 0–6.
- (5) Senanayak, S. P.; Ashar, A. Z.; Kanimozhi, C.; Patil, S.; Narayan, K. S. Room-Temperature Bandlike Transport and Hall Effect in a High-Mobility Ambipolar Polymer. *Phys. Rev. B - Condens. Matter Mater. Phys.* **2015**, *91* (11), 1–16.
- (6) Kang, K.; Watanabe, S.; Broch, K.; Sepe, A.; Brown, A.; Nasrallah, I.; Nikolka, M.; Fei, Z.; Heeney, M.; Matsumoto, D.; et al. 2D Coherent Charge Transport in Highly Ordered Conducting Polymers Doped by Solid State Diffusion. *Nat. Mater.* **2016**, *15* (5), 896–903.
- (7) Zanettini, S.; Chaumy, G.; Chávez, P.; Leclerc, N.; Etrillard, C.; Leconte, B.; Chevrier, F.; Dayen, J.-F.; Doudin, B. High Conductivity Organic Thin Films for Spintronics: The Interface Resistance Bottleneck. *J. Phys. Condens. Matter* **2015**, *27* (46), 462001.





# Tunable metal-organic interfaces for spin electronics

## Résumé

L'objet de cette thèse est l'étude de l'interface entre les métaux et les matériaux organiques, avec pour objectif la réalisation de vannes de spin organiques. Pour ce faire, nous avons étudié des transistors organiques à effet de champ à grille électrolytique dans une structure planaire, et analysé leurs propriétés de transport et d'interface sous l'application de différents stimuli (température, dopage, champ magnétique...). Cette structure nous permet de nous rapprocher des conditions optimales pour l'injection et la détection de spin, mais elle nous a amenés à revoir la définition standard de la propriété intrinsèque des interfaces. Nous avons mis en évidence une résistance spécifique de contact particulièrement faible qui décroît avec la miniaturisation des dispositifs, ainsi que la magnétorésistance des résistances (spécifiques) d'interface.

Mots clés : polymère conjugué, électronique organique, spintronique organique, résistance d'interface.

## Abstract

This thesis studies the interface between metals and organic materials, aiming the realization of organic spin-valves. To that end, we studied planar electrolyte-gated field-effect organic transistors and analysed their transport and interface properties under the application of different stimuli (temperature, doping, magnetic field...). This structure allowed us to approach the optimal conditions for spin injection and detection but led to redefine the standard intrinsic property of interfaces. We exhibited a very low specific contact resistance, that decreases with the downscaling of the devices, and the magneto-resistance of specific interface resistances.

Keywords: conjugated polymer, organic electronics, organic spintronics, interface resistance.